

ISSN 0377-9416



[www.pmai.in](http://www.pmai.in)

# TRANSACTIONS OF POWDER METALLURGY ASSOCIATION OF INDIA

Vol. 42 No.1, June 2016

Chief Editor - P. Ramakrishnan



ISSN 0377-9416



[www.pmai.in](http://www.pmai.in)

**Vol. 42 No.1, June 2016**

Chief Editor - P. Ramakrishnan



## **Powder Metallurgy Association of India**

### **Office Bearers**

#### **President**

Shri N. Gopinath

#### **Vice President**

Shri Deepak Grover

Shri Narendra Dhokey

Shri Rajendra Sethiya

#### **General Secretary**

Dr. Deep Prakash

#### **Hon. Treasurer**

Dr. Murli Gopal Krishnamoorty

#### **Joint Secretary**

Shri Aniket Gore

Shri Rajat Varshney



### Chief Editor

Prof. Ramakrishnan P.

### Editorial Advisory Board

Dr. Ashok S.

Mr. Chandrachud N.L.

Dr. Rama Mohan T. R.

### Editorial Board

Dr. Appa Rao G.

Dr. Bhargava Parag

Dr. Dabhade Vikram

Dr. Deep Prakash

Dr. Dhokey N.B.

Dr. Kumar Y.V.S.

Dr. Malobika Karanjai

Dr. Murli Gopal K.

Dr. Panigrahi B.B.

Dr. Sastry I.S.R.

Dr. Tarasankar Mahata

Published by :

### Powder Metallurgy Association of India (PMAI)

1002, B-Wing, Kingston, High Street, Hiranandani Complex, Powai, Mumbai - 400076.

Tel. : +9122 25704588

E-mail : info@pmai.in

Neither the Powder Metallurgy Association of India nor the editor assumes responsibility of opinions expressed by the authors of the papers published in this transaction.

# Editorial



The PM16, International Conference on Powder Metallurgy and Particulate Materials along with the Trade Exhibition and 42<sup>nd</sup>. Annual Technical Meeting of PMAI held at Hotel Hyatt Regency, Pune during Feb. 2016 was a great success. Selected papers from this event is included in this issue of *Trans. PMAI, Vol.42, No.1, 2016*. The first article by Mr. Gopinath, President PMAI is on Status of Indian PM industry followed by an Overview of the Status and Trends in European PM industry by Dr. Cesar Molins, Vice President EPMA and Status of PM in Taiwan by

Mr.C.L.Chu, President of Taiwan Powder Metallurgy Association. The next paper is on the warm compaction of engineered steel powders, resulting in densities exceeding  $7.4\text{g/cm}^3$  for high density components along with the cost competitiveness. Preparation and characterization of nano-crystalline alumina powders produced by sol-gel process is the subject matter of the following article. The next two papers are on the Titanium powder metallurgy for the bio medical applications. First one is on the effects of Fe and Mo content on the microstructure and mechanical properties of Ti-Mo based alloys prepared by elemental blend and mechanical alloying and the second one on the experimental investigations of compressibility and mechanical properties of Ti powder metallurgy components. This is followed by an article on additive manufacturing for automotive applications which will result in assemblies thereby cutting the supply chains with inherent cost and time saving. The next article deals with the dimensional control in powder metal parts, suggesting suitable compositions to get maximum stability and provide good dimensional precision for heat treated as well as for sinter hardened condition. This is followed by a paper dealing with the studies on the effect of Nb on sintering and properties of gas atomized MIM440C made by pre-alloy as well as master alloy routes and concluded that both approaches are suited to produce high performance components to close tolerances with excellent control of carbon leading to uniform shrinkage and predictable properties.

Experimental evaluation of sintered properties for sintering time and modulus density and hardness of  $\text{Al/SiC}_p$  composites have been dealt with in the next article. Followed by an article on the development of  $\beta$  -  $\text{FeSi}_2$  by mechanical alloying and the response of the same to hot pressing. The effect of cyclic heat treatment and swaging of Mo and Co containing heavy alloys have resulted in the improvement in mechanical properties is discussed in the next paper. Synthesis of nano structured duplex and  $\text{Y}_2\text{O}_3$  dispersed duplex stainless steel modified carbon paste by mechanical alloying for the detection of dopamine is covered in the following article. The next paper is on the synthesis and evaluation of mechanical behavior of MA-6061Al- $\text{Al}_2\text{O}_3$  nano-composite. Improvement in transparency of Nd:YAG ceramics through hot pressing is covered in the next paper. This is followed by two articles on the nuclear materials, the first one on the development of Li based ceramics for breeder application and the other on the fabrication of  $(\text{Th,Pu})\text{O}_2$  MOX fuel pellets using POP and CAP process for experimental irradiation in research reactor. The final paper is an effort to increase the corrosion behavior of Co-Cr-Mo alloy with laser engineered net shaping and heat treatment.

**P. Ramakrishnan**

TRANSACTIONS OF  
POWDER METALLURGY ASSOCIATION OF INDIA

Vol. 42 No.1, June 2016

CONTENTS

<b>1</b>	<b>Status of Indian PM Industry</b> <i>N. Gopinath</i>	<b>1-3</b>
<b>2</b>	<b>Overview of the Status and Trends in the European PM Industry</b> <i>Cesar Molins</i>	<b>4-7</b>
<b>3</b>	<b>Status of PM in Taiwan</b> <i>C. L. Chu</i>	<b>8-10</b>
<b>4</b>	<b>Enhanced Processing Developments in Steel Powders</b> <i>Bruce Lindsley, Fran Hanejko and Cecilia Borgonovo</i>	<b>11-20</b>
<b>5</b>	<b>Preparation and Characterization of Nano-Crystalline <math>\alpha</math>-Al<sub>2</sub>O<sub>3</sub> Powder by Sol-Gel Process</b> <i>V. Rathod, C. Jariwala, R. Pillai, D.K. Basa and B. Sarkar</i>	<b>21-24</b>
<b>6</b>	<b>Effects of Fe and Mo Content on the Microstructure and Mechanical Properties of Ti-Mo based alloys prepared by Elemental blend and Mechanical alloying technique</b> <i>P. Mohan, A. Amigo, V. Amigo</i>	<b>25-31</b>
<b>7</b>	<b>Experimental Investigation of the Compressibility and Mechanical Properties of Cp-Ti Powder Metallurgy Components</b> <i>Arunangsu Das, Susenjit Sarkar, Malobika Karanjai, Goutam Sutradhar</i>	<b>32-38</b>
<b>8</b>	<b>Additive Manufacturing for Making Fully Dense Automotive Parts</b> <i>S. R. Sundaram</i>	<b>39-44</b>
<b>9</b>	<b>Dimensional Control in Powder Metal Parts</b> <i>Fran Hanejko, Bruce Lindsley, Kalathur. S. Narasimhan and Mahesh Kamble</i>	<b>45-52</b>
<b>10</b>	<b>Studies on the Effects of Nb on Sintering and Properties of MIM 440C made by Prealloy and Master Alloy Routes</b> <i>Martin A. Kearns, Mary-Kate Johnston, Keith Murray, Paul A Davies, Viacheslav Ryabinin and Erainy Gonzalez</i>	<b>53-62</b>
<b>11</b>	<b>Experimental Evaluation of Sintered Properties for Sintering Time and Modulus on Density and Hardness of Al/SiCp by PM Process</b> <i>K.C. Nayak, K.K. Rane, Girish N Kotwal, P.P. Date</i>	<b>63-67</b>
<b>12</b>	<b>Development of Thermoelectric <math>\beta</math>-FeSi<sub>2</sub> by Mechanical Alloying and its Response to Hot Press Sintering</b> <i>N. B. Dhokey, V. S. Poddar, N. B. Revade, Rohit Garbade, Priyanka Lalge, S. P. Butee, R. D. Purohit, Deep Prakash</i>	<b>68-76</b>

<b>13</b>	<b>Effect of Cyclic Heat Treatment and Swaging on Mechanical Properties of Molybdenum and Cobalt Containing Tungsten Heavy Alloys</b> <i>U. Ravi Kiran, M. Sankaranarayana, G. V. S. Nageswara Rao, T. K. Nandy</i>	<b>77-82</b>
<b>14</b>	<b>Fabrication of Planetary Milled Nano-structured Duplex and Y<sub>2</sub>O<sub>3</sub> Dispersed Duplex Stainless Steel Modified Carbon Paste Electrode for the Detection of Dopamine</b> <i>R. Shashanka, D. Chaira, B.E. Kumara Swamy</i>	<b>83-93</b>
<b>15</b>	<b>Synthesis and Evaluation of Mechanical Behavior of MA 6061Al-Al<sub>2</sub>O<sub>3</sub> Nanocomposite</b> <i>Nitika Kundan, Arpit Khemka, P. R. Soni</i>	<b>94-100</b>
<b>16</b>	<b>Improvement in Transparency of Nd:YAG Ceramics through Hot Press Sintering</b> <i>S P Butee, K R Kamble, Prashant Dixit, M D Joshi, S A Dhawanjewar</i>	<b>101-108</b>
<b>17</b>	<b>Development of Lithium Based Ceramics for Breeder Application</b> <i>Sathi R. Nair, Amit Sinha and P. K Sinha</i>	<b>109-114</b>
<b>18</b>	<b>Fabrication of (Th, Pu)O<sub>2</sub> MOX Fuel Pellets Using POP and CAP Process for Experimental Irradiation in Research Reactor</b> <i>A. K. Mishra, P. M. Khot, S. K. Shotriya, K. Subbaraya, Niraj Kumar, B. Singh, B.Surendra, P. G. Behere, Mohd Afzal</i>	<b>115-120</b>
<b>19</b>	<b>Influence of Heat Treatment on Corrosion Behavior of Co-Cr-Mo Alloy Deposited with Laser Engineered Net Shaping</b> <i>Dr. Mantrala Kedar Mallik, Sk. Abdul Munaf</i>	<b>121-125</b>

# A REVIEW OF PM IN INDIAN INDUSTRY: OPPORTUNITIES AND CHALLENGES

N. Gopinath

President, PMAI

## Introduction:

PM in Indian Industry may be linked with automotive industry, since this is the largest consumer of P/M parts. In this context, it is interesting to note that Indian automotive industry maintains a promising place among global manufacturers, and its World Ranking is as below:

- The Largest Tractor manufacturer
- 2<sup>nd</sup> Largest Two-wheeler manufacturer
- 2<sup>nd</sup> Largest Bus manufacturer
- 5<sup>th</sup> Largest Heavy Truck manufacturer
- 6<sup>th</sup> Largest Car manufacturer
- 8<sup>th</sup> Largest Commercial Vehicle manufacturer

Fig. 1 shows the total sales of vehicle of top ten countries in the world in years 2013-14 and 2014-15. Indian sales was steady at 3.2 million in the last two years. China was leader (23.5 M) in 2014-15, followed by USA (16.8 M), Japan (5.6 M), Brazil (3.5 M), Germany (3.4 M), India, UK (2.8 M), France (2.2 M), Canada (1.9 M) and South Korea (1.7 M). Fig. 2 (a - b) shows Indian statistics of vehicle production in 2014-15. These data are indicative of significant P/M industry as well as its robust growth potential.

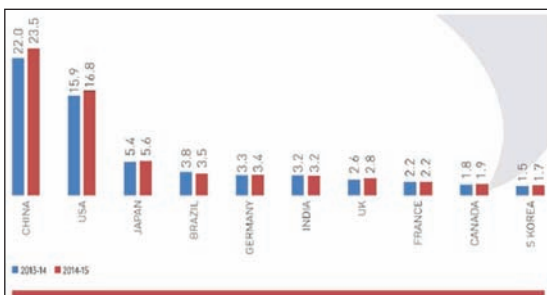


Fig. 1. Vehicle sales-Top 10 countries (in millions)  
Source: ACMA annual report 2014-15

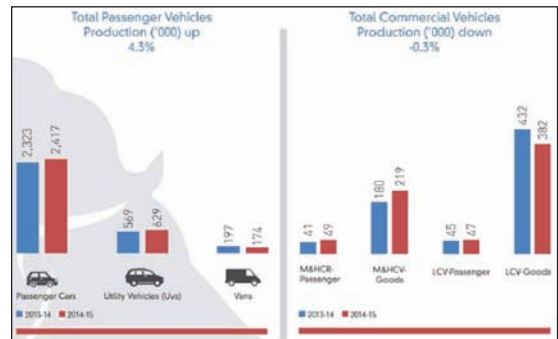


Fig.2 (a): Indian Vehicle Production (Passenger and Commercial vehicles)

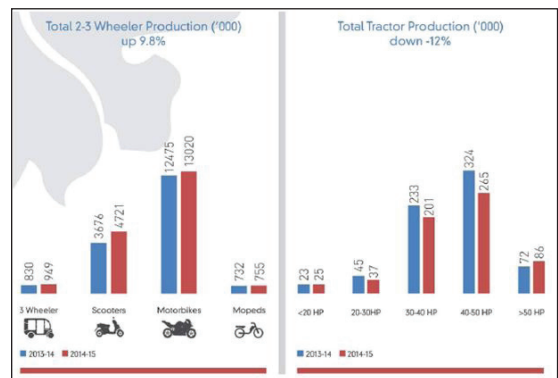


Fig.2 (b): Indian Vehicle Production (Two/Three wheelers and Tractors)

## PM Parts Production:

PM metallic parts produced in India are shown in Fig. 3 and Table - 1. Production of total parts including Iron based as well as copper based peaked at ~ 50,000 tons in Year 2011, and decreased to ~40,500 tons in 2015. Small scale industry produces approximately 95% iron based and 5% copper based parts. In the iron based parts, major share (80%) is automotive parts, whereas appliances, bush bearings and

other electrical/ mechanical parts constitute 8%, 5% and 7%, respectively (Fig.4). On the other hand, copper based parts mainly contribute towards domestic appliances (80%), followed by automotive sector (10%) (Fig.5).

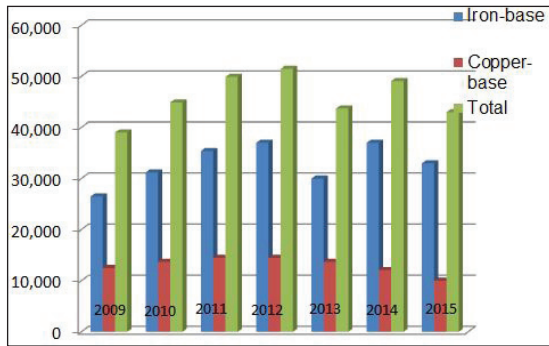


Fig.3: Production of Iron and copper based P/M parts in India (tons/year)

India Data -- All PM applications (estimate)							
	2009	2010	2011	2012	2013	2014	2015
Production Weight:							
Iron-base	26,500t	31,200t	35,400t	37,000t	30,000t	37,000t	30,500t
Copper-base	12,500t	13,700t	14,500t	14,500t	13,700t	12,100t	10,000t
Total	39,000t	44,900t	49,900t	51,500t	43,700t	49,100t	40,500t

Table 1 : Production of Iron and copper based P/M parts in India (tons/year)

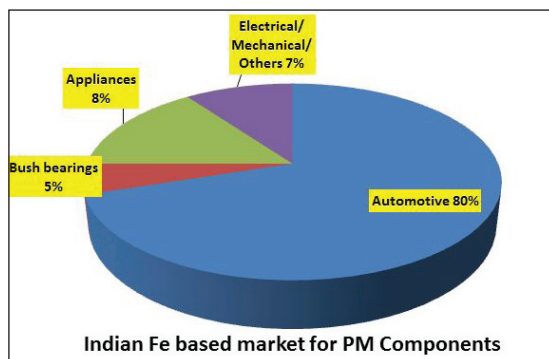


Fig.4: Production of Iron based P/M parts in India

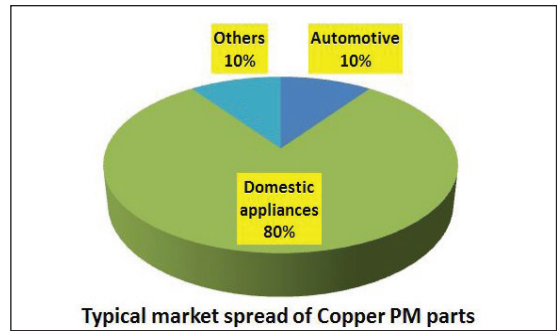


Fig.5: Production of copper based P/M parts in India

There are approximately 140 P/M related industries in India that include metal powder manufacturers, part producers and equipment manufacturers (Table – 2).

Number of Manufacturers:	2009	2010	2011	2012	2013	2014	2015
PM Products	50	50	50	52	53	53	65*
Metal Powders	30	30	30	31	31	28	28
Equipment	40	40	40	42	42	52	52

Table – 2: P/M related industries in India

### Opportunities in Indian P/M industry:

Automobile industries market in India shows promising growth and turnover which might be taken as optimistic trend for P/M industry (Table – 3). Various automobile manufacturers in India, indigenous as well as foreign companies, are giving impetus to compact cars. In this context they have invested large funds to increase locally manufactured content and thereby creating global competence (Table – 4). This opens up new opportunity for P/M industry. Some of the new parts which might be produced by P/M route in automotive applications are as following:

- VVT parts
- Cam lobes
- High strength speed gears
- Powdered forged parts like connecting rods, synchro rings

## A REVIEW OF PM IN INDIAN INDUSTRY: OPPORTUNITIES AND CHALLENGES

- Stainless steel parts for exhaust systems, EGS and turbo chargers

Other opportunities by Indian P/M industry are to adapt newer and more efficient processes, such as:

- Multi Platen CNC Advanced Compaction presses typically up to 500 Tons or Higher to 800 tons
- Warm compaction / warm die compaction systems with advanced lubricant mixes for high density single compaction single sintering parts
- High temperature (1300°C ) sintering capability for high performance parts, stainless steel parts and improved usage of Manganese / Chromium alloy powders
- Surface Densification Facilities
- Powder Forging Facilities
- Improved and reliable machining facilities

Another area may be P/M aluminium, where various applications such as engine parts, transmission, compression, hydraulics, electrical and optical components may be initiated.

Metal injection moulding (MIM) is another emerging field; this process is capable of manufacturing various intricate parts. Further, there are tremendous possibilities in another emerging area, additive manufacturing.

### Challenges to Indian P/M industry:

Though good opportunities exist for Indian P/M industry, they need to take up some forthcoming challenges such as:

- High cost of capital equipment and tooling in the face of inadequate initial volumes
- OEMs want parts after all the tests required for initial source approval at competitive terms

- Availability of trained technical manpower for pre- production engineering activities and also to run critical shop floor operations like compaction and sintering
- Low awareness of PM Technology and 'Think PM' approach at OEMs

Figures in INR' 00 Crs						
	2009-10	2010-11	2011-12	2012-13	2013-14	2014-15
Turnover	1,386	1,883	2,046	2,160	2,117	2,348
Growth rate(%)	25.3	35.9	8.7	5.6	-2.0%	11.1%
Export	189	303	427	526	614	685
Growth rate(%)	-19.2%	60.3%	40.9%	23.2%	16.7%	11.4%
Import	360	497	667	744	771	829
Growth rate(%)	-4.3%	38.1%	34.2%	11.5%	3.6%	7.5%
Investment	77	91-102	72-92	69-95	32-44	20-28

Table - 3 : Automobile industry market in India

Table - 4: Capacity and investment of leading auto manufacturers in India

Sl. No.	Auto Manufacturer	Capacity	Investment (US \$)
1.	Maruti Suzuki	25,00,000	380 million
2.	Hyundai	6,00,000	2 billion
3.	Tata Motors	5,00,000	240 million
4.	Toyota	2,00,000	310 million
5.	Ford	2,00,000	500 million
6.	General Motors	1,40,000	650 million
7.	Nissan - Renault	4,00,000	1 billion
8.	VW	1,10,000	750 million
9.	Honda	60,000	250 million

### Summary:

In summarising it may be concluded that the growth of Indian P/M industry appears to be promising which may be due to robust and growing auto industry. In this context, it may be further seen that there are some futuristic developments in auto industry on the cards – such as electric cars, hybrid vehicles and driverless cars.



# OVERVIEW OF THE STATUS AND TRENDS IN THE EUROPEAN PM INDUSTRY

Cesar Molins

Vice-President EPMA

## Introduction - European economic magnitudes:

The status and trends in the European PM industry can be seen in the perspective of major European economic magnitudes. In the last five years, European economy has seen a growth pattern, although very small, as shown in Fig.1. The EU GDP growth rate has registered a positive trend, albeit very small, as compare to negative values of 2013. Further, the commodities remained at lowest level since 2002 (Fig. 2). Nonetheless, other major economic factors such as oil and coal prices were found sharply declined, which has been a reason for moderate industrial drive [Fig.3 (a-b)].

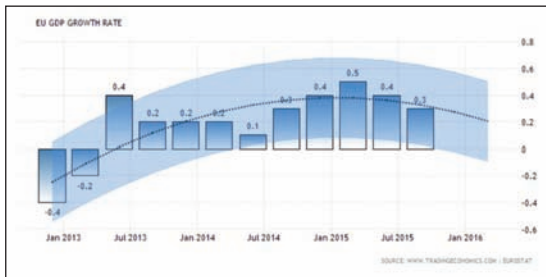


Fig.1: EU GDP growth rate, from 2013 to 2016

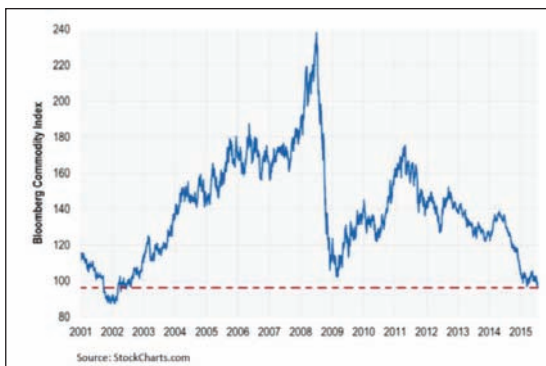


Fig.2: Commodity Index, from 2001 to 2015

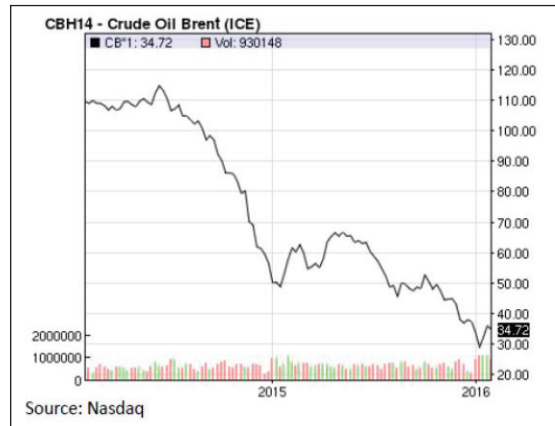


Fig.3(a): Crude Oil Brent, yearwise

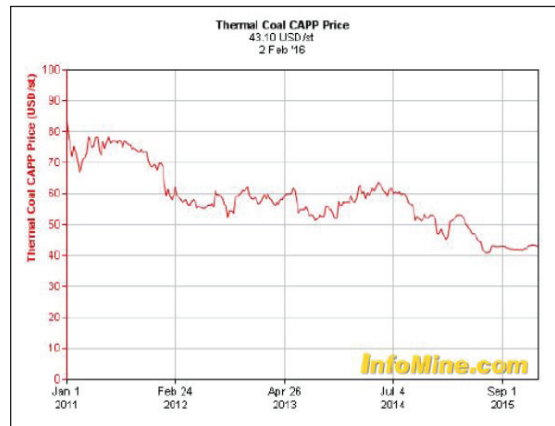


Fig.3(b): Thermal coal price

## European PM industry figures

Industrial growth recovery has also been effective PM industry. One major driver in the industry has always been automobile sector. Fig. 4 (a-b) shows that the European car production as well as registration were back to growth trend. As is well known, parts made

## OVERVIEW OF THE STATUS AND TRENDS IN THE EUROPEAN PM INDUSTRY

by PM are important constituent to automobile. In the years 2008-14, PM parts per cars made in Europe continued to increase (Fig.5). This trend is helpful for PM industry. Europe possesses a strong PM supply chain, consisting of powder manufacturers, equipment manufacturers, part makers as well as research centres. Europe has production sites of two of the largest powder manufacturers in the world. Besides, last few years have also witnessed growth of some specialty powder manufacturers. In addition, several of the world's well known equipment manufacturers are concentrated in Europe. The equipment manufacturers responded to strong world competition with more sophisticated machines. In order to gain technological, market and financial strength, some mergers have taken place. Overall, equipment sales recorded a growth pattern.

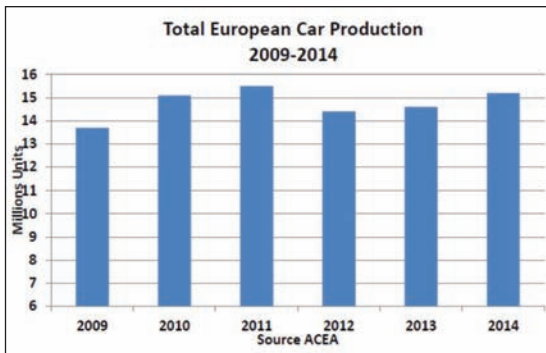


Fig. 4(a): Total European Car Production, 2009-2014.

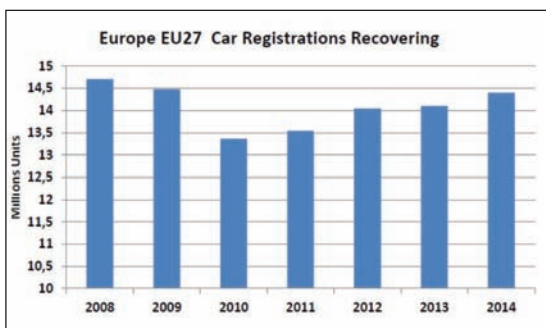


Fig. 4(b): European Car registrations, 2008-2014.

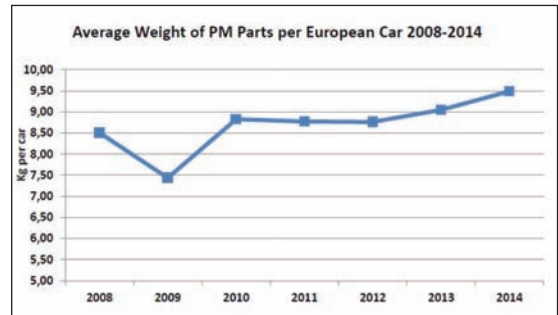


Fig. 5: Average weight of PM parts per European car, 2008-2014.

### Main PM technological trends

European PM Industry appears to be strong and sustained industry. In the year 2014, the total PM parts produced in EU were 228 ktonnes, the largest part being structural ferrous parts, 81% and 1% MIM parts, which is significant, MIM being relatively newer technology (Fig. 6). Value wise, the total PM parts were estimated to be ~ €10.2 billion, and the high technology fabricated parts such as MIM and HIP contributing 3% each (Fig.7). Sector wise, structural parts as well as hard materials were steady (Fig.8-9), whereas MIM and additive manufacturing recorded increasing trends (Fig. 10-11). Additive manufacturing sector of PM needs special mention. It is to be noted here that for AM, Europe has strong position across supply chains, the revenue form metals for AM has been in continued growth. Further, many application are foreseen in aerospace and other sectors. EPMA has recently formed the European Additive Manufacturing Group with over 30 members.

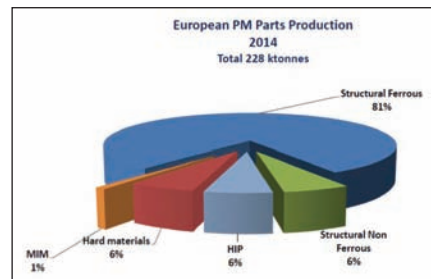


Fig. 6: European PM parts production, 2014.

## OVERVIEW OF THE STATUS AND TRENDS IN THE EUROPEAN PM INDUSTRY

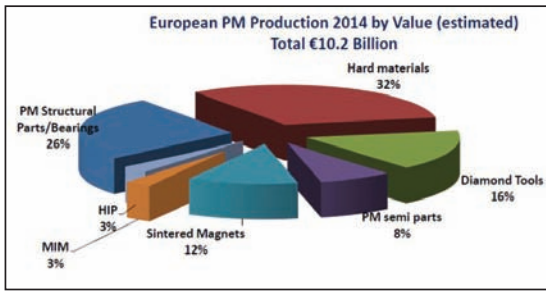


Fig. 7: European PM production, value wise, 2014.

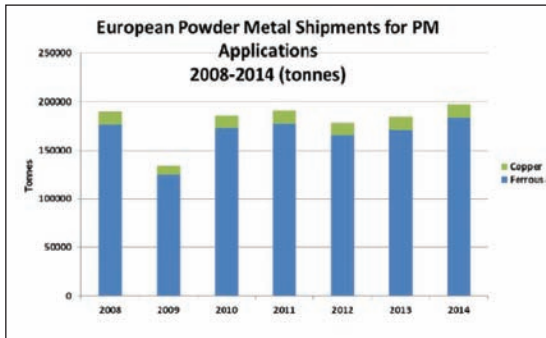


Fig. 8: European structural PM parts, 2008-2014.

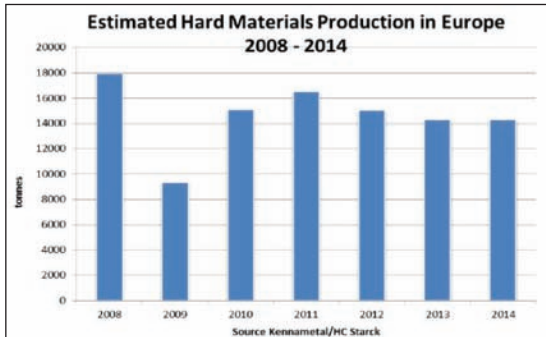


Fig. 9: European hard materials production, 2008-2014.

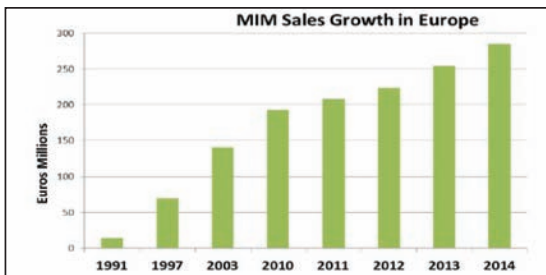


Fig. 10: MIM sales growth in Europe, 1991-2014.

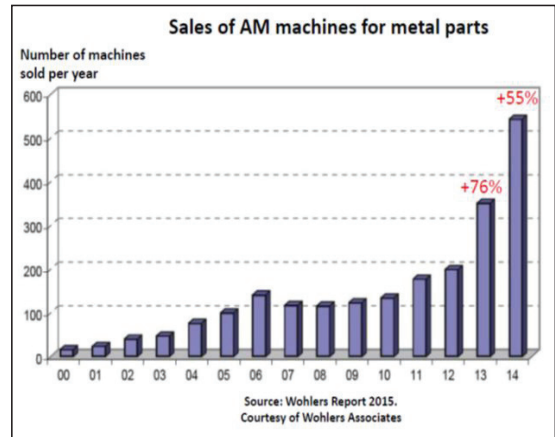


Fig. 11: Sales of AM machines.

Europe also has powerful research and development network for PM. Due to historic and strategic reasons, European PM research is strong in many countries viz. Germany, Spain, Austria, Sweden, Italy, France, UK, Czech Republic, Romania etc. Across Europe, there are at least 20 significant centres of PM academic research. This is besides numerous independent R&D suppliers and R&D centres of large commercial companies. There are strong links to all sectors of PM industry across the supply chain. Various cooperative research projects are in progress involving several countries, industrial partners, universities and research centres.

PM technological trends in Europe can be summarised as following''

- Strong cooperative push to prove PM as a viable technology for main gearbox gears.
- Development of surface densification as fatigue improvement technology.
- VVT applications in growing demand require sophisticated machining including green machining and very high tolerances.

## OVERVIEW OF THE STATUS AND TRENDS IN THE EUROPEAN PM INDUSTRY

---

- New lubricants capable of lubricating at reduced amounts to reach higher compacting densities.
- Increasing electrification of vehicles seem to call for new soft magnetic applications, but scope is still unclear.
- Developments in bimetal high-performance bushings.

### **Conclusions**

In conclusion it can be said that the European PM industry is evolving positively. Some mergers and some casualties taken place recently as a result of economic crisis and stronger demands on technology. Technological revolution is witnessed in all fields of PM- raw materials and lubricants, equipments, part production and emerging PM forming routes like AM, MIM and HIP.



# STATUS OF P/M IN TAIWAN

C. L. Chu

President, TPMA

## Introduction:

Powder Metallurgy Industry has been more than four decades old in Taiwan. This paper overviews the status of powder metallurgy in Taiwan. That includes the current PM market, emerging MIM market, application of PM parts in different sectors, and the strategy of promoting PM in Taiwan as adapted by the Taiwan Powder Metallurgy Association.

## PM market in Taiwan:

PM production in Taiwan started in 1968. By the year 2015, the total production of PM parts and components reached ~32,000 tons, the major share occupied by iron based parts (Table-1). Of the all parts produced by PM, the majority were used for Transportation sector.

There are currently 4 manufacturers of metal powders, 60 manufacturers making various types of PM products and 10 engaged in related equipment in the country. The PM market in Taiwan is largely export oriented, around 85% of the parts produced are exported and only 15% are used for domestic consumption. Fig.1 shows sales of various PM parts sectorwise.

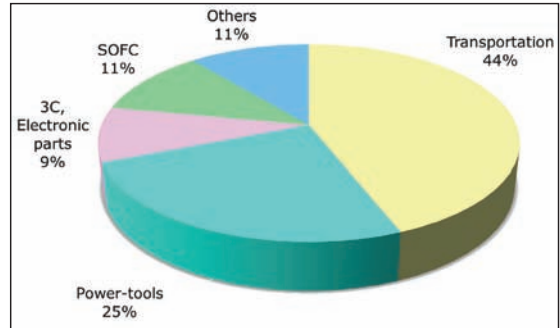


Fig.1: Sales of PM parts produced in Taiwan.

## MIM in Taiwan:

Taiwan PM industry has taken early initiative in emerging metal injection moulding (MIM) technology. Currently there are over 30 MIM producers in the country. The total sales of MIM parts is estimated to be over US\$ 200M in 2015. Out of all MIM parts produced, the largest share belong to components of mobile phones(55%), followed

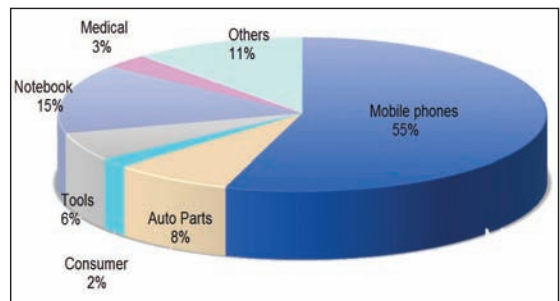


Fig.2: MIM parts application in Taiwan.

	2008	2009	2010	2011	2012	2013	2014	2015
<b>Production weight</b>								
Iron-Base	23000t	18000t	24,000t	27,000t	26,000	29,000	30,000	30,250
Copper Base	1800t	1350t	1,800t	1,800t	1,200	1,500	2,000	1,705
Total	24800t	21500t	25,800 t	28,800t	27,200	30,500	32,000	31,955
<b>Application Field Ratio</b>								
Transportation Machine	30%	35%	34%	35%	40%	45%	38%	44%
Industry Machine	40%	33%	39%	39%	24%	25%	25%	25%
Electronic Machine	25%	19%	15%	16%	7%	10%	9%	9%
Others	5%	13%	11%	10%	29%	20%	28%	29%
<b>Number of Manufactures</b>								
PM Products	60	50	48	51	52	55	58	60
Metal Powders	3	3	3	3	4	4	4	4
Equipments	10	10	10	10	10	10	10	10

Table-1: Summary of PM Market in Taiwan

by Notebook computers (15%), whereas auto parts, consumer durables, tools and medical applications comprise of 8%, 2%, 6% and 3%, respectively (Fig.2).

**Application of PM parts:**

Parts and components made by PM route are used in a variety of applications. Some of them are – micro bearings, auto parts, power tools and SOFC etc. Fig.3 shows some micro bearings. Examples of MIM parts are some components for minimal invasive surgery, head-up auto navigation display holder, hollow turbine wheel, hinge of convertible roof in car etc. as shown in Fig. 4 (a-d).



*Fig.3: Microbearings made by powder metallurgy route.*



*Fig. 4(c): Hollow turbine wheel (Inconel 713C)*



*Fig. 4(a): Component for surgery*



*Fig. 4(d): Hinge for convertible roof of car*



*Fig. 4(b): Navigation display holder (SS 316L)*

As state earlier, PM parts find application in various fields, some more examples include power tools, auto parts and SOFC. Fig. 5 - 6 show some of these components.



*Fig. 5: PM parts for power tools*

## STATUS OF P/M IN TAIWAN



6 (a)



6 (b)



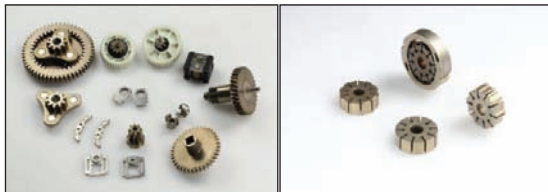
6 (c)



6 (d)



6 (e)



6 (f)



6 (g)

*Fig. 6: PM parts for automobile applications, (a) synchroniser hub (b) pulley (c) VVT, engine (d) seat adjustment (e) steering column (f) power window (g) oil pump*

### Promoting PM in Taiwan:

Taiwan Powder Metallurgy Association was founded in 1981 and since then it has been striving to promote PM in Taiwan. Currently it has 80 companies and 199 individual members. It carries out PM short courses and meetings for research, academy and industry interactions and brings out four issues of Bulletin of Powder & Powder Metallurgy every year.

### Summary:

In conclusion, it can be said that PM in Taiwan is a growing industry with emerging technological trends. There is a robust mechanism for research, academy and industry convergence and looking forward to international cooperation.



# ENHANCED PROCESSING DEVELOPMENTS IN STEEL POWDERS

Bruce Lindsley, Fran Hanejko and Cecilia Borgonovo

Hoeganaes Corporation, Cinnaminson, NJ 08077

**Abstract:** Powder Metallurgy is a cost effective manufacturing route for many automotive and industrial components, and its use in India is expected to expand in the coming years. Engineered powders with enhanced attributes are an important tool being used to help drive this expansion. Hoeganaes Corporation continues to develop and expand its product line to empower parts makers to produce components more efficiently and drive density to higher levels to achieve improved performance. Warm die compaction with AncorMax 225 enables green and sintered densities in excess of 7.4 g/cm<sup>3</sup> at compaction pressures of approximately 750 MPa. This new advanced premixing technology is currently being utilized in the production of high density automotive and non-automotive ferrous components. Additionally, improved PM steel machinability is an ongoing focus as part tolerances become tighter, thereby requiring machining for production of the final part. The machining enhancer AncorCut improves both turning and drilling operations in PM components made with different alloy grades.

## Introduction

PM components are widely used in the automotive and off highway industries. Often, PM is preferred for parts that are characterized by intricate shapes, attainable directly after press and sinter. Porous PM components pose some challenges, however, as machinability is often different than fully dense materials. Additionally, certain mechanical properties that are especially sensitive to density may limit the use of PM. Both powder and component manufacturers strive to improve the performance of PM, enabling greater market penetration and increased value.

While the PM process produces net or near-net shape components, many parts are machined to deliver high precision features, cross holes, transverse grooves, etc. It is estimated that 40-50% of PM steels require additional machining in applications where wrought steels are normally employed [1]. Components with poor machinability result in higher insert costs, reduced capital utilization and unpredicted downtime. It is known that the machinability of PM steels differs from that of wrought steel due to the presence of porosity and often heterogeneous microstructure [2]. Additionally, PM alloys

typically contain higher levels of carbon (>0.5%) to achieve similar strengths as fully dense wrought products. The resulting higher micro-indentation hardness in combination with the porosity is most responsible for the different machining response of PM compared with wrought steels.

One of the advantages of PM is that machinability enhancers can be incorporated into the powder prior to compaction. Free-machining additives improve machinability by assisting in chip formation, lubrication of the tool face and reduction of both flank and crater wear [2]. The most common additive used is MnS. Many studies have shown the benefits of MnS additions to the machinability of PM steels [2-13]. While manganese sulfide has many beneficial attributes, it has some limitations and potentially negative effects. High humidity environments can quickly oxidize the MnS and deteriorate the machinability enhancing properties [4-6,10]. Component rusting is accelerated when MnS is present and staining due to lubricant burn out worsens [8]. Chemically inert additives are therefore desirable. A recently introduced machining additive, AncorCut, has proved to be a stable additive as well as provide improved machining performance in PM steels

The ability to produce higher density components increases the number of potential parts that can be made with PM. Achieving high densities (>7.2 g/cm<sup>3</sup>) in powder metallurgy parts can be achieved via double pressing, copper infiltration, die wall lubrication, high pressure compaction, and high velocity compaction [14]. Die wall compaction, high pressure compaction (>1000 MPa) and high velocity compaction are limited because of reduced press speeds, tool breakage issues and inability to produce multi-level components. The typical PM approach of using admixed lubricants has proven to be the most economical approach for the production of PM parts. However, the traditional amounts of lubricants required reduce the maximum attainable green density because lubricants have a density of approximately 1.1 g/cm<sup>3</sup> compared to iron having a density of about 7.85 g/cm<sup>3</sup> [15]. This difference in densities of the lubricant and iron implies that for every 0.1% lubricant added there is a loss in green density of approximately 0.05 g/cm<sup>3</sup>. Thus, for an FC-0208 type material with 0.75% admixed lubricant, the maximum attainable green density is 7.10 to 7.15 g/cm<sup>3</sup>.

Increasing compacted part densities can be achieved by reducing the amount of premixed lubricant; however, reducing the internal lubricant must be done with caution. Simply reducing the amount of the lubricant can result in excessively high ejection pressures with a corresponding unacceptable surface finishes. To facilitate reduced lubricants levels, the high density lubricants used must give the same performance at the reduced level as the traditional lubricants and amounts. A newer lubricant system, AncorMax 225, has been utilized to produce parts with as little as 0.25% internal lubricant. This system requires warm-die compaction, where the die is heated into a range that optimizes the performance of the lubricant. In addition to promoting higher green densities, this new system demonstrates good lubrication, higher apparent densities in premixed powders and higher part green strengths. Additionally, because there is no need for die wall lubrication,

compaction rates are equivalent to lower density PM parts. Component production experience with this advanced lubricant system is discussed.

**Experimental Procedure**

Machining trials were performed in the Machining Laboratory within the Innovation Center at Hoeganaes Corporation. Premixes with no machining additive, 0.35% MnS and 0.2% AncorCut were investigated with several alloy systems, shown below in Table -1. Standard transverse rupture bars and machining rings measuring nominally 45 mm outer diameter, 25 mm inner diameter and 32 mm tall were compacted to 6.9 g/cm<sup>3</sup> density and sintered in an Abbott belt furnace at 1120°C in 90% N<sub>2</sub> - 10% H<sub>2</sub> atmosphere. Time in the hot zone was 45 minutes. The sintered density of the compacts was nominally 6.8 g/cm<sup>3</sup>.

*Table - 1. Alloys studied in the machinability study*

Alloy	Mo	Ni	Mn	Cu	Gr
FC-0208	-	-	0.1**	2.0	0.9
FD-0405	0.5*	4.0*	0.1**	1.5*	0.6
FLC2-4808	1.2**	1.4**	0.4**	2.0	0.9

\* diffusion alloyed, \*\* prealloyed

Turning studies were run using a 0.25 mm depth of cut and 0.25 mm feed at cutting speeds of 150 smm (surface meters/min) for FLC-4808 and 230 smm for FC-0208 and FD-0405. Twenty five cuts were made on each ring so that final diameter of a machined ring was nominally 32 mm. The target number of rings per test was 60, for a total of 1500 cuts per test. For FLC-4808, extended tests were run as tool life exceeded 1500 cuts. The turning tests were run using a Haas ST-10 CNC lathe with no coolant. Machinability was measured as the change in diameter of the machined ring after the first pass using an automated probe within the lathe. This data was then normalized to zero at the start of the test so that the change in part diameter could be observed. An increase

in machined part diameter over several parts is an indicator of tool wear. The tools used in this experiment were an alumina-TiCN coated carbide insert (Kennametal KCP25) in a CNMG 432 FN geometry and a polycrystalline boron nitride (cBN) tipped insert in a CNGA 432 geometry, with a light hone edge preparation, from Shape-Master Tool.

Drilling studies were conducted on a HAAS VF-1 vertical milling center. Maximum torque at 2000 rpm is 12.5 kg-m. A 2 mm tungsten carbide ball stylus 50 mm long from Renishaw was employed to measure variation in diameter. The setup (Fig.1a) involves three specimens (pucks) clamped by an aluminum fixture. The solid pucks had the same dimensions and density as the cylindrical turning samples with the exception of no inner diameter. Every puck can contain 33 holes which leads to a total of 99 holes drilled per cycle. Infinite life has been set at 990 holes (10 cycles).

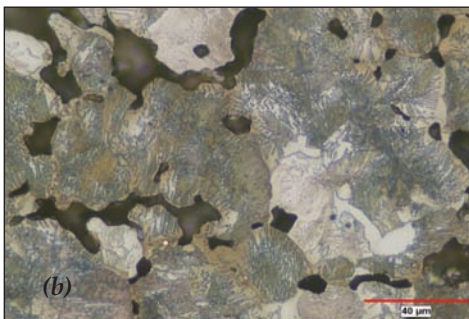
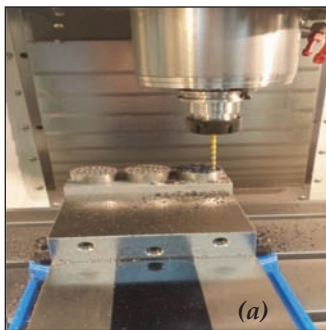


**Fig.1: a) Drilling set up with aluminum fixture; b) Nital etched microstructure. FC-0208.**

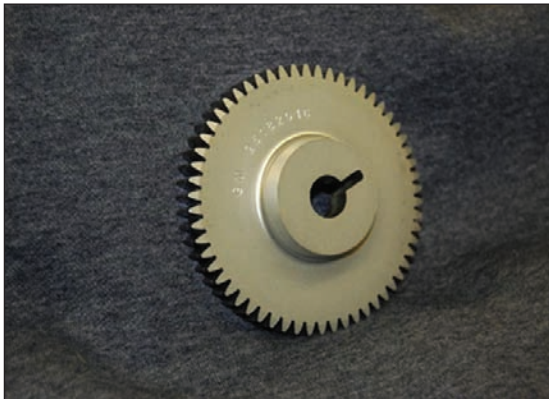
Drill bit diameter was 4.75 mm and depth of drilling about 25 mm. Screw machine length drill bits have been chosen over jobbers to minimize bending and wobbling of the bit. Diameter was probed every 5 – 10 holes depending on tool material. Table 1 also reports speeds, feeds, and coolant conditions (LUBRICUT 4265 diluted with water in a 5:100 ratio has been selected for coolant) used for the investigation.

High density compaction tests and production components were pressed with alloy FLN2-4400, made with a highly compressible base iron Ancorsteel 85 HP (0.85% Mo) and mixed with 2% Ni powder and 0.35% graphite. The AncorMax225 lubricant system also utilizes binder-treatment, so Ni dusting is reduced. Powder flow and apparent density was determined using MPIF standard test methods 3 and 4. Compressibility was determined using standard green strength bars at compaction pressures of 550, 690, and 830 MPa with a die preheat temperature of 107 °C. Laboratory sintering was also done at 1120 °C in a 90% nitrogen – 10% hydrogen atmosphere with conventional cooling. TRS and tensile properties were determined using MPIF test standard methods 41 and 10.

Joint development was performed with Cloyes Gear [16], and during production, the gears shown in Fig. 2 were evaluated for the following key characteristics:

- weight variability
- press tonnage

Both parts were compacted on standard mechanical PM compaction equipment. The tools were modified to incorporate cartridge heating elements into the stress ring of the die. No powder heating was done prior to introducing the powder into the die cavity. To measure the repeatability of the binder-treated premix, multiple set-ups and production runs were completed to insure product and press performance consistency.



2 a. Main running gear, weight ~450 grams



2 b. Sprocket, weight ~1100 grams

Fig.2. Automotive valve train components produced by Cloyes Gear (material: pre-alloyed 0.85% molybdenum steel with 2% nickel, 0.35% graphite (FLN2-4400)[16]

## Results and Discussion

### Turning of FC-0208

The turning comparison of no additive, MnS and AncorCut in FC-0208 are shown in Fig.3. The AncorCut (blue) results in a clear improvement to the no additive (red) condition. As shown later, the time between sintering and machining can play a role in machinability. Tests were run within one day of sinter and after several weeks.

Neither the AncorCut nor the no additive material exhibited any significant change in behavior. The orange curves represent 0.35% MnS material, where two distinct behaviors were observed. The machinability of MnS after 1 day was excellent and found to be slightly better than AncorCut, however, after storage of 3 weeks in closed containers, the MnS performed worse than AncorCut. It is known that MnS has poor shelf life in the powder form, but this is also true of MnS within PM parts. MnS degrades over time causing reduced machinability. This will be explored further in latter parts of the paper. All subsequent machining tests run with MnS were performed within one day of sintering unless otherwise noted.

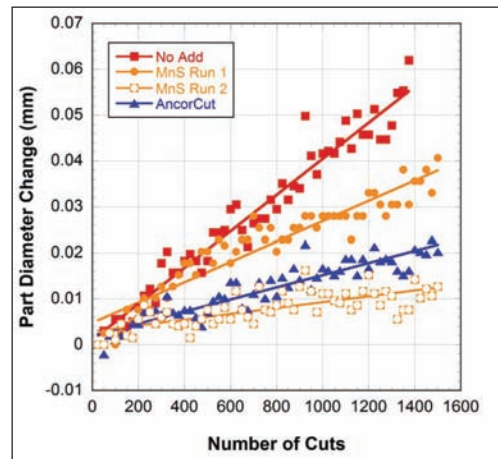


Fig.3. Turning comparison of no additive, AncorCut with MnS after 1 day (run 2) and after 3 weeks (run 1)

### Turning of FD-0405

The 4% Ni diffusion alloy is a popular alloy system for higher performance applications, where compressibility, toughness and robust processing are important. It is also known as an alloy that is difficult to machine given the mixed microstructures of ferrite, pearlite, martensite and Ni-rich austenite present after sintering. Fig. 4 illustrates the difficulty turning this material

with no additive (red). The test did not even reach 200 cuts before tool failure. The addition of machining additive is greatly beneficial for this alloy, as both MnS and AncorCut result in the tests reaching the 1500 cut goal. Less tool wear was observed with AncorCut, indicating that this additive is the better choice for this more highly alloyed material.

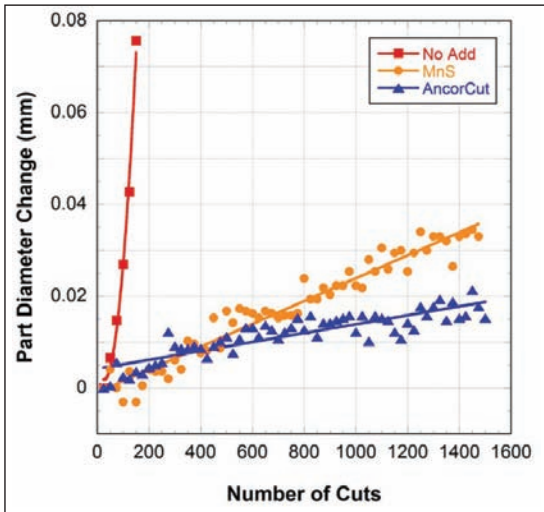


Fig. 4. FD-0405 turning comparison of no additive, AncorCut with MnS

### Turning of FLC2-4808

The final material turned was FLC2-4808, a sinter-hardening grade with poor machinability. It was determined that the carbide insert could not be used to machine this fully martensitic material, so tests were run with a cBN insert. Even with the cBN insert, a slower cutting speed of 150 s/mm had to be used. The test results in Fig. 5 show extreme tool wear in the no additive condition, whereas the AncorCut tests ran for 2000 cuts with almost no tool wear. The combination of the cBN insert and the AncorCut machining additive was found to be extremely beneficial.

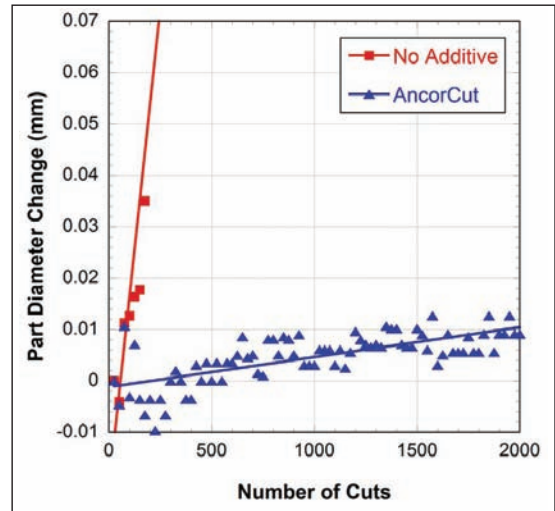


Fig. 5. Turning behavior of FLC2-4808 at 150 s/mm using a cBN insert

### Drilling of FC-0208

Table 2 displays number of holes drilled for each test condition. MnS showed the best performance for high speed steel bits at low feeds and no coolant. MnS also provided the longest tool life in drilling with carbide bits for both feeds. AncorCut exhibited excellent behavior for high speed steel with coolant at high feeds and also provided 2 to 3 times the tool life vs no additive for carbide. The results shown here demonstrate that tool life is highly dependent on the cutting conditions and drill bit materials, and that test results from one test can not necessarily be used as a guide to predict the response under different test conditions.

Given that MnS resulted in the longest tool life for carbide drill bits, it was initially assumed that it was the best machining additive for carbide. The precision of each hole, however, suggests otherwise. Fig. 6 shows the variation in hole diameter for the three conditions. A much greater variation is found with MnS than either

the no additive or the AncorCut condition. If hole precision and reasonable tool life are paramount, the best premix contained AncorCut.

*Table 2. Drill life for FC-0208 under different machining conditions*

Test Code	Coolant	Additive		
		No add	MnS	AncorCut
HSS (159 mm/min)	NO	98	921	357
HSS (159 mm/min)	YES	313	334	445
HSS (318 mm/min)	NO	2	186	3
HSS (318 mm/min)	YES	366	183	403
Carbide (318 mm/min)	YES	254	990	598
Carbide (508 mm/min)	YES	103	425	348

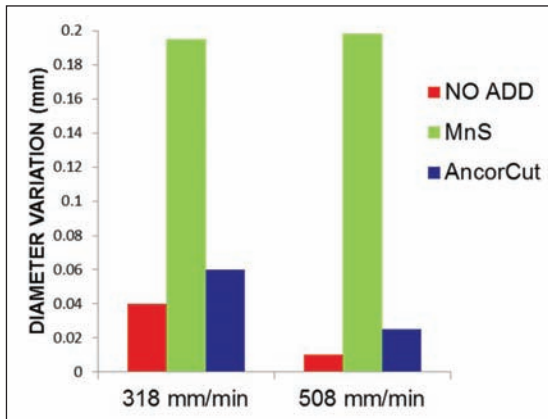


*Fig. 6. Drilled hole diameter variation in FC-0208 with no additive, MnS and AncorCut*

**Drilling of FD-0405**

FD-0405 exhibited very short tool life with high speed steel drill bits, so only the carbide bit results were pursued and included in the paper. Fig. 7 shows the drilling results using coolant

and a cutting speed of 508 mm/min at 3500 rpm. In a similar fashion to the turning results, attempting to machine FD-0405 without the addition of a machining enhancer leads to poor results. Far fewer than 100 holes were machined without an addition. A nine time improvement in tool life was found with MnS and a 17 time improvement was found with AncorCut. From the machining results presented in the paper, it is clear that higher alloy materials greatly benefit from machining enhancers. Fe-Cu-C steels also show an improvement with enhancers, but it is less dramatic.

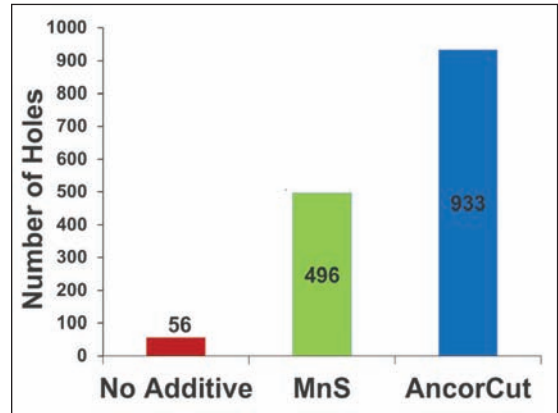


*Fig. 7. Carbide drill life in FD-0405 with no additive, MnS and AncorCut at 3500 rpm and 508 mm/min feed*

**Rusting Tests**

One of the primary benefits of MnS-alternative machining enhancers is the reduction in rusting and staining on the surface of PM components. Fig. 8 shows the accelerated rusting when MnS is present, whereas the no additive and the AncorCut samples had similar appearances, when exposed to higher humidity. MnS oxidizes to form manganese oxide or manganese sulfate type compounds and sulfuric acid may be evolved in the presence of water, thereby

causing accelerated corrosion. Additionally, MnS can alter how lubricants are removed from PM parts during the de-lubrication process, leading to staining on the surface of parts. In many applications, MnS can not be used for these reasons. The earlier turning results illustrated how MnS machinability can degrade under typical lab environments. For drilling, samples were exposed to humidity levels of 92% for three days and then machined. These were compared with the results of samples drilled within one day of sintering. It was found that the no additive machinability decreased 30%, MnS decreased 85% and AncorCut decreased 5% (Fig. 9). AncorCut provided the best stability in machinability with respect to humidity expose.

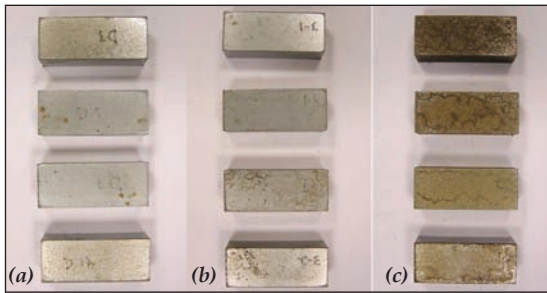


Fig. 8. Surface rusting of FC-0205 test bars with (a) no additive, (b) AncorCut and (c) MnS exposed for 10 days at nominally 80% humidity.

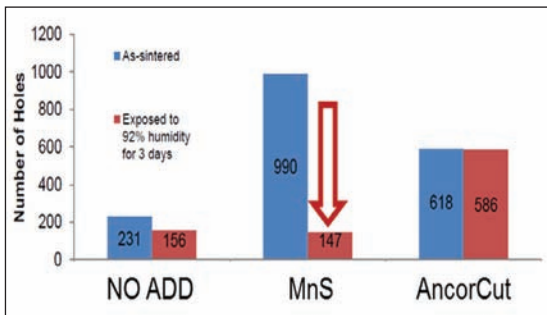


Fig. 9. Drilling response before and after humidity exposure (92% for 3 days)

### High Density Processing

The AncorMax 225 system was successfully utilized in the production of the automotive components shown in Fig. 2. These parts have a pressed weight of approximately 500 grams and 1100 grams with a minimum green density of 7.25 g/cm<sup>3</sup> and 7.2 g/cm<sup>3</sup>, respectively. The AncorMax system replaced a warm compaction system, where the powder had to be heated in addition to the die. The eliminated complication of powder heating was cited as a benefit of this system.

A summary of the flow and apparent density (AD) of the material produced to date is given in Table 3. The AD of this material averaged 3.35 g/cm<sup>3</sup> with a powder flow of <26 seconds per 50 grams through a Hall flow cup. The first production lot was sampled and evaluated for standard MPIF testing of compressibility, green strength, as-sintered TRS and tensile, and heat treated TRS and tensile. For the heat treated properties, the samples were first austenitized at 870 °C for one hour at temperature followed by oil quenching into heated oil (70 °C) and then tempering at 200 °C for one hour. Results from this laboratory testing are shown in Table 4 and Table 5.

Table 3. Powder Properties of the FLN2-4400 Premix Prepared via AncorMax 225 Processing. Compact produced at 755 MPa and a die temperature of 107 °C.

Characteristic	Average
AD(g/cm <sup>3</sup> )	3.36
Flow(per 50 g)	25
Compressibility (g/cm <sup>3</sup> )	7.40
Green strength( MPa)	32
As sintered Density( g/cm <sup>3</sup> )	7.44

## ENHANCED PROCESSING DEVELOPMENTS IN STEEL POWDERS

*Table 4. Laboratory Compressibility, Green Strength, As-Sintered and Heat Treated TRS values*

Compaction Pressure (MPa)	Green density (g/cm <sup>3</sup> )	Green Strength (MPa)	As sintered			Heat Treated		
			Density (g/cm <sup>3</sup> )	TRS (MPa)	HRA	Density (g/cm <sup>3</sup> )	TRS (MPa)	HRA
550	7.20	29	7.20	1175	45	7.21	1535	57
690	7.37	34	7.37	1325	48	7.38	1875	57
830	7.49	35	7.47	1455	49	7.48	2105	59

*Table 5. Laboratory Sintered Tensile Data*

Compaction Pressure	As sintered				Heat Treated			
	YS MPa	UTS MPa	Elong. %	HRA	YS MPa	TS MPa	Elong %	HRA
550	390	545	2.1	49	850	920	1.0	61
690	410	600	2.8	51	905	1025	1.1	64
830	415	605	3.0	52	955	1050	1.1	64

The production experience of the main running gear and sprocket shows good consistency in pressing tonnage and weight control. Shown in Figures 10 and 11 are graphs representing the total compaction tonnage applied and the part-to-part weight variability. In each plot two evaluations are presented. These evaluations represent two distinct production sequences run approximately 4 weeks apart using two distinct lots of premixed powder. The results show a maximum deviation of less than 1% over the two distinct production trials, with improvements evident in the second production run. In addition to the good compaction performance, ejection and surface finish are key attributes. It was determined in both the lab and in production of these components that the surface finish was equivalent or better than the warm compaction method being used previously.

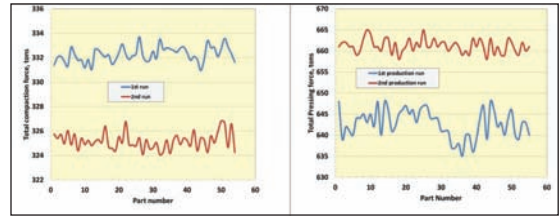


*Fig. 10. Compaction force required for the main running gear and sprocket for two distinct set ups approximately 1 month apart.*

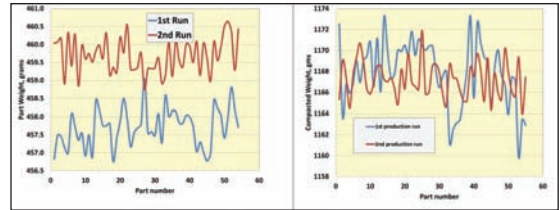


*Fig. 11. Weight control for the main running gear and sprocket for the two initial production runs.*

A further benefit observed with this new premix alternative is the enhanced uniformity of green density throughout the compacted part. Fig. 12 is an unetched photomicrograph of the cross section of a non-automotive gear at the 'neutral' zone. It demonstrates the uniformity of density in the body of the gear plus at the gear tips. This gear was compacted to an overall density of ~7.45 g/cm<sup>3</sup> utilizing FLN2-4405 material and a lube content of 0.25 wt%. Details of the gear are a major diameter of 18.5 mm with a height of 5 mm and module of ~0.8 mm. Larger components up to 45 mm tall have been successfully produced to densities approaching 7.4 g/cm<sup>3</sup> with 0.40 wt% lubricant.

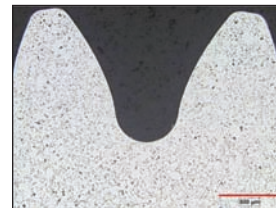


*Fig. 12. As-polished microstructure showing uniform density in gear teeth.*

### Conclusions

Engineered powders with enhanced attributes are an important tool for developing new parts and improving current applications. A newly introduced machining enhancer, AncorCut, was found to improve machinability of a variety of alloy systems and microstructures. This benefit in machinability was observed with both turning and drilling of several different alloy systems. The new additive also avoids the accelerated corrosion (rusting) found in sintered PM parts containing MnS, and provides stable machining characteristics. Warm die compaction with AncorMax 225 enables green and sintered densities in excess of 7.4 g/cm<sup>3</sup> at compaction pressures of approximately 750 MPa. This new advanced premixing technology is currently being utilized in the production of high density automotive and non-automotive ferrous components, thus providing parts producers another tool to improve the manufacturing and cost competitiveness of PM components.

### References

1. S. Kalpakijan and S. R. Schmid S. R., *Manufacturing Processes for Engineering Materials*, Pearson Education Inc., Upper Saddle River, NJ (2008).
2. R. Causton and C. Schade, "Machinability: a material property or process response?", *Advances in Powder Metallurgy & Particulate Materials*, part 7, pp. 154-169, Edited by R. Lawcock and M. Wright, Metal Powder Industries Federation, Princeton, NJ (2003).
3. H. Sanderow, J. Spirko and R. Corrente, "The machinability of P/M materials as determined by drilling tests", *Advances in Powder Metallurgy & Particulate Materials*, part 15, pp. 125-143, Edited by R. A. McKotch and R. Webb, Metal Powder Industries Federation, Princeton, NJ (1997).
4. A. Salak, M. Selecka and H. Danninger, *Machinability of powder metallurgy steels*, 2nd edition, Cambridge International Science Publishing, Cambridge (2006).
5. S. Cleays and K. Chopra, "Enhanced machinability and oxidation resistance with MnS containing additions to iron", *Advances in Powder Metallurgy & Particulate Materials*, part 15, pp. 111-123, Edited by R. A. McKotch and R. Webb, Metal Powder Industries Federation, Princeton, NJ (1997).
6. C. Stringer, D. Merritt and B. Lindsley, "Influence of Post Sinter Conditions on the Machinability of PM Copper Steel", *Advances in Powder Metallurgy & Particulate Materials*, part 6, pp. 16-23, Edited by I. Donaldson and N. Mares, Metal Powder Industries Federation, Princeton, NJ (2012).
7. B. Hu and S. Berg, "Optimizing the use of manganese sulfide in P/M applications", *Advances in Powder Metallurgy & Particulate Materials*, part 5, pp. 191-197, Edited by H. Ferguson and D. Wychell, Metal Powder Industries Federation, Princeton, NJ (2000).
8. B. Lindsley and C. Schade, "Machinability additives for improved hard turning of PM steel alloys", *Advances in Powder Metallurgy & Particulate Materials*, part 6, pp. 16-26, Edited by W. Gasbarre and J. von Arx, Metal Powder Industries Federation, Princeton, NJ (2006).
9. J. Engquist and R. Hennen, "Improving value in machined PM parts by material selection", *Advances in Powder Metallurgy & Particulate Materials*, part 13, pp. 1-12, Edited by T. Jesberger and S. Mashl, Metal Powder Industries Federation, Princeton, NJ (2009).
10. B. Lindsley and C. Stringer, "Additives for Improved Machining of Copper PM Steels",

## ENHANCED PROCESSING DEVELOPMENTS IN STEEL POWDERS

---

- Advances in Powder Metallurgy & Particulate Materials*, part 6, pp. 50-61, Edited by I. Donaldson and N. Mares, Metal Powder Industries Federation, Princeton, NJ (2012).
11. R. M'Saoubi , T. Czotscher , O. Andersson, D. Mayer , "Machinability of Powder Metallurgy Steels Using PcBN Inserts", *Procedia CIRP*, Vol.14, 83-88, (2014).
  12. C. Blais , G. L'Esperance and I. Bourgeois , "Characterization of Machinability of Sintered Steels During Drilling Operations", *Powder Metallurgy*, Vol. 44 (1), 67-76, (2001).
  13. W. Jandeska W., "Effect of Drilling and Tooling Parameters on the Machinability of Select Powder Metallurgy Materials", The Center for Powder Metallurgy Technology, Princeton, NJ, (2010).
  14. W. James, K. Narasimhan, "Warm Compaction and Warm-Die Compaction of Ferrous PM Materials", Presented at PM-13 International Conference and Exhibition on Powder Metallurgy for Automotive and Engineering Industries, Precision and Additive Manufacturing in Pune, India, (2013).
  15. H. G. Rutz, F. G. Hanejko, "High Density Processing of High Performance Ferrous Materials", *Advances in Powder Metallurgy and Particulate Materials*, Vol. 5, pp.117-133, Metal Powders Industries Federation, (1994).
  16. S. Shah, Gregory Falleur, F. Hanejko and S. Patel, "Production of High Density PM Automotive Components Utilizing Advanced Warm Die Compaction Technology" *Advances in Powder Metallurgy and Particulate Materials*, part 3, pp. 117-139, Metal Powders Industries Federation, (2014).



# PREPARATION AND CHARACTERIZATION OF NANO-CRYSTALLINE $\alpha$ - $\text{Al}_2\text{O}_3$ POWDER BY Sol-Gel PROCESS

V. Rathod<sup>1,2</sup>, C. Jariwala<sup>1</sup>, R. Pillai<sup>1</sup>, D.K. Basa<sup>2</sup> and B. Sarkar<sup>1</sup>

<sup>1</sup>Fusion Reactor Materials Development and Characterization Division, Institute for Plasma Research, Gandhinagar, INDIA.

<sup>2</sup>Department of Metallurgical and Materials Engineering, Indus University Ahmedabad, INDIA.

**Abstract :** Nano crystalline  $\alpha$ -alumina powders were prepared by Sol-Gel method using aqueous solution of Aluminum Nitrate Nona-Hydrate [ $\text{Al}(\text{NO}_3)_3 \cdot 9\text{H}_2\text{O}$ ] and Ammonium Hydroxide. Aluminum Nitrate Nona-Hydrate was stirred continuously for various intervals of time while adding ammonium hydroxide continuously till a desired pH was achieved. Through rigorous process optimization, it was observed that for maximizing efficiency of the Sol-gel process for the synthesis of Nano crystalline  $\alpha$ -alumina powders, the pH level of the solution must be kept constant at 3. It is well-known that maintaining pH of the solution is one of the most critical steps in the production of Nano crystalline  $\alpha$ -alumina powders. The resultant solution was dried at 110°C for 110 hours and subsequently calcined at different temperatures. XRD analysis confirmed the formation of  $\alpha$ -alumina powders in samples calcined at 1500°C; whereas samples calcined showed evidence of formation of amorphous powder. Particle analysis showed that the stirring time during the sol-gel process had significant effect on the size of  $\alpha$ -alumina particles in samples calcined at 1500°C. The smallest particle size of 322nm was achieved when the stirring time was 48 hours in samples calcined at 1500°C. The effect of stirring during sol-gel process on preparation  $\alpha$ -alumina powders is discussed in this paper.

**Keywords:** Nano Particles, Sol-gel, Alumina,

## Introduction:

Alumina ( $\text{Al}_2\text{O}_3$ ) has long been known as a high performance ceramic for various applications due to high mechanical strength and hardness [1], abrasive and chemical resistance, and superior optical and dielectric properties [2]. In addition, Alumina is structurally stable to radiation damage. Hence, there is a huge potential to use alumina for various applications in nuclear industry. In particular,  $\text{Al}_2\text{O}_3$  ceramic windows are one of the prime candidates for Radio Frequency windows applications in fusion reactors because of their low dielectric loss characteristics and high mechanical strength. However, despite of several advantages, the usage of alumina is limited due to its relatively low toughness. The toughness of alumina can be greatly enhanced by producing Nano crystalline alumina in lieu of microcrystalline alumina. The major problems in producing Nano crystalline

alumina of high quality are due to high grain growth during calcinations and greater tendency to form agglomerates. In recent years, significant efforts have been made in the research and development for producing Nano crystalline alumina powder of high quality through various routes.

Processes for producing alumina powder can be broadly categorized into two types: 1) Physical methods, and 2) Chemical methods. Physical methods for producing alumina powder consist of mechanical milling [3], laser ablation [4], flame spray [5], thermal decomposition by plasma [6] and various chemical methods for producing alumina powder are sol-gel processing [7], hydrothermal [8], precipitation [9], combustion [10], vapor deposition [11], and microemulsion [12]. Each of these processes has their advantages and limitations. Mechanical synthesis routes are usually expensive and

## PREPARATION AND CHARACTERIZATION OF NANO-CRYSTALLINE $\alpha$ - $\text{Al}_2\text{O}_3$ POWDER BY Sol-Gel PROCESS

introduce foreign particles as contaminants that adversely affect properties of sintered alumina. Other processes such as vapor phase, precipitation, hydrothermal usually involve high processing temperature and required longer processing time. Amongst them sol-gel process is the most promising and widely investigated technique for producing nano-sized  $\text{Al}_2\text{O}_3$  powder owing to its efficiency in producing Nano crystalline alumina particles of high purity and high specific surface area. However, sol-gel technique also suffers from the formation of agglomerates and requires subsequent grinding operation. As compared to combustion method, the agglomerates are less hard and hence it is relatively easy to grind and transform agglomerates into particles. In general, hard agglomerates are produced at high temperature. Therefore, it is very important to produce alumina powder at lower temperature to prevent the formation of hard agglomerates. Sol-gel technique comprises of formation of an amorphous gel using precursor solution, followed by calcinations to transform the amorphous alumina to Nano crystalline alumina. Sol-gel method is relatively less expensive, consumes less energy and maintains high degree of chemical homogeneity.

In the present study, Nano crystalline  $\alpha$ - $\text{Al}_2\text{O}_3$  powder is produced by sol-gel process. The process details are discussed and the role of sol-gel process parameter namely, stirring time on  $\alpha$ - $\text{Al}_2\text{O}_3$  particle size is studied. The amorphous  $\alpha$ - $\text{Al}_2\text{O}_3$  powder produced by sol-gel method is dried, calcined at various temperatures to produce Nano crystalline  $\alpha$ - $\text{Al}_2\text{O}_3$  powder.

### Experimental Methods:

In this study, Nano crystalline  $\alpha$ - $\text{Al}_2\text{O}_3$  powder is prepared by sol-gel process. The process comprises of using calculated amount of Aluminum Nitrate Nona-Hydrate  $[\text{Al}(\text{NO}_3)_3 \cdot 9\text{H}_2\text{O}]$  as precursor solution and adding ammonium hydroxide continuously while stirring for various interval of time. Amount of ammonium hydroxide

added to Aluminum Nitrate Nona-Hydrate was controlled to maintain the pH of solution at 3. The stirring operation was continued for following time intervals: 24, 48, 72 and 96 hrs. The final solution taken at different stirring time interval was dried in hot air oven at  $110^\circ\text{C}$  for 110 hours, followed by calcinations at different temperatures (i.e.  $500^\circ\text{C}$ ,  $1000^\circ\text{C}$  and  $1500^\circ\text{C}$ ). The calcined powders were ground using mortar and pestle and characterized using XRD, SEM, and particle analyzer. The process flow chart for the preparation of Nano crystalline  $\alpha$ -alumina is shown in Fig. 1.

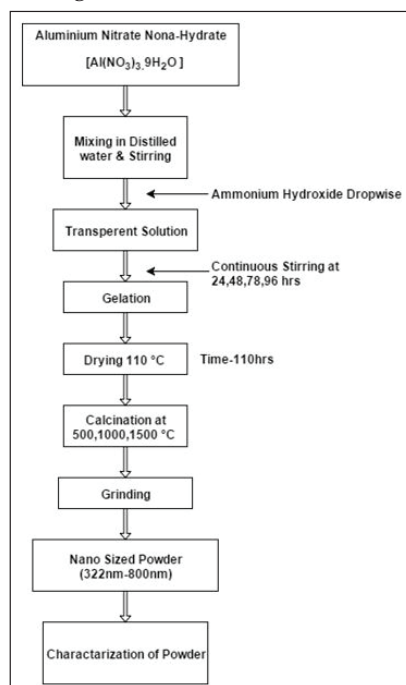


Fig. 1: Process flow chart for the synthesis of  $\alpha$ -alumina by sol-gel method.

### Results and Discussion:

#### X-Ray Diffraction (XRD) Analysis

The XRD measurement was performed on samples after calcination at various temperatures. The X-ray diffractograms of various calcined samples are shown in Fig. 2.

# PREPARATION AND CHARACTERIZATION OF NANO-CRYSTALLINE $\alpha$ - $\text{Al}_2\text{O}_3$ POWDER BY Sol-Gel PROCESS

The XRD analysis confirmed the formation of  $\alpha$ - $\text{Al}_2\text{O}_3$  phase in samples calcined at 1000°C and 1500°C. However, the relative intensity of  $\alpha$ -alumina peaks in sample calcined at 1500°C was much greater than those calcined at 1000°C. This shows that the sample calcined at 1000°C underwent partial crystallization. In other words, the sample calcined at 1000°C consisted of both crystalline  $\alpha$ -alumina and amorphous alumina. On contrary, the sample calcined at 500°C predominantly consisted of amorphous alumina with no evidence for the formation of  $\alpha$ -alumina powder. This is an expected behavior since crystallization of  $\alpha$ -alumina from amorphous alumina takes place at higher temperature.

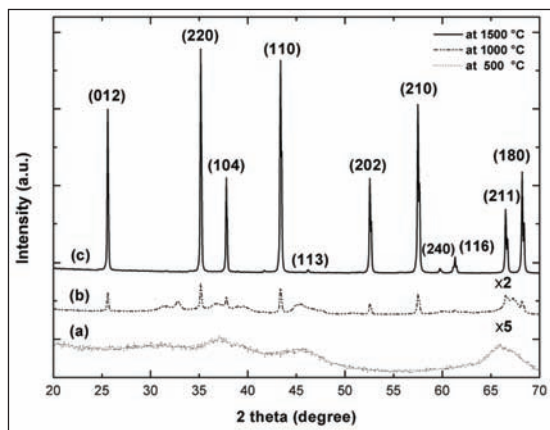


Fig.2: (1) XRD spectra for  $\text{Al}_2\text{O}_3$  powder calcined at (a) 500°C (Data amplified with factor of 5 - X5), (b) 1000°C (Data amplified with factor of 2 - X2) and (c) 1500°C..

## Scanning Electron Microscopic (SEM) Analysis

Scanning electron micrographs of  $\alpha$ - $\text{Al}_2\text{O}_3$  powder calcined at 1500°C at various magnifications are shown in Fig. 3A-D. Scanning electron microscopic (SEM) observation showed that  $\alpha$ - $\text{Al}_2\text{O}_3$  powder exhibited typical particulate morphology uneven shape. Further, they formed agglomerates during calcinations. These agglomerates were ground to produce fine powder. The formation of agglomerates

is a result of sintering of fine powder during calcination treatment.

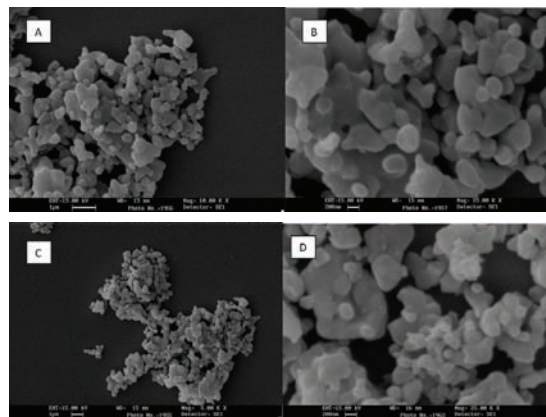


Fig. 3: Typical SEM image of calcined powder at 1500°C with 25 KX magnification.

## Particle Analyzer

The particle size analysis measurement was performed by Zeta analyzer. Variation of particle with stirring time during sol-gel process is shown in Fig. 4 for samples calcined at 1500°C. Particle size analysis clearly shows that stirring time played significant role on  $\alpha$ -alumina particlesize. The size of  $\alpha$ -alumina particles is in the range of 322-810 nm depending up on the stirring time during sol-gel process. The finest particle size is observed in samples that were stirred for 48 hrs during sol-gel process.

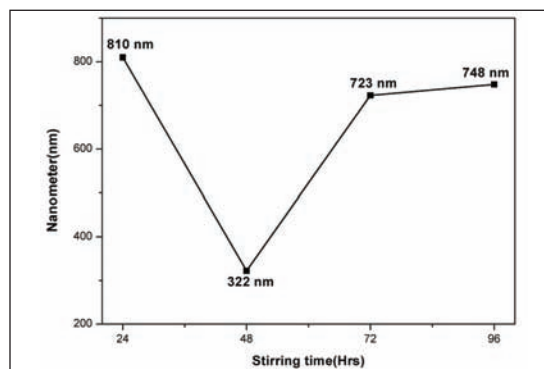


Fig. 4: Variation of particle size of  $\alpha$ -alumina particles with stirring time during sol-gel process in samples calcined at 1500°C.

## PREPARATION AND CHARACTERIZATION OF NANO-CRYSTALLINE $\alpha$ - $\text{Al}_2\text{O}_3$ POWDER BY Sol-Gel PROCESS

### Conclusions:

Nano crystalline  $\alpha$ - $\text{Al}_2\text{O}_3$  powders were successfully produced by sol-gel process. The optimum stirring time for the preparation finest  $\alpha$ -alumina particles is 48 hours. The XRD analysis confirmed the formation of  $\alpha$ -alumina particles in samples calcined at 1500°C. The SEM analysis showed typical agglomerated particles in the sample calcined at 1500°C. To reduce agglomeration of  $\alpha$ -alumina particles, future work is planned to perform calcinations at lower temperatures and study the phase transformation behavior.

### References:

1. S. Junlong, L. Changxia, Z. Xihua, W. Baowei and N. Xiuying, "Effect of diopside addition on sintering and mechanical properties of alumina", *Ceram. Int.*, **35**, 1321-1325, (2009).
2. I. Piwonski and K. Soliwoda, "The effect of ceramics nanoparticles on tribological properties of alumina sol-gel thin coatings", *Ceram. Int.*, **36**, 47-54, (2010).
3. M. Bodaghi, A. Mirhabibi, M. R. Tahriri, H. Zolfonoon and M. Karimi, "Mechanochemical assisted synthesis and powder characteristics of nanostructure ceramic of  $\alpha$ - $\text{Al}_2\text{O}_3$  at room temperature", *Mater Sci Eng*, **162**, 155-161, (2006).
4. G. Johnston, R. Munenchausen, D. M. Smith, W. Fahrenholtz and S. Foltyn, "Reactive laser ablation synthesis of nanosize alumina powder", *J. Am. Ceram. Soc.*, **75**, 3293-3298, (1992)
5. A. I. Tok, F.Y.C. Boey and X. L. Zhao, "Novel synthesis of  $\text{Al}_2\text{O}_3$  nano-particles by flame spray pyrolysis", *J. Mater. Process. Tech.*, **178**, 270-273, (2006).
6. A. Pivkina, D. Ivanov, Y. Frolov, S. Mudretsova, A. Nickolskaya and J. Schoonman, "Plasma synthesized nano-aluminum powders", *J. Therm. Anal. Calorim.*, **86**, 733 (2006)
7. M. Nguéfack, A. F. Popa, S. Rossignol and C. Kappenstein, "Preparation of alumina through a sol-gel process. Synthesis, characterization, thermal evolution and model of intermediate boehmite", *Chem. Chem. Phys.*, **5**, 4279-4289, (2003)
8. D. Mishra, S. Anand, R. K. Panda and R.K. Das, "Hydrothermal preparation and characterization of boehmites", *Mater Lett.*, **42**, 38-45, (2000)
9. O. Rahmanpour, A. Shariati, M. R. Khosravi Nikou, "New method for synthesis nano size  $\alpha$ - $\text{Al}_2\text{O}_3$  catalyst for dehydration of methanol to dimethyl ether", *Int. J. Chem. Eng. Appl.*, **3**(2), 125-128, (2012)
10. X. Zhai and Y. Fu, "Combustion synthesis of the nano structured alumina powder", *Nanoscience*, **11**, 286-292, (2006)
11. K. Kamata, T. Mochizuki, S. Matsumoto, A. Yamada and K. Miyokawa, "Preparation of submicrometer  $\text{Al}_2\text{O}_3$  powder by gasphase oxidation of tris (acetylacetonato) aluminum (111)", *J. Am. Ceram. Soc.*, **68**, 193-194, (1985)
12. X. Wang, G. Lu, Y. Guo, Y. Wang and Y. Guo, "Preparation of high thermal-stabile alumina by reverse microemulsion method", *Mater. Chem. Phys.*, **90**, 225-229, (2005)



# EFFECTS OF Fe AND Mo CONTENT ON THE MICROSTRUCTURE AND MECHANICAL PROPERTIES OF Ti-Mo BASED ALLOYS PREPARED BY ELEMENTAL BLEND AND MECHANICAL ALLOYING TECHNIQUE

P. Mohan, A. Amigo, V. Amigo

Institute of Materials Technology (ITM-UPV), Universidad Politécnica de Valencia, Spain

**Abstract:** Ti and its alloys are mostly used as biomaterials due to its unique properties like high corrosion resistance, low elastic modulus, high mechanical strength/ density ratio, good biocompatibility etc. Ti- $\beta$  alloys based on the Ti-Mo alloy system shows much more interest for biomaterials. Addition of Zr and small amount of Fe improves the  $\beta$ -phase stability and improving the properties of Ti-Mo alloy. These alloys can be produced by powder metallurgy (PM) using Elemental Blend (EB) technique (600 MPa compaction pressure) and Mechanical Alloying (MA) technique with (600 and 900 MPa compaction pressure). This paper describes the microstructural characterization obtained by SEM and mechanical properties obtained by bending test, Archimedes test and ultrasonic test of Ti-Mo-Zr-Fe alloys made by elemental blend and Mechanical Alloying. Mechanical properties and Microstructure of these powder mixing processes also compared. The addition of small amounts of Fe further increases  $\beta$ -phase stability, improving the properties of Ti-15Mo-6Zr-xFe alloy. In the search for a better implant material, Ti-12Mo-6Zr-2Fe, with its low modulus, ductile property, and reasonably high strength, is a promising candidate.

**Key words:** Elemental Blend, Mechanical Alloying, Biocompatibility

## 1. Introduction

The development of titanium and its alloys used as implant material perfectly reflect the research goal of biomaterials. Ti6Al4V is the first most useful implant materials, However, Ti6Al4V alloy is composed of cytotoxic elements like Al and V, Which may causes several problems for long term implant due to ion liberation inside body. To overcome the potential V toxicity, V was replaced by Nb and Fe, leading to two new V-free  $\alpha + \beta$ -type Ti-based alloys, i.e., Ti-6Al-7Nb and Ti-5Al-2.5Fe [1-2] Both alloys show good mechanical and metallurgical behaviour comparable to those of Ti-6Al-4V. Nevertheless, several studies have recently shown that the elastic modulus of  $\alpha$ -type and some  $\alpha + \beta$ -type Ti-based alloys is much higher than that of human bone [3-7], which can cause stress shielding effect [8]. Therefore, low modulus  $\beta$ -type Ti-based alloys have been extensively developed [9-11], among which the representatives are Ti-

15Mo, Ti-13Nb-13Zr, Ti-12Mo-6Zr-2Fe, Ti-35Nb-5Ta-7Zr, and Ti-29Nb-13Ta-4.6Zr [12-14]. So, for achieving better mechanical properties like elastic modulus, Flexural strength, microstructure etc. we start developing better biomaterials with Ti-Mo binary alloy, Ti-Mo-Zr ternary alloy and Ti-Mo-Zr-Fe Quaternary alloy.

In this paper we compared between two powder processing techniques 1<sup>st</sup> Elemental blend (EB) and 2<sup>nd</sup> is Mechanical alloying (EB). Initially, we worked with Elemental Blend technique but due to lack of diffusion we started working with Mechanical Alloying technique. Production of binary, ternary and quaternary alloys with different milling parameters, compaction parameters, sintering temperatures and different composition of each elemental powders obtained. The influences of Mo and Fe addition on its flexural strength, microstructure, elastic modulus is investigated in detail.

# EFFECTS OF Fe AND Mo CONTENT ON THE MICROSTRUCTURE AND MECHANICAL PROPERTIES OF Ti-Mo BASED ALLOYS PREPARED BY ELEMENTAL BLEND AND MECHANICAL ALLOYING TECHNIQUE

## 2. Experimental Procedure

The different metal powders used for preparing Ti12Mo6Zr2Fe are Ti, Mo, Zr and Fe and properties of powders are shown in table 1:

**Table 1: Ti, Mo, Zr and Fe powder characteristics**

Powder	supplier	Purity (%)	Powder size (mesh)
Titanium	Alfa Aesar	99.7	325
Molybdenum	Alfa Aesar	99.95	250
Zirconium	Alfa Aesar	99.95	325
Iron	Hoganas	99.8	230

The blend of elemental powders was conducted in a closed vial in a blender model Bioengineering Inversin for 30 min with the speed of 300 rpm.

Mechanical alloying was performed in a planetary ball mill model PM 400/2 Retsch using a rotation speed of 180 RPM and 300 RPM, vial and balls of FeCr steel were used. The ball to powder weight ratio was 10:1 and 15:1. The milling batch had a mass of 20-25 gram for each run. To prevent an excessive temperature rise of the powder during milling, milling was stopped at 45 min and 52 min., and then the grinding bowl was allowed to cool for 30 min. To minimize powder oxidation, milling was carried out under an argon atmosphere. The powders of elemental blend and mechanical alloying were compacted in a universal testing machine Instron 432 Model with a load cell of 500 kN, with a compaction pressure of 600 MPa and 900 MPa. The matrix used was rectangular with dimensions of 30 × 12 mm, the powder mass required to obtain a sample height of 5 mm was about 7 g.

The specimens were sintered under high vacuum (approximately 10<sup>-4</sup> to 10<sup>-5</sup> mbar) in a tubular furnace carbolite HVT 15/75/450 model, at 1250 °C, After a dwell time of 3 h, the samples were furnace cooled at 10 °C/min. Powder filling done by hand in matrix; Compaction done by uniaxial hydraulic press. Compaction pressure for elemental blend technique is 600 MPa and for Mechanical alloying technique is 600 MPa and

900 MPa. The specimens were sintered under high vacuum tubular furnace (approximately 10<sup>-4</sup> to 10<sup>-5</sup> mbar) in a Carbolite HVT 15/75/450 model.

For MA of Ti12Mo6Zr2Fe parameters are initially compaction pressure is 600 Mpa, milling speed is 300 RPM and milling time is 45 min. Then after for this alloy compaction pressure was changed (600 MPa to 900 MPa) for betterment of alloy and milling speed and time remaining same. For Ti15Mo and Ti15Mo6Zr2Fe with MA, parameters are: compaction pressure-900 MPa, milling speed- 180 RPM and milling time is 52 min.

### 2.2 Powder Characterization and Microstructure

Here mixing of powder shown very clearly by SEM images with different magnification in Fig. 1. Mixing of powder by MA enhances the homogeneity of the powder. From figure 1(b), it is clear that cold deformation occurs after MA mixing. Distribution of the particle can easily see by Fig. 1(a) and interparticle distribution clearly shown by fig. 1(b).

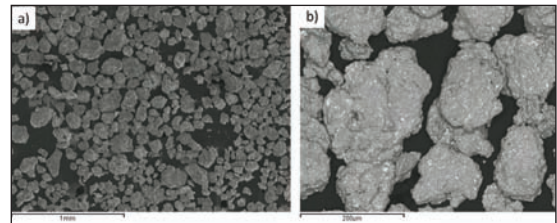


**Fig. 1 : SEM images of Ti12Mo6Zr2Fe powder by mechanical alloying method for 45 min (a) General aspect of the powder, secondary image (b) Detail of the powder, backscattered image. [15]**

To characterise the microstructure initially cut the transversal section of the sintered sample, mount the sample and then do metallographic preparation very well. The microstructure was observed using an optical microscope

# EFFECTS OF Fe AND Mo CONTENT ON THE MICROSTRUCTURE AND MECHANICAL PROPERTIES OF Ti-Mo BASED ALLOYS PREPARED BY ELEMENTAL BLEND AND MECHANICAL ALLOYING TECHNIQUE

Nikon LV100. For measuring overall porosity Archimedes test is suitable. For quantifying the ( $\alpha$  and  $\beta$  phases) and internal porosity NIS-Elements® image analysis software was used. Backscattered electron images (BSE) and secondary electron image (SEI) of the microstructure at different magnifications were obtained in a scanning electron microscope (SEM) Jeol JSM6300. Microanalysis was performed by energy dispersive spectroscopy (EDS) for quantification of chemical composition, using an Oxford Instruments X-ray detector installed in microscope. Fractography of the breaking sample also seen by SEM which we can analyse the fragile or ductility of the sample.

## 2.3. Mechanical Properties

Mechanical properties determined by different test like bending test, ultrasonic test, Archimedes test etc. Total porosity determined by Archimedes test. The measurements were performed with 10 kg applied load. For obtain elastic modulus, Ultrasonic test was done with Karl Deutsch digital Echograph. Mechanical properties like bending strength and bending modulus, bending test were done by a Universal testing machine Instron 4204 model, with 50 kN load. All mechanical tests were carried out according to EN ISO-3325 [16].

## 3. Results and Discussion

Mechanical alloying technique is a solid- state powder processing technique involving repeated welding, fracturing and rewelding of a powder particles in a high energy ball mill, blending element is also an solid state powder processing technique with a lower energy ball mill than mechanical alloying Total porosity obtained for mechanical alloying samples after sintering is higher in comparison to elemental blend samples, due to plastic deformation which occurs in MA process the particle size of powder obtained are bigger than EB powder. The porosity also

affect the mechanical properties, with higher porosity smaller flexural strength was obtained. Minimum relative density ( means higher porosity) obtained for Mechanical alloying (MA) samples which is clearly shown in Fig. 2. When we applies compaction pressure for 600 MPa for MA samples then porosity is very high, after that increasing of compaction pressure gives better results for mechanical properties. And we also explored different milling parameters, working with a compaction pressure of 900 MPa, where we changed milling speed from 300 RPM to 180 RPM and milling time from 45 min. to 52 min. and found better results in mechanical properties than before.

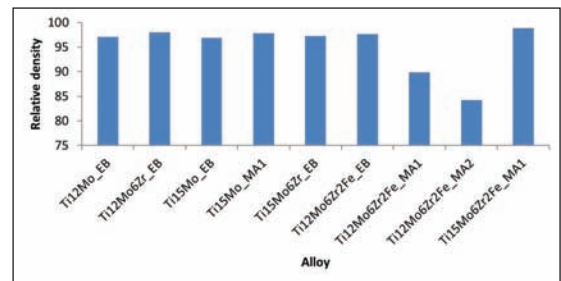


Fig. 2: Relative density calculated by Archimedis test. Where MA 1 stands for mechanical alloying samples compacted at 900 MPa & MA 2 stands for mechanical alloying samples compacted at 600 MPa

Here maximum value of porosity is for Ti12Mo6Zr2Fe prepared by MA process at 600 MPa with 300 RPM and 45 Min., which is due to least inter molecular bondation within the particles. The lower value of porosity found for Ti15Mo6Zr2Fe prepared by MA techniques at 900 MPa with 180 RPM and 52 Min., it shows that with these parameters, we obtain better bondation between the particles during compaction and sintering. Porosity reflects the diffusion characterisation between the particles during sintering process.

Fig.3 shows the flexural strength (FS) of different alloy with different composition and with

# EFFECTS OF Fe AND Mo CONTENT ON THE MICROSTRUCTURE AND MECHANICAL PROPERTIES OF Ti-Mo BASED ALLOYS PREPARED BY ELEMENTAL BLEND AND MECHANICAL ALLOYING TECHNIQUE

different preparation method. FS for binary alloy is higher than quaternary alloy, explaining the effect of the beta stabilizing element on the alloy that make decrease flexural strength, as shown in fig. 3. The Flexural strength obtained for Elemental Blend alloy is higher than the Mechanical alloying alloy in most of the samples, but for Ti15Mo6Zr2Fe (prepared by MA at 900 MPa), the value of the porosity is less and flexural strength is also high (Table 2), which is a better combination for bio-materials because lower porosity improves fatigue strength.. Inreasing in compaction pressure plays main role for MA samples, when we applied 600 MPa pressure then porosity is very high and flexural strength is very less.After applying 900 MPa pressure, porosity and Flexural strength improves. So, then after we applied 900 MPa for betterment of the alloy.

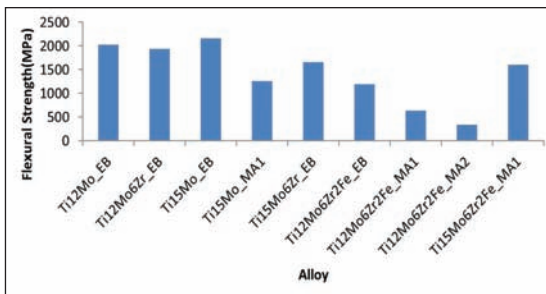


Fig. 3 : Flexural strength of different alloy

Fig. 4 shows the Micro hardness for different alloy with different composition and different powder processing techniques(MA & EB).The minimum value of hardnesss is for Ti12Mo prepared by EB technique (283HV) approx. and the the maximum value is for Ti12Mo6Zr2Fe prepared by EB method (512HV) approx., so the range for these alloys is (283HV-512 HV). The minimum value of hardness is for binary alloy (like Ti12Mo and Ti15Mo) prepared by EB technique. The results show that the addition of Zr and Fe increases hardness.

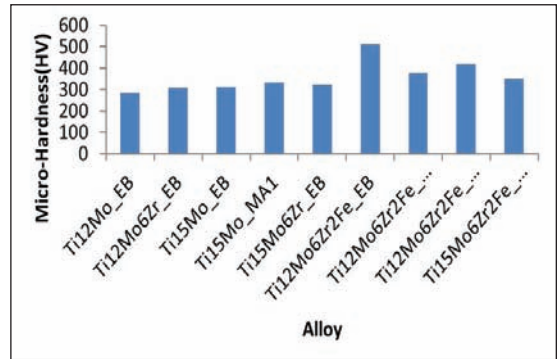


Fig. 4: Hardness for different alloy

Hardness of the EB process are higher in comparison to MA process due to its lower porosity.

Table 2: Mechanical properties of different alloy

Alloy	Relative density	Flexural strength (MPa)	Hardness (HV)	Elastic modulus(GPa)
Ti12Mo_EB	97.1	2023	283	104
Ti12Mo6Zr_EB	97.9	1931	308	103
Ti15Mo_EB	96.8	2161	309	104
Ti15Mo_MA1	97.8	1261	330	-
Ti15Mo6Zr_EB	97.2	1658	322	98.5
Ti12Mo6Zr2Fe_EB	97.6	1194	512	97.8
Ti12Mo6Zr2Fe_MA1	89.8	637	376	82
Ti12Mo6Zr2Fe_MA2	84.1	329	419	66.3
Ti15Mo6Zr2Fe_MA1	98.8	1597	348	-

Elastic modulus is one of the main mechanical property for the Bio-Materials due to the shielding stress effect. Elastic modulus for  $\alpha$ -alloy is 102.7(for pure Ti grade 1) and it is 104.1 GPa for Ti grade 4. For Ti64 value of elastic modulus is (101-110 GPa). Biomedical implants need to have a higher strength to support load required for its functionality. and an elastic modulus close to human bone. Therefore, biomedical alloy must have low elastic modulus combined with high strength. we calculated the elastic modulus of different composition with Ultrasonic method.

EFFECTS OF Fe AND Mo CONTENT ON THE MICROSTRUCTURE AND MECHANICAL PROPERTIES OF Ti-Mo BASED ALLOYS PREPARED BY ELEMENTAL BLEND AND MECHANICAL ALLOYING TECHNIQUE

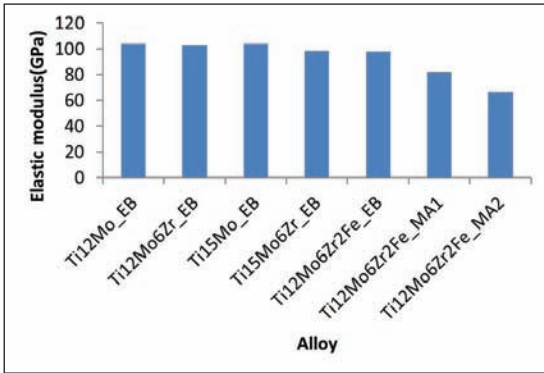


Fig. 5: Elastic modulus of different alloy

Total porosity influenced elastic modulus, when porosity is less then elastic modulus is high, so for MA samples, elastic modulus is less in comparison to EB alloy due to its porosity. Binary alloy have more elastic modulus than ternary and quaternary alloy. Addition of Zr and Fe reduces the value of elastic modulus because both of them are  $\beta$ -stabilizer elements. If porosity and elastic modulus is less for the alloys, that is good combination for biomaterials.

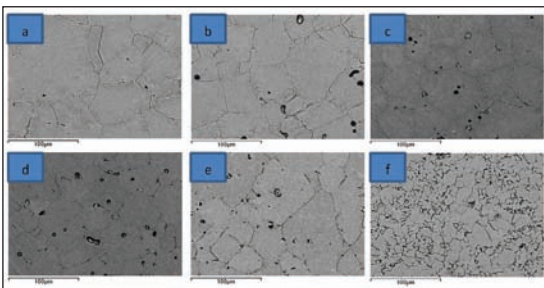


Fig. 6: SEM image by Back scattered image with 500x of (a) Ti12Mo with EB method (b) Ti12Mo6Zr with EB method. (C)Ti15Mo with EB mehod (d) Ti15Mo6Zr with EB mehod (e) Ti12Mo6Zr2Fe with EB mehod (f) Ti12Mo6Zr2Fe with MA at 900 MPa.

Fig.(6) shows the Microstructure of Ti-Mo-Zr-Fe samples prepared by both methods EB and MA powder processing Method.

Binary alloys shows irregular surfaces like some bigger grain size and some smaller, it may be due to distribution of the particles is not uniform. Samples prepared by MA shows bigger porosity [Fig. 6(f)], than samples prepared by EB mehod. Number of grain boundary is also high in case of MA samples but the grain size is bigger in case of EB alloy due to its better diffusion during sintering. Addition of Fe increases porosity of the samples, grain size and decreases no. of grain boundary as shown in Fig. 6(e).  $\alpha$ -phase appears for MA samples insides the alloy, but for EB samples  $\alpha$ -phase appears at the grain boundary of the microstructure, due to its lack of diffusion (Fig. 7). Therefore  $\alpha$ -phase is more in case of MA samples.

The addition of Fe stabilizes the beta phase, which significantly reduces the amount of alpha phase formed.

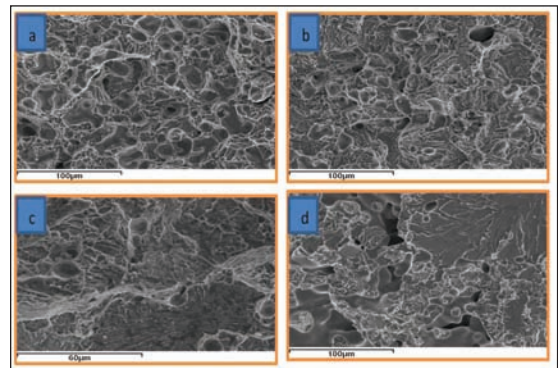


Fig. 7: Fractography of different alloy by secondary image for (a) Ti12Mo Prepared by EB method (b) Ti12Mo6Zr by EB Method (c) Ti12Mo6Zr2Fe prepared by EB method (d) Ti12Mo6Zr2Fe prepared by MA method at 900 MPa compaction pressure

Fractography character for the EB samples is a mixed type of fracture like (ductile and brittle both) From Fig. [7(a)-7(c)], but due to higher porosity present in the MA samples, fracture is intragranular type with brittle character which is shown in Fig. 8(d). For the Ti-Mo binary alloy

# EFFECTS OF Fe AND Mo CONTENT ON THE MICROSTRUCTURE AND MECHANICAL PROPERTIES OF Ti-Mo BASED ALLOYS PREPARED BY ELEMENTAL BLEND AND MECHANICAL ALLOYING TECHNIQUE

fracture is like mostly ductile with some voids and when we added Zr and Fe brittle character of the samples increases than binary alloy.

## 4. Conclusions:

MA samples shows more porous character than EB samples, therefore flexural strength is bigger for EB alloy with same parameters than MA samples. But for Ti15Mo6Zr2Fe samples prepared by MA technique at 900 MPa compaction pressure have less porosity (1.21 %) [Table 2] and good flexural strength [1597.74 MPa], which is suitable for Biomaterials application. So, this alloy is a promising alloy for the application. Binary alloy have very high flexural strength (2100 MPa) but also very high elastic modulus (approx 103 GPa) and higher elastic modulus is less suitable for biomaterials, so we add Zr and Fe to this alloy for reducing elastic modulus value. Elastic modulus is smaller for MA samples than EB samples, which is suitable for biomaterials application. In both cases have a great influence of porosity. Hardness for MA samples is less than EB samples in general, binary alloy have less microhardness value than ternary and quaternary alloy. Addition of Fe and Zr increases  $\beta$ -phase stability for Ti-Mo alloy.

Fractography shows mixed type of fracture in case of EB alloy like brittle and ductile both, but for MA samples, due to high porosity intragranular fracture with brittle fracture appears. From SEM study it is clear that MA samples have more  $\alpha$ -phase in comparison to EB samples.  $\alpha$ -phase appears inside the alloy for MA samples and for the EB alloy  $\alpha$ -phase appears on grain boundary.

## 5. Acknowledgement

The authors wish to thank the Ministry of Economy and competitiveness through the financial support of the research project MAT2014-53764 -C3-1 -R, The European commission the Erasmus mundus scholarship program Namaste and the

Generalitat Valenciana through support ACOMP / 2014/151 . The European Commission via FEDER funds that have allowed the purchase of equipment for research and Microscopy Service of the Polytechnic University of Valencia.

## 6. References:

1. M. Long, H.J. Rack, "Titanium alloys in total joint replacement – A materials science perspective", *Biomaterials*, **19**, 1621–1639, (1998)
2. M. Niinomi, "Recent metallic materials for biomedical applications", *Metall. Mater. Trans.*, **33 A**, 477–486, (2002).
3. F.G. Evans, "Mechanical properties and histology of cortical bone from younger and older men", *Anat. Rec.*, **185**, 1–11, (1976).
4. O. Lindahl, A.G. Lindgren, "Cortical bone in man II. Variation in tensile strength with age and Sex", *Acta Orthop. Scand.*, **38**, 141–147, (1967).
5. J.Y. Rho, T.Y. Tsui, G.M. Pharr, "Elastic properties of human cortical and trabecular lamellar bone measured by nanoindentation", *Biomaterials*, **18**, 1325–1330, (1997).
6. O. Lindahl, "Mechanical Properties of Dried Defatted Spongy Bone", *Acta Orthop. Scand*, **47**, 11–19, (1976).
7. M. Ding, M. Dalstra, C.C. Danielsen, J. Kabel, I. Hvid, F. Linde, "Age variations in the properties of human tibial trabecular bone", *J. Bone J. Surg.*, **79**, 995–1002, (1997).
8. S. Gross, E.W. Abel, "A finite element analysis of hollow stemmed hip prostheses as a means of reducing stress shielding of the femur", *J. Biomech.*, **34**, 995–1003, (2001).
9. D. Kuroda, M. Niinomi, M. Morinaga, Y. Kato, T. Yashiro, "Design and mechanical properties of new  $\beta$  type titanium alloys for implant materials", *Mater. Sci. Eng.*, **243 A**, 244–249, (1998).

## EFFECTS OF Fe AND Mo CONTENT ON THE MICROSTRUCTURE AND MECHANICAL PROPERTIES OF Ti-Mo BASED ALLOYS PREPARED BY ELEMENTAL BLEND AND MECHANICAL ALLOYING TECHNIQUE

---

10. Y.L. Hao, M. Niinomi, D. Kuroda, K. Fukunaga, Y.L. Zhou, R. Yang, "Aging response of the Young's modulus and mechanical properties of Ti-29Nb-13Ta-4.6Zr", *Metall. Mater. Trans.*, **34 A**, 1007-1012, (2003).
11. N. Sakaguchi, M. Niinomi, T. Akahori, J. Takeda, H. Toda, "Relationship between tensile deformation behavior and microstructure in Ti-Nb-Ta-Zr", *Mater. Sci. Eng.*, **25 C**, 363-369, (2005).
12. M. Niinomi, T. Akahori, S. Katsura, K. Yamauchi, M. Ogawa, "Mechanical characteristics and microstructure of drawn wire of Ti-29Nb-13Ta-4.6Zr for biomedical applications", *Mater. Sci. Eng.*, **27 C**, 154-161, (2007).
13. D. Kuroda, H. Kawasaki, A. Yamamoto, S. Hiromoto, T. Hanawa, "Mechanical properties and microstructures of new Ti-Fe-Ta and Ti-Fe-Ta-Zr system alloys", *Mater. Sci. Eng.*, **25 C**, 312-320, (2005).
14. S. Nag, R. Banerjee, H.L. Fraser, "Microstructural evolution and strengthening mechanisms in Ti-Nb-Zr-Ta, Ti-Mo-Zr-Fe and Ti-15Mo biocompatible alloys", *Mater. Sci. Eng.*, **25 C**, 357-362, (2005).
15. P.Mohan, A. Amigo, Abou Bakr Elshalakany, V. Amigo, "Effect of powder processing on the microstructure and mechanical properties of ti-mo alloys", CNPM-15 congress (2015)
16. EN ISO-3325.2000. Sintered metal materials, excluding hardmetals. Determination of transverse rupture strength



# EXPERIMENTAL INVESTIGATION OF THE COMPRESSIBILITY AND MECHANICAL PROPERTIES OF Cp-Ti POWDER METALLURGY COMPONENTS

Arunangsu Das<sup>1\*</sup>, Susenjit Sarkar<sup>1</sup>, Malobika Karanjai<sup>2</sup>, Goutam Sutradhar<sup>1</sup>

<sup>1</sup>Department of Mechanical Engineering, Jadavpur University, Kolkata, West Bengal, India

<sup>2</sup>International Advanced Research Centre for Powder Metallurgy and New Materials (ARCI), Hyderabad

**Abstract :** In recent years there has been an increasing demand for using Titanium alloys in bio-medical applications. It is non-toxic and bio-compatible material, hence widely used as prosthetics, as well as dental implants. Since it is non-ferromagnetic, so patients with titanium implants can easily be examined with MRI. Due to its high tensile strength to density ratio, high corrosion resistance & good fatigue resistance, it is also widely used in aircrafts & high-cost automobiles. The aim of this work is to investigate the sintered behaviour of commercially pure Titanium powder metallurgy components. Powders was uni-axially pressed at designated pressures in a suitable die ranging from 125 kN to 135 kN to form cylindrical samples and the green compacts were sintered at 0.001 mbar pressure for about 4 hours with maximum sintering temperature varying from 1350°C to 1450°C. The metal matrix structures were examined in SEM. The micro-hardness of the samples were also investigated. The influence of the compacting pressure and sintering temperature on the relative densities of the preform have been investigated. The deformation characteristics are discussed critically.

**Keywords:** Titanium, powder metallurgy, SEM, micro-hardness, relative density, compressibility

## Introduction

The forging of metal powder preform has aroused considerable interest in recent years, the technique combining some of the best features of two well established technologies, namely powder metallurgy and forging. Cull [1] has reported the advantages of metal powder preform forging associated with conventional powder metallurgy processes along with additional strength provided by the elimination of porosity by forging. The mechanical and metallurgical properties of metal powder components compare favorably with those of wrought materials. Jones [2] had pointed out technical and economical advantages of sintered forged powder products. Green [3], had carried extensive investigations during compression of metal powders and established the plasticity upper-bound and slip-line field theories for

sintered powder components. Tabata and Masaki [4] studied the plastic yield behavior of porous metals and proposed the principal strain increments, volumetric strain increments and corresponding yield criterion for powder metallurgy components. Ramakrishnan [5] had conducted basic experiments of preform forging. Jha and Kumar [6] carried out experimental investigations to analysis pressure distribution on die preform interface and die load during axisymmetric cold forging of sintered iron powder preform and plain strain forging of copper powder strips.

The processing of titanium and its alloys by means of powder metallurgy (PM) techniques is claimed to be a suitable way to reduce the fabrication cost of titanium products as well as offering the possibility to design new alloys which are difficult to obtain through conventional

## EXPERIMENTAL INVESTIGATION OF THE COMPRESSIBILITY AND MECHANICAL PROPERTIES OF Cp-Ti POWDER METALLURGY COMPONENTS

metallurgical processes. Titanium is very difficult to cast because it readily oxidizes at elevated temperatures. Production of cast titanium part is possible only under high vacuum. Machining of titanium is also difficult - its high chemical reactivity causes the chip to weld to the tool, leading to crater formation & premature tool failure. The low thermal conductivity of it does not allow the heat generated to dissipate from the tool edge. It causes high tool tip temperature and excessive tool deformation & wear.

Timet [7] reported that titanium is categorized as a transition element. It has relatively low density of 4.506 g/cm<sup>3</sup>. Its melting point is 1668° C and its elastic modulus is 107 GPa. Astana et al., [8] and Joubert, [9] reported that titanium has good corrosion resistance and good creep resistance above 500°C. However, it is highly reactive with other metals at temperatures above 400°C. Froes et al., [10] reported that manufacturing of complex Ti-parts are challenging and expensive by conventional methods, whereas it can be easily achieved with powder metallurgy. Impurities on grain boundaries can also be controlled and up to 97%. W. Chen et al., [11] investigated that Ti-6Al-4V powder exhibited a significantly higher sinterability than commercially pure Titanium (CP-Ti) powder. The results showed that the green density of Ti-6Al-4V increased from 71% to 99.6% upon sintering while that of CP-Ti changed from 84% to 94.1% at 1300° C.

The aim of this work is to investigate and characterize the pressed Ti sintered components. Powder was uni-axially pressed at designated pressures from 125 kN to 135 kN to form cylindrical samples and the green compacts were sintered at 0.001 mbar for about 4 hours with maximum sintering temperature varying from 1350°C to 1450°C. Developed metal matrix structures were examined under SEM. The micro-hardness of the samples were also investigated. The influence of the compacting

pressure and sintering temperature on the relative density of the preform has been investigated thoroughly. The deformation characteristics are discussed critically. In particular, properties achievable (i.e. relative density, microstructure and mechanical properties) and problems related to the processing of elemental titanium by PM route of pressing and sintering are discussed. The micro-structure of the sintered samples was examined at different magnification and micro-hardness of the samples was investigated.

### Experiment

Air atomized Titanium powder (average particle size of 325 mesh, 99% metals basis, Make-Alfa-Aesar) are used as the test material and fabricated by powder metallurgy technique. The metal powders were blended in a drum with a cylindrical mixer (diameter 40 mm, height 35 mm), at a constant speed of 1500 rpm for 1h. Blending is one of the crucial processes in P/M where the metallic powders were mixed with the binder acrawax (0.01 % by weight). Good blending produces no agglomeration of both the metallic and binder particles.



*Fig.1: Die and punch set to fabricate cylindrical preform*

A mixture of the particles and the binder has been poured into a cylindrical die with 30 mm height, 14.5 mm inner diameter and 90 mm outer diameter. After pouring, the powder

# EXPERIMENTAL INVESTIGATION OF THE COMPRESSIBILITY AND MECHANICAL PROPERTIES OF Cp-Ti POWDER METALLURGY COMPONENTS

mixtures was cold iso-pressed at 125 kN to 135 kN pressures in an Universal testing machine (Capacity 400 kN, Model: KUT-40, Sl. No. 2K7/85 at ARCI, Hyderabad) for 5 min to obtain green compacts.



*Fig.2: Universal Testing Machine for preparing the green compacts at ARCI, Hyderabad*

The green compacts were then subsequently preheated at 400°C in Nitrogen atmosphere to remove the binder ACRAWAX in a floor-stand quartz made tubular furnace (diameter of hot zone 75 mm, length of hot zone 150 mm and maximum temp 1000°C). The samples were preheated to 400°C with 5°C/min heating rate, thereby holding at 400°C for 2 hours and then cooled in a furnace under nitrogen atmosphere to remove the ACRAWAX completely from the samples.

The green compacts were sintered in an Electric Resistance Batch type Vacuum Furnace (working space dimensions: width-100 mm, length-300 mm & height-100 mm upto a temperature of 1350°C in 0.001mbar vacuum to avoid oxidation.

*Table 1 Sintering parameters*

Operation	Temperature from	Temperature to	Duration
Heating	Ambient 30°C	550°C	55 min
Soaking	550°C	550°C	60 min
Heating	550°C	1350°C	80 min
Soaking	1350°C	1350°C	30 min
Furnace cooling	1350°C	Ambient 30°C	120 min



*Fig.3: Electric Resistance Batch-type Vacuum Furnace at ARCI, Hyderabad*

## Results & Discussion

### Microstructural Examination

The samples were prepared and examined in a Scanning Electron Microscope (Make-JEOL). Samples for metallographic examination have been prepared by grinding through 320, 400, 600, 800, 1200 and 1500 grit papers followed by polishing with 6 µm diamond paste. Then the samples were etched with an etchant (2.5 ml Nitric Acid, 15 ml HCl, 1 ml HF and 95 ml water). The etched samples were dried and their microstructure observed by using SEM at different magnifications. Fig. 4 show the microstructures of the sintered compacts at different magnifications using optical microscope.

# EXPERIMENTAL INVESTIGATION OF THE COMPRESSIBILITY AND MECHANICAL PROPERTIES OF Cp-Ti POWDER METALLURGY COMPONENTS

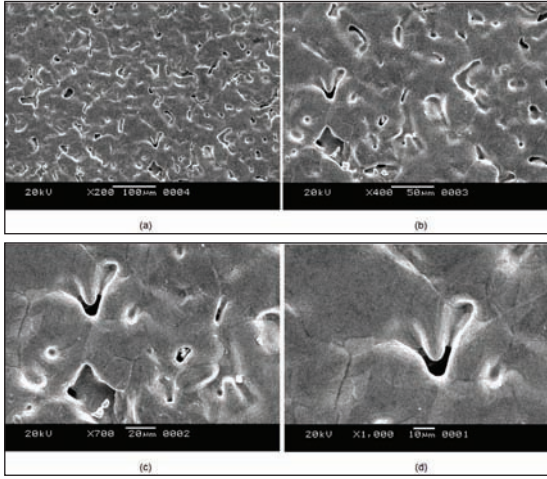


Fig.4(a-d): SEM micrographs of the samples at different magnifications

## Mechanical Properties

### Density Measurement

The densities of the green and sintered samples were measured. The average relative density of the green compacts was about 77.5 % whereas; the average relative density of sintered compacts was approximately 92.5 %. The density Vs sintering temperature & compaction load plot is shown in Fig. 5.

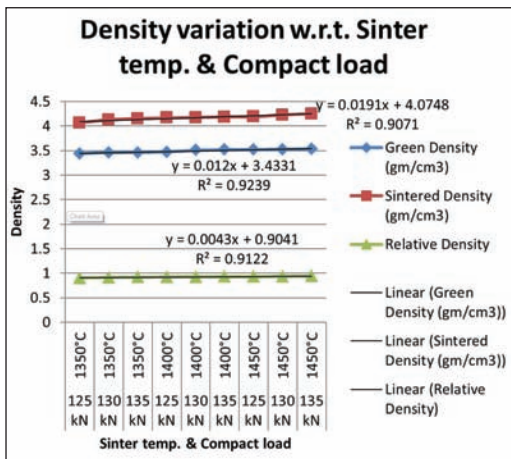


Fig.5: Density variation of with respect to Sinter temp. and Compact load

## Microhardness

The micro-hardness of the sintered samples was measured in Mtsuzawa make AMT Series MMT-X microhardness tester with maximum load capacity 2 kg. The microhardness of the samples (sintered at 1350°C) increases with increasing compacting load. It is also observed that micro-hardness of the samples increases with increasing sintering temperature at same compacting load. It is shown in Figs 6 & 7.

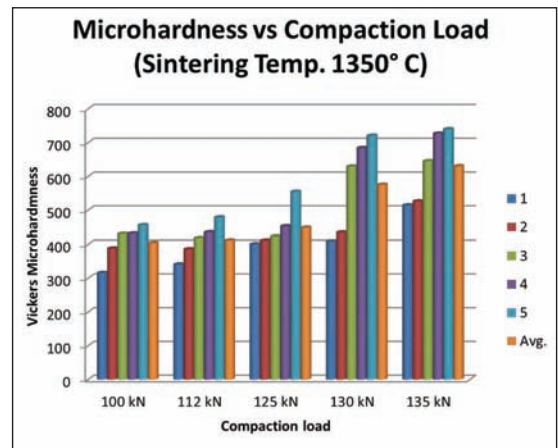


Fig.6: Variation of micro-hardness with respect to compaction load (at const. sintering temperature)

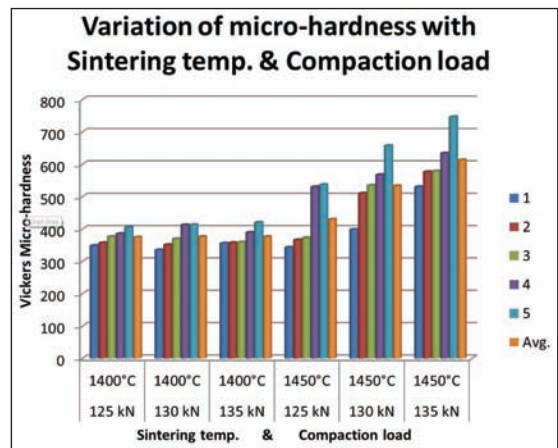


Fig.7: Variation of micro-hardness with respect to compaction load and sintering temperature.

# EXPERIMENTAL INVESTIGATION OF THE COMPRESSIBILITY AND MECHANICAL PROPERTIES OF Cp-Ti POWDER METALLURGY COMPONENTS

## Compressibility

The compressibility characteristics of the sintered samples were tested in an Instron (5500R) and the load Vs deformation curves were obtained. It is also shown in Fig.s 9, 10 & 11.



Fig.8 Instron 5500R for compressibility test

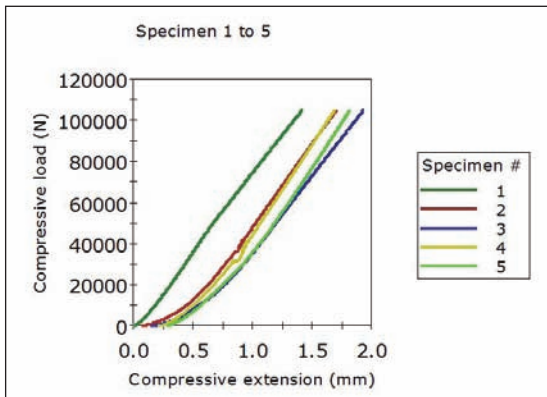


Fig.9: Compressive load – deformation characteristics for 1350°C sinter temperature

Table 2 Compressibility test data for 1350°C sinter temperature samples

	Spec. label	Diameter (mm)	Max. Comp. load (N)	Max. Comp. Stress (MPa)	Max. Comp. stress (kgf/cm <sup>2</sup> )	Compressive extension at Maximum Comp. load (mm)
1	A-10	14.10	105,000.305	672.45	6,857.12	1.421
2	B-10	14.10	105,000.781	672.46	6,857.15	1.639
3	A-1	14.10	105,002.344	672.47	6,857.25	1.793
4	A-2	14.10	105,000.922	672.46	6,857.16	1.480
5	A-3	14.10	105,001.094	672.46	6,857.17	1.536
Mean		14.10	105,001.089	672.46	6,857.17	1.574
S. D.		0.00	0.76	0.00	0.05	0.15
C.V.(%)		0.00	0.00	0.00	0.00	9.31

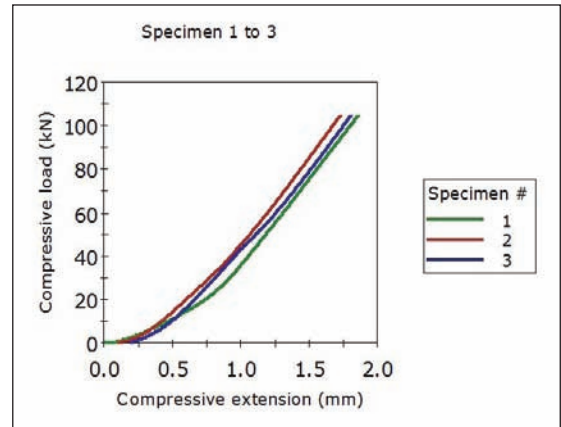


Fig.10: Compressive load – deformation characteristics for 1400°C sinter temperature

Table 3 Compressibility test data for 1400°C sinter temperature samples

	Spec. label	Diameter (mm)	Max. Comp. load (kN)	Max. Comp. Stress (MPa)	Max. Comp. stress (kgf/cm <sup>2</sup> )	Compressive extension at Maximum Comp. load (mm)
1	A-4	14.10	105.001	672.46	6,857.18	1.865
2	A-5	14.10	105.003	672.47	6,857.27	1.641
3	A-6	14.10	105.003	672.47	6,857.27	1.622
Mean		14.10	105.002	672.47	6,857.24	1.709
S. D.		0.00	0.00	0.01	0.05	0.13
C.V.(%)		0.00	0.00	0.00	0.00	7.89

# EXPERIMENTAL INVESTIGATION OF THE COMPRESSIBILITY AND MECHANICAL PROPERTIES OF Cp-Ti POWDER METALLURGY COMPONENTS

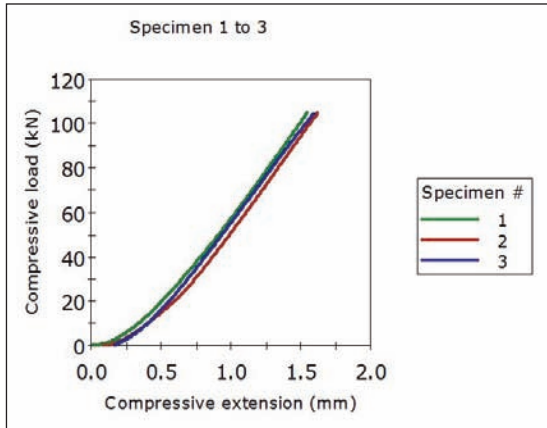


Fig.11: Compressive load – deformation characteristics for 1450°C sinter temperature

Table 4 Compressibility test data for 1450°C sinter temperature samples

	Spec. label	Diameter (mm)	Max. Comp. load (kN)	Max. Comp. Stress (MPa)	Max. Comp. stress (kgf/cm <sup>2</sup> )	Compressive extension at Maximum Comp. load (mm)
1	A-7	14.10	105.000	672.45	6,857.12	1.549
2	A-8	14.10	105.001	672.46	6,857.14	1.546
3	A-9	14.10	105.002	672.46	6,857.20	1.444
Mean		14.10	105.001	672.46	6,857.15	1.513
S. D.		0.00	0.00	0.00	0.04	0.06
C.V. (%)		0.00	0.00	0.00	0.00	3.97

From the compressibility characteristics (Figs 9,10 & 11) and compressibility Test data (tables 2,3 & 4) it can clearly be stated that compressibility decreases with increasing sintering temperature as well as compaction load.

## Conclusion

The variation of the relative density versus sintering temperature shows that relative density increases from 90.1% to 94.3% as sintering

temperature increases from 1350°C to 1450°C. The micro-hardness of the samples increases with increasing sinter temperature and compaction load. The deformation characteristics curves indicate that as sintering temperature as well as compaction load increases, compressibility decreases. The value of maximum compression is found to be decreasing from 1.793 mm to 1.444 mm.

## Acknowledgements

Authors thankfully acknowledge the financial support provided by C.S.I.R., New Delhi under Major Research Project Grant [Sanction letter No. 22(0587) /12 / EMR-II dated 02.04.2012] without which this work could not be attempted.

## References

1. G. W. Cull, "Mechanical and metallurgical properties of powder forging", *Powder Metallurgy*, **13** (26), 156-164, (1970).
2. P. K. Jones, "The technical and economic advantages of powder forged product", *Powder Metallurgy*, **13** (26), 114-129, (1970).
3. R. J. Green, "A plasticity theory for porous solids", *Int. J. Mech. Sci. Engg.*, **14**, 215-224, (1971).
4. T. Tabata, M. Masaki, "A yield criterion for porous metals and analysis of axial compression of porous discs", *Memoirs of Osaka Institute of Technology, Series-B, Science and Technology*, **22** (2), 45-55, (1978).
5. P. Ramakrishnan, "Forging of metal powder performs", *Proc. Int. Seminar on Metal Working Technology Today and Tomorrow*, NIFFT, Ranchi, (1980)
6. A. K. Jha, S. Kumar, "Deformation characteristics and fracture mechanism of sintered copper powder strips during cold forging", *J. Mech. Working Tech.*, **16**, 145-164, (1988).

## EXPERIMENTAL INVESTIGATION OF THE COMPRESSIBILITY AND MECHANICAL PROPERTIES OF Cp-Ti POWDER METALLURGY COMPONENTS

---

7. Timet (Titanium Metals Corporation USA.), 1997, Corrosion resistance of titanium, Online : <http://www.timet.com>.
8. F.H. Froes, "Titanium Alloys", in *Handbook of Advanced Materials*, Edited by James K. Weasel, McGraw-Hill Inc., New York, (2000).
9. R. Astana, R., A. Kumar, N. Dahotre, *Material Science in manufacturing*, Elsevier USA, (2006).
10. H. J. Joubert, "Investigation of lubrication strategies in Ti6Al4V milling operations", *Masters Thesis*, Stellenbosch University, (2008).
11. W. Chen et al., "The investigation of die-pressing and sintering behaviour of ITP CP-Ti and Ti-6Al-4V powders", *J. Alloys Comp.*, **541**, 440-447, (2012).



# ADDITIVE MANUFACTURING FOR MAKING FULLY DENSE AUTOMOTIVE PARTS

S.R.Sundaram

Pricol Ltd., Coimbatore, India

**Abstract :** Only in the last 10 years companies have started looking at additive manufacturing as way of changing their global supply chain. In 2013, Additive Manufactured (AM) goods collected globally an estimated \$ 967 Million). US accounts for 38% of global production of AM goods. It is feared that in the next twenty years manufacturing industry may lose a billion blue-collar jobs.

When we talk of additive manufacturing we think of making the Penrose Triangle-complex shapes, which can't be made by any other method.

Can we make smaller, fully dense, normal automotive parts? Helical gears, forged two- wheeler Con rods, transmission gears, which we forge, or sinter-forge now? Can we save energy and material?

This paper looks at the cost factors involved in AM produced parts, and the possibility of applying AM technology to the above parts.

**Key Words:** Additive manufacturing, fully dense Automotive parts, Cost factors.

## The Additive manufacturing, current scene:

Although additive manufacturing allows the manufacture of customized and increasingly complex parts, the slow print speed of additive manufacturing systems limits their use for mass production. 3D scanning technologies have enabled the replication of real objects without using expensive molds. As the costs of additive manufacturing systems decrease, this technology may change the way that consumers interact with producers. The customization of products will require increased data collection from the end user. An inexpensive 3D printer allows the end user to produce polymer-based products in his or her own home or office. Currently, there are a number of polymer systems that are within the budget of the average consumer.

In 2013, Additive Manufactured (AM) goods collected globally an estimated \$ 967 Million). At \$367 million, US accounts for 38% of global production of AM goods. [1]

**Table 1: Additive manufactured goods shipped in 2011[1]**

Category	Relevant NAICS Codes	Percent of Total AM Made Products	Shipments of US Made AM Products (\$millions, 2011)*	Total Shipments (\$millions, 2011)
Motor vehicles	NAICS 3361, 3362, 3363	19.5%	48.0	445 289.4
Aerospace	NAICS 336411, 336412, 336413	12.1%	29.8	157 700.7
Industrial/business machines	NAICS 333	10.8%	26.6	365 734.8
Medical/dental	NAICS 3391	15.1%	37.2	89 519.5
Government/military	NAICS 336414, 336415, 336419, 336992	6.0%	14.8	32 784.4
Architectural	NAICS 3323	3.0%	7.4	72 186.9
Consumer products/electronics, academic institutions, and other	All other within NAICS 332 through 339	33.6%	82.7	895 709.8
<b>TOTAL</b>	<b>NAICS 332 through 339</b>	<b>100.0%</b>	<b>246.1</b>	<b>2 058 925.5</b>

NAICS is North American Industry Classification System.

\*These value calculations assume that % of each AM product is the same for US and globally. It is also assumed that the share of AM systems sold is equal to share of revenue for AM products. N°s may not add up to total due to rounding off.

## Additive manufacturing – The three Scenarios:

The first is considered by many to be the most extreme where a significant proportion of consumers purchase additive manufacturing systems or 3D printers and produce products themselves.

The second is a copy shop scenario, where individuals submit their designs to a service provider that produces it.

Höganäs' Digital Metal is, where individuals share their ideas as a project and then Digital metals does all design conversion into Additive Manufacturing logistics, and produce and supply the part.

Both of these scenarios are considered by many to be somewhat less likely.

The third scenario involves additive manufacturing being adopted by the commercial manufacturing industry, changing the technology of design and production. Additive manufacturing is seen as a practical alternative for commercial manufacturing in high wage economies.

If additive manufacturing has a saturation level between 5 % and 35 % of the relevant sectors, it is forecasted that it might reach 50 % of market potential between 2031 and 2038, while reaching near 100 % between 2058 and 2065. The industry would reach \$50 billion between 2029 and 2031, while reaching \$100 billion between 2031 and 2044. [1]

The greatest advantage is seen as a whole assembly can be AM produced, and all supply chain, and associated problems can be done away with. Below is a complete Jet engine, AM Produced. [3]By the side on right is a swirler component used in Aerospace industry. [4]



*Fig 1. Additive manufactured, completeJet engine*

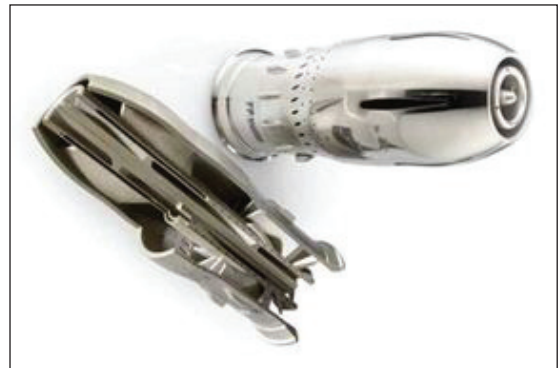


*Fig 2. Aero space part*

In 2016, GE Aviation's additive production facility will begin printing fuel nozzles for the new LEAP jet engine—an engine that will be used to fly Airbus A320s, Boeing 737s and Comac 919s.

These are 100% 3-D printed components, designed by GE engineers and printed on GE equipment in GE factories, which will be churning out 30,000 to 40,000 of them per year by 2020. [5]

### **Additive manufacturing- is it only for making complicated and expensive parts?**

The general view is, normal PM parts are mass produced very cost effectively- why use a new technology which is time consuming and expensive and can be better used for making critical complex parts like Medical implants, Complete aircraft engines. This view is pretty much correct.

- But there are PM parts which have constraints in meeting requirements of a forged part.
- Helical gear compaction needs special attachments and even then with restrictions on the helix angle. All PM tools are expensive with a substantial cost contribution to the part
- Since Direct Metal Laser Sintering (DMLS) process of Additive Manufacturing melts

any alloy powder and deposits layer by layer, it is fair to conclude that the part produced by DMLS would be almost dense. The parts needing special equipment or special operations like Sinter forging can be explored for manufacture by AM production route, as the Sinterforged parts still need substantial machining.

1. **Helical gears:** 3-D Printed helical gear image [6] is seen on Fig.3.

We can make the helical gear without:

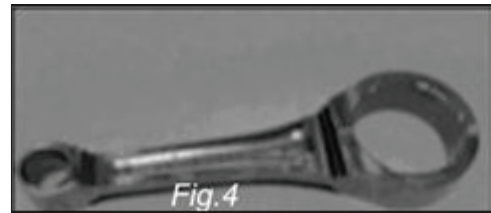
- Special tooling;
- Compaction press with a helical gear attachment;
- Sintering and distortion in sintering,

We would have a near full density part without the usual worries of equipment, raw materials and variance in product properties.

2. **Two-wheeler Conrods:** Currently these are forged. There is a report about powder forging a two-wheeler conrod [7]. The conrod is shown in Fig.4. But there are design issues of the conrod shape, which is to be altered to suit PM by Two-wheeler manufacturer.

If we are considering manufacture by 3 D printing, then there are no shape constraints.

We can possibly save energy and material.



3. **Two wheeler transmission gears:** Forging is the conventional method for making Transmission gears for two-wheelers. See Fig5. Probably the Two Wheeler Transmission gears are good candidates for exploring making by 3 D Printing.

These three are components used in automobiles, which can perhaps be considered for manufacture by DMLS, one of the many Additive Manufacturing techniques.

Constraints preventing application of AM techniques for producing these items are required to be examined.

A large number of additive processes are now available. The main differences between processes are in the way layers are deposited to create parts and in the materials that are used. Some methods melt or soften the material to produce the layers, for example, Selective laser melting or direct metal laser sintering (DMLS), selective laser sintering (SLS), fused deposition modeling (FDM), or fused filament fabrication (FFF), while others cure liquid materials using different sophisticated technologies, such as Stereolithography (SLA), With Laminated object manufacturing (LOM), thin layers are cut to shape and joined together

# ADDITIVE MANUFACTURING FOR MAKING FULLY DENSE AUTOMOTIVE PARTS

(e.g., paper, polymer, metal). Each method has its own advantages and drawbacks, which is why some companies offer a choice of powder and polymer for the material used to build the object. The main considerations in choosing a machine are generally speed, costs of the 3D printer, of the printed prototype, choice and cost of the materials, and color capabilities.[13]

**Table 2: Cost structure in, Additive Manufacturing\*\*, Press & Sinter and Sinter Forge production\*:**

Costs	Euros (€)		Euros (€)
	Helical gear	Connecting Rod	AM part
	Press & Sintered	Sinter forged	Additive manufactured
Raw material cost	0.47	0.58	1.63
Tooling	0.21	0.22	-
Labour cost	0.06	0.41	0.04
Machine +operating costs	0.73	1.28	0.52
After operatios / machining	0.30	0.80	-
Total per piece (€)	1.77	3.29	2.19

\* Calculated using costs normal in PM industry. \*\* Costs taken from Table 3

**Table 3: Costs breakup (Hopkinson and Dickens 2003) [2]**

Other	Fused deposition modeling		
	Stereolithography	Laser sintering	Laser sintering
Number per platform	190	75	1056
Platform build time	26.8	67.27	59.78
Production rate per hour	7.09	1.11	17.66
Hours per year in operation	7 884	7 884	7 884
production volume total per year	55 894	8 790	139 269
Machine and ancillary equipment (€)	1 040 000	101 280	340 000
Equipment depreciation cost per year (€)	130 000	12 660	42 500
Machine maintenance cost per year (€)	89 000	10 560	30 450
Total machine cost per year (€)	219 000	23 220	72 950
Machine cost per part (€)	3.92	2.64	0.52
Machine operator cost per hour (€)	5.30	5.30	5.30
Set-up time to control machine (min)	33	10	120
Post-processing time per build (min)	49	60	360
Labor cost per build (€)	7.24	6.18	42.37
Labor cost per part (€)	0.04	0.08	0.04
Material per part (kg)	0.0047	0.0035	
Support material per part (kg)		0.0016	
Build material cost per kg (€)	275.20	400.00	54.00
Support material cost per kg (€)		216.00	
Cost of material used in one build (€)			1 725.72
Material cost per part (€)	1.29	1.75	1.63
Total cost per part (€)	5.25	4.47	2.20

## Raw materials currently available for Additive Manufacturing technologies (DMLS)

Currently AM technologies are targeting parts for aerospace or medical implants, the alloys are used are stainless steels, Titanium and Nickel alloys which are expensive.

M/s Electro Optical Systems (EOS) makers of DMLS equipment for many years, also sell a range of powders, to be used on their equipment. M/s Sandvik Osprey [7] powders can also be used in AM equipment.

**Table 3: Some EOS Raw Materials currently available. [10]**

Material name	Material type	Typical applications
DirectMetal 20	Bronze-based mixture	Injection moulding tooling; functional prototypes
DirectSteel H20	Steel-based mixture	Injection moulding tooling; functional prototypes
EOS MaragingSteel MS1*	18 Mar 300 / 1.2709	Injection moulding series tooling; engineering parts
EOS StainlessSteel 17-4	Stainless steel 17-4 / 1.4542	Functional prototypes and series parts; engineering and medical
EOS CobaltChrome MP1	CoCrMo superalloy	Functional prototypes and series parts; engineering, medical, dental
EOS Titanium Ti64*	Ti6Al4V light alloy	Functional prototypes and series parts; aerospace, motor sport etc.
EOS Titanium TiCP*	Pure titanium	Functional prototypes and series parts; medical, dental

One producer of powders for Additive Manufacturing, indicates that Iron based alloy powders could cost 80-120 \$ per Kg. [9]

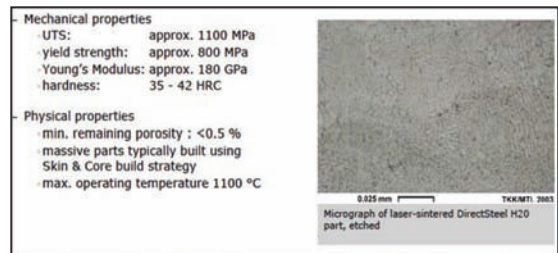


**Fig 6: Mechanical Properties: EOS Direct Steel H20 powders. [11]**

## Build speeds in DMLS technology currently available

Talks with M/s 3D Engineering, the Indian partners of EOS GmbH gave us an insight into the operation, build speeds and dimensional and surface finish accuracy of the part produced in DMLS machine made by EOS. We had looked at EOS equipment -EOS M 400. The data is given in TABLE 4 [12].

**Table 4: Data on size, operating and manufactured part parameters for EOS M 400[12]**

Build Dimensions -mm	400 x 400 x 400
Process	Selective Laser Sintering
In put material	Granular powders
Layer thickness	20-100µ
Build speed	2-20 cm <sup>3</sup> /hr.* varies with powder composition
General tolerance on dimensions, closer dimensions by using beam offset.	± 50µ
Surface finish-After shot peening	R <sub>a</sub> 0.16-0.25

### Estimated time for making one part

Roughly estimated, we can fabricate a part in 1.98 minutes / part by the Press & Sinter Route, and 6.27 minutes per part by the Sinter forge Route.

If we consider making a two-wheeler con rod, 100 mm by 28 mm wide (average of central beam and big end and small end), which is 10 mm thick (average of central beam, big and small ends), you have a volume of 28 Cm<sup>3</sup> will take about 1.4 hours at present available build speeds. It is stated that equipment with "build speed" quicker than 20 cm<sup>3</sup> / hr. will be available in near future.

If build speeds increase, by use of multiple laser beams, and become double in say the next five years, then we have a conrod in 40 minutes and with multi part loading platforms, and lower raw material price you could increase the numbers, and at lower prices.

Considering the investment in a Sinter Forging and after machining equipment expenses, as also the increased carbon foot print created by the forging process, the investment in AM equipment will be cheaper, and process eco friendly.

**Future: Can we Additive manufacture the entire gear assembly as shown and save weight, space and reduce CO<sub>2</sub>.**



### Conclusions:

Additive manufacturing has become a significant technology, no longer considered as a prototyping technique.

While it is being currently used for very complicated parts plans are afoot to make complete assemblies by Additive Manufacturing, thereby cutting the supply chains with inherent cost and time saving.

The view, PM parts are being made cost and material effective in Press & Sinter Route, so why should we use Additive manufacturing which is expensive and more time consuming is largely correct.

But there are some parts, Helical gears, Two wheeler conrod, or two-wheeler transmission gears are being made in special equipment and special processes, which are expensive and use lot of time. Perhaps consideration can be given to be to produce these parts by Additive Manufacturing.

In the foregoing paragraphs it is shown that if you have machines with a better build speed, these may be viable products for Additive Manufacturing.

Raw materials are currently limited to Aero Space, and Medical applications. If the forged transmission gears are to be made by Additive Manufacturing, the volumes will reduce Raw material cost as also make suitable powders available.

### References:

1. Cost and Cost Effectiveness of Additive Manufacturing by Douglas S. Thomas and Stanley W. Gilbert- National Institute of Standards and Technology- U.S. Department of Commerce, NIST special publication, December 2014.
2. Costs breakup (Hopkinson and Dickens 2003)

## ADDITIVE MANUFACTURING FOR MAKING FULLY DENSE AUTOMOTIVE PARTS

---

3. GE-Advanced manufacturing, inventing the way we look -GE.com, June 2013.
4. Laser sintering-versatile production of tooling inserts, prototype parts, and end products from metal powder- Review 12, January 2011
5. "Will 3-D supply meet GE's sky high demand?" by Travis Hessman- Material Handling & Logistics, February 13, 2014.
6. Metal Laser Sintering Technology, A Solid Concepts Video, 2013.
7. "Powder forging a Motorcycle Con Rod" by Guangchun Wang and Guaqun Zhao, J Journal of Material Science Technology, Vol 18, No6, 2002.
8. "Sandvik powders for Additive Manufacturing", Brochure.
9. "Additive Layer Manufacturing=ALM=3 D Printing" Metalysis Brochure, 2015.
10. EOSINT M Materials, Page 2, Range of materials. Year 2007
11. EOSINT M Materials, Page 8, Direct steel H20, Characteristics & Properties, Year 2007.
12. EOS M 400, The Additive Manufacturing system for Industrial Production of Large Parts, as also discussion with 3 D Engineering, the Indian partner of EOS, GmbH, year 2013.
13. 3 D Printing -Wikipedia.
14. Auto Application Trends and Opportunities for PM by Thomas Schmidtsteifer, Höganäs, Slide 21, Down sizing (Space & weight saving -> Co2 Reduction) - February, 2013



# DIMENSIONAL CONTROL IN POWDER METAL PARTS

Fran Hanejko, Bruce Lindsley, Kalathur S. Narasimhan and Mahesh Kamble\*

Hoeganaes Corporation, U.S.A., \*Speciality Sintered.Pune

**Abstract :** Powder metallurgy is a netshape process and hence an understanding what controls dimensional change is important. The alloying elements such as C, Mo, Ni, Mn, Cr and Cu will increase the hardenability of steel. The amount of pre-alloyed elements in the base iron will affect the transformation products found after sintering. The cooling rate, pre-alloyed elements and admixed additions will determine the final microstructure and mechanical properties in the sintered compact. Investigations on pure iron powder alloyed with Cu and graphite, pre-alloyed Mo alloyed with graphite reveal that better dimensional control is achieved using 0.3% prealloyed Mo powder in heat treated condition. Four Sinter hardening grades were evaluated and results suggest Ancorsteel 4300 is most stable and provides a good dimensional precision.

**Key words:** Dimensional precision, prealloyed, sinter hardening, tempering

## Introduction:

Powder Metallurgy is a green process with over 97% material utilization and lowest energy per kilogram of part produced compared to other metal working processes [1]. The major advantage of powder metal parts is that it is produced in net shape configuration with very little machining. The technology is well accepted by automotive companies globally and applications continue to increase. Dimensional precision although good but efforts continue to improve the precision of powder metal parts. Understanding the factors involved in improving precision are being addressed by the industry globally. Hoeganaes developed number of dimensionally stable materials and in this paper we review the work done in the past in these areas. FC-0208 is used extensively in the industry because of the ease of manufacturing. Dimensional precision of parts made from these powders needs improvement, Cu diffusion in iron is often controlled by the graphite diffusion which is controlled by the heat up rate to sintering temperature. Although the elemental copper addition melts during initial sintering, complete homogenization of the copper is not

achieved at conventional sintering temperatures and sintering times. This lack of microstructural homogeneity coupled with the potential for large pores can often lead to reduced strength and greater dimensional variability during sintering and subsequent heat treatments In this study we compared a 0.3% prealloyed Mo powder with FC-0208 premixes [2].

The demand for higher mechanical properties and lower cost for increasing powder metal penetration in the automotive applications resulted in the development of a number of sinter hardening grades [3]. We compare four sinterhardening grades and studied dimensional precision after various heat treatments.

## Experimental:

### Comparison of FC-0208 to 0.3% molybdenum with 0.8% graphite

Four premixes were prepared as shown in Table 1. The mixes containing atomized Acrawax C were conventional premixes prepared via double cone blending. The premixes containing the warm die lubricant (AncorMax 200™) were prepared via a proprietary premixing process.

## DIMENSIONAL CONTROL IN POWDER METAL PARTS

*Table 1. Composition of Premixes*

Mix	Baselron	%Copper	%G	% Lube &Type
1	Unalloyed ironpowder	2	0.8	0.75%Acrawax
2	Unalloyed ironpowder	2	0.8	0.4% warm die lubricant
3	Prealloyed0.3% Molybdenum	NA	0.8	0.75%Acrawax
4	Prealloyed0.3% Molybdenum		0.8	0.4% warm die lubricant

The following test specimens were compacted from the four premixes listed in Table1.

Compressibility test specimens at 415, 550, and 690 MPa.

For the warm-die premixes additional compressibility data was generated at 830 MPa. The conventional premixes were compacted in dies at room temperature; whereas, the AncorMax 200 premixes were compacted at 93 °C, no powder preheating.

Transverse rupture strength bars for both as-sintered and heat treated strength at the various compaction pressures.

MPIF standard dog-bone type tensile specimens for both as sintered and heat- treat conditions (MPIF standard10).

Sintering of all samples was done at 1120 °C in a continuous belt furnace in an atmosphere of 90% nitrogen / 10% hydrogen for ~20 minutes at temperature; the cooling rate after sintering was ~0.6 °C per second (no accelerated cooling). All samples were sintered on ceramic trays. Heat-treated samples were re-austenitized at 815°C in a 75% hydrogen / 25% nitrogen atmosphere for 1 hour at temperature. They were oil quenched in 65 °C oil and subsequently tempered at 205°C for 1 hour in a nitrogen atmosphere.

These premixes were utilized to evaluate the dimensional change variability during the heat-treat response of a prototype gear. The gear geometry used is shown in Fig. 1. Approximately 1,000 gears were made from each premix, the two

conventional double- cone premixes were run in unheated tooling with a target part density of 7.1 g/cm<sup>3</sup> and the warm-die lubricant premixes were run in a die heated to 93 °C without top punch heating and a target part density of ~7.1 g/cm<sup>3</sup>. The compacted gears were sintered at 1120 °C for 20 minutes at temperature in a 90% nitrogen / 10% hydrogen atmosphere in a 6-inch ceramic belt furnace without accelerated cooling. From these sintered gears 50 were randomly chosen and sent to a commercial heat-treat facility for a quenching and tempering operation. The heat treat cycle used was to austenitize at 870 °C for 1 hour in a 0.8% carbon atmosphere followed by oil quenching and tempering. From these 50 heat-treated gears ~20 were then measured for part-to-part dimensional variation via a measurement over wire (MOW) of the gearform.



*Fig 1: Spur gear produced to evaluate part-to-part consistency in the heat-treated condition*

Gear dimensions were major O.D. 28.3 mm, major I.D. 21.6 mm, pitch diameter 24.5 mm, pressure angle 20°, I.D. 9.5 mm, number of teeth 16, module 1.66.

Property comparison of FC-0208 vs. 0.3% prealloyed molybdenum steel with 0.8% graphite:

Fig. 2 presents the compressibility curves of the four materials listed in Table 1. As previously noted, compaction of the Acrawax containing premixes took place in unheated dies at room temperature; whereas, compaction conditions

## DIMENSIONAL CONTROL IN POWDER METAL PARTS

of the warm-die powder premixes was in dies heated to 93°C without any prior powder heating. The compressibility of the prealloyed 0.3% molybdenum steel is identical to the FC-0208 material at both room temperature and at die temperatures of 93°C. Utilizing warm die processing results in a 0.05 to 0.10-g/cm<sup>3</sup> increase in green density relative to conventional lubricants for both material options. The optimal benefit with warm-die compaction is observed at compaction pressures greater than 550 MPa.

Although not shown, warm die processing also promotes higher green strength with reduced green expansion and reduced ejection forces.

The as-sintered and heat-treated transverse rupture strengths as a function of sintered density for the FC0208 and 0.3% molybdenum prealloy with 0.8% added graphite are presented in Fig 3. Warm-die processing did not affect the sintered or heat-treated strength. As anticipated, in the as-sintered condition, the FC-0208 material possesses higher strengths when compared to the prealloyed 0.3% molybdenum material.

However, once heat-treated the strengths of the two materials are nearly equivalent.

As-sintered tensile properties and heat-treated tensile properties for the 0.8% graphite additions are presented in Table 3. Similar to the trend observed with transverse rupture strength testing, the as-sintered yield and ultimate tensile strengths of the FC-0208 are greater than the prealloyed 0.3% molybdenum steel. Elongation values are nearly the same. Also presented in Table 3 are the ultimate tensile strengths of the FC-0208 vs. the 0.3% molybdenum steel in the quenched and tempered condition. Similar to what was found in TRS testing, in the heat-treated condition the prealloyed 0.3% molybdenum steel with 0.8% graphite and heat-treated FC-0208 have nearly identical ultimate tensile strengths. The data presented Table 3 represent compaction at 415, 550, and 690 MPa. The prealloyed 0.3% molybdenum material has lower growth relative to the FC-0208, thus the sintered densities at the

same compaction pressure are higher for the prealloyed molybdenum material.

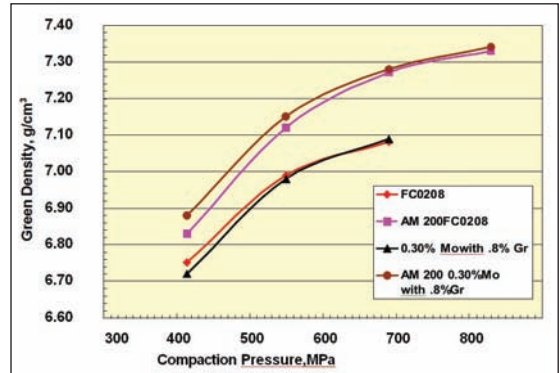


Fig 2: Compressibility of the four premixes

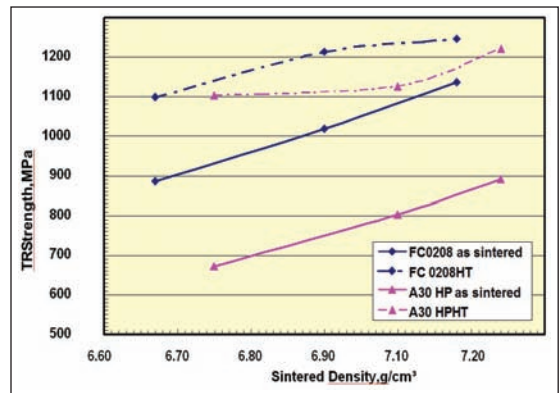


Fig 3 As-sintered and heat-treated transverse rupture strength.

Table 3: Summary of Tensile Properties of FC0208 and Prealloyed 0.3% Molybdenum Steel

Material	Sintered Density, g/cm <sup>3</sup>	Heat Treated	0.2% YS (MPa)	UTS, (MPa)	Total Elongation (%)	Hardness, (HRA)
FC0208	6.67	No	393	470	1.4	47
	6.90		448	564	1.8	50
	7.04		467	597	1.9	53
	6.67	Yes	NA	672	<1.0	64
	6.90		771	69		
	7.04		870	69		
0.30% Mo Pre-alloy with 0.80% Graphite	6.75	No	293	334	1.2	40
	7.00		333	415	1.6	45
	7.14		359	435	1.7	47
	6.75	Yes	NA	705	<1.0	64
	7.00		805	69		
	7.14		855	71		

**Results of heating treating of the gear shown in Fig. 2.**

Prototype gears were produced using the four materials discussed in part one of this study. They were made on a Dorst 140 metric ton compaction press at a rate of 10 per minute. The gears were sintered in a continuous belt sintering furnace at 1120°C in a 90% nitrogen / 10% hydrogen atmosphere with a time at temperature of ~20 minutes. After sintering approximately 50 gears from each material grouping were heat-treated by quenching and tempering utilizing a commercial heat-treat cycle for FC0208. After quenching, the gears were then tempered at 205°C. The gears were checked for dimensional variation using 3.162 mm diameter pins. Measurements were taken at four locations per gear starting with the front of the gear (as compacted) and then measuring three additional locations around the outside diameter. The results of the measurement over wires (MOW) are presented in Table 4.

*Table 4 Dimensional Variations of Heat Treated Gears*

Material	Av.MOW Inches (mm)	MaxMOW Inches (mm)	MinMOW Inches (mm)	Max-Min Inches (mm)	St Dev MOW
FC-0208 (regular premix)	1.2096 (30.72)	1.2118 (30.78)	1.2075 (30.67)	0.0043 (0.11)	0.0013 (0.03)
0.3%Mo with 0.8%gr (regular premix)	1.2090 (30.71)	1.2096 (30.72)	1.2081 (30.69)	0.0015 (0.04)	0.0003 (0.01)
FC-0208 (bonded premix)	1.2099 (30.73)	1.2117 (30.78)	1.2082 (30.69)	0.0036 (0.09)	0.0008 (0.02)
0.3%Mo with 0.8%gr (bonded premix)	1.2084 (30.69)	1.2089 (30.71)	1.2075 (30.67)	0.0014 (0.04)	0.0003 (0.01)

*Table 5 Apparent Hardness Values of Gears in the Heat-Treated Condition*

Material	Sintered Density, g/cm <sup>3</sup>	Average Hardness, HRA	Range of Hardness, HRA
FC-0208 (regular premix)	7.01	68.1	64.0 / 71.4
0.3-0% Mo with 0.8% gr (regular premix)	7.05	70.4	67.1 / 72.7
FC-0208 (bonded premix)	7.04	69.3	64.2 / 73.5
0.3% Mo with 0.8% gr (bonded premix)	7.10	71.0	67.5 / 73.5

The data presented in Table 4 clearly demonstrate the reduced scatter realized with the prealloyed 0.3% molybdenum steel relative to a standard FC-0208 material. The absolute magnitude of the MOW is different for the two material combinations; this is a result of the absolute DC differences between an FC-0208 and a 0.3% molybdenum prealloyed steel with 0.8% graphite. Thus, it can be clearly seen that a molybdenum steel gives greater dimensional stability in the heat-treated condition. No green or sintered gears were measured because the focus of this report was to investigate heat-treated results.

For the FC-0208 material, the binder treated warm-die powder gave a reduced overall scatter as measured by the maximum measurement minus the minimum measurement and also the standard deviation of the measurement differences. Thus, the binder treatment does result in reduced part-to-part scatter even for the copper-containing steel. No difference in dimensional variation was observed for the binder treated 0.3% molybdenum steel.

Apparent hardness data collected on the gears are presented in Table 5. The gears were initially compacted to a 7.1 g/cm<sup>3</sup> green density; the densities given in the table are heat-treated densities. Another benefit of the low alloy steel powder is the greater uniformity of heat-treated hardness as measured by the range of hardness readings.

One potential benefit of eliminating the copper may be a reduced tendency for cracking during induction hardening. Induction hardening of copper containing PM steels has shown sensitivity to cracking. A possible explanation is the non-uniform microstructure inherent with copper containing PM steels. Eliminating the copper would eliminate one potential for crack initiation during induction hardening of the PM materials.

**Sinterhardenable Grades:**

Austenite is the highest density phase in steel, followed by ferrite plus carbide, and finally

## DIMENSIONAL CONTROL IN POWDER METAL PARTS

martensite, which is the lowest density phase. This decrease in density results in a corresponding increase in compact size, and martensite formation leads to the largest growth resulting from microstructural changes. Length changes in pore free materials can reach 1.4% upon transformation from austenite to martensite. Tempering of martensite leads to a ferrite and carbide structure, which has a higher density. The post sintering operation of tempering should therefore decrease the dimensional change of a martensitic sintered compact. However, retained austenite is not a stable phase at temperatures below the eutectoid temperature. A reduction in temperature below room temperature will continue to drive the martensite transformation, while an increase above ambient temperature will encourage bainite formation. Transformation of retained austenite to either martensite or bainite will result in compact growth. The purpose of this study is to investigate the effects of post-sinter processing on the dimensional change and microstructure of sinter hardened steels.

### Experimental Procedure

The alloys studied were FLC2-4808 (Ancorsteel\* 737 + 2wt% Cu + graphite), FLNC - 4408 (Ancorsteel 85HP + 2wt% Ni + 1.5wt% Cu + graphite), FLC-4608 (Ancorsteel 4600 + 2wt% Cu + graphite) and Ancorsteel 4300 + graphite. The compositions are listed below in Table 6. The mixes were compacted into standard TRS, dogbone tensile, Charpy impact and dilatometry test specimens at a compaction pressure of 690 MPa at room temperature. The samples were sintered in a 90% nitrogen - 10% hydrogen atmosphere at 1120 °C and accelerated cooling was used to achieve a cooling rate of 1.6°C/sec between part temperatures of 650°C and 315°C. Tempering was carried out in a nitrogen purged furnace at 205°C for the majority of test conditions. After sintering, samples were subjected to a variety of tempering (T) and liquid nitrogen quench (LNQ) operations: 1. as- sintered, 2. LNQ, 3. T/1hr, 4. LNQ + T/1hr, 5. T/1hr, cool to room temperature + T/1hr .

*\*Ancorsteel is a registered trademark of Hoeganaes Corporation*

*Table 6. Nominal compositions (in wt.%) of the alloys studied, balance Fe.*

Alloy#	Designation	Ni	Mo	Mn	Cu	Cr	Si	C
1	FLC2-4808	1.4	1.2	0.4	2	-	-	0.8
2	FLNC-4408	2.0	0.8	0.1	1.5	-	-	0.8
3	FLC-4608	1.8	0.5	0.1	2	-	-	0.8
4	Ancorsteel4300	1.0	0.8	0.1	-	1.0	0.6	0.6

### Results

The as-sintered microstructure of the four sinter-hardenable alloys is shown in Fig 4. Alloy 1 (FLC2- 4808) is fully martensitic, while the other three alloys are predominately martensitic with a small percentage of bainitic regions. Nickel-rich regions can be found in the FLNC-4408 (Alloy 2) microstructure. Alloy 1 has the highest hardenability of the four alloys and can be cooled at a relatively slow rate while still maintaining a

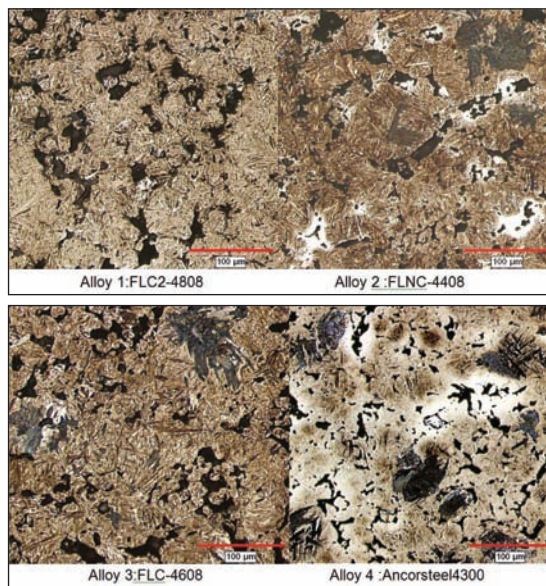


*Fig 4. As-sintered microstructures of sinter-hardened Alloys 1-4 (2% Nital/4%PicralEtch).*

fully martensitic microstructure. The other three alloys have lower hardenability, and cooling rate of the sintered compact will play an important role in the final microstructure. One should be aware that the amount of martensite will play a role in the final dimensions of the part and how it responds to tempering. Therefore cooling rate must be well controlled to develop reproducible microstructures and dimensions.

Alloys high in carbon and copper with martensitic microstructures, such as Alloys 1-3, often contain a large fraction of retained austenite. Fig 5a shows the martensitic microstructure of Alloy 1 using a typical etchant, whereas Fig 5(b) shows the same field etched to reveal retained austenite (white). The majority of the retained austenite is directly associated with copper rich regions. Notice the retained austenite is present surrounding the pore network where copper concentrations are highest. Earlier work on this alloy has shown retained austenite levels as high as 10% . Given that the retained austenite is not uniformly distributed, local concentrations of austenite near the pore network will be much higher than the average value reported in the earlier work. Dimensional control of these sinter-hardened structures will be governed by not only tempering of martensite but also the transformation of retained austenite.

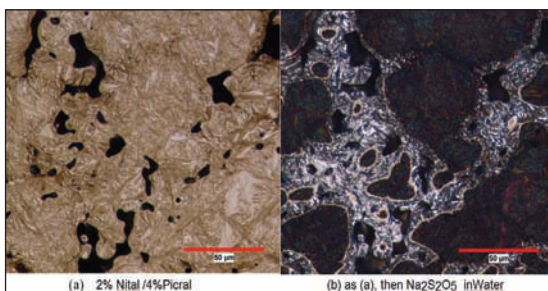


**Fig 5. Microstructure of the sinter-hardened Alloy 1 (FLC2-4808) at 1.6 °C/sec etched to reveal (a) martensite and (b) retained austenite (white) in Cu-rich regions (same field).**

The early stages of tempering involve 3 phenomena: 1) rapid stress-relieve and diffusion of C to dislocations at relatively low temperature, 2) transformation of retained austenite to bainite, and 3) further C diffusion out of the martensite associated with the formation of carbides above 200 °C. The first and third phenomena involve a reduction in length, as the body center tetragonal (bct) structure of martensite changes to bcc ferrite and carbide. The second produces a length increase, as the high density austenite phase transforms to the lower density bainite.

The dimensional change of Alloys 1 - 4 for the various thermal treatments is given in Table 7 . The results have been normalized to an as-sintered dimensional change of zero. Alloys 1 - 3 have significant levels of retained austenite, resulting in significant growth (+0.13% to +0.14%) with the LNQ. Tempering of the martensite results in shrinkage, as the bct structure of martensite converts to a bcc ferrite and carbide structure. Shrinkage results are seen in Table 7, where the pre and posttempercondition of the as-sintered and LNQ samples are compared. More shrinkage occurs during tempering of the LNQ sample, as there is no growth contribution from conversion of retained austenite. It is interesting to note that the growth of Alloys 1-3 upon LNQ was similar, but the shrinkage during tempering is consistently lower for Alloy 2. The double tempered samples and the samples show growth relative to the single tempered samples as the retained austenite transforms to bainite. Samples only grew between 0.05% and 0.08% relative to the tempered condition, whereas the LNQ samples grew between +0.13% and +0.14 %.

## DIMENSIONAL CONTROL IN POWDER METAL PARTS

*Table 7. Dimensional change (%) of post sinter operations normalized to the as-sintered length. Alloy 1 is FLC2-4808, Alloy 2 is FLNC-4408, Alloy 3 is FLC-4608 and Alloy 4 is Ancorsteel 4300 with 0.6%graphite.*

Alloy#	1. <u>As-Sinter</u>	2. <u>LNQ</u>	3. <u>T</u>	4. <u>LNQ +T</u>	5. <u>T+ T</u>
1	0	+0.13	-0.10	+0.01	-0.08
2	0	+0.13	-0.06	+0.04	-0.04
3	0	+0.14	-0.10	+0.01	-0.07
4	0	+0.06	-0.03	+0.02	-0.03

The dimensional change results indicate that higher carbon alloys 1-3 have greater amounts of retained austenite and highly stressed plate or acicular martensite, due to the large growth resulting from the LNQ and the large shrinkage due to the tempering, respectively. Alloy 4 is relatively insensitive to post sintering thermal treatments. This is a result of the lower carbon content (0.53% sintered C) and no admixed copper. The improved hardenability of Alloy 4 via a combination of Cr, Ni, Mo and Si allows this lower carbon content to be used in sinter-hardening. The lower carbon content results in lath martensite formation, which is less stressed than the higher carbon acicular martensite. Shrinkage upon tempering is therefore reduced. The lower carbon and lack of copper greatly reduce the amount of retained austenite, thereby reducing the sintered compact growth upon LNQ. Alloy 4 had a much smaller growth (+0.06%) resulting from the LNQ quench as compared to Alloys 1-3 that had growths more than double this amount. Alloy 4 is therefore more dimensionally stable after sintering

*Table 8. Hardness and TRS for all four alloys with the different thermal treatments.*

Condition	Alloy 1 -FLC2-4808		Alloy 2 -FLNC-4408		Alloy 3 -FLC-4608		Alloy 4 -4300	
	Hardness (HRA)	TRS (MPa)	Hardness (HRA)	TRS (MPa)	Hardness (HRA)	TRS (MPa)	Hardness (HRA)	TRS (MPa)
As-sintered	75	979	69	959	74	676	71	1690
LNQ	77	786	70	828	75	600	72	1593
T	71	1869	65	1517	69	1521	69	2062
LNQ+T	72	1621	68	1586	72	1362	70	1903
T+T	71	1807	66	1614	68	1528	69	2007

Hardness and strength of all four alloys studies is shown in Table 8. The as-sintered properties of Alloy 4 were the best of all alloys tested and the LNQ had little effect on properties. Tempering improved TRS and tensile properties by roughly 25%, and while significant for developing the best properties, tempering was much less important in this alloy system compared to Alloys 1-3. Again, this is a function of the martensite type that is present in the lower carbon steel. As-sintered hardness in Alloy 4 was lower than Alloys 1 and 3, but after tempering, Alloy 4 had similar hardness. The transverse rupture strength of Alloy 4 is equivalent or better than Alloy 1 (Table 8) and the tensile properties are similar. It should be noted that the sintered density of Alloy 4 was 0.05 to 0.10g/cm<sup>3</sup> higher than the other alloys due to a combination of improved compressibility and less growth during sintering. Given the ability to properly sinter a Cr-containing PM alloy, Alloy 4 provides a more dimensionally stable sinter-hardening system as compared with more traditional sinter-hardening alloys.

### Summary:

We reviewed the benefit of using a 0.3 prealloyed Mo grade powder with FC-0208 type of powder both in as sintered and heat treated condition. Spur gears were produced and tested for dimensional control. For heat treated parts the use 0.3%Mo without Cu gives a better dimensional precision than FC-0208.

## DIMENSIONAL CONTROL IN POWDER METAL PARTS

---

FC-0208 parts made with Ancorbonded process used in making higher density AncorMax 225 powder provides a tighter dimensional tolerance by ensuring all the graphite goes in to alloying compared a non- bonded mix.

In the case higher performance sinter-hardenable grades Ancorsteel 4300 provides good dimensional precision. Also shown are the benefits of tempering as a key part of maintaining dimensional precision in the case of sinterhardenable alloys .

### References:

1. K. Narasimhan, E. Boreczky "New Transmission Technologies on Gear Requirements for Global Powder Metal Industry" Paper Number 06M-432; 2006 SAE publication, Published by Society of automotive Engineers, Inc. 400 Commonwealth drive, Warrendale, PA 15096-001
2. Francis Hanejko, "A Comparison of FC-0208 to a 0.3 % Molybdenum Prealloyed Low-Alloy Powder with 0.8 % Gr" Powder Metal World Congress & Exhibition, Las Vegas, Nevada, Compiled by Thomas J. Jesberger and Stephen J. Mashl, Metal Powders Industries Federation, June 28-July 1, Las Vegas, NV pp. 7-59 to 7-72, (2009).
3. Bruce Lindsley and Thomas Murphy "Dimensional Precision in Sinter-Hardening PM Steels" Powder Metal World Congress & Exhibition, Busan, South Korea, Edited by Kwang Yong Eun and Yong-Seog Kim, Korean Powder Metallurgy Institute, September 24-28, Part 1, pp 407-408, (2006)



# STUDIES ON THE EFFECTS OF Nb ON SINTERING AND PROPERTIES OF MIM 440C MADE BY PREALLOY AND MASTER ALLOY ROUTES

Martin A. Kearns<sup>1</sup>, Mary-Kate Johnston<sup>1</sup>, Keith Murray<sup>1</sup>, Paul A Davies<sup>1</sup>  
Viacheslav Ryabinin<sup>2</sup> and Erainy Gonzalez<sup>2</sup>

<sup>1</sup>Sandvik Osprey Ltd., Red Jacket Works, Milland Road, Neath, SA11 1NJ, United Kingdom

<sup>2</sup>TCK S.A., Zona Franca Industrial Las Americas, Santo Domingo, Dominican Republic

**Abstract:** Metal Injection Moulding (MIM) is being adopted for the production of an increasing variety of components used in diverse applications. One of the most versatile alloys in use is 440C martensitic stainless steel which offers high hardness and good corrosion resistance. This combination is suited to service in automotive fuel injector parts, medical pliers and a range of tool parts e.g. in textile machinery. Achieving reproducible properties and consistent hardness requires close control of carbon levels in particular. There are a number of variants on 440C in use today: some with enhanced carbon levels to achieve higher hardness and some with additions of Nb which are claimed to increase the sintering process window for the alloy. In this study, we examine the sintering behaviour at different temperatures of 440C and 440C + Nb made by prealloy and master alloy routes. Differences in hardness and mechanical properties are discussed with reference to chemistry and microstructures of sintered parts.

**Keywords:** Metal Injection Moulding (MIM), 440C martensitic stainless steel & sintering.

## Introduction

There are numerous applications where, in addition to high strength, hardness and wear resistance, good corrosion resistance is also required. The 4xx series of hardenable stainless steels is a versatile family of alloys offering a range of hardness and strength level to suit specific applications. Processing of the 420 alloy has been described elsewhere [1-3] and is a popular choice for power tools and firearms parts. If still higher strength and wear resistance is required, then the 440A, B and C alloys offer increasing hardness by virtue of increased carbon and chromium levels. 440C typically has 0.95-1.20%C, but this level can be customised for particular end uses. Fuel injection components, bearings, valves, shafts, cams, knives, pliers etc. are all examples of the increasing range of applications for this alloy.

It is recognised that the 4xx series of stainless steel alloys present significant challenges

[1-3] in ensuring that requisite harness levels and that dimensional tolerances are met consistently. Critical to both of these requirements is control of carbon content throughout the MIM process and particularly during sintering where the percentage of carbon governs the volume fraction of liquid at any given sintering temperature. A number of variants on the base alloy have been developed over the years including alternatives containing up to 3.5%Nb, which is claimed to enhance control of sintering by suppressing the rate of formation of liquid as temperature rises [4]. This may be advantageous when furnace temperature uniformity is in question, but may not always justify the cost associated with Nb addition.

Another variable which will have a significant influence on C activity in the sintering process is the presence of oxygen associated with the metal powder feedstock. In the case of water atomised powders the O level can be in the range

## STUDIES ON THE EFFECTS OF Nb ON SINTERING AND PROPERTIES OF MIM 440C MADE BY PREALLOY AND MASTER ALLOY ROUTES

0.3-0.5% compared with <0.1% typically for gas atomised powders [1-4]. As the sintering process progresses, oxygen is removed by reaction with carbon and while compensatory additions of carbon can be made to maintain carbon at a desired level, the overall process is more difficult to control.

Wan Harun et al. [5] carried out studies on sintering behaviour of water atomised 440C powder in hydrogen and vacuum atmospheres. Sintering was done for 30 min and optimum powder loading of 63% was adopted. In hydrogen, decarburisation was very apparent while in vacuum, an increasing amount of C is lost as the sintering temperature increases in the range 1240-1260°C. This is associated with rapid grain growth and the formation of grain boundary carbide networks. Subsequent heat treatment involving heating at 1000°C for 30 min before quenching in oil to room temperature then immersing in liquid N<sub>2</sub> for 30 min, then tempering for 2 h at 180°C yielded best properties of 1500 MPa, 1%El, 60 H Rc which correlate well with values reported on a number of web-sites [6-7].

In a separate study on 440C, Li et al. [8] took gas atomised powder and prepared feedstock with a powder loading level of 57%. This appears low for a gas atomised powder, especially compared with the figure reported in ref 5 for a water atomised powder. They report inferior mechanical properties of 880 MPa and ~58 H Rc after heat treatment albeit density levels after vacuum sintering appear as expected. The details of the heat treatment process are unclear but the tempering temperature was 150°C and the authors report that retained austenite was present. It is possible that differences in heat treatment are responsible for the divergent mechanical properties reported here and in other studies. Interestingly, the authors [8] note that

if left in air for a few days, green parts become oxidised and that this leads to distortion of parts on sintering.

*Table 1: Published values for 440C in heat treated condition*

Reference	UTS MPa (ksi)	0.2%PS MPa (ksi)	El %	Density g cm <sup>-3</sup>	Hardness HRC
MIM vac, 1240°C [5]	1500 (217)	-	1.2	7.52	60
MIM vac, 1240°C [8]	880 (128)	-	-	7.56	57.7
Kinetics [6]	1660 (240)	1240 (180)	1	7.69*(HIP)	-
AFT [7]	1590 (230)	1340 (195)	4	7.5	59
MPIF 35 (minimum)	1030 (150)	-	-	-	-
MPIF 35 (typical)	1310 (190)	1170 (170)	<1	7.5	56

In this study, we examine the sintering behaviour of 440C and 440C+Nb alloys in a nitrogen atmosphere and go on to determine mechanical properties in the as sintered and heat treated conditions. Recognising the criticality of carbon control, one objective of the current study is to evaluate benefits of low-oxygen gas atomised powders on control of chemistry and therefore finished parts properties. There has been little reported about the effect of Nb on processing and the properties of finished parts and this is one goal of this study. In addition, it is of interest to investigate the possible advantages of adopting a master alloy approach to making 440C products using a mixture of master alloy and carbonyl iron powders (CIP). Previous investigations [1, 9-11] relating to AISI 4xxx low alloy steels and 420 stainless steel, show that there are potential benefits in the MA approach in terms of higher sintered density and UTS.

### Experimental Procedure

A series of prealloyed and master alloy 440C powders was produced by Sandvik Osprey's proprietary inert gas atomisation process using nitrogen gas. The 'as-atomised' powders were air classified to 80%-22µm. The chemistry and particle size distribution data of each powder batch used in the study is shown in Tables 2

## STUDIES ON THE EFFECTS OF Nb ON SINTERING AND PROPERTIES OF MIM 440C MADE BY PREALLOY AND MASTER ALLOY ROUTES

and 3 respectively. In the case of master alloys, additions were made of carbonyl iron powders made by Sintez. A mixture of HC and BC grades with different carbon levels was used to achieve the desired final chemistry.

**Table 2: Chemical analysis of powders used in this study.**

Alloy	Fe	Cr	Ni	Nb	Mn	Si	Mo	N	C	P	S	O
440C PA 121014-1	Bal	16.8	0.11	-	0.84	0.85	0.65	0.11	1.10	0.01	0.01	0.058
440C PA 121014-2	Bal	16.6	0.10	-	0.68	0.64	0.62	0.11	1.06	0.01	0.01	0.057
440C Nb PA 121114-1	Bal	16.7	0.15	2.91	0.82	0.88	0.62	0.12	1.23	0.01	0.01	0.066
440C Nb PA 121114-2	Bal	17.4	0.20	2.97	0.70	0.63	0.62	0.10	1.35	0.01	0.01	0.054
440C Nb MA 121214-1	Bal	52.4	0.28	4.58	0.67	0.6	1.88	0.22	2.21	0.01	0.014	0.095
Fe50Cr4.5Nb 121214-2	Bal	50.7	0.28	4.42	0.8	1.2	0.02	0.42	2.30	0.03	0.01	0.04
Sintez HC 669	Bal	-	-	-	-	-	-	0.81	0.78	-	-	0.25
Sintez BC 477	Bal	-	-	-	-	-	-	0.005	0.02	-	-	0.43

The carbonyl iron powders are significantly finer than the gas atomised powders and, when added to the master alloy, mean that the effective size distribution is more akin to a 90%-16 $\mu$ m powder than the 80%-22 $\mu$ m typical of the prealloys. Note that the second master alloy variant has a finer particle size range than the first. It was also made without addition of Mo.

**Table 3: Particle size data**

Lot	Particle Size	Grade	Tap Density gcm <sup>3</sup>	Particle Size Data ( $\mu$ m)		
				D10	D50	D90
031813-1	80%-22 $\mu$ m	440C(Nb)MA	4.9	4.2	12.0	24.5
121014-1	80%-22 $\mu$ m	440C	4.9	4.0	12.2	27.6
121014-2	80%-22 $\mu$ m	440C	4.9	4.1	12.2	27.3
121114-1	80%-22 $\mu$ m	440C Nb	4.8	4.1	12.3	27.8
121114-2	80%-22 $\mu$ m	440C Nb	5.0	4.3	12.5	26.9
121214-1	80%-22 $\mu$ m	440C(Nb)MA	4.7	4.4	12.7	27.4
121214-2	90%-22 $\mu$ m	Fe50Cr4.5Nb	4.8	3.7	10.2	21.7
669	90%-12 $\mu$ m	Sintez BC	-	2.6	5.1	10.6
477	90%-12 $\mu$ m	Sintez HC	-	2.6	5.6	11.2

Feedstocks were prepared by TCK using their proprietary binder formulation and aiming for a 61.8% powder loading corresponding to a 17.4% shrinkage factor. The shrinkage factor is the scale factor applied to the target final part dimensions in order to design the mould. The value reported here is typical of previous studies with gas atomised powders. The feedstocks were moulded in an Arburg injection moulding

unit and sintered by TCK in an Elnik furnace, to produce standard MIMA tensile and Charpy test specimens.

Moulded green parts were subject to an initial solvent debind followed by thermal debind at 500°C for 3.5h and sintered in a nitrogen atmosphere. A series of sintering cycles was run at temperatures in the range 1240°C to 1320°C. 2°C / min ramp to 1000°C, 60 min hold, 2°C/min ramp to sintering temperature, 60 min hold and furnace cool.

Charpy bars were suspended both cantilever style (20mm overhang) and across refractory supports, (38mm separation) to determine the extent of distortion as a function of chemistry, particle size range and sintering temperature. Sintered parts were allowed to slow cool under a nitrogen atmosphere. As-sintered tensile samples were tested in triplicate in accordance with ASTM E8-08. Vickers hardness testing was carried out on tensile bar tabs using a 10kg weight. Sintered density measurements were carried out using a Micromeritics Accupyc model 1340 Helium Pycnometer. Polished cross-sections of Charpy bars were prepared for microstructural analysis by etching in dilute aqua regia. The carbon level of the final sintered specimens was measured using Leco combustion analysis.

The heat treatment applied to all samples involved austenitizing at 1000°C for 30 min before quenching in oil to room temperature then immersing in dry ice for 30 min, followed by tempering for 2h at 165°C.

### Results

Four series of sintering runs were completed with different material types and different temperatures.

**Series 1** examined sintering behaviour of 440C (Nb) MA (Lot#031813-1) at three temperatures:

## STUDIES ON THE EFFECTS OF Nb ON SINTERING AND PROPERTIES OF MIM 440C MADE BY PREALLOY AND MASTER ALLOY ROUTES

1260, 1280 and 1320°C. Fig. 1 shows a summary of results including metallographic sections of the as sintered Charpy specimens (surface and centre). This shows that densification is only complete at 1320°C and that this is accompanied by gradual carbon loss and grain coarsening. It is also clear that the surface microstructure differs from that at the centre in exhibiting a lamellar phase of variable depth (typically ~ 500µm. All samples show precipitation at the grain boundaries and at pore edges. Modest hardness levels of as sintered samples reflect low density and low carbon. After heat treatment, with and without cryogenic stabilisation (HT1 and HT2 respectively), significantly higher hardness was measured.

Lot 031813-1	1260°C	1280°C	1320°C
Density g/cm <sup>3</sup>	7.14 (92%)	7.22 (93%)	7.77 (100%)
Final %C	0.89	0.97	0.84
Hv10 hardness	247	238	322
HRC after HT1	46	50	54
HRC after HT2	41	N/A	48
0.2%PS (MPa)	526	534	589
UTS (MPa)	737	590	826
%El	2.5	1.0	3.0

Surface 500x Micron bar = 500µm			
Centre 500x Micron bar = 500µm			

**Fig. 1** Progress of densification of 440C(Nb) MA with increasing sintering temperature.

**Series 2** investigated sintering behaviour of prealloy 440C (with and without Nb) alongside 440C(Nb) made by the master alloy route. The temperature chosen was 1260°C which was expected to be low for densification of master alloy, but at the high end of the normal range for sintering prealloys. On removal from the furnace, it was apparent that all of the suspension and cantilever samples for prealloy samples were broken but the master alloy samples were intact. Table 5 shows a summary of results for as sintered specimens. This does indeed bear out the fact that full density was obtained in

prealloys with and without Nb but that the MA-based samples are only 93-95% dense: the higher figure being obtained with the 90%-22µm master alloy. The prealloy samples therefore show superior mechanical properties to the master alloy material and the Nb-containing prealloy in turn shows superior UTS and hardness compared with the Nb-free material. It may be noted however that the carbon level in the Nb-containing prealloy is significantly higher than other variants. Also worth mention in Table 5 is the carbon loss on sintering. This is low and consistent for the prealloys and higher, but still consistent, for the master alloy-based material.

**Table 5: Mechanical Properties of As sintered specimens after 1260°C Cycle**

Alloy	Lot ID	0.2%PS (MPa)	UTS (MPa)	%El	Hv 10kg	%T.D.	Start %C	Final %C	%C loss
440C PA	121014-1	688	839	2.0	310	99.4	1.08	1.06	0.02
	121014-2	656	828	3.7	311	100.0	1.08	1.08	0.00
440C(Nb) PA	121114-1	665	1097	2.8	413	99.2	1.23	1.21	0.02
	121114-2	675	924	1.5	421	100.0	1.35	1.33	0.02
440C(Nb) MA	121214-1	510	713	2.8	244	93.3	1.18	1.09	0.09
	121214-2	600	735	3.2	294	95.3	1.21	1.10	0.11

The microstructures exhibited by the three materials types are quite different as shown in Fig. 2. The prealloy without Nb displays predominantly intergranular eutectic precipitation surrounding large grains with little intragranular carbide. The prealloy containing ~ 3%Nb exhibits a much finer and uniform grain size with extensive intragranular precipitation of NbC. Finally the master alloy based product shows residual porosity, intermediate grain size and a lower concentration of intragranular NbC precipitation reflecting its lower Nb content.

# STUDIES ON THE EFFECTS OF Nb ON SINTERING AND PROPERTIES OF MIM 440C MADE BY PREALLOY AND MASTER ALLOY ROUTES

Lot #	121014-1 (440C)	121114-1 (440C(Nb))	121214-1 (440C(Nb) MA)
Density %	99.4	99.2	93.3
Final %C	1.06	1.21	1.09
Hv10 hardness	310	413	244
Surface 500x Micron bar = 500µm			
Centre 500x Micron bar = 500µm			

**Fig. 2** Microstructures of different alloy variants after sintering at 1260°C.

**Series 3** further investigated sintering behaviour of prealloy 440C (with and without Nb) at the lower sintering temperature of 1240°C which was intended to avoid some evidence of overheating at 1260°C. On removal from the furnace, all the suspension and cantilever samples were again broken, but the failure of the Nb-containing prealloy samples was less dramatic than that of the Nb-free samples (see Fig. 3). Table 6 shows a summary of mechanical and carbon test results for as sintered specimens. This shows that the Nb-containing prealloy samples have slightly higher density and strikingly higher ultimate tensile strength and hardness values. Again it must be noted that the carbon level in these samples is significantly above that in the Nb-free samples.

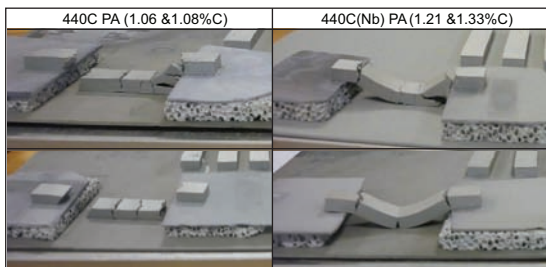


**Fig. 3** Condition of suspension test samples after sintering at 1240°C

The carbon loss on sintering is again seen to be small and consistent. The magnitude of the loss is comparable with that seen in series 2 samples sintered at 1260°C.

**Table 6: Mechanical Properties of As sintered specimens after 1240°C Cycle**

Alloy	Lot ID	0.2%PS (MPa)	UTS (MPa)	%EI	Hv 10kg	%T.D.	Start %C	Final %C	%C loss
440C PA	121014-1	639	821	4.5	301	99.0	1.08	1.06	0.02
	121014-2	613	764	3.0	288	97.1	1.08	1.06	0.02
440C(Nb) PA	121114-1	653	874	2.0	391	99.8	1.23	1.21	0.02
	121114-2	675	920	1.3	430	99.7	1.35	1.34	0.01

**Series 4** focused on achieving full density in master alloy samples without adopting excessive temperatures where carbon loss and distortion could become a concern – see series 1. A sintering temperature of 1290°C was therefore chosen. On removal from the furnace, all of the suspension and cantilever samples were intact.

Table 7 shows a summary of mechanical and carbon test results for as sintered specimens. This shows that the master alloy samples have achieved higher density and higher ultimate tensile strength and hardness values than evident in series 2 at 1260°C and also in series 1 at 1280°C. The master alloy variant with the finer particle size distribution of 90% vs 80% -22µm, in fact achieved full density. Again it should be noted that the carbon level in series 2 and 4 was significantly above that in the series 1 samples. The carbon loss on sintering is a little higher than that seen in series 2 for master alloy specimens and is higher than seen in prealloy samples.

**Table 7: Mechanical Properties of As sintered specimens after 1280°C Cycle**

Alloy	Lot ID	0.2%PS (MPa)	UTS (MPa)	%EI	Hv 10kg	%T.D.	Start %C	Final %C	%C loss
440C(Nb) MA	121214-1	577	842	5	290	97.1	1.18	1.07	0.11
	121214-2	638	986	5	358	100.0	1.21	1.08	0.13

## Slump Tests

Many of the test samples from the different sintering series failed but Table 8 summarises the deflections recorded for samples that did remain intact. This shows, not surprisingly, that the master alloy samples were most resilient, and the Nb-free prealloy samples were least resilient. The deflections are greater for the 80%-22µm sample

# STUDIES ON THE EFFECTS OF Nb ON SINTERING AND PROPERTIES OF MIM 440C MADE BY PREALLOY AND MASTER ALLOY ROUTES

compared with the 80%-22µm sample at a given temperature and the deflections also get larger as temperature increases.

**Table 8: Deflections measured in different sintering series.**

Series	Lot #	Alloy type	Deflection (mm)	
			Cantilever	Suspension
2 (1260°C)	121214-1 (80%-22µm)	440C(Nb)MA	0.996	1.055
	121214-2 (90%-22µm)	440C(Nb)MA	0.653	1.102
	121114-1	440C(Nb) PA	All failed	All failed
3 (1240°C)	121114-1	440C(Nb) PA	All failed	Some ligaments
	121014-1	440C PA	All failed	All failed
4 (1280°C)	121214-1 (90%-22µm)	440C(Nb)MA	0.849	1.424
	121214-2 (90%-22µm)	440C(Nb)MA	1.155	1.514

## Heat Treatment

The heat treatment adopted was chosen after assessing the benefit of an intermediate cryogenic stabilising treatment after oil quenching and before tempering. Omitting the dry ice treatment typically led to a reduction in final hardness of ~ 5-6 H Rc units and therefore the stabilisation step was used as standard. Results of hardness measurements and tensile tests carried out after heat treatment on each of the series are shown in Table 9. As expected in all cases the hardness and tensile strength values have risen after tempering, but elongation has decreased. The hardness values, when translated into HRC generally exceed the MPIF Standard 35 typical values albeit premature sample failures mean that UTS values appear low.

**Table 9: Mechanical Properties of Heat treated specimens. HRC in italics are calculated from UTS**

Series #	Alloy	Lot ID	As sintered				Heat treated			
			0.2%PS (MPa)	UTS (MPa)	%El	Hv 10kg	0.2%PS (MPa)	UTS (MPa)	HRC	Hv 10kg
2 (1260°C)	440C PA	121014-1	688	839	2.0	310	-	746	54	580
		121014-2	656	828	3.7	311	-	807	53	558
	440C(Nb)PA	121114-1	665	1097	2.8	413	-	1000	58	655
		121114-2	675	924	1.5	421	-	620	49	499
	440C(Nb)MA	121214-1	510	713	2.8	244	-	880	56	610
		121214-2	600	735	3.2	294	-	866	54	584
3 (1240°C)	440C PA	121014-1	639	821	4.5	301	-	844	60	679
		121014-2	613	764	3.0	288	-	738	56	616
	440C(Nb) PA	121114-1	653	874	2.0	391	-	950	61	693
		121114-2	675	920	1.3	430	-	891	60	677
4 (1280°C)	440C(Nb) MA	121214-1	577	842	5	290	944	936	50	515
		121214-2	638	986	5	358	1227	1211	57	630

Phase stability charts were constructed for each of the starting alloy chemistries and these generally predicted liquidus values around 1290°C. It was noticeable that the amount of liquid phase formed at the eutectic point (T<sub>liq</sub>) varied with chemistry and the rate of formation of liquid above the melting point also varied. In Table 10, these values are shown for each of the alloy families.

**Table 10: Thermocalc values of T<sub>liq</sub> and the % liquid at T<sub>liq</sub> and at 1300°C**

Alloy	Cr	Nb	N	C	T <sub>liq</sub>	% liq T <sub>liq</sub>	% liq 1300°C
440C PA 121014-1	16.8	-	0.11	1.10	1290	8	9
440C PA 121014-2	16.6	-	0.11	1.06	1290	4	5.5
440C Nb PA 121114-1	16.7	2.91	0.12	1.23	1288	5	8
440C Nb PA 121114-2	17.4	2.97	0.10	1.35	1288	11	15
440C Nb MA 121214-1	17.5	1.53	0.53	1.18	1285	6	10
Fe50Cr4.5Nb 121214-2	16.9	1.47	0.60	1.21	1292	6	8

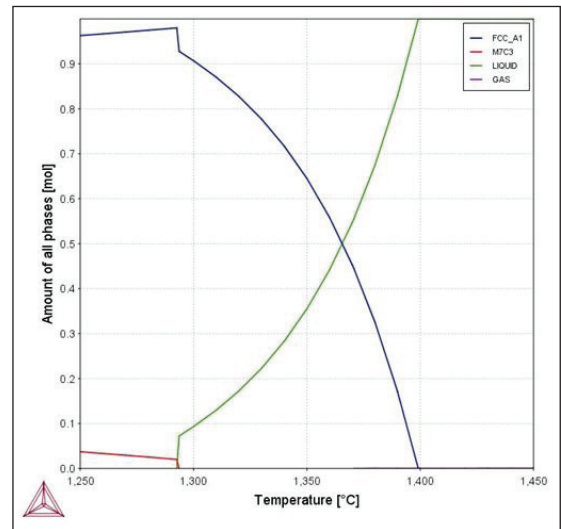


**Fig. 4 Example of Thermocalc phase stability chart for 440C PA 121014-1**

## Discussion

The results demonstrate that by sintering at an appropriate temperature, it is possible to achieve fully dense 440C parts using either prealloy or master alloy routes. Full density is achieved at lower temperature for prealloys and, while Table

## STUDIES ON THE EFFECTS OF Nb ON SINTERING AND PROPERTIES OF MIM 440C MADE BY PREALLOY AND MASTER ALLOY ROUTES

6 may suggest that the addition of Nb stimulates earlier densification in the prealloy, the comparison is ambiguous because of differences in carbon level also. Indeed one of the prealloys with Nb has a carbon level in excess of the 440C specification. This contributes to the superior levels of strength and hardness observed in these variants (Table 5 & 6).

Fig. 5 shows that the prealloy can be sintered to full density at 1240°C while the master alloy needs to be sintered at or above 1280°C to achieve full density. At 1260°C, master alloy variants only reach 95% theoretical density at best and this is for the finer grade (90%-22 $\mu$ m). The microstructure of the sintered parts (Fig. 1) shows varying amounts of residual porosity particularly in parts sintered at 1260°C and this is in part responsible for the variable ductility and therefore UTS seen in these specimens. Low carbon levels in this series of alloys limited the sintering process.

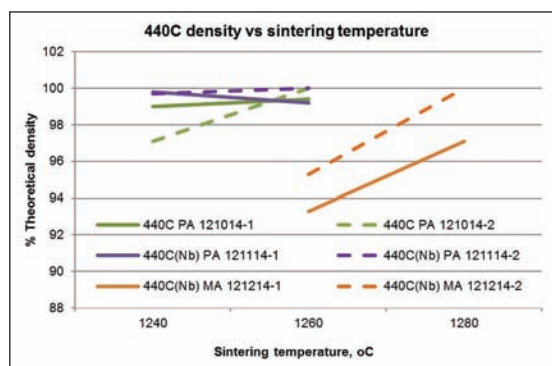


Fig. 5 Theoretical density vs sintering temperature for different 440C variants

The sintering window is quite narrow and final properties and part distortion is highly sensitive to the carbon level in the alloy. Good control of carbon level in relation to the sintering window is therefore key to achieving best results. The data for carbon loss demonstrate that this is predictable and low for gas atomized prealloy powders. It is rather higher for master alloy/

CIP combinations but again is predictable: these higher losses are associated with oxygen present in the CIP components (see Table 2). In all cases, the C loss can be explained by the starting level of oxygen associated with the powder(s). The measured oxygen level of ~0.06% in the starting powder would equate to a loss in carbon of ~0.02% if converted to and lost as CO<sub>2</sub>. For the master alloy, the high level of oxygen present in the CIP contributes to the higher starting O level of ~ 0.22% which leads to a C loss of ~ 0.09% which is close to the typical loss observed.

The master alloy approach offers one approach to achieving better control of 440C during sintering. The carbon level in the master alloy component can be controlled tightly so if the CIP component also has tight control of C, O the final C level should fall within tighter limits than a simple prealloy. In this study, only the Nb-containing master alloy has been evaluated but it should not be overlooked that simpler Fe50Cr master alloys are available with different levels of carbon and these are used successfully with CIP addition for manufacture of 440C and 420 alloys [1-3]. Interestingly, the master alloy variant shows more resilience in the cantilever/suspension test than the prealloys and this may be advantageous for components with overhang features where full density is also important.

Fig. 6 shows the relationship between sintering temperature and hardness levels in the heat treated samples. It is apparent that while increasing the sintering temperature is advantageous in terms of achieving highest density, it can have a negative effect on the ultimate hardness level that can be achieved. Niobium and carbon levels are also influential in determining mechanical properties: niobium in particular through its role as a grain refiner. It has already been commented that the austenitizing heat treatment is usually kept to a minimum in order to minimize grain

## STUDIES ON THE EFFECTS OF Nb ON SINTERING AND PROPERTIES OF MIM 440C MADE BY PREALLOY AND MASTER ALLOY ROUTES

growth. Figs. 1 & 2 show that appreciable grain coarsening occurs when stepping up in sintering temperature and that the presence of Nb has a dramatic effect in grain refinement. The prealloy containing ~3%Nb has much finer grain size than the master alloy based material which has ~1.5%Nb.

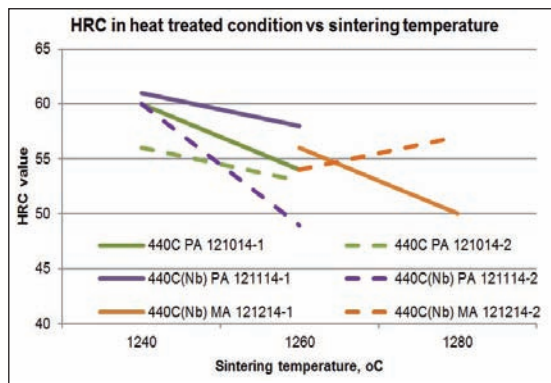


Fig. 6 HRC values vs sintering temperature. Red dotted line shows typical MPIF level.

In assessing hardness values in particular, the microstructures shown in Fig. 2 suggest that role of the nitrogen sintering atmosphere needs to be recognised as a hardening mechanism, providing a benefit vs sintering in vacuum for example. The observation of grain boundary phases and lamellar phases is consistent with previous studies of these alloys and the predominance of the lamellar phase at surfaces suggests that this phase is rich in nitrogen. Babakr et al. [13] mention a 'lamellar phase resembling pearlite is often observed in other stainless steels which is believed to be an austenite/carbonitride structure. Note that cryogenic stabilization after quenching appears to be advantageous in developing full hardness. In addition to influences of C, Nb, N levels and grain size on hardness values, Fig 1 highlights that it is necessary to achieve a satisfactory level of densification in order to realize best hardness levels.

The absolute strength and hardness values achieved in this study compare well with other studies and sources of information (compare Tables 9 & 1). Full density of  $\sim 7.65\text{gcm}^{-3}$  was achieved for each alloy and peak hardness values in the heat treated condition are in excess of MPIF typical levels and consistent with ref. 12 for 440Nb with 2.5-3.5%Nb sintered in nitrogen. While UTS values are often disappointing owing to premature specimen failure, in some cases, the UTS of the as sintered material (440C(Nb) PA) exceeds the minimum MPIF standard for heat treated 440C.

The role of Nb in 4xx stainless steels has received some attention over the years, notably the original study by Wohlfromm et al. [4] which highlighted the role of Nb in suppressing liquid formation at the eutectic point during sintering of 440C which was said to provide a wider process window for making 440C parts. What is clear from that and this study and the various thermocalc simulations is that it is the relationship between C and Nb level that will affect the onset of the eutectic reaction ( $\gamma + M_7C_3 \leftrightarrow \text{Liquid}$ ) and that the amount of liquid forming is dependent on the amount of C and Nb. Attention must be paid to both levels when selecting the best sintering conditions. Evidence from this study is that Nb in combination with high C level enhances hardness and resistance to deformation compared with Nb-free prealloy sintered at the same temperature. Slump tests (Table 8) also reveal that at any given temperature, the master alloy - based materials show less distortion than prealloys. This is probably related to the presence of weak, low melting point grain boundary phases which will appear at an earlier stage for 440C and will be last to form in the master alloys where diffusion of alloying elements needs to occur before the eutectic reaction can take place uniformly throughout the sample.

# STUDIES ON THE EFFECTS OF Nb ON SINTERING AND PROPERTIES OF MIM 440C MADE BY PREALLOY AND MASTER ALLOY ROUTES

## Summary and Conclusions

The present study shows that sintering 440C in nitrogen at 1240-1260°C is effective in achieving virtually full part density for 80%-22µm PA powders with and without Nb present and that the sintering temperature required for full density is dependent on the balance of C and Nb in the alloy. Higher temperatures are needed to get full density in parts made via a master alloy route: a 90%-22µm grade enables full densification at 1280°C while the 80%-22µm grade reaches 97% density at this temperature. The densification behaviour can be rationalized with reference to Thermocalc studies.

While achieving peak density is desirable, this study shows that this may be at the cost of enlarged grain size and lower final hardness levels. Niobium is helpful in restricting grain growth and maintaining hardness levels. Carbon loss during the sintering process is predictable for gas atomized powders with and without blended CIP and is dependent only on the amount of oxygen present in the starting powder(s) and not apparently on the sintering temperature in the normal sintering range 1240-1280°C.

Hardness and strength levels achieved in the as sintered and heat treated conditions compare favourably with reference industry values and depend on a number of factors: final density, carbon level, hardenability (Nb and other elements), grain size and nitrogen level. While not measured in detail, it is clear that there is a lamellar carbonitride structure ~500µm deep on exposed surfaces and this should enhance surface hardness and provide an advantage vs sintering in other atmospheres.

In common with previous studies on other master alloy systems, part distortion appears more pronounced in parts made with prealloy powders compared with master alloy powders.

This may be one reason to adopt a MA route albeit a higher sintering temperature will be needed to achieve full density.

It is concluded that gas atomized 440C prealloy and master alloy powders are both ideally suited to producing high performance components to close tolerances with excellent control of carbon leading to uniform shrinkage and predictable properties.

## Acknowledgements

Thanks are due to Ms Linn Larsson of Sandvik Materials Technology for detailed metallographic analyses; also to Mr Chris Phillips of Sandvik Osprey for deflection measurements.

## References

1. A. J. Coleman, K. Murray, M. Kearns, T. A. Tingskog, B. Sanford, E. Gonzalez, "Properties of MIM AISI 420 via Pre-alloyed and Master Alloy Routes", PowderMet, (2013).
2. G. Goto, "Sintering of 420 Stainless Steel", MIM2012 Conference, San Diego, (2012).
3. Sintering of 420 Stainless Steel, P. Gopinath-Awan, MIM2013 Conference, Orlando 2013
4. Metal Injection Moulding of a Modified 440C-type Martensitic Stainless Steel, H. Wohlfromm, P.J. Uggowitzer, M Bloemacher, J. ter Maat, A Thom, A. Pistillo & A Ribbens Euro PM2005 333-340
5. W.S. Wan Harun, K. Toda, T. Osada, H. Kang, F. Tsumori and H. Miura, Effect of MIM Processing Parameters on Properties of 440C Stainless Steel. J. Japan Soc. Powder Metall. 59(5) 264-271 (2012).
6. [www.kinetics.com](http://www.kinetics.com)
7. [www.aft.com](http://www.aft.com)
8. D.Li, H. Hou, L.Liang, K.Lee, Powder Injection Moulding of 440C Stainless Steel, Int. J. Adv. Manuf. Technol. 49, 105-110 (2010)

## STUDIES ON THE EFFECTS OF Nb ON SINTERING AND PROPERTIES OF MIM 440C MADE BY PREALLOY AND MASTER ALLOY ROUTES

---

9. M.A.Newel, H.A.Davies, P.F.Messer, D.J.Greensmith, MIM of Scissors using Hardenable Stainless Steel Powders, Powder Metall. 48(3), 227-230 (2005).  
Particle Size Distribution on Processing and Properties of Metal Injection Moulded 4140 and 4340", PowderMet 2011, San Francisco, CA
10. Processing and Properties of PM440C Stainless Steel, P.K.Samal, J.C.Valko & J.D.Parnell, PowderMet 2009, Las Vegas, USA 1-10, June 29th 2009.
11. A.J. Coleman, K. Murray, M.A. Kearns, T. A. Tingskog, B. Sanford, E. Gonzalez, "Effect of
12. BASF Datasheet - Catamold® 440Nb, June 2006. [www.basf.de/catamold](http://www.basf.de/catamold)
13. A. M. Babakr, A. Al-Ahmari, K. Al-Jumayiah, F. Habiby, 'Sigma Phase Formation and Embrittlement of Cast Iron-Chromium-Nickel (Fe-Cr-Ni) Alloys'. J. Min. Mater. Character. Engg., 7 (2), 127-145, (2008).



# EXPERIMENTAL EVALUATION OF SINTERED PROPERTIES FOR SINTERING TIME AND MODULUS ON DENSITY AND HARDNESS OF Al/SiC<sub>p</sub> BY PM PROCESS

K. C. Nayak\*, K. K. Rane, Girish N Kotwal, P. P. Date

Department of Mechanical Engineering, IIT Bombay, Mumbai

\*Corresponding author: nayakkanhu83@gmail.com

**Abstract :** Recent developments towards light-weighting of structural components by synthesis and processing of MMCs using novel powder metallurgy find applications in automotive, aircraft and aerospace industries. In the present work, process parameters like sintering time, compaction pressure and modulus of the parts were identified as the most crucial factors, which influence the sintered properties.

Al/SiC<sub>p</sub> metal matrix composite was synthesized using PM processing. Reinforcement phases were first mixed using low energy ball-milling in aluminum powder to form homogenous mixing. Powder mixture was then cold compacted to different shapes and sizes. This variation is quantified by modulus (which is a ratio of volume to surface area). Green Al/SiC<sub>p</sub> parts were sintered at 700°C in inert gas atmosphere with variable sintering time. Density and hardness of sintered Al/SiC<sub>p</sub> composites for different modulus were evaluated. Sintered density and hardness of sintered parts were characterized and correlated with evolution of microstructure. Porosity, interfacial bonding between Al matrix and reinforcement phases were discussed for improvement of sintered properties. This study provides the desired sintering time to enhance properties of various shape and sizes of PM components.

**Keywords:** MMCs, hardness, sintering, interfacial bonding

## Introduction

Most of the automotive and aerospace components are manufactured by light weight composite material. Aluminum and aluminum alloy matrix material is the common for light weighting to automotive and aerospace industry [1, 2]. Aluminum metal matrix composites are produced by casting and powder metallurgy (PM) methods. Sintering is the most crucial stage in PM process. The basic mechanism in sintering process is the diffusion of particles. This diffusion mechanism causes the reduction of free energy of the system when a material is heated and material transport begins [3].

PM based composites have less density and hardness with higher porosity compared to stir casting based composites. However,

reinforcements are uniformly distributed in matrix through PM method than in stir casting process [4]. That is, uniform distribution of reinforcements in matrix is not controlled by casting process which may cause inhomogeneous physical and mechanical properties in composite material. In casting based Al/SiC composite, the agglomerated SiC particles form weaker bonding with aluminum matrix [5].

Many studies were carried out for Al/SiC composites through PM process to evaluate their physical and mechanical properties [6-9]. Silicon carbide is commonly selected as reinforcement due to its suitable properties (high strength, thermal shock resistance) and it can form a strong bond to aluminum matrix [10]. Porosity and sintered properties of PM based composite

## EXPERIMENTAL EVALUATION OF SINTERED PROPERTIES FOR SINTERING TIME AND MODULUS ON DENSITY AND HARDNESS OF Al/SiC<sub>p</sub> BY PM PROCESS

can be controlled by controlling the sintered parameters such as temperature and sintering time. Therefore, it is necessary to investigate the porosity level, density and hardness with sintering time and part modulus.

In the present study, different part modulus of cylindrical specimens was synthesized through conventional powder metallurgy process. Each specimen contains 7vol. % of SiC<sub>p</sub> reinforcements in aluminum matrix. Physical and mechanical properties of sintered Al/7vol. %SiC<sub>p</sub> composite material were investigated with different part modulus and sintering time. Microstructural analysis was carried out to study the interface bonding between reinforcement and matrix. In addition to this, porosity of sintered specimens was examined.

### Experimentation

#### Material details

Commercially available pure aluminum powder (Fe-0.1%, Mn-0.02%, Ti-0.03%, Cu- 0.02% Si-0.1% and balance Al) with mean particle size of 46.16 μm was used as matrix material in Al MMCs. In addition, laboratory based silicon carbide (mean particle size 8.13 μm) were blended with pure aluminum powder for making aluminum composite material. The homogeneous mixture of Al and 7vol. % of SiC<sub>p</sub> was prepared using low energy ball milling. This mixture was compacted to cylindrical shape with compaction pressure of 500MPa. Three different cylindrical compacts were produced with varying ratio of volume to surface area (1.25, 1.67 and 1.87).

#### Experimental procedure

Aluminum metal matrix composites were manufactured through powder metallurgy (PM) process. This process consists of basic three steps; blending or mixing of powders, compaction of mixture and sintering of compacted samples. The synthesis process of aluminum metal matrix composites is shown in Fig. 1.

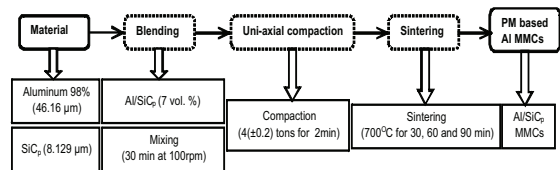


Fig. 1: Flow chart for synthesizes of aluminum metal matrix composites

The homogeneous powder mixtures were cold compacted in a uni-axial press in a metallic die of inner diameter of 10.2 mm. A mixture of weighing 1, 2 and 3(± 0.080)g was taken for compaction to produce H/D ratio of 0.5, 1.0 and 1.5 respectively. The homogeneous mixture was pressed in the uni-axial pressing machine (Make-SOILLAB, Type-Hydraulic) to render the green cylindrical test samples of 10 mm outer diameter. Cold compacted cylindrical samples were sintered at 700°C in a tubular furnace in argon gas atmosphere to prevent oxidation. In the present study, three different sintering times; 30, 60 and 90 minutes were selected for the sintering to study its effect on density, hardness and microstructure evolution. The sintered Al/7 vol. % SiC<sub>p</sub> composites with different modulus ( $m=1.25, 1.67$  and  $1.87$ ) are illustrated in Fig. 2

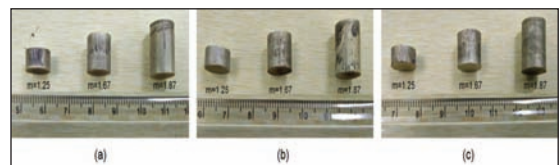


Fig. 2: PM based Al/7vol.% SiC<sub>p</sub> composites ( $m= 1.25, 1.67, 1.87$ ) sintered at 700°C for (a) 30min, (b) 60min and (c) 90min

The sintered specimens (Al/7vol.% SiC<sub>p</sub>) were characterized for evaluation of physical and mechanical properties such as density and hardness. The variation of densities (green and sintered density) with respect to theoretical density was quantified by densification parameter ( $\phi$ ). Densification parameter was calculated from green, sintered and theoretical density by implementing Eq. (1).

## EXPERIMENTAL EVALUATION OF SINTERED PROPERTIES FOR SINTERING TIME AND MODULUS ON DENSITY AND HARDNESS OF Al/SiC<sub>p</sub> BY PM PROCESS

$$\phi = \frac{\rho_s - \rho_g}{\rho_{th} - \rho_g} \quad (1)$$

where,  $\rho_s$ ,  $\rho_g$  and  $\rho_{th}$  are the sintered density, green density and theoretical density respectively.

Hardness of each specimen was measured using Rockwell hardness tester (RASN-T) with superficial scale (15T, 1/16" ball indenter). Microstructure of sintered specimens was examined under an optical microscope, Leica (DM2500M). The interface bonding between ceramic particles and matrix, crack and porosity were revealed by the microstructural analysis.

### Results and Discussion

#### Change in Density and Hardness with Sintering Condition

Parts sintered with 60 and 90 minutes of sintering time shows similar trend of increasing densification with part modulus of 1.25 to 1.67 as shown in Fig. 3. Densification decreases at 1.87 part modulus because of unavailability of part surface area to densify the part. Densification for sintered specimen having lower part modulus (1.25) does not show any significant variation with proposed sintering time. That means, 30-minute sintering time may be sufficient for diffusion of particles. Hence, further densification is not possible. With increase in part modulus (beyond 1.25), the 30 minute sintering time shows uneven variation of densification. This variation was not observed in other sintering time of 60 and 90 minutes, which implies that homogeneous sintering is obtained beyond 30min for higher part modulus. As can be seen in Fig. 3, there is improvement of sintered density by increase in sintering time for part modulus of 1.67.

Rockwell hardness tests were carried out on flat surface of cylindrical sintered specimen (Fig. 4(a)). A similar trend of variation (as observed for densification in Fig. 3) of hardness is shown in Fig. 4(b) with respect to part modulus for 60 and 90 minutes sintering time. Few samples having 1.25 and 1.67 modulus shows variation in hardness with the opposite side of applied load during compaction. This is because of varying frictional condition in particles during compaction cause distinct level of densification along the part length. Uneven interface bonding between SiC<sub>p</sub> and Al particles and, movement of reinforcement clusters also may cause the hardness variation. Improvement in hardness of cylindrical samples at modulus of 1.67 is observed (Fig. 4(b)) due to strong interface bonding between SiC<sub>p</sub> and Al. Fig. 4(b) further reveals that decrease in hardness at modulus of 1.87, which indicates the lower densification of Al composite.

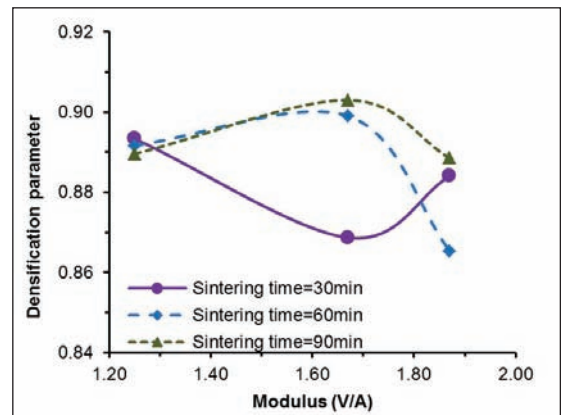


Fig. 3: Densification parameter of Al/7vol. % SiC<sub>p</sub> with (a) modulus and (b) sintering time

## EXPERIMENTAL EVALUATION OF SINTERED PROPERTIES FOR SINTERING TIME AND MODULUS ON DENSITY AND HARDNESS OF Al/SiC<sub>p</sub> BY PM PROCESS

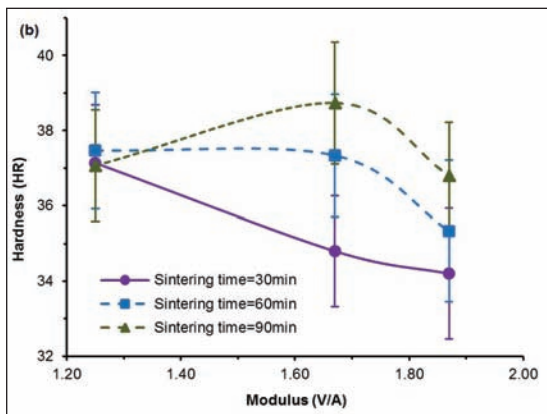
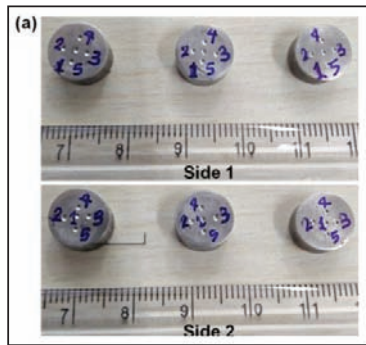


Fig. 4: Hardness of sintered aluminum MMCs (a) indentation location on specimen and (b) variation of hardness with modulus

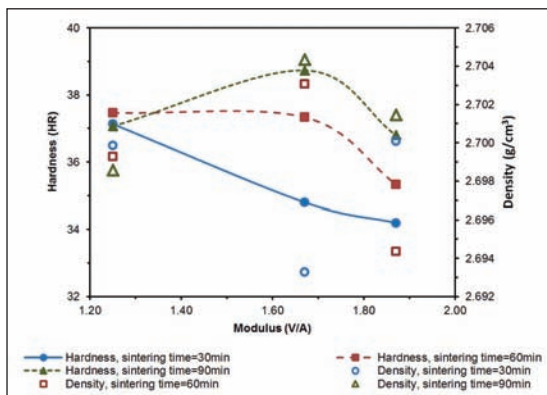


Fig. 5: Correlation between hardness and density of Al/7vol. % SiC<sub>p</sub> at different part modulus

Fig. 5 shows the correlation between hardness and density with respect to part modulus. Parts sintered for 60 to 90 minutes show improved properties (density and hardness). High density (2.7g/cm<sup>3</sup>) with low hardness (~34HR) was seen in Fig. 5 for part modulus of 1.87. Higher sintered density of Al-MMCs may not give the higher hardness as achieved by aluminum and aluminum alloy. It may be due to presence of hard particle phases like SiC in aluminum and its distribution. The correlation holds good for part modulus of 1.25 and 1.67 with sintering time 60 to 90minutes. Sintered density is achieved 2.69g/cm<sup>3</sup> and above by controlling the compaction pressure and sintering parameter (sintering temperature and time).

### Microstructure Evolution during Sintering

Metallographic analysis of Al-MMCs was carried out to investigate the effect of changing part modulus and sintering time on the distribution of reinforcements (SiC particles) in aluminum matrix. Distribution of SiC particles in aluminum matrix and aluminum grain boundaries are presented in Fig. 6. for part modulus of 1.87

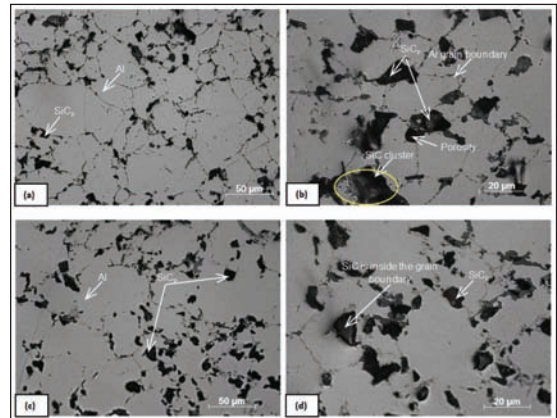


Fig. 6: Micrographs of Al/7vol.% SiC<sub>p</sub> MMCs sintered at 700°C: (a) for sintering time 30 min, 20X magnification; (b) for sintering time 30 min, 50X magnification; (c) for sintering time 90 min, 20X magnification; (d) for sintering time 90 min, 50X magnification

## EXPERIMENTAL EVALUATION OF SINTERED PROPERTIES FOR SINTERING TIME AND MODULUS ON DENSITY AND HARDNESS OF Al/SiC<sub>p</sub> BY PM PROCESS

From Fig. 6 (a) and (c), the distribution of reinforcing phases is found to be changed on increasing sintering time. Most of the SiC particles are situated on grain boundaries. Reinforcements are moved along the grain boundary of aluminum due to the increase in grain growth at 90 min of sintering time. Moreover the improved distribution of SiC reinforcement resulted at 90 min of sintering time, also improves part's sintered density and hardness. Porosity level reduces in sintered Al/7vol. %SiC<sub>p</sub> with increase in sintering time. Clustered SiC<sub>p</sub> in grain boundary increases the hardness as observed in Fig 5.

### Conclusion

The following conclusions could be drawn:

- 1) Improvement in densification is evident from sintered density, hardness and metallographic analysis by increasing sintering time from 30 min to 90 min.
- 2) Marginal variation in sintered properties is seen on varying part modulus but parts with 1.67 modulus gives highest sintered properties.
- 3) On increasing sintering time the distribution of reinforcing phases (SiC) increases, which is reflected in terms of improved sintered properties but 60-minute sintering time improves density and hardness.
- 4) Interfacial bonding between SiC particles and aluminum matrix is not influenced by changing part modulus but significantly altered by interaction effect between of sintering parameters (sintering temperature and sintering time).

### References

1. G. S. Cole, A. M. Sherman, "Lightweight materials for automotive applications", *Mater. Charact.*, **35**, 3-9, (1995).
2. J. W. Kaczmar, K. Pietrzak, W. Wlosinski, "The production and application of metal matrix composite materials", *J. Mater. Proc. Tech.*, **106**, 58-67, (2000).
3. H. E. Exner, E. Arzt, "Sintering Processes", in *Physical Metallurgy*, fourth revised and enhanced edition (Eds. R. W. Cahn and P. Haasen), Elsevier Science, (1996).
4. H. Abdizadeh, R. Ebrahimifard, M. A. Baghchesara, "Investigation of microstructure and mechanical properties of nano MgO reinforced Al composites manufactured by stir casting and powder metallurgy methods: A comparative study", *Composites: Part B*, **56**, 217-221, (2014).
5. R. Chen, G. Zhang, "Casting defects and properties of cast A356 aluminum alloy reinforced with SiC particles", *Composites Sci. and Tech.*, **47**, 51-56, (1993).
6. M.T. Milan, P. Bowen, "Tensile and fracture toughness properties of SiC<sub>p</sub> reinforced Al alloys: Effects of Particle Size, Particle Volume Fraction, and Matrix Strength", *JMEPEG*, ASM International, **13**, 775-783, (2004). DOI: 10.1361/105994904213581059-9495/\$19.0
7. V. Umasankar, M. Anthony Xavier, S. Karthikeyan, "Experimental evaluation of the influence of processing parameters on the mechanical properties of SiC particle reinforced AA6061 aluminium alloy matrix composite by powder processing", *J. Alloys Comp.*, **582**, 380-386, (2014).
8. C. Ghit, I. N. Popescu, "Experimental research and compaction behavior modelling of aluminum based composites reinforced with silicon carbide particles", *Computational Mater. Sci.*, **64**, 136-140, (2012).
9. Ege Anil Diler, Rasim Ipek, "An experimental and statistical study of interaction effects of matrix particle size, reinforcement particle size and volume fraction on the flexural strength of Al-SiC<sub>p</sub> composites by P/M using central composite design", *Mater. Sci. Engg A*, **548**, 43-55, (2012).
10. J.A. Ballantine, J.J. Conner, J.L. Handrock, *Fundamentals of Metal Fatigue Analysis*, first ed., Prentice Hall, (1990).



# DEVELOPMENT OF THERMOELECTRIC $\beta$ -FeSi<sub>2</sub> BY MECHANICAL ALLOYING AND ITS RESPONSE TO HOT PRESS SINTERING

N. B. Dhokey<sup>1</sup>, V. S. Poddar<sup>1</sup>, N. B. Revade<sup>1</sup>, Rohit Garbade<sup>1</sup>, Priyanka Lalge<sup>1</sup>, S. P. Butee<sup>1</sup>, R. D. Purohit<sup>2</sup>, Deep Prakash<sup>2</sup>

<sup>1</sup>Department of Metallurgy and Materials Science, College of Engineering Pune-5 (India)

<sup>2</sup>Powder Metallurgy Division, Bhabha Atomic Research Centre, Navi Mumbai-400 705 (India)

**Abstract :** Thermal management and energy crisis have been two major problems in 21<sup>st</sup> century. The thermoelectric concept is seen as a perfect solution for both the issues as heat energy can be directly converted into electrical energy. Thermoelectric materials which operate at temperatures up to 700–900°C such as semiconducting  $\beta$ -FeSi<sub>2</sub> may be an attractive proposition. In current work,  $\beta$ -FeSi<sub>2</sub> is synthesized by three step route that is mechanical alloying the Hot Press Sintering followed by annealing of hot pressed pellet. Elemental powders of electrolytic iron (98.9% purity, 400mesh), silicon (98.5% purity, 200mesh) have been mechanically alloyed either in Attritor mill (Argon atmosphere) or in Cryo mill (liquid Nitrogen) for 6 hours (250 rpm, SS 304 balls of 6 mm diameter, BPR = 10:1). Powders produced by two different mechanical alloying routes were then hot press sintered by optimizing temperature, pressure and holding period to get densified compact. Subsequent isothermal annealing of sintered compacts was done at 800°C for 12 hours in vacuum to get substantial amount of  $\beta$ -FeSi<sub>2</sub> phase formation. Comparison of both processes was done. Phase transition during the process was investigated using XRD, SEM and EDS. Characterization tools of XRD and SEM-EDS have confirmed the formation of  $\beta$ -FeSi<sub>2</sub>, in addition to traces of allied phases. It has established that for mechanically alloyed powders, Hot Press Sintering (HPS) followed by annealing gives  $\beta$ -FeSi<sub>2</sub> with nearly 90% relative density.

**Keywords:** Thermoelectric,  $\beta$ -FeSi<sub>2</sub>, Attritor Milling, Cryo Milling, Hot Press Sintering

## Introduction:

$\beta$ -FeSi<sub>2</sub> is an intermetallic phase in the iron-silicon system with 53.4 – 58.2 wt% Si [1]. The increasing interest in bulk semiconducting Iron Disilicide,  $\beta$ -FeSi<sub>2</sub> is due to its wide scope of applications like in thermoelectric generator, photovoltaic and optical fiber communications [2-3]. In this research work, a combination of mechanical alloying, hot press sintering and isothermal annealing has been tried to reduce the time period required to produce  $\beta$ -FeSi<sub>2</sub>. Mechanical Alloying carried out through attritor milling (AM) or Cryo Milling (CM) results in reduction in powder particle size and intense mixing effect which later on assist in phase homogenization. Resistance heating process was

carried out using Hot Press Sintering Equipment (Model: TSN - 25/8, Make: KEJETHERM, Capacity: 25 KVA, Tonnage: 8 tons) (HPS) where the sample to be heated was held in secondary circuit of voltage step down transformer. To heat the sample to specified temperature a current of low voltage (usually 3 – 8 Volts) and high value (up to several Kilo-Amps) was passed through the sample which was clamped across at the secondary of the transformer. In HPS, the phase homogenization advantage is carried one step ahead to the desired phase transformation by applying high temperature and high pressure simultaneously. It thus provides thermodynamic conditions (high temperature, high pressure) required for densification of sample during hot compaction itself. Optimization of process

## DEVELOPMENT OF THERMOELECTRIC $\beta$ -FeSi<sub>2</sub> BY MECHANICAL ALLOYING AND ITS RESPONSE TO HOT PRESS SINTERING

parameters (viz. time, temperature, pressure) in HPS to obtain maximum density was carried out. The samples were then subjected to sintering in Tubular Furnace (Maximum Temperature: ~ 1100°C, Vacuum: 10-5 mbar).

The effect of milling atmosphere and milling time on particle size distribution, HPS parameters on density and phase transformation, sintering parameters on  $\beta$ -FeSi<sub>2</sub> phase formation were investigated in this study. A comparative study between AM and CM was done. The primary focus of this study was to find out optimized process conditions to achieve maximum  $\beta$ -FeSi<sub>2</sub> phase formation with high density (Theoretical density of  $\beta$ -FeSi<sub>2</sub> = 4.93 g/cc) in minimum time period and less energy consumption, which later, can be engaged in mass production of the same.

### Experimental Procedure:

In current research work, elemental powders of iron (99.9% purity, 200 mesh) and silicon (98.5% purity, 400 mesh) have been mechanically alloyed for 6 h by using milling route either high-energy Attritor ball-mill (water cooled SS 304 vial, 400 rpm, 6mm  $\Phi$  SS 304 balls, BPR= 10:1, Ar atmosphere ) or Cryo Mill (SS 304 vial, 400 rpm, 6mm  $\Phi$  SS 304 balls, BPR= 10:1, liq. N<sub>2</sub> atmosphere with flow rate 6.5 lit/hr). Lower milling time (< 6 h) gave poor density on cold or hot compaction and higher milling time (> 6 h) shown agglomeration of Fe powder. The milled powder was then hot pressed in HPS using a square high - strength graphite die to produce samples with the dimensions nearly 10 X 10 X 3 mm under vacuum atmosphere of around 2.7 mbar. In HPS, effect of temperature, pressure and time on densification of FeSi<sub>2</sub> was studied. The process variables were varied as: (1) Holding period was varied from 2 min to 6 min at the interval of 2 minutes, temperature and pressure was kept constant, (2) Pressure was varied from 25 to 35 MPa at the interval of 5 MPa keeping holding period and Temperature constant, (3) Temperature was varied from 900°C

to 1100°C at the interval of 100°C, pressure and holding period were kept constant. The samples were subsequently sintered at 800°C for nearly 6 h in vacuum of 10-5 mbar and furnace cooled to room temperature. They were again sintered at 800°C for nearly 6 h in vacuum of 10-5 mbar and furnace cooled to room temperature. The sintered samples were then characterized using XRD and SEM - EDS. The amount of  $\beta$ -FeSi<sub>2</sub> phase formation got enhanced due to the thermal cycling treatment. Overall, the  $\beta$ -FeSi<sub>2</sub> phase can be produced by following above mentioned process without giving long time mechanical alloying treatment to the elemental powders and long duration heat treatment cycle.

Attritor mill consists of a vertical stationary vial with a series of impeller blades which are set progressively at right angles to each other. The blades energize the ball charge, causing powder size reduction because of abrasion between the balls and wall of the vial, and between balls, agitator shaft, and impeller blades. A powerful motor rotates the agitator shaft, which in turn agitates the steel balls in the vial. Cryo mill uses basically the same set up as that of Attritor Mill except that here instead of Ar gas, liquid Nitrogen is purged into the stationary vial. The temperature inside the vial is maintained at nearly -196°C which is lower than the DBTT of Fe (-159°C) and Si (brittle at RT). In CM powder size reduction is observed due to impact between milling balls, impeller blades and wall of the vial. Laser particle size analysis was carried out to study the particle size distribution in powder stage, SEM was performed at powder stage to understand maximum and minimum size of the particle, shape of the powder particles and morphological changes happened during milling. Also EDS study was performed to find out whether the process parameters have initiated any phase formation during milling. DTA study was performed to find out the transformation temperatures for powder samples in Nitrogen atmosphere (Gas flow: 200

# DEVELOPMENT OF THERMOELECTRIC $\beta$ -FeSi<sub>2</sub> BY MECHANICAL ALLOYING AND ITS RESPONSE TO HOT PRESS SINTERING

m/min) and its response to heating and cooling over a temperature range of room temperature to 1200 °C. Here, alumina was used as a reference material and around 10.4 mg of milled powder was analyzed with scanning rate of 50°C/min. The degree of alloying and phase transformation during milling and sintering were investigated using X-ray diffraction (XRD) analysis which was carried out using Cu K $\alpha$  radiation. Further, SEM and EDS were performed on the sintered samples to observe the microstructure and identify the phases formed.

## Results and Discussions:

Change in process parameters right from milling to annealing have been studied and compared. Comparison between the powder morphology obtained through various milling routes was made. HPS process parameters were varied and their effect on density was studied. Annealing process parameters were investigated and optimized to get maximum beta phase in the final microstructure.

### 1. Particle Size Distribution after Mechanical Alloying

The effect of 6 h CM and 6 h AM on particle size is shown in Fig. 1a and Fig 1b respectively. The plot shows that particle size reduction has taken place in both the processes. The size range squeezes from around 0.04 - 74 $\mu$ m to 0.04 - 30  $\mu$ m. First peak corresponds to Si particles whereas the second peak corresponds to Fe particles. This has been confirmed from the SEM study of the Fe and Si particles milled independently. The two peaks in Fig 1a may also be due to the difference in the initial particle sizes of the two as well as the difference in the response of the two types of material to milling. However, this condition is desired for  $\beta$ -FeSi<sub>2</sub> phase formation as the more the Si particles surrounding the Fe particle the more are the chances to get  $\beta$ -FeSi<sub>2</sub>

phase. In AM however, a different situation exist. The height of first peak has lowered down with increase in second peak height. This may be due to agglomeration of Fe particles and the Si particles may have got entrapped in the Fe agglomerates. This situation is also desired as it supports  $\beta$ -FeSi<sub>2</sub> phase formation.

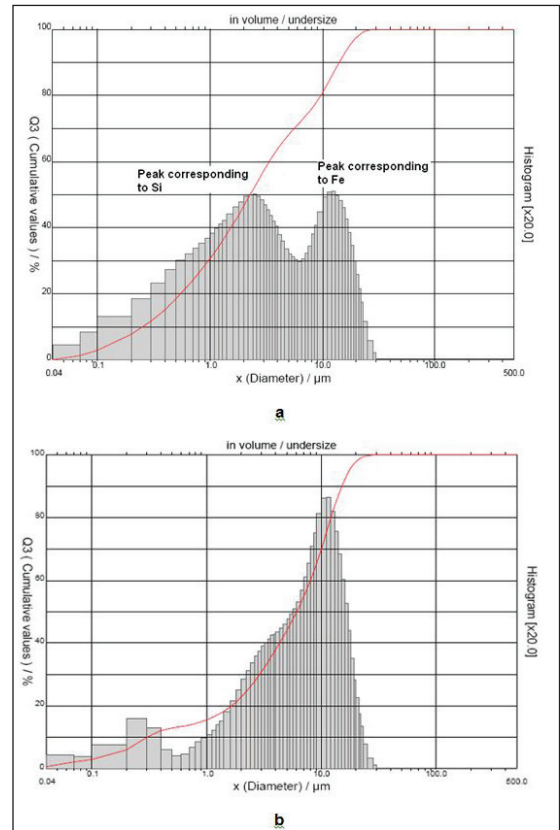


**Fig.1: Laser Particle Size Analysis for Fe-Si a. Cryo milled powder, b. Attritor milled powder**

The particle size variation can be confirmed from SEM images of milled powders in Fig.2. Cryo milled powder particles show comparatively fine powder proportion higher than that in attritor milled powder. Agglomeration can be seen in AM and at some locations  $\epsilon$ -FeSi formation was observed and confirmed through EDS analysis.

# DEVELOPMENT OF THERMOELECTRIC $\beta$ -FeSi<sub>2</sub> BY MECHANICAL ALLOYING AND ITS RESPONSE TO HOT PRESS SINTERING

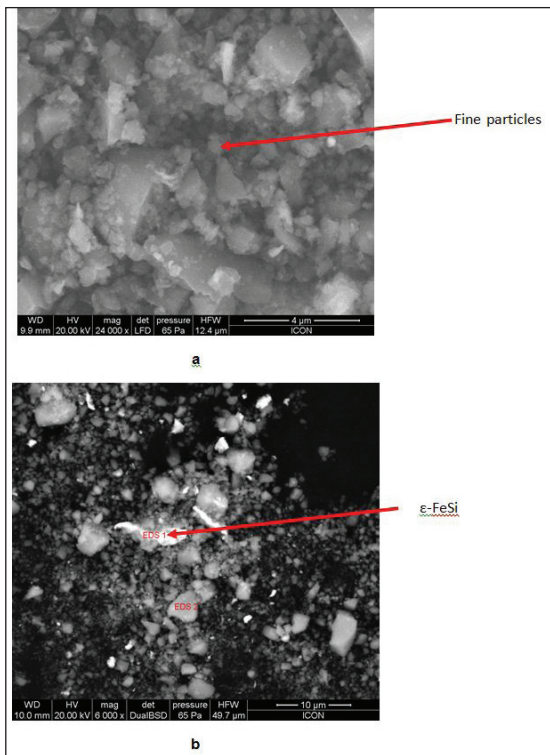


Fig. 2 SEM image of Fe-Si milled for 6 hr a. CM, b. AM

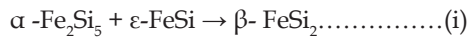
## 2. Effect of Particle Size on Phase Transformation Temperature:

Semiconducting  $\beta$ -FeSi<sub>2</sub> is a promising material for high temperature thermoelectric applications due to its high resistance to oxidation, good thermo power, relatively high electrical conductivity and non-toxicity [3]. However,  $\beta$ -FeSi<sub>2</sub> is stable only up to 982° C, above which it decomposes into metallic  $\alpha$ -Fe<sub>2</sub>Si<sub>5</sub> and  $\epsilon$ -FeSi phases. The formation of the FeSi<sub>2</sub> phase occurs through a sluggish peritectoid reaction. In the Fe-Si binary system, there are five equilibrium silicide phases: Fe<sub>3</sub>Si (cubic), Fe<sub>2</sub>Si (cubic), Fe<sub>5</sub>Si<sub>3</sub> (hexagonal),  $\epsilon$ -FeSi (cubic),  $\beta$ -FeSi<sub>2</sub> (base-centered orthorhombic), and  $\alpha$ -FeSi<sub>2</sub> or  $\alpha$ -Fe<sub>2</sub>Si<sub>5</sub> (tetragonal). The stable phases are either  $\beta$ -FeSi<sub>2</sub> or  $\alpha$ -FeSi<sub>2</sub>, depending on temperature.  $\beta$ -FeSi<sub>2</sub>

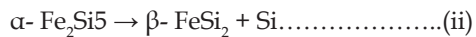
phase is stable below  $\leq 937^\circ\text{C}$  and transforms to the  $\alpha$ -phase at higher temperatures [1].

## Expected behavioral pattern of Fe and Si powders

The powders of Fe and Si are mechanically alloyed stoichiometrically for  $\beta$ - FeSi<sub>2</sub> phase formation. Depending on the availability of Si around Fe particles either  $\alpha$ -Fe<sub>2</sub>Si<sub>5</sub> or  $\epsilon$ -FeSi forms during heating the powdered mixture of Fe and Si as shown in Fig. 3. The peritectoid reaction of the solidified  $\alpha$ - Fe<sub>2</sub>Si<sub>5</sub> and  $\epsilon$ -FeSi to the semiconducting  $\beta$ -FeSi<sub>2</sub> phase at 982 °C,



On lowering the temperature of the system, the eutectoid decomposition of the remaining phase at 937 °C is expected as,



Further lowering of temperature favors another reaction

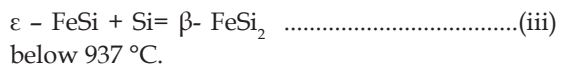


Figure 3 shows the schematic illustration of the phase transformations possible with nearly Fe:Si ::47:53 combination under equilibrium conditions.

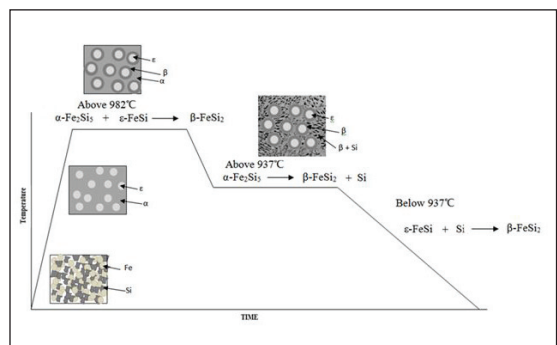


Fig. 3: Phase transformation temperatures and the schematic illustration of the  $\beta$ -phase formation process

## DEVELOPMENT OF THERMOELECTRIC $\beta$ -FeSi<sub>2</sub> BY MECHANICAL ALLOYING AND ITS RESPONSE TO HOT PRESS SINTERING

In powder metallurgy route, a change in response to increasing temperature was observed and confirmed from the DSC-DTA Analysis. As the particle size reduction is carried out mechanically, surface energy might have increased thereby enhancing the kinetics of the reactions which resulted in decrease in transformation temperatures (refer Fig. 4)

### DTA Analysis:

The DTA analysis of CM 6 h powder in Fig. 4a was carried out to determine  $\beta$ -FeSi<sub>2</sub> transformation temperature. A distinct exothermic peak was seen at around 596-606°C. This temperature is believed to which indicate the “low temperature transformation temperature below which primary transformation of  $\alpha$  - Fe<sub>2</sub>Si<sub>5</sub> →  $\beta$  - FeSi<sub>2</sub> + Si and secondary transformation of  $\epsilon$  - FeSi + Si →  $\beta$  - FeSi<sub>2</sub> take place. Hence this shows that, eutectoid decomposition of  $\alpha$ -FeSi<sub>2</sub> and  $\epsilon$ -FeSi into  $\beta$ -FeSi<sub>2</sub> is taking place at 596-607°C.

In figure 4b, a small peak and valley pair is observed in the temperature range of 50 - 110°C. This may be corresponding to the initiation of  $\epsilon$  - FeSi phase formation. A step is observed at the temperature of around 312°C where initiation of  $\alpha$  - Fe<sub>2</sub>Si<sub>5</sub> and growth of  $\epsilon$  - FeSi phases might have taken place. An exothermic peak appears at 585°C which indicate the “low temperature transformation temperature below which primary transformation of  $\alpha$  - Fe<sub>2</sub>Si<sub>5</sub> →  $\beta$  - FeSi<sub>2</sub> + Si and secondary transformation of  $\epsilon$  - FeSi + Si →  $\beta$  - FeSi<sub>2</sub> take place. It is observed that the eutectoid temperature is reduced from 937°C to 585°C. On continuous slow heating to 865°C, an endothermic peak is observed. This peak corresponds to the equilibrium peritectoid temperature. The peritectoid reaction,  $\epsilon$  - FeSi +  $\alpha$  - Fe<sub>2</sub>Si<sub>5</sub> →  $\beta$  - FeSi<sub>2</sub> takes place at nearly 865°C, the temperature lower than the actual peritectoid temperature of 982°C. This shift in reaction temperatures to the lower values compared to

the equilibrium values may be attributed to the reduction in particle size after Attritor Milling for 6 h.

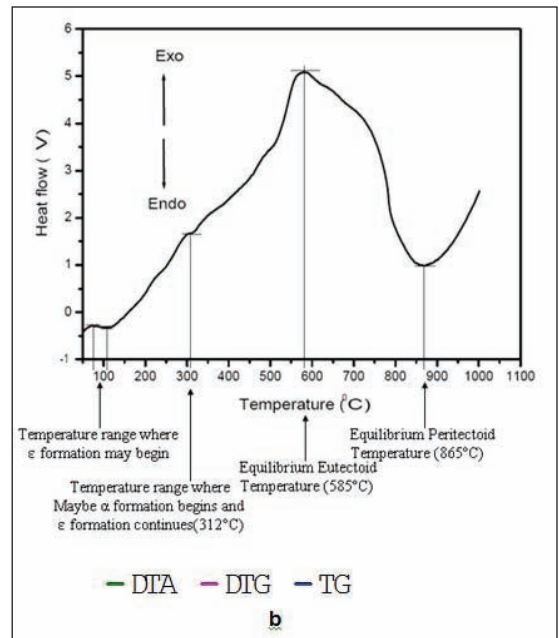
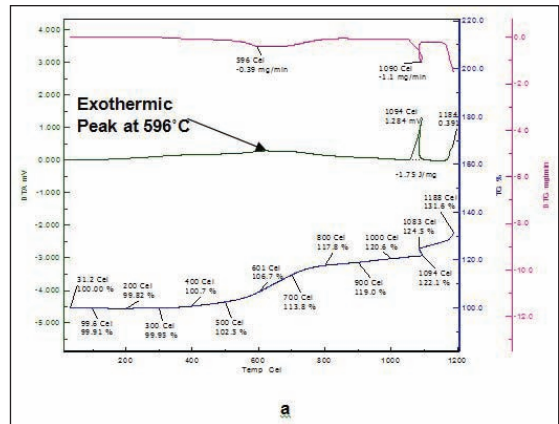
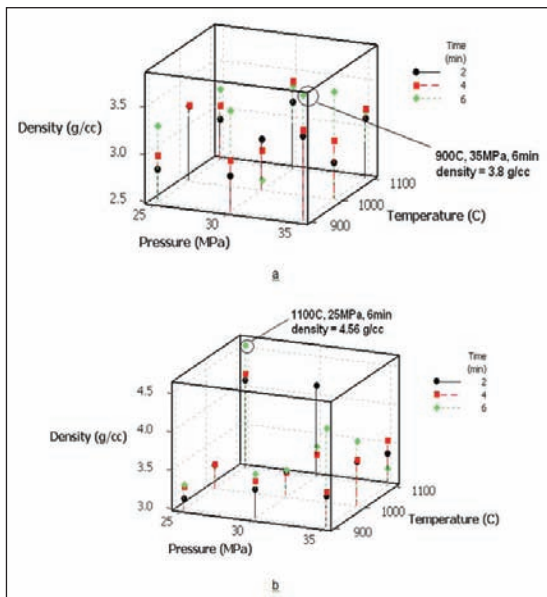


Fig.4 a. DTA curve CM 6 h powder at 596°C, b. DSC curve for AM 6 h powder

## DEVELOPMENT OF THERMOELECTRIC $\beta$ -FeSi<sub>2</sub> BY MECHANICAL ALLOYING AND ITS RESPONSE TO HOT PRESS SINTERING

### 3. Optimization of parameters for hot press sintering to achieve maximum densification of FeSi<sub>2</sub>

In few trials it was observed that with increase in density, the percent of  $\beta$ -FeSi<sub>2</sub> phase formation after sintering increased. In HPS, the effect of holding period, temperature and pressure on densification of FeSi<sub>2</sub> was studied. The process variables were varied as: (1) Holding period was varied from 2 min to 6 min at the interval of 2 minutes, temperature and pressure was kept constant, (2) Pressure was varied from 25 to 35 MPa at the interval of 5 MPa keeping holding period and Temperature constant, (3) Temperature was varied from 900°C to 1100°C at the interval of 100°C, pressure and holding period were kept constant. The data was analyzed to find out the optimum combination of holding period, temperature and pressure to get maximum relative density.



*Fig.5: Effect of temperature, pressure and holding time on density in HPS for a. Cryo Milled powder, b. Attritor milled powder*

Fig. 5a shows that for CM powders when temperature was increased from 900 to 1100°C at a constant pressure of 25 MPa the density increases. Similarly, when holding time was increased from 2 min to 6 min at a constant pressure of 25 MPa, increase in density was observed. However, in case of CM powders, melting of specimen was observed for trials of temperature of about 1100°C. This may be contributed to the increased surface energy of CM powder. Maximum density obtained after HPS was 3.8 g/cc (77% relative density) with the process parameters were 900°C, 35 MPa, 6 min.

In AM powders also, there were few exceptions (Fig. 5b). When the compaction pressure was 35 MPa and temperature ranges from 900 to 1100°C, at holding time of 2 min for each permutation, increase in density was observed. Further increase in holding time resulted in partial melting of sintered specimen which reduced the density. Similarly, at temperature of 1100°C highest density was observed when the compaction pressure was minimum that is 25 MPa and the holding time was 6 min. In this case longer holding time resulted again in partial melting of the sintered specimen. Melting in each case happened because with increase in holding period, according to Joules law ( $H=I^2RT$ ) heat generation increases. At higher temperature of 1100°C, higher pressures of 35 MPa and higher holding period of 6 min, Melting of sintered specimen was observed. This was because excessive heat was generated which caused melting according to joules law ( $H=I^2Rt$ ) which lead to decrement in density. Also when lower temperature of 900°C, lower pressure of 25 MPa and holding period of 2 min was chosen as process parameters, lowest density, 63% of Theoretical density of  $\beta$ -FeSi<sub>2</sub> (3.11 g/cc) was observed. Hence critical process parameters combination was needed, which

## DEVELOPMENT OF THERMOELECTRIC $\beta$ -FeSi<sub>2</sub> BY MECHANICAL ALLOYING AND ITS RESPONSE TO HOT PRESS SINTERING

would give good densification as well as avoid melting of sintered specimen. From all the trials performed above, when Temperature was 1100°C, Compaction pressure was 25 MPa and Holding period was 6 min, maximum density 92% of Theoretical density of  $\beta$ -FeSi<sub>2</sub> (4.56 g/cc) was achieved. This process combination gave maximum densification according to these trials. It is seen in Fig. 5b that at constant temperature of 1100°C and constant pressure of 25 MPa density of FeSi<sub>2</sub> was getting increased as holding period in HPS was increased from 2 min to 6 min. Also when pressure was increased to 30MPa at constant temperature of 1100°C, higher density was observed when holding period was 2 min beyond that partial melting of sintered specimen was seen; because of this drop in density was observed. When pressure was increased to 35 MPa at constant temperature of 1100°C, increase in density with increasing holding period was seen up to 4 min but when holding period was increased to 6 min partial melting of sintered specimen did occur hence drop in density was seen.

When compaction pressure was 25 MPa, Holding period was 6 min and temperature was 1100°C, maximum density of 4.56 g/cc (92% Relative Density) was achieved.

### 4. XRD Analysis:

As higher densities were achieved with AM powders, study of AM specimen was prioritized. For AM specimens during HPS, at temperature above 900°C,  $\beta$ -phase formation was seen to a little extent. Major phases that were formed were  $\alpha$  - Fe<sub>2</sub>Si<sub>5</sub> and  $\epsilon$  - FeSi. Unreacted Si remained dispersed uniformly. As higher density was achieved at temperature 1100°C, a focused approach was given on those specimens.

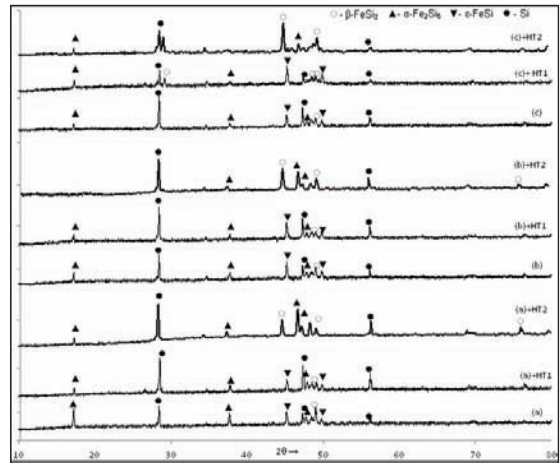


*Fig.6 : XRD Analysis of Vacuum hot pressed Fe-Si (AM) (a)1100°C, 25 MPa, 2 min (b)1100°C, 25 MPa, 4 min (c) 1100°C, 25 MPa, 6 min ,All three were later on sintered at 800°C for the period of 6 hours viz.: (a) + HT1, (b) + HT1 and (c) + HT1 respectively, Also all three were again sintered at 800°C for the period of 6 hours viz.: (a) + HT2, (b) + HT2 and (c) + HT2 respectively*

Density is a major factor as it directly affects the thermoelectric material performance (electrical conductivity reduces with increase in porosity or otherwise decrease in density). With increase in temperature to 1100°C,  $\alpha$  - Fe<sub>2</sub>Si<sub>5</sub> and  $\epsilon$  - FeSi phases were formed (refer Fig.6). However,  $\beta$ -phase formation reaction was just initiated. The physical conditions that are required for  $\beta$ -phase formation were present but the time period given for it was very less. So further the pellets were subjected to sintering at 800°C for 6 h under vacuum of 10-5 mbar (HT1).

Increase in progress of  $\beta$ -phase formation was observed but still unreacted  $\alpha$  - Fe<sub>2</sub>Si<sub>5</sub> and  $\epsilon$  - FeSi phases were observed (refer fig.6). So again the specimen were subjected to sintering at 800°C for 6 h under vacuum of around 10-5 mbar (HT2) and it was observed that almost all  $\epsilon$  - FeSi phase got utilized in  $\beta$ -phase formation. Very little amount of  $\alpha$  - Fe<sub>2</sub>Si<sub>5</sub> remained along

# DEVELOPMENT OF THERMOELECTRIC $\beta$ -FeSi<sub>2</sub> BY MECHANICAL ALLOYING AND ITS RESPONSE TO HOT PRESS SINTERING

with finely dispersed Si. Finely dispersed Si is desirable. Si promotes phonon scattering thereby decreasing the thermal conductivity and hence increasing the ZT value of TM [4-6].

For CM specimen, XRD analysis was carried out. The specimen with higher density i.e. 3.8 g/cc were subjected to sintering at 800°C for 6 h under vacuum of around 10-5 mbar and it was observed that  $\beta$ -phase formation was initiated to some extent. Again the specimens were subjected to sintering at 800°C for 6 h under vacuum of around 10-5 mbar. However, unreacted Si,  $\epsilon$ -FeSi still existed as confirmed from fig. 7. This may be because of less density which resulted in decrease in number of reaction sites for  $\beta$ -phase formation.

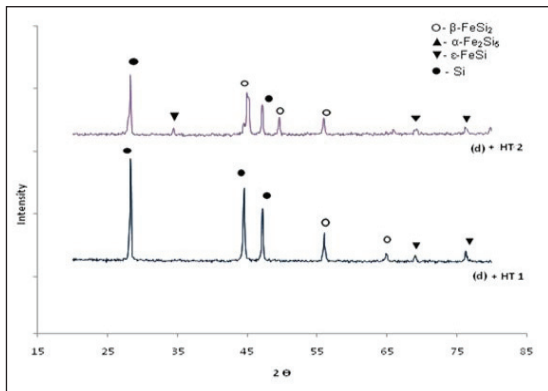


Fig.7: XRD Analysis of Vacuum hot pressed Fe-Si (CM) (d)900°C, 35 MPa, 6 min + HT1, (d)900°C, 35 MPa, 6 min + HT2

## 5. SEM - EDS:

Results from XRD reports were confirmed through SEM-EDS analysis. Fig. 8a shows AM specimen with few Si particles and formation of  $\beta$  phase after HT2. Fig. 8b shows CM specimen with dispersed Si particles,  $\epsilon$ -FeSi and  $\beta$  phase. This was as earlier mentioned because of lower density.

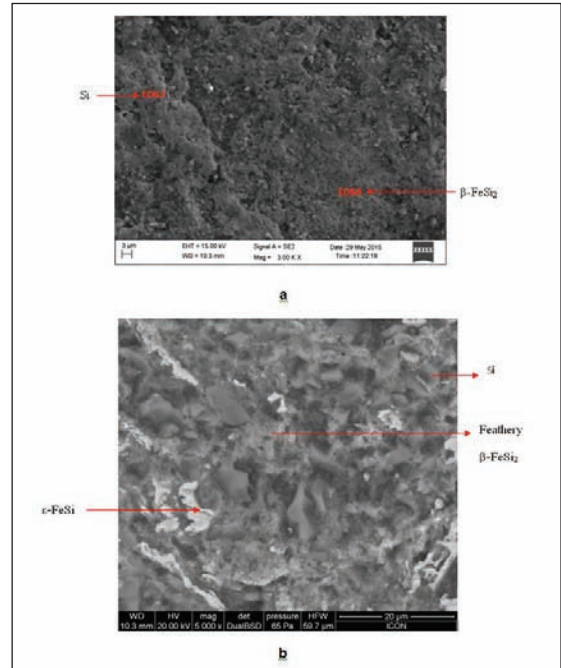


Fig. 8 SEM-EDS analysis of a. AM + HT2 specimen, b. CM + HT2 specimen

## Conclusions:

In this research work high temperature thermoelectric material  $\beta$ -FeSi<sub>2</sub> was synthesized through two milling routes, i.e. Attritor milling and Cryo milling.

1. The above results indicate that obtaining  $\beta$ -phase i.e.  $\beta$ -phase formation is a function of many parameters and varying these parameter one by one can lead to the complete  $\beta$ -phase synthesis. Mathematically, it can be expressed as-

$$\text{Formation of } \beta\text{-phase} = f(t_s, T_s, d_p, M_t)$$

Where,  $t_s$ : Sintering Period;  $T_s$ : Sintering Temperature;  $d_p$ : Particle size after milling

$M_t$ : Type of Milling

## DEVELOPMENT OF THERMOELECTRIC $\beta$ -FeSi<sub>2</sub> BY MECHANICAL ALLOYING AND ITS RESPONSE TO HOT PRESS SINTERING

---

2. Laser particle size analysis of the CM 6 h and AM 6 h powders was done. Fine particles (mean particle size 3.75  $\mu\text{m}$ ) was observed for CM whereas agglomeration was observed in AM (mean particle size 7.08  $\mu\text{m}$ ).
3. After milling, reduction in phase formation temperature was observed, i.e. from 937°C to around 600°C.
4. When AM specimen prepared by using optimized hot press sintering parameters and heat treated at 800°C for 6 hours furnace cooled and again annealed at same temperature for 6 hours (HT 2), nearly complete  $\beta$ -FeSi<sub>2</sub> phase formation has taken place.
5. For CM powders lower HPS temperature is required for higher density, but increased pressure i.e. greater than 35 MPa have to be tried for better results with CM powders.

### References:

1. Alloy Phase Diagram, Vol. 3, 860-861, (1992)
2. Soon-Chul Ur, Il-Ho Kim, "Thermoelectric Properties of Mechanically Alloyed Iron Disilicides Consolidated by Various Processes", *Int. J. Met. Mater.*, **11** (4), 301~308, (2005).
3. U. Stohrer, R. Voggesberger, G. Wagner, U. Birkholz, "Sintered FeSi<sub>2</sub> for Thermoelectric Power Generation", *Energy Convers. Mgmt*, **30** (2), 143-147, (1990).
4. Soon-Chul Ur, "Mechanical Alloying and Thermoelectric Properties of Co doped FeSi<sub>2</sub>", *M.Tech. Thesis*, Dept. of Materials Science & Engineering, Chungju National University, (2003).
5. I. Yamauchi, A. Sukanuma, T. Okamoto, I. Ohnaka, "Effect of copper addition on the  $\beta$ -phase formation rate in FeSi<sub>2</sub> thermoelectric materials", *J. Mater. Sci.*, **32**, 4603-4611, (1997).
6. Qiu Yue., S. Hong-lie, Y. Yu-gang, W. Kai-hua, "Fabrication and thermoelectric properties of  $\beta$ -FeSi<sub>2</sub> prepared by mechanical alloying", *Trans. Non-ferrous Met. Soc. China*, **17**, 618-621, (2007).



# EFFECT OF CYCLIC HEAT TREATMENT AND SWAGING ON MECHANICAL PROPERTIES OF MOLYBDENUM AND COBALT CONTAINING TUNGSTEN HEAVY ALLOYS

U. Ravi Kiran, M. Sankaranarayana, G. V. S. Nageswara Rao<sup>1</sup>, T. K. Nandy

Defence Metallurgical Research Laboratory, Kanchanbagh, Hyderabad, India.

<sup>1</sup>National Institute of Technology, Warangal, India.

**Abstract :** Tungsten heavy alloys (WHAs) prepared by liquid-phase sintering, are composite materials in which quasi-spherical shaped hard bcc particles are embedded in the ductile Ni-Fe-W solid solution fcc matrix. One of the strategic applications for these alloys is in ordnance, such as kinetic-energy (KE) penetrators. In the present study, a tungsten heavy alloy containing molybdenum and cobalt was subjected to thermo-mechanical processing that employed cyclic heat treatments in order to explore the possibility of enhancing mechanical properties. The alloy was synthesized by liquid phase sintering followed by heat treatments which consisted single as well as multiple cycles. Subsequently, these were subjected to swaging imparting about 30% deformation. Discernible changes were observed in the microstructure following cyclic heat treatment in both heat treatment and swaged conditions. Cyclic heat treatment results in separation of tungsten grains thereby decrease in contiguity of the alloys. While there was marginal improvement in tensile properties, impact toughness showed significant enhancement. A detailed analysis of microstructure and fractographs was undertaken in order to understand the reasons for the enhancement in impact toughness and also the implication of these results in the development of heavy alloys with enhanced properties.

**Keywords:** Tungsten heavy alloy, Swaging, Tensile properties, Impact strength, Fractography.

## 1. Introduction

Tungsten alloys are being increasingly used in a variety of applications such as kinetic energy penetrators, radiation shielding, balancing weights and electrical contacts due to their high density, excellent physical and mechanical properties [1-3]. These alloys, prepared by liquid-phase sintering, are composite materials in which quasi-spherical shaped hard bcc particles are embedded in ductile Ni-Fe-W solid solution fcc matrix. Liquid phase sintering (LPS) offers advantages namely relatively low sintering temperature enhanced densification, microstructural homogenization and attainment of near theoretical sintered densities. In addition, LPS also enables high material utilization (>95%), near-net shaping, high productivity, and superior properties [4]. Tungsten heavy alloys offer a unique combination of properties such as

high density (16-18 g/cm<sup>3</sup>), high strength (UTS ranging from 1000-1700 MPa), high ductility (10-30%), good corrosion resistance, and easy machinability. One of the strategic applications for these alloys is in ordnance, such as kinetic-energy (KE) penetrators. While the high density of tungsten heavy alloy helps in realization of superior ballistic properties, their excellent mechanical properties such as high strength, ductility and impact property ensure the survival of penetrator in extremely demanding conditions experienced during their launch and terminal ballistics [5].

A thermo mechanical processing comprising heat treatment and swaging is an important step in tungsten heavy alloys in order to realise superior mechanical properties. The heat treatment which consists of vacuum annealing with temperatures ranging from 1100-1200°C

# EFFECT OF CYCLIC HEAT TREATMENT AND SWAGING ON MECHANICAL PROPERTIES OF MOLYBDENUM AND COBALT CONTAINING TUNGSTEN HEAVY ALLOYS

followed oil quenching results in improved mechanical properties which may be ascribed to: (a) removal of trapped hydrogen, (b) elimination of tungsten-matrix interfacial segregation, and suppression of intermetallic formation (c) chemical homogenisation [6-8].

While a single heat treatment which involves soaking the alloy at a given temperature followed by oil or water quenching leads to enhancement in properties, further improvement has been attempted by employing a cyclic treatment [9-11]. In such a treatment, while the soaking temperature is maintained the same, the dwell time is divided into a number of cycles with reduced period. Each cycle consists of soaking for a small time period followed by water quenching. By employing such a treatment, considerable improvement in impact property has been realized. However, the limitation of such a technique is since the alloy is in heat treated condition, the strength values are considerably less in comparison to the desired values that render them suitable for ammunition applications. In the present investigation cyclic heat treatment with swaging effect on molybdenum and cobalt added tungsten heavy alloys have been studied in order to realize enhanced properties and correlated it with underlying microstructure and failure behaviour.

## 2. Experimental

Two tungsten heavy alloys 90W-6Ni-2Fe-0.5Co-1.5Mo (WNM) and 90W-6Ni-2Fe-2Co (WNC) were prepared as per their weight percent. Tungsten powders were mixed with matrix powders such as Ni, Fe, Co and Mo in the required proportions by ball milling. The powders were then cold iso-statically pressed and subjected to sintering in a hydrogen sintering furnace. The sintered blanks were then subjected to vacuum heat treatment employing three cycles. The vacuum heat treatment cycles are designated as cycle 1 (V1), cycle 2 (V2) and cycle 3 (V3). All the heat treated blanks were subjected to swaging (30%) followed by heat treatment at 1150°C/2 h/oil quench. The tungsten grain size, volume fraction of the matrix phase and contiguity of

the specimens were measured from scanning electron micrograph. Contiguity was measured from the following

$$C_{ss} = 2N_{ss}/(2N_{ss}+N_{sl}) \dots\dots\dots(1)$$

where  $N_{ss}$  and  $N_{sl}$  are the number of W-W grain boundary and W-matrix interface boundary intercepted, respectively. The bulk hardness of the alloys was measured using Vickers hardness tester. The tensile specimens were prepared as per ASTM-E8 and tested at room temperature using universal tensile testing machine. Charpy impact test specimens were prepared as per ASTM-E23 [12] and evaluation was carried out in a pendulum type impact tester at room temperature.

## 3. Results

### 3.1 Microstructure

The scanning electron micrographs of the alloys processed by cyclic heat treatment are shown in Fig. 1. W-W separation by liquid penetration is seen in all heat treatment conditions, where the separation is more in case of 3 cycles of heat treatment.

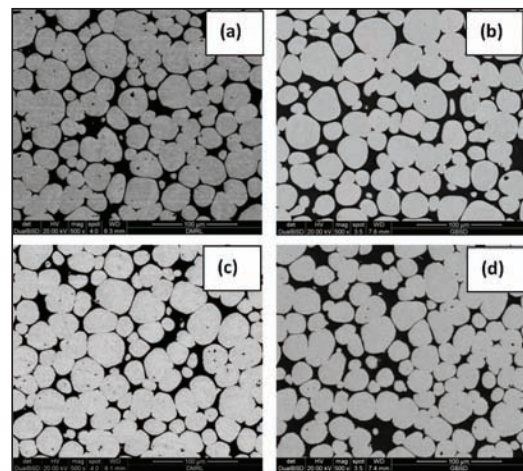


Fig.1. Back scattered electron micrographs of tungsten heavy alloy in: (a) 1 cycle (WNM), (b) 1 cycle (WNC), (c) 3 cycle (WNM) and (d) 3 cycle (WNC) of vacuum heat treatment after sintering.

# EFFECT OF CYCLIC HEAT TREATMENT AND SWAGING ON MECHANICAL PROPERTIES OF MOLYBDENUM AND COBALT CONTAINING TUNGSTEN HEAVY ALLOYS

Fig. 2 shows a magnified scanning electron micrograph of the alloys after 3 cycles of heat treatment. It clearly shows that the matrix phase has penetrated between tungsten grains even when W-W separation is less. Such evidences are relatively lesser in single cycle specimen.

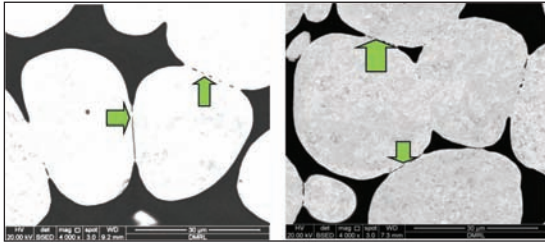


Fig.2. Back scattered electron micrograph of tungsten heavy alloy after 3 cycles of heat treatment showing penetration of the matrix phase (shown by arrow).

Quantitative microstructural parameters after heat treatment are shown in Table 1. It shows contiguity of W-W grain decreases with increasing number of cycles in both alloy systems. Additionally, the volume fraction of matrix increases with increasing number of cycles.

Table 1. Microstructural parameters of the alloys after sintered plus heat treatment.

Designation	Tungsten grain size ( $\mu\text{m}$ )		Volume fraction of matrix (Pct)		Contiguity		Dihedral angle ( $\phi$ )		Tungsten solubility in matrix (Wt.%)	
	WNM	WNC	WNM	WNC	WNM	WNC	WNC	WNC	WNM	WNC
V1	26	28	0.16	0.20	0.43 $\pm$ 0.04	0.32 $\pm$ 0.03	42	37	17	30
V2	25	28	0.17	0.22	0.37 $\pm$ 0.06	0.29 $\pm$ 0.03	40	32	19	34
V3	24	27	0.18	0.23	0.32 $\pm$ 0.03	0.26 $\pm$ 0.04	36	30	22	36

## 3.2 Mechanical Properties

Tensile curves of the alloys in swaged condition are shown in Fig. 3 and mechanical properties are shown in Table 2. High tensile and elongation failure are obtained Co added alloy as compared to Mo added alloys. While there is significant improvement in impact is observed in both the alloy systems after 3 cycles of heat treatment plus swaging (Fig. 4).

Table 2. Mechanical properties of the alloys after swaging.

Designation	Tensile strength (MPa)		Yield strength (MPa)		Elongation (%)		Impact strength ( $\text{J}/\text{cm}^2$ )		Bulk-hardness (VHN)	
	WNM	WNC	WNM	WNC	WNM	WNC	WNM	WNC	WNM	WNC
V1	1295	1407	1277	1369	8	7	23	42	482 $\pm$ 3	460 $\pm$ 3
V2	1319	1391	1278	1358	6	8	35	116	483 $\pm$ 3	458 $\pm$ 3
V3	1343	1389	1293	1360	8	10	83	130	478 $\pm$ 2	455 $\pm$ 3

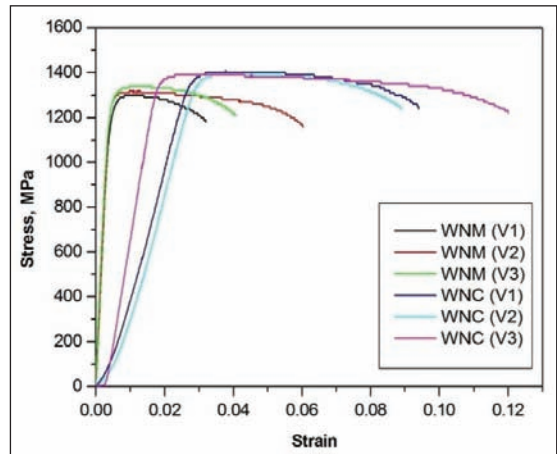


Fig.3. Stress vs strain curves of alloys in swaged condition.

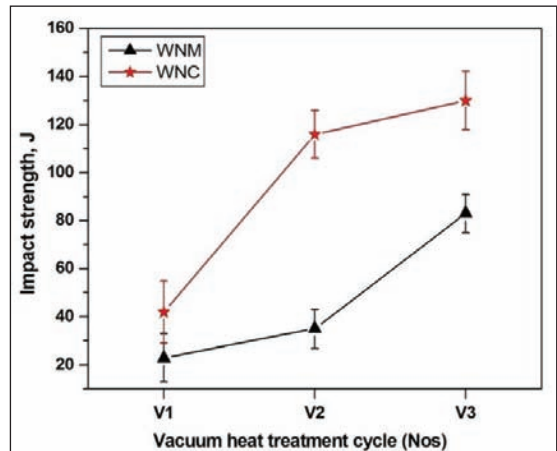


Fig. 4. Impact strength variation of the alloys after swaging.

# EFFECT OF CYCLIC HEAT TREATMENT AND SWAGING ON MECHANICAL PROPERTIES OF MOLYBDENUM AND COBALT CONTAINING TUNGSTEN HEAVY ALLOYS

## 3.3. Fractograph analysis

Scanning electron micrographs of failed tensile specimens are shown in Fig.5. Similarly, the fracture features of impact specimens are shown in Fig.6. These are not very different from those seen in the failed tensile specimens in that the surface is dominated by W cleavage, W-W separation and matrix tearing. Here the area fraction of tungsten cleavage and W-W de-cohesion have been determined in the failed specimens. It is apparent that in cyclic heat treatment as the number of cycle increases the relative fraction of W-W de-cohesion decreases.

## 4. Discussion

Heat treatment is one of the essential components in thermo-mechanical processing of tungsten heavy alloy. As sintered alloy exhibits inferior properties because the presence of weak W-matrix and W-W interfaces. W-matrix interfaces are weak due to the segregation of C, O, N and S [13]. This can be ameliorated by solution treatment at elevated temperature (900-1300° C) that leads to homogenisation of composition.

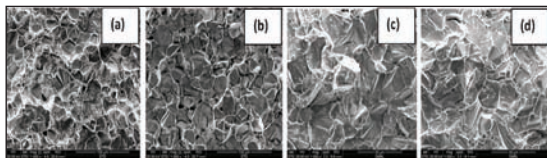


*Fig.5. Tensile fractographs of tungsten heavy alloy: (a) 1 cycle (WNM), (b) 1 cycle (WNC), (c) 3 cycle (WNM), (d) 3 cycle (WNC) of swaging after vacuum heat treatment plus sintering.*

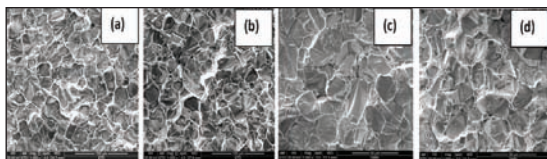


*Fig.6. Impact fractographs of tungsten heavy alloy: (a) 1 cycle (WNM), (b) 1 cycle (WNC), (c) 3 cycle (WNM), (d) 3 cycle (WNC) of swaging after vacuum heat treatment plus sintering.*

This is followed by water/oil quenching so as to prevent any possible segregation of these elements again during cooling. However, W-W interface remain intact and they still act as crack nucleating sites leading to impairment of properties. Thus, the presence of contiguous tungsten grains remains an item of concern in the microstructure of tungsten heavy alloys. Efforts have been made to develop small grain-small contiguity alloys. On the other hand alloys with coarser microstructure cyclic heat treatment is able to address this issue of W-W contact by replacing them with stronger W-matrix interface [14].

Pioneering work by Noh and co-workers [15] addressed this problem by introducing a cyclic heat treatment which resulted in significant reduction in W-W interfacial area. The treatment consists of soaking the alloy at temperatures ranging from 900-1300° C, holding at that temperature followed by water quenching and repeating this process multiple times. Owing to mismatch in the coefficient of thermal expansion between tungsten ( $4.6 \times 10^{-6}/^{\circ}\text{C}$ ) and matrix phase ( $2.0 \times 10^{-6}/^{\circ}\text{C}$ ), mechanical stresses are generated in the vicinity of W-matrix interface and this results in ingress of the matrix phase thereby separating tungsten particles. While the tensile properties such as ultimate tensile strength and % elongation remain unaffected, there is substantial improvement in impact properties.

Rheological parameters (Table 1) show the beneficial effects of cyclic heat treatment. While the volume fraction of the matrix phase shows only a marginal increase, there is discernible drop in contiguity values. This is also associated with decrease in dihedral angle. It has been shown earlier that there is one to one correlation between dihedral angle and contiguity values [16]. Additional corroborating evidence is the

## EFFECT OF CYCLIC HEAT TREATMENT AND SWAGING ON MECHANICAL PROPERTIES OF MOLYBDENUM AND COBALT CONTAINING TUNGSTEN HEAVY ALLOYS

ingress of the matrix phase between tungsten particles (Fig. 2). Tensile properties of the alloys (Table 3) following cyclic heat treatment have shown improvement in properties. Noh et al. [15] who do not show any observable improvement in tensile properties. This is consistent with the present study that marginal improvement in tensile properties for molybdenum alloy and no improvement of tensile values in cobalt containing alloy. However, improvements in elongation are observed in case of cobalt alloy. Improvement in tensile or elongation is expected in tensile properties since the volume fraction of the matrix phase increases and the contiguity values decrease in both alloys in the present study. However, the impact shows significant improvement in both the alloys. This is consistent with the fracture surface that shows increasing fracture of W cleavage and decrease in W-W decohesion (Fig. 7).

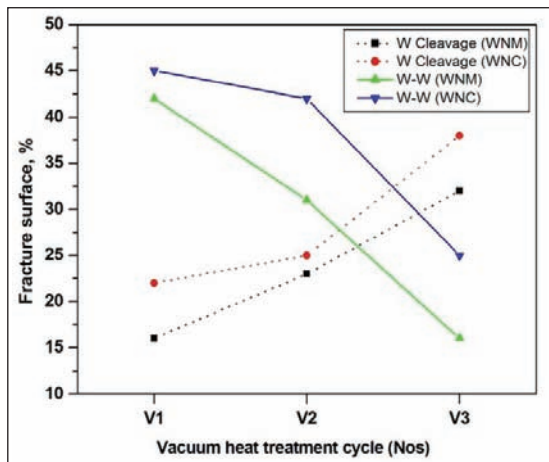


Fig.7. Relative percentage of fracture features in tungsten alloys tested under impact.

In summary, it has been clearly shown in this study that the mechanical properties of heavy alloys show considerable improvement, particularly impact toughness, if cyclic heat treatment is incorporated in the thermomechanical processing cycle. This is of considerable

technological significance since this will help in the development of superior penetrators without the need to tweak compositions.

### 5. Conclusions

A cyclic heat treatment was incorporated in thermo-mechanical processing of tungsten heavy alloy. Its effect on microstructure and mechanical properties was studied in detail. The conclusions are follows:

1. Microstructural parameters such as contiguity and dihedral angle decreased after cyclic heat treatment. Also, tungsten solubility in the matrix, matrix volume fraction increased with increase in the number of heat treatment cycles.
2. Marginal improvement in tensile properties in heat treated condition was noticed with cyclic heat treatment.
3. The advantages gained following cyclic heat treatments were also retained after swaging treatment.
4. Improvements in mechanical properties were further corroborated by the fractographic features that were associated with lesser instances of W-W decohesion, thereby suggesting more efficient matrix penetration.

### Acknowledgements

Authors convey their sincere gratitude to Dr. S. V. Kamat, Distinguished Scientist & Director, DMRL for encouragement and kind permission to publish this work. Authors gratefully acknowledge the financial support provided by DRDO. They would also like to thank the staff members of Powder Metallurgy Group, DMRL for their help in experimentation. Thanks are also due to Tapan Malik, B.B. Siva Koti, Jitender Reddy, Venkat, Kumar and Sunil for their help in tensile testing, impact, fracture toughness testing, microstructure and machining of samples.

## EFFECT OF CYCLIC HEAT TREATMENT AND SWAGING ON MECHANICAL PROPERTIES OF MOLYBDENUM AND COBALT CONTAINING TUNGSTEN HEAVY ALLOYS

---

### References

1. F.V. Lenel, Metal Powder Industry Federation, Princeton (1980).
2. R.M. German, L.L.Bourguignon, B.H. Rabin, *Powder Metall.*, **5**, 3-13, (1992).
3. R. Gero, D.Chaiat. *Mater. Eng. Conf*, 46-50, (1981).
4. R.M. German, *Sintering Theory and Practice*, Wiley, New York. (1996).
5. S.Pappu, C.Kennedy, L.E. Murr, L.S. Magness, D, Kapoor, *Mater.Sci.Eng. A*, **262**, 115-128, (1999).
6. F.E.Sczerzenie, H.C.Rogers, Hydrogen in metals, ASM, NewYork (1974).
7. L.G. Bazenova, A.D.Vasiljev, R. V. Minakova, V.J.Trefilov, *Powder. Metall. Int.*, **1**, 45-51, (1980).
8. B. Katavic, *Sci. Sinter*, **32**, 153-166, (2000).
9. J.W. Noh, E.P. Kim, H.S. Song, W.H. Baek, K.S. Chum, and S.J.L, Kang, *Metall. Trans. A*, **24 A**, 2411-16, (1993).
10. J.W. Noh, M.H. Hong,G.H.Kim and D.Y.Yoon, *Metall. Trans. A*, **25 A**, 2828-31, (1994).
11. Y.M. Lee, J.Kyung, U.S. Patent, No: 5 294269 (1994).
12. ASTM E23-0a. Standard test methods for un-notched bar impact testing of powder structural parts (2002).
13. J.B.Posthill, M.C.Hogwood, D.V.Edmonds, *Powder Metall*, **29**, 45 (1986).
14. Song et al. U.S Patent No: 5956559 (1999).
15. J.W.Noh, E.P.Kim, H.S.Song, W.H.Baek, K.S.Churn and S. J. L. Kang, *Metall. Trans. A*, **24A**, 2411-16, (1993).
16. R.M.German and L.L.Bourguignon, *Powder Metallurgy in Defence Technology*, **6**, 117-131 (1985).



# FABRICATION OF PLANETARY MILLED NANO-STRUCTURED DUPLEX AND $Y_2O_3$ DISPERSED DUPLEX STAINLESS STEEL MODIFIED CARBON PASTE ELECTRODE FOR THE DETECTION OF DOPAMINE

R. Shashanka<sup>1,2\*</sup>, D. Chaira<sup>2</sup>, B. E. Kumara Swamy<sup>3</sup>

<sup>1</sup>Fluidtherm Technology Private Limited, AIE, Chennai, India

<sup>2</sup>Department of Metallurgical and Materials Engineering, National Institute of Technology Rourkela, India

<sup>3</sup>Department of P. G. Studies and Research in Industrial Chemistry, Kuvempu University, Jnana Sahyadri, Shimoga, Karnataka, India

**Abstract:** Nano structured duplex stainless steel powders were synthesized by mechanical alloying in a specially designed dual drive planetary mill (DDPM). The elemental Fe, Cr and Ni powders were milled in DDPM for 10h. The prepared duplex powders were characterized by X-ray diffraction and scanning electron microscope. In another set of experiment, the prepared duplex stainless steel was dispersed with 1wt. % of  $Y_2O_3$  nanoparticles in a turbula mixer for 3h. Then fabricated a carbon paste electrode (CPE) modified by duplex and  $Y_2O_3$  dispersed duplex stainless steel powder for the detection of neurotransmitter like dopamine (DA). Both the modified carbon paste electrodes showed excellent sensitivity towards the oxidation of DA in 0.2M phosphate buffer solution (PBS) at 7.2 pH. Electrochemical oxidation of dopamine was investigated at 2, 4, 6, 8, 10 and 12mg concentrations of modifier (duplex and  $Y_2O_3$  duplex stainless steel). 4mg duplex and 8mg of  $Y_2O_3$  duplex stainless steel modified carbon paste electrode show maximum anodic peak current of 25.61 and 28.48 $\mu$ A respectively. Therefore, 4mg duplex modified carbon paste electrode (DMCPE) and 8mg yttria dispersed duplex modified carbon paste electrode (YDMCPE) are used as the modifier to study the electrochemical properties of dopamine. We also studied the effect of scan rate, effect of concentration of both modifier and analyte, effect of pH on anodic peak potential by using cyclic voltammetric technique. The anodic peak current obtained was linearly related to DA concentrations in the range of 2mM to 3mM with correlation co-efficient of 0.9614 which reveals the adsorption controlled electrode process. The anodic peak potential of dopamine goes on decreasing with higher pH due to the higher probability of oxidation at higher pH values. The above studies shows that the DMCPE and YDMCPE exhibits resplendent sensitivity towards dopamine and their responses are fast, stable, reliable and resistant to material fouling and this can be applied for the real sample analysis in medical, pharmaceutical and biotechnological sectors. The adsorption-controlled processes and kinetic parameters of the modified electrodes were determined using electrochemical approaches.

**Keywords:** Duplex stainless steel; Cyclic voltammetry; Planetary milling; Dopamine; Electrochemical oxidation; Carbon paste:

## 1. Introduction

Dopamine (DA) is one of the bioactive compounds which play a vital role in animals[1]. The deficiency of DA can cause many severe diseases; hence it is very important to measure the concentration of these bioactive compounds. Electrochemical methods proved to be the better methods to determine the above

bioactive compounds than fluorometric [2, 3], chromatographic[4-6], spectrophotometric[7], chemiluminescent [8,9] and capillary electrophoresis [10]. Cyclic voltammetry is one of the simple, efficient and popular electrochemical methods used to detect DA concentration [11, 12]. Mammalian central nervous system contains naturally occurring catecholamine called DA and it plays a fundamental role in neurotransmission

# FABRICATION OF PLANETARY MILLED NANO-STRUCTURED DUPLEX AND $Y_2O_3$ DISPERSED DUPLEX STAINLESS STEEL MODIFIED CARBON PASTE ELECTRODE FOR THE DETECTION OF DOPAMINE

[13-15]. The deficiency of DA leads to the serious diseases like Schizophrenia and Parkinson's diseases [16]. DA possesses a very strong electrochemical response to its oxidation product dopamine-o-quinone [17]. It is very difficult to detect DA electrochemically in real biological samples due to the coexistence of other bioactive compounds such as Ascorbic acid (AA). The AA exists at a much higher concentration than DA and undergoes oxidation nearly at same potential results in the overlapping of the both the peaks. Therefore we fabricated duplex and yttria dispersed duplex stainless steel modified carbon paste electrodes (YDMCPE) to detect DA and AA individually. But the present paper depicts the investigation of electrochemical sensor application of only DA.

The synthesise of nano structured duplex stainless steel powder by high energy dual drive planetary ball mill (DDPM) and the details of milling parameters, mill fabrication were explained by the authors in their previous publication [18]. The prepared duplex stainless steel powder was mixed with 1wt% of  $Y_2O_3$  nano particles in a turbula mixer for 2h.  $Y_2O_3$  is an air stable solid substance attracted the attention of material researchers due to its crystallographic stability at higher temperature. It possess high mechanical strength, high thermal conductivity, very good protective coating in highly reactive environments [19, 20] and is stable with graphite up to 1600°C [21]. Dispersed  $Y_2O_3$  in duplex stainless steel improves the surface properties of electrode by imparting robust, covalently bound, hydrolytically stable layer, which is capable of being functionalised easily [22]. This results in the free movement of electrons between carbon paste and electrolytes.

Till now, only dyes, surfactants and polymer based modified carbon paste electrodes are reported. No literature is available so far

related to yttria dispersed duplex stainless steel modified carbon paste electrodes to detect DA concentration. Shashanka et al. investigated the electrocatalytic detection of folic acid by using duplex and yttria dispersed duplex stainless steel [23]. They studied the electro catalytic response of yttria dispersed and yttria free duplex stainless steel modified carbon paste electrode with respect to bare carbon paste electrode (BCPE). They reported that yttria dispersed modified carbon paste electrode (YDMCPE) shows better electro catalytic response in oxidising DA compared to duplex modified carbon paste electrode (DMCPE) and BCPE. Hence YDMCPE and DMCPE were found to be a suitable sensor for the determination of DA.

## 2. Experimental part

### 2.1. Reagents and chemicals

Fe (99.5% pure), Cr (99.8% pure) and Ni (99.5% pure) elemental powders were purchased from loba chemicals and  $Y_2O_3$  (99.99%) was purchased from Alfa Aesar. Dopamine, perchloric acid, sodium dihydrogen orthophosphate dehydrate and di-sodium hydrogen phosphate anhydrous of analytical grade quality was purchased from sd. Fine chemicals. All the above reagent solutions were prepared by dissolving in double distilled water. Graphite powder was purchased from Merck chemicals.

### 2.2. Apparatus

Milling of elemental Fe, Cr and Ni powders of duplex stainless steel composition (Fe-18Cr-13Ni) were carried out in a specially designed DDPM. Carbon paste electrode and duplex stainless steel powder morphology was characterized by scanning electron microscopy (SEM) using JEOL JSM-6480LV. X-ray diffraction (XRD) was carried out in PAN analytical Xpert Pro XRD. The particle size was measured by

# FABRICATION OF PLANETARY MILLED NANO-STRUCTURED DUPLEX AND $Y_2O_3$ DISPERSED DUPLEX STAINLESS STEEL MODIFIED CARBON PASTE ELECTRODE FOR THE DETECTION OF DOPAMINE

Malvern Mastersizer. The duplex stainless steel powders were mixed separately with 1wt. % nano structured  $Y_2O_3$  powder particles by turbula shaker mixture (TURBULA® T2F, Willy A. Bachofen AG Maschinenfabrik, Switzerland) for 2hours. The electrochemical experiments were carried out using electrochemical work station CHI-660c model. All the experiments were carried out in a conventional three electrode system composed of working electrode (carbon paste electrode of 3mm diameter), a platinum wire as counter electrode and Ag/AgCl saturated KCl electrode as reference electrode. The pH of the buffer solutions was measured with the digital pH meter MK VI.

## 2.3 Preparation of Duplex stainless steel powders by DDPM

The elemental Fe, Cr and Ni powders of duplex stainless steel composition (Fe-18Cr-13Ni) is milled in DDPM for 10h using toluene to prevent oxidation. The composition of duplex stainless steel (Fe-18Cr-13Ni) is selected from Schaeffler diagram. The milling media consist of 1kg stainless steel balls of diameter 8mm and ball-to-powder weight ratio of 6:1 are maintained. The angular velocity of the jars and the supporting main shaft are kept at 620 and 275 rpm respectively. The detailed synthesis and mill fabrication part was explained elsewhere [18] by the author. The prepared duplex stainless steel powder sample is mixed with 1wt. % nano structured  $Y_2O_3$  powder particles by turbula shaker mixture.

## 2.4 Fabrication of the carbon paste electrode

The graphite powder and silicon oil are mixed in an agitate mortar at a ratio of 70:30 for 30minutes to prepare bare carbon paste electrode (BCPE). DMCPE and YDMCPE can be fabricated by hand mixing of duplex and yttria dispersed

duplex stainless steel powder individually with 70:30 ratio of graphite powder and silicone oil using mortar pestle. The homogeneous carbon paste electrode was packed into a cavity of carbon paste electrode of 3mm diameter. The YDMCPE was prepared by mixing 2, 4, 6, 8, 10 and 12mg of yttria dispersed duplex stainless steel powder individually along with graphite powder and silicon oil. After packing in to the cavity of electrode, the surface was smoothed by rubbing slowly on a piece of weighing paper. At the tube end, the electrical contact was provided by copper wire which is directly connected to the paste. The BCPE was prepared by without adding modifier.

## 3. Results and discussion

### 3.1 X-Ray Diffraction study

Fig. 1 depicts the XRD spectra of 0h and 10h milled duplex and yttria dispersed duplex stainless steel powders. At 0h, the XRD spectra of duplex stainless steel show crystalline and very sharp diffraction peaks of individual Fe, Cr and Ni elements. As milling starts Cr and Ni goes in to the solid solution of Fe and results in the disappearance of individual elemental peaks. Milling of duplex composition in high energy DDPM results in maximum defects, internal strain and highly refined grain size. Author explained the effect of milling time on lattice strain, grain size, lattice parameter in detail in their previous publications [24, 25]. Lattice strain and lattice parameter goes on increasing with increase in milling time. After 10h of milling, all the diffraction peaks of duplex stainless steel are broadened due to the interstitial diffusion of Cr and Ni atoms, presence of more defects, strains and decrease in the grain size. It is found that there is no much appreciable difference in the phases of yttria dispersed and yttria free duplex stainless steel.

**FABRICATION OF PLANETARY MILLED NANO-STRUCTURED DUPLEX AND  $Y_2O_3$  DISPERSED DUPLEX STAINLESS STEEL MODIFIED CARBON PASTE ELECTRODE FOR THE DETECTION OF DOPAMINE**

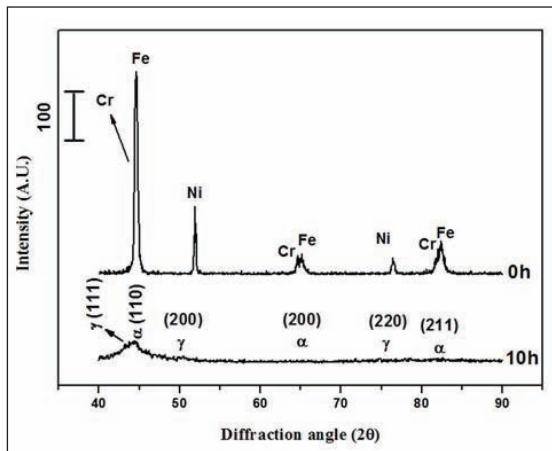


*Fig. 1 XRD spectrum of Fe-18Cr-13Ni (duplex stainless steel composition) milled for 0h and 10h respectively*

### 3.2 Microstructure study

Fig. 2 (a) and 2 (b) shows the SEM images of duplex stainless steel milled for 0h and 10h in DDPM. The particles are irregular and large before milling and become spherical and small after 10h as shown in the SEM microstructures. During milling the particles undergo flattening, repeated welding; plastic deformation and fragmentation to form very fine duplex stainless steel powder particles. Final powders show some river like structures due to the diffusion of Cr and Ni atoms in to the Fe lattice. SEM images of BCPE and YDMCPE is represented in fig. 2 (c) and 2 (d) respectively and we studied the topography of carbon paste electrode. SEM microstructure of BCPE depicts irregular surface due to the graphite flakes, but YDMCPE electrode surface is flat and regular shape with graphite flakes. This surface difference is due to the use of modifier and results in easy movement of electrons from carbon paste to electrolyte and vice versa.

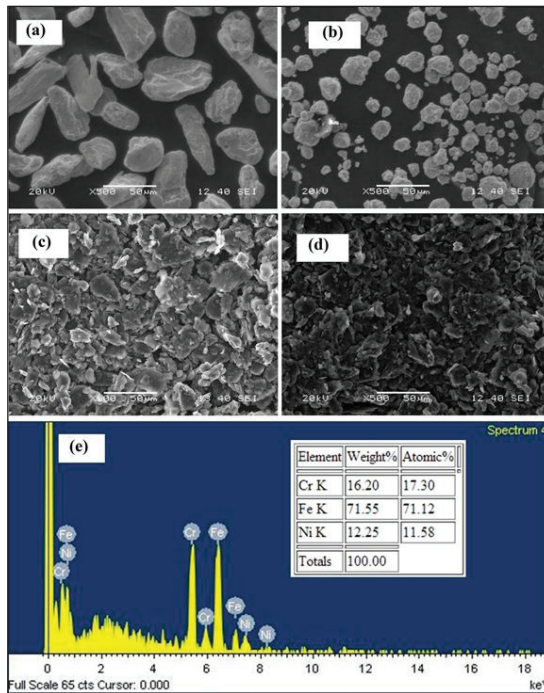


*Fig. 2 SEM micrographs of duplex stainless steel powder milled for (a) 0h (b) 10h (c) SEM image of BCPE (d) SEM image of YDMCPE (e) EDX spectra of duplex stainless steel after 10h*

EDX was carried out to study the quantitative and qualitative analysis of 10h milled duplex stainless steel as shown in fig. 2 (e). From the EDX analysis it is confirmed that there is no much difference in the chemical compositions of 0h and 10h milled duplex stainless steel powder.

### 3.3 Particle size analysis

Properties of the materials vary as the particle size changes hence it is very important to know the size of the particles. The quality, performance, flow and compaction properties of any materials depend upon the size and shape of the powder particles [26]. Fig. 3 represents the particle size distribution of duplex stainless steel powder milled in DDPM for 0h and 10h. As milling progress, the cumulative size distribution curves

# FABRICATION OF PLANETARY MILLED NANO-STRUCTURED DUPLEX AND $Y_2O_3$ DISPERSED DUPLEX STAINLESS STEEL MODIFIED CARBON PASTE ELECTRODE FOR THE DETECTION OF DOPAMINE

shift towards left side indicating the refinement and reduction of powder particles. From the graph it is confirmed that particle size of duplex stainless steel powder decreases with increase in milling time. The initial median particle size is around  $80\mu\text{m}$  and decreases with increase in milling time and becomes  $14\mu\text{m}$  after 10h.

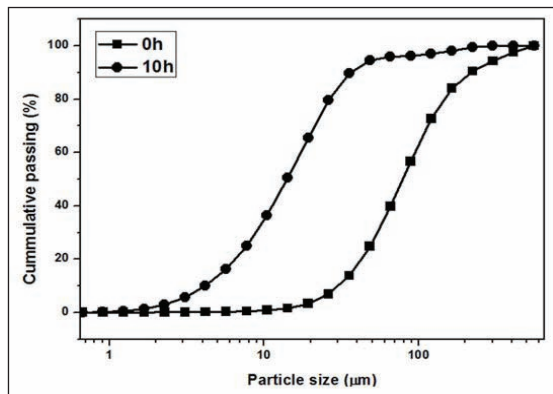


Fig. 3 Median particle size of duplex stainless steel powder at 0 and 10h

## 3.4 Electro catalytic response of DA at DMCPE

### 3.4.1 Concentration variation of nano structured duplex stainless steel powder

One of the important parameter is the study of effect of different concentrations of modifier, which decides the efficiency of the electrode performance as a sensor. In the present work, we fabricated nanostructured duplex stainless steel powder as a modifier to study the electrochemical behaviour of DA. The concentration of duplex stainless steel is varied from 2 to  $8\text{mg}$  to study the electro catalytic behaviour of  $2\text{mM}$  DA in  $0.2\text{M}$  phosphate buffer (pH 7.2) at sweep potential from  $-200$  to  $600\text{mV}$  and scan rate of  $100\text{mVs}^{-1}$ . Among 2, 4, 6 and  $8\text{mg}$  concentration of DMCPE,  $4\text{mg}$  DMCPE had shown maximum anodic peak current of  $25.61\mu\text{A}$ .

Fig. 4 (a) shows a plot of variation of anodic peak currents with different concentration of duplex stainless steel. From the plot it is clear

that anodic peak current increases with modifier concentration up to  $4\text{mg}$  and then decreases with further increase in the concentration. This is due to the resultant decrease in actual electrode area and reduced number of oxidation sites in the electrode surface [27]. Therefore modifier is used to enhance the peak current and to decrease the over potential for the oxidation and reduction of DA. Duplex stainless steel satisfies the above conditions and hence used as a modifier in the present work. Fig. 4 (b) shows the cyclic voltammogram of bare carbon paste electrode (BCPE) and  $4\text{mg}$  DMCPE. The dotted curve and straight line curve voltammograms represent the  $2\text{mM}$  DA at BCPE and DMCPE respectively. The anodic peak current of BCPE is  $13.95\mu\text{A}$  and that of DMCPE is  $25.61\mu\text{A}$ . Hence  $4\text{mg}$  DMCPE is selected as the modifier for the further determination of DA.

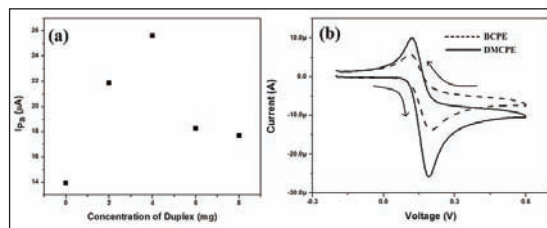


Fig. 4 (a) Plot of anodic peak currents with different concentration of duplex stainless steel in  $2\text{mM}$  DA (b) Cyclic voltammogram of bare carbon paste electrode (BCPE) and  $4\text{mg}$  DMCPE in  $2\text{mM}$  DA at  $100\text{mVs}^{-1}$  and in PBS of pH 7.2

### 3.4.2 Effect of scan rate

The effect of scan rate from  $50$  to  $500\text{mVs}^{-1}$  for  $2\text{mM}$  DA in phosphate buffer solution (PBS) of pH 7.2 is investigated. Scan rate is an important parameter to study the kinetics of the electrode reaction. Fig. 5 (a) shows the voltammogram of DA at  $4\text{mg}$  DMCPE. From the figure it is clear that, increase in scan rate from  $50$  to  $500\text{mVs}^{-1}$  increases the anodic peak current of DA due to the direct electron transfer between DA and the modified electrode surface. Fig. 5 (b) shows the plot of anodic peak current vs. scan rate; their

## FABRICATION OF PLANETARY MILLED NANO-STRUCTURED DUPLEX AND $Y_2O_3$ DISPERSED DUPLEX STAINLESS STEEL MODIFIED CARBON PASTE ELECTRODE FOR THE DETECTION OF DOPAMINE

correlation coefficient is found to be 0.9924. Similarly Fig. 5 (c) depicts the plot of anodic peak current vs. square root of scan rate and its correlation coefficient is 0.9488. Hence all the electrode process is found to be adsorption controlled.

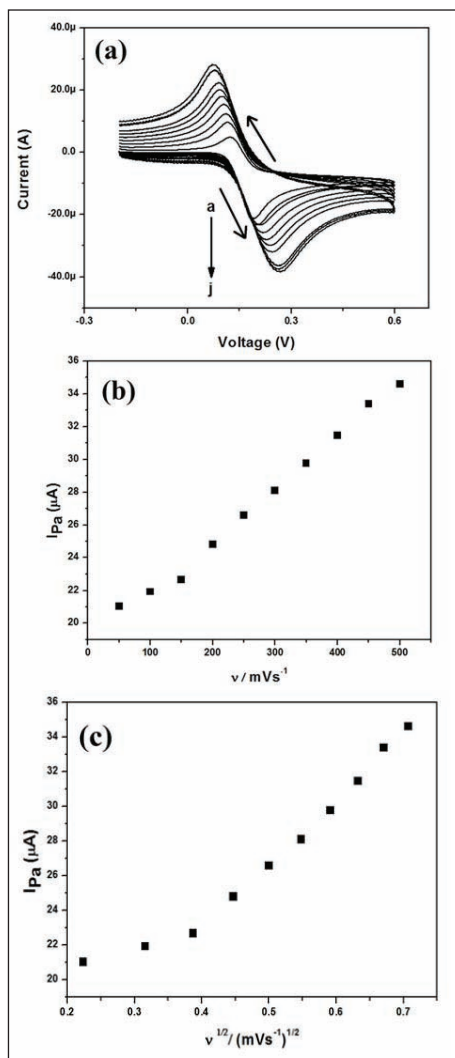


Fig. 5 (a) Cyclic voltammogram of 2mM DA at 50 to 500mVs<sup>-1</sup> scan rate (a=50, b=100, ....., j=500mVs<sup>-1</sup>) in PBS of pH 7.2 (b) Plot of anodic peak current vs scan rate (c) Plot of anodic peak current vs. square root of scan rate

### 3.4.3 Effect of Dopamine concentration

Generally, anodic peak current increases with increase in the concentration of DA. Electrochemical response of DA at 2 to 3mM concentration is studied by using 4mg DMCPE. The voltammogram of different concentration of DA is shown in the fig. 6 (a). From the figure it is clear that increase in DA concentration increases the anodic peak current. Fig. 6 (b) shows the plot of anodic peak current vs. different concentration of DA. Plot depicts the linear relationship between peak current and concentration of DA with correlation coefficient of 0.9614. Anodic peak current at 2 and 2.1mM DA concentration show linear relationship but from 2.1 to 2.3mM there is no much increase in current and from 2.3 to 3mM DA concentration, the current increases linearly as shown in the plot. The anodic peak current at 2mM DA is 15.51 $\mu A$  and at 3mM DA concentration is increased to 19.10 $\mu A$ .

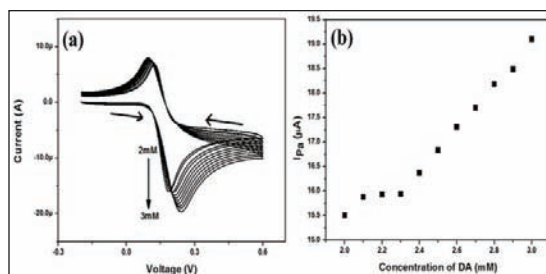


Fig. 6 (a) Cyclic voltammogram of 2 to 3mM concentration of DA at 100mVs<sup>-1</sup> in PBS of pH 7.2 (b) Plot of anodic peak current vs. different concentration of DA

### 3.4.4 Effect of pH

The effect of pH variation on the peak potential of DA is studied successfully using 4mg DMCPE at 0.2M phosphate buffer solution with scan rate of 100mVs<sup>-1</sup>.

# FABRICATION OF PLANETARY MILLED NANO-STRUCTURED DUPLEX AND $Y_2O_3$ DISPERSED DUPLEX STAINLESS STEEL MODIFIED CARBON PASTE ELECTRODE FOR THE DETECTION OF DOPAMINE

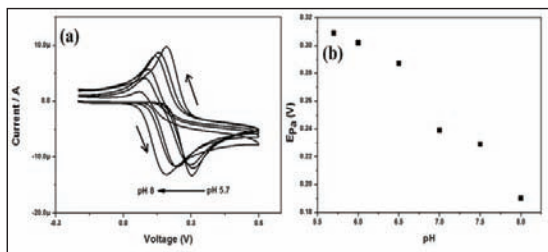


Fig. 7 (a) Cyclic voltammogram of 2mM DA at different pH of PBS buffer solutions at 100mVs<sup>-1</sup> (b) Plot of anodic peak current vs. different pH from values 5.7 to 8

The anodic peak potential of 2mM DA is measured at different pH from 5.7 to 8. The voltammogram of different pH is shown in Fig. 7 (a). From the figure it is clear that, both anodic and cathodic peak potentials of DA are shifted to a lower potential side with increase in pH. This is due to the increased rate of DA oxidation at higher pH. The graph shows good linearity and it obeys the Nernst Equation for equal number of electron and proton transfer reactions. Fig. 7 (b) represents the plot of pH vs. anodic peak potential of DA. Anodic peak potential gradually decreases from pH 5.7 to 8 with correlation coefficient of 0.9574. At pH 5.7 the oxidation peak potential is 309mV and at pH 8 it is decreased to 190mV as shown in the plot.

## 3.5 Electro catalytic response of DA at YDMCPE

### 3.5.1 Concentration variation of yttria dispersed duplex stainless steel powder

The efficiency of the electrode sensor depends upon optimum concentration of modifier. Hence it is very important to measure the redox current at optimum concentration level of modifier. We studied the effect of different concentrations of yttria dispersed and yttria free duplex stainless steel powder on the anodic peak current of 2mM DA. The yttria dispersed duplex stainless steel

powder concentration has been varied from 2mg to 12mg to study the electrochemical response of 2mM DA in 0.2M phosphate buffer solution (PBS) of pH 7.2 at sweep potential from -200 to 600mV and scan rate of 100mVs<sup>-1</sup>. Fig. 8 (a) depicts the plot of anodic peak current with different concentrations of yttria dispersed duplex stainless steel. Among all, 8mg YDMCPE shows better electro catalytic response to oxidise 2mM DA. From the voltammogram it is clear that oxidation peak current increases with the increase in the concentration of modifier up to 8mg and then decreases with further increase in the concentration. This is due to the decrease in the number of oxidation sites in the paste and resultant reduction in the actual electrode area [28]. In case of yttria free duplex stainless steel, 4mg DMCPE shows maximum anodic peak current in detecting 2mM DA.

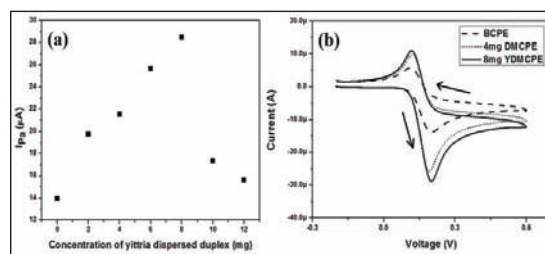


Fig. 8 (a) Plot of anodic peak currents with different concentration of yttria dispersed duplex stainless steel in 2mM DA (b) Cyclic voltammogram of bare carbon paste electrode (BCPE), 4mg DMCPE and 8mg YDMCPE in 2mM DA at 100mVs<sup>-1</sup> and in PBS of pH 7.2

Fig. 8 (b) shows the cyclic voltammogram of bare carbon paste electrode (BCPE), 4mg DMCPE and 8mg YDMCPE at 2mM DA in 0.2M phosphate buffer of pH 7.2 at a scan rate of 100mVs<sup>-1</sup>. The anodic peak current of BCPE is 13.95µA, 4mg DMCPE is 25.61µA and 8mg YDMCPE is 28.48µA. YDMCPE shows maximum anodic peak current than DMCPE due to the presence of  $Y_2O_3$  nanoparticles. The  $Y_2O_3$  nanoparticles

# FABRICATION OF PLANETARY MILLED NANO-STRUCTURED DUPLEX AND $Y_2O_3$ DISPERSED DUPLEX STAINLESS STEEL MODIFIED CARBON PASTE ELECTRODE FOR THE DETECTION OF DOPAMINE

improve the surface properties of electrode and increase the bonding strength between carbon paste electrode and the modifier. Thereby increases the free movement of electrons between carbon paste electrode and electrolytes. Hence 8mg YDMCPE is selected as the modifier for the further determination of DA.

### 3.5.2 Effect of scan rate

Scan rate is varied from 50 to 500mVs<sup>-1</sup> in PBS of pH 7.2 to study the electrochemical behaviour of 2mM DA. The effect of scan rate is an important parameter which controls the kinetics of surface electrode reactions. Fig. 9 (a) shows the voltammogram of DA in 8mg YDMCPE at different scan rates. From the figure it is clear that the redox peak current increases linearly with increase in the scan rate. This is due to the direct electron transfer between DA and the modified carbon paste electrode surface. Increase in scan rate also increases anodic and cathodic peak potential difference [29]. The plot of anodic peak current vs scan rate is shown in the fig. 9 (b) and the plot shows linear relation between oxidation peak current and scan rate with correlation coefficient 0.9654. Similarly Fig. 9 (c) depicts the plot of anodic peak current vs. square root of scan rate and its correlation coefficient is 0.9040. This confirms the electrode process is adsorption controlled [30].

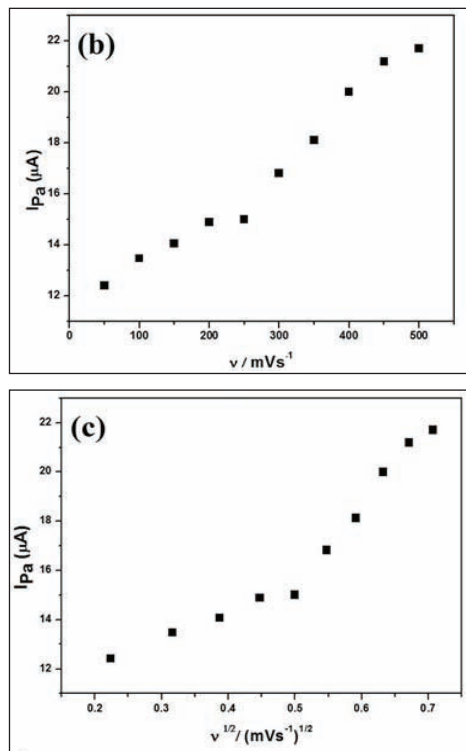
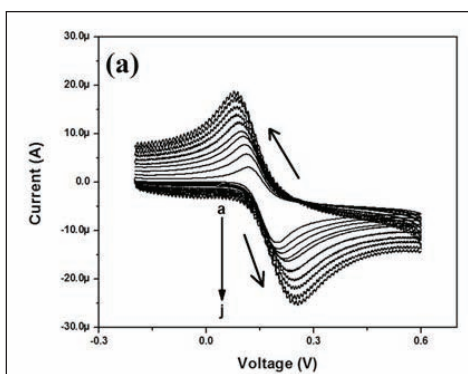


Fig. 9 (a) Cyclic voltammogram of 2mM DA at 50 to 500mVs<sup>-1</sup> scan rate ( $a=50, b=100, \dots, j=500mVs^{-1}$ ) in PBS of pH 7.2 (b) Plot of anodic peak current vs. scan rate (c) Plot of anodic peak current vs. square root of scan rate

### 3.5.3 Effect of Concentration of Dopamine

Usually anodic peak current increases with increase in the analyte concentration. Therefore we can expect the similar trend during electrochemical response of DA at 2 to 3mM concentration using 8mg YDMCPE at scan rate of 100mVs<sup>-1</sup>. Fig. 10 (a) represents the cyclic voltammogram at different concentration of DA. From the voltammogram it is confirmed that anodic peak current increase with increase in concentration of DA. A plot of anodic peak current vs different concentration of DA is as shown in the Fig. 10 (b). Plot depicts the linear

# FABRICATION OF PLANETARY MILLED NANO-STRUCTURED DUPLEX AND $Y_2O_3$ DISPERSED DUPLEX STAINLESS STEEL MODIFIED CARBON PASTE ELECTRODE FOR THE DETECTION OF DOPAMINE

relationship between different concentration of DA and oxidation peak current with correlation coefficient of 0.9668. At a concentration of 2 to 2.2mM DA, the anodic peak current do not show linear relationship but from 2.2 to 3mM anodic peak current increases linearly as shown in the plot. The anodic peak current at 2mM DA is  $21.86\mu A$  and at 3mM DA concentration it increased to  $26.04\mu A$ .

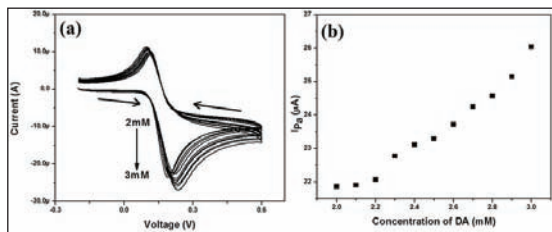


Fig. 10 (a) Cyclic voltammogram of 2 to 3mM concentration of DA at  $100mVs^{-1}$  in PBS of pH 7.2 (b) Plot of anodic peak current vs. different concentration of DA

## 3.5.4 Effect of pH

Variation of pH values in buffer solution plays a very important role in determining the stability, selectivity and sensitivity of carbon paste electrodes. Hence selection of optimum pH solution increases the electrode performance. Therefore we studied the effect of pH variation on the peak potential of 2mM DA using 8mg YDMCPE at 0.2M phosphate buffer solution with scan rate of  $100mVs^{-1}$ . The anodic peak potential of 2mM DA is measured at different pH from 5.7 to 8 and their voltammograms are shown in Fig. 11 (a). From the voltammogram it is clear that anodic peak potential of 2mM DA is shifted to a lower potential side with the increase in pH. This is due to the enhanced rate of oxidation at higher pH values. Cathodic peak potential also shift towards the lower potential side with increase in pH value but the rate of shift is very less. Anodic peak current goes on increasing with

increase in the pH values due to the higher rate of oxidation at maximum pH. The higher rate of oxidation generates more number of electrons and the generation of more electrons increases the anodic peak current. Fig. 11 (b) represents the plot of pH vs anodic peak potential at 2mM DA. From the plot it is confirmed that anodic peak potential gradually decreases from pH 5.7 to 8 with correlation coefficient of 0.9858. The oxidation peak potential at pH 5.7 is 315mV and starts decreasing linearly to 180mV at pH 8. The graph has good linearity and it nearly obey the Nernst Equation for equal number of electron and proton transfer reactions [31].

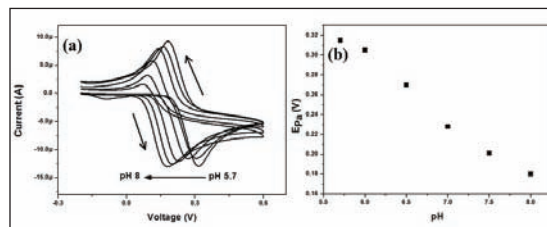


Fig. 11 (a) Cyclic voltammogram of 2mM DA at different pH of PBS buffer solutions at  $100mVs^{-1}$  (b) Plot of anodic peak current vs. different pH from values 5.7 to 8

## 4. Conclusion

The following conclusions can be made from the present investigation:

- Successfully prepared duplex stainless steel powder by DDPM milled for 10h and the powder was characterized through XRD, SEM and particle size analysis.
- The prepared powder was mixed with 1wt. % nano structured  $Y_2O_3$  powder particles by turbula shaker mixture for 2h.
- 8mg YDMCPE show strong electro catalytic activity towards the oxidation of DA than 4mg DMCPE.

# FABRICATION OF PLANETARY MILLED NANO-STRUCTURED DUPLEX AND $Y_2O_3$ DISPERSED DUPLEX STAINLESS STEEL MODIFIED CARBON PASTE ELECTRODE FOR THE DETECTION OF DOPAMINE

- Both DMCPE and YDMCPE can be used as sensor in medical field for the diagnosis of DA deficiency diseases.
- All the electrode reactions at the DA are adsorption controlled reactions.
- Although we reported very efficient YDMCPE as a sensor for detecting DA, there is still a need for further research to scale-up the issues.
- There is always a plenty of scope to fabricate sensitive, selective and material fouling resistant electrodes. YDMCPE satisfy the above needs with excellent performance.

## Acknowledgements

Financial support for this work from the Council of Scientific & Industrial Research (CSIR), India (Grant No. 22/561/11/EMR II Dated 11.04.2011) is gratefully acknowledged.

## References

1. R. Shashanka, B.E. Kumara Swamy, S. Reddy, D. Chaira, "Bestimmung des mophins im opium", *Anal Bioanal Electrochem*, **5**, 455-466, (2013)
2. Z. Wang, Y. Wang, G. Luo, *Analyst*, **127**, 1353-1358, (2002).
3. D. Martin-Perez, M.L. Ferrer, C.R. Mateo, *Anal Biochem*, **322**, 238-242, (2003).
4. K. Innoue, T. Namiki, Y. Iwesaki, Y. Yoshimora, H.J. Nakazawa, *J Chromatogr B*, **785**, 57-63, (2003).
5. S. Sarre, Y. Michotte, P. Herregodts, D. Deleu, N. D. Klippel, G. Ebinger, *J Chromatogr B*, **575**, 207-212, (1992).
6. C.L. Guan, J. Ouyang, Q. L. Li, B.H. Liu, W. R. G. Baeyens, *Talanta*, **50**, 1197-1203, (2000).
7. M.C.C. Tullia, Filisetti-Cozzi, Nicholas C. Carpita, *Anal Biochem.*, **197**, 157-162, (1991).
8. C. Zhang, J. Huang, Z. Zhang, M. Aizawa, *Anal Chim Acta.*, **374**, 105-110, (1998).
9. H.C. Hong, H.J. Huang, *Anal Chim Acta.*, **499**, 41-46, (2003).
10. Y. Guan, Q. Chu, J. Ye, "Determination of uric acid in human saliva by capillary electrophoresis with electrochemical detection: potential application in fast detection of gout", *Anal Bioanal Chem.*, **380**, 913-917, (2004).
11. R. Raghavendra Naik, E. Niranjana, B.E. Kumara Swamy, B.S. Sherigara, H. Jayadevappa, *Int J Electrochem Sci.*, **3**, 1574-1583, (2008).
12. Ongera Gilbert, B.E.Kumara Swamy, Umesh Chandra, B.S.Sherigara, *Int J Electrochem Sci.*, **4**, 582-591, (2009).
13. R.M. Wightman, L. J. May, A.C. Michael, *Anal Chem.*, **60**, 769A-779A, (1988).
14. B. J. Venton, R. M. Wightman, *Anal Chem.*, **75**, 414A-421A, (2003).
15. R.D. O'Neill, *Analyst*, **119**, 767-779, (1994).
16. O. Gilbert, U. Chandra, B.E. Kumara Swamy, M. Panduranga Char, C. Nagaraj, B.S. Sherigara, *Int J Electrochem Sci.*, **3**, 1186-1195, (2008).
17. S. S. Shankar, B. E. Kumara Swamy, B. N. Chandrashekar, K. J. Gururaj, *Chemical Sensors*, **2**, 1-7, (2012).
18. R. Shashanka, D. Chaira, *Powder Tech.*, **259**, 125-136, (2014).
19. Z.M. Larimi, A. Amirabadizadeh, A. Zelati, International Conference on Chemistry and Chemical Process IPCBEE, IACSIT Press, Singapore. 10, 86-90, (2011).
20. T. Gougousi, Z. Chen, *Thin Solid Films*, **516**, 6197-6204, (2008).
21. P.V.A. Padmanabhan, S. Ramanathan, K.P. Sreekumar, R.U. Satpute, *Mater Chem Phys.*, **106**, 416-421, (2007).
22. C.A. Traina, J. Schwartz, "Surface Modification of  $Y_2O_3$  Nanoparticles", *Langmuir*, **23**, 9158-9161, (2007).
23. R. Shashanka, D. Chaira, B.E. Kumara Swamy, *Int. J. Electrochem. Sci.*, **10**, 5586 - 5598, (2015).

**FABRICATION OF PLANETARY MILLED NANO-STRUCTURED DUPLEX AND  $Y_2O_3$   
DISPERSED DUPLEX STAINLESS STEEL MODIFIED CARBON PASTE ELECTRODE FOR  
THE DETECTION OF DOPAMINE**

---

24. R. Shashanka, D. Chaira, *Powder Technol.*, **278**, 35-45, (2015).
25. R. Shashanka, D. Chaira, *Mater Charact.*, **99**, 220-229, (2015).
26. T. Allen, *Particle Size measurement*, 5th Edition, Volume 1. Chapman and Hall, (1997).
27. R. Shashanka, D. Chaira, B.E. Kumara Swamy, *Int. J. Sci. Engg. Res.*, **6**, 1863-1871, (2015).
28. J.G. Manjunatha, B.E. Kumara Swamy, G.P. Mamatha, O. Gilbert, M.T. Shreenivas, B.S. Sherigara, *Int. J. Electrochem. Sci.*, **4**, 1706-1718, (2009).
29. J.G. Manjunatha, B.E. Kumara Swamy, R. Deepa, V. Krishna, G.P. Mamatha, Umesh Chandra, S. Sharath Shankar, B.S. Sherigara, *Int. J. Electrochem. Sci.*, **4**, 662-671, (2009).
30. K.R. Mahanthesha, B.E. Kumara Swamy, *J. Electroanal. Chem.*, **703**, 1-8, (2013).
31. S. Mahshid, C. Li, S.S. Mahshid, M. Askari, A. Dolati, L. Yang, S. Luo, Q. Cai, *Analyst*, **136**, 2322-2329, (2011).



# SYNTHESIS AND EVALUATION OF MECHANICAL BEHAVIOR OF MA 6061Al- $\text{Al}_2\text{O}_3$ NANOCOMPOSITE

Nitika Kundan, Arpit Khemka, P. R. Soni

Department of Metallurgy and Materials Engg.  
Malaviya National Institute of Technology, Jaipur, India

**Abstract :** In the present work, 6061Al powder with varying (1-5 wt.%) of  $\text{Al}_2\text{O}_3$  nanoparticles is processed optimally mechanically alloyed in a Sezgavari high energy mill in nitrogen atmosphere. After degassing, the mechanically processed powder samples were consolidated by hot pressing at 460°C under a pressure of 120MPa and were given heat treatment (T6). The prepared samples were then characterized for their microstructure using transmission electron microscopy. The nano  $\text{Al}_2\text{O}_3$  particles were found to be uniformly distributed in the matrix. The matrix grains were found to be submicron size. The interface was clean and free of residual stresses. The tensile strength and % elongation were found to decrease with increasing wt.%  $\text{Al}_2\text{O}_3$  nanoparticles. In all the cases the nanocomposite fracture was ductile in nature. It could be possible to increase the hardness to the level of 251HB, by an improvement of over 100% as compared to 6061 Al-T6 matrix. Aim of the investigations was to prepare a 6061 Al- T6 based nanocomposite with sufficient ductility as these nano composites have drawback of brittleness.

**Keywords:** mechanical alloying, 6061Al powder,  $\text{Al}_2\text{O}_3$  nanoparticles, heat treatment, nanocomposites

## 1. Introduction

Material competition in the automotive industry has been traditionally intensive. Steel has been the dominant material used in building automobiles since the 1920s [1]. Weight reduction is particularly important because average vehicle weight is expected to increase since the automobile industry will continue to market new models with increased luxury, convenience, performance, and safety as demanded by their customers. The use of lightweight materials can help reduce vehicle weight and improve fuel economy. In particular, the most interesting metals for industrial applications are Al [2-10], Mg [11-14] and their alloys.

Aluminium, the second most plentiful metallic element on earth, became an economic competitor in engineering applications as recently as the end of the 19th century [15]. Aluminium is remarkable due to its low density and ability to resist corrosion due to the phenomenon of

passivation. Increased demand for light weight components, primarily driven by the need to reduce energy consumption in a variety of societal and structural components, has led to increased use of aluminum.

Nanocomposite is a multiphase solid material where one of the phases has one, two or three dimensions of less than 100 nanometers (nm) [16], or structures having nano-scale repeat distances between the different phases that make up the material. In recent years, synthesis and application of nanostructured materials have received a great attention, because of their superior mechanical properties compared with coarse-grained counterparts [17, 18]. Metal matrix nanocomposites (MMNCs) have inherent high temperature stability, high strength, high modulus, wear resistance, and thermal and electrical conductivity over the polymeric composited. MMNCs can be synthesized by various processes such as powder metallurgy, deformation processing, vapor phase processing,

# SYNTHESIS AND EVALUATION OF MECHANICAL BEHAVIOR OF MA 6061Al-Al<sub>2</sub>O<sub>3</sub> NANOCOMPOSITE

and in some cases solidification processing. These composites are also known for improvement in their properties by relatively very small addition of the nano dispersoids. However, these composites have drawback of having very low ductility due to which they are very brittle. It puts major hurdle in their uses in many engineering applications [19]

The mechanical alloying (MA) process, using ball-milling and/or rod-milling techniques, has received much attention as a powerful tool for fabrication of several advanced materials including equilibrium, nonequilibrium (e.g., amorphous, quasicrystals, nanocrystalline, etc.), and composite materials [20, 21, 22], and more recently the nanocomposites. The MA technique is known for providing a uniform distribution of alloying elements/ reinforcement particles in the matrix powder [23].

In the present work, 6061 Al alloy powder along with 1-5 wt. % of nano-Al<sub>2</sub>O<sub>3</sub> particles was optimally mechanically alloyed to get uniform distribution of dispersoids but preserve the matrix ductility. The composite powder was then consolidated by hot pressing to evaluate its mechanical behaviour. The aim of the present studies was to develop 6061 Al based nanocomposite with sufficient ductility to be used for engineering applications.

## 2. Experimental Procedure

In the present work, atomized 6061 aluminum alloy powder (size~44µm, procured from the M/S EKCA Granulate Veldem GmbH, Germany) and Al<sub>2</sub>O<sub>3</sub> nanopowder (size~50nm, procured from the Sigma Aldrich) were used. The chemical composition of 6061Al is given in Table 1.

*Table 1: Chemical composition of 6061Al powder*

Component	Al	Mg	Si	Fe	Cu	Zn	Ti	Mn	Cr	others
wt. %	Balance	0.8-1.2	0.4-0.8	Max.0.7	0.15-0.40	Max.0.25	Max.0.15	Max.0.15	0.04-0.35	0.05

6061Al alloy powder with varying (1-5%) wt% of Al<sub>2</sub>O<sub>3</sub> nanoparticles was mechanically alloyed in laboratory attrition mill for 2h at a rotation speed of 350 rpm in an inert atmosphere of purified nitrogen atmosphere to prevent the oxidation. Hardened steel balls of diameter 10 mm were used as milling media. Acrowax C (1 wt %) was used as process controlled agent. The weight ratio of the powder to that of milling media was kept 1:10. The MA powder was then degassed for 2h in a vacuum oven (10-1 torr) at 200°C. Particle size and size distribution in the powders was carried out using Mastersizer 2000 particle size analyzer.

Powder was then characterized by x-ray diffraction (XRD) technique using P' analytical X Pert Pro X-ray diffraction unit with Cu Kα radiation (kα =0.1542nm) to access the grain size in it. Powders were also studied using FEI-NOVA NANOSEM-450 SEM for their morphology.

Consolidation of the powder samples was done by hot pressing at temperature of 460°C under pressure of 120MPa for 30 minutes. Specimens of 40 x 10 x 5 (all dimensions in mm) were prepared.

The hot pressed specimen were then heat treated for precipitation hardening. It involved two steps – solution heat treating and aging. Solution heat treatment was done by raising the samples temperature to 580°C in a muffle furnace and holding it there for 1h. The artificial ageing of these specimen was then done by T6 tempering by reheating the samples to the temperature of 180°C in a muffle furnace for 4h in air atmosphere [24].

Transmission electron microscopy of these specimen was carried out to study microstructural details and access the grain size. Tensile behavior was studied using a Tinius oisen tensometer and Brinell hardness was measured.

## 3. Results and Discussion

### 3.1 Mechanical alloying

SEM micrographs of MA powder (Fig 1(c-g)) show flake type structure. These micrographs basically show semi-mechanically alloyed powders due

# SYNTHESIS AND EVALUATION OF MECHANICAL BEHAVIOR OF MA 6061Al- $\text{Al}_2\text{O}_3$ NANOCOMPOSITE

to optimal mechanical alloying period of 2h. (If mechanical alloying is carried out beyond 2h the matrix becomes nanostructured making it very brittle [25]). It is quite likely that many of the nanoparticles may have got embedded on the surfaces of these flakes leading to less risk of agglomeration during further handling (for vacuum degassing, filling in die, etc) of the composite powder.

The average particle size in MA powder samples, as obtained by Mastersizer 2000, (given in Table 2) show an increase in particle size after MA processing, which may be due to the flaky shape obtained by the spherical shaped 6061 Al powder (as received). A look on the size distribution curves (Fig 2), show that powder is tending to achieve bimode distribution due to two modes of milling (steel balls and nanoballs particles of  $\text{Al}_2\text{O}_3$  particles) working simultaneously.

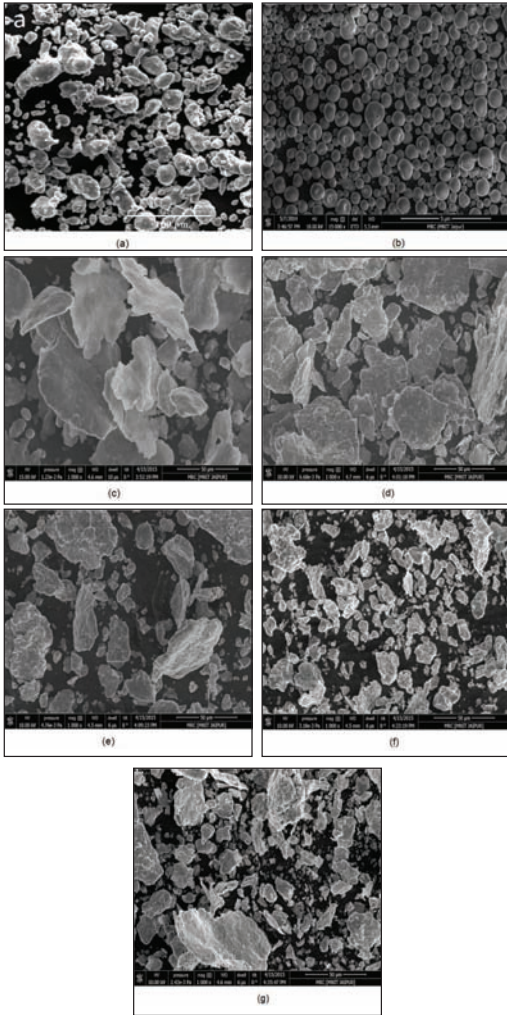


**Fig 1:** FESEM micrographs of MA powders: (a) 6061 Al as received, (b)  $\text{Al}_2\text{O}_3$  nanopowder, and (c-g) 6061 Al+(1-5 wt%)  $\text{Al}_2\text{O}_3$  respectively.

**Table 2:** Particle and grain size in the powder samples

Sample no.	Composition	Particle size ( $\mu\text{m}$ )	Grain size (nm)
1	6061 Al	44	107
2	6061Al +1% $\text{Al}_2\text{O}_3$	82	115
3	6061Al+2% $\text{Al}_2\text{O}_3$	104	126
4	6061Al +3% $\text{Al}_2\text{O}_3$	89	136
5	6061Al +4% $\text{Al}_2\text{O}_3$	87	109
6	6061Al +5% $\text{Al}_2\text{O}_3$	85	136

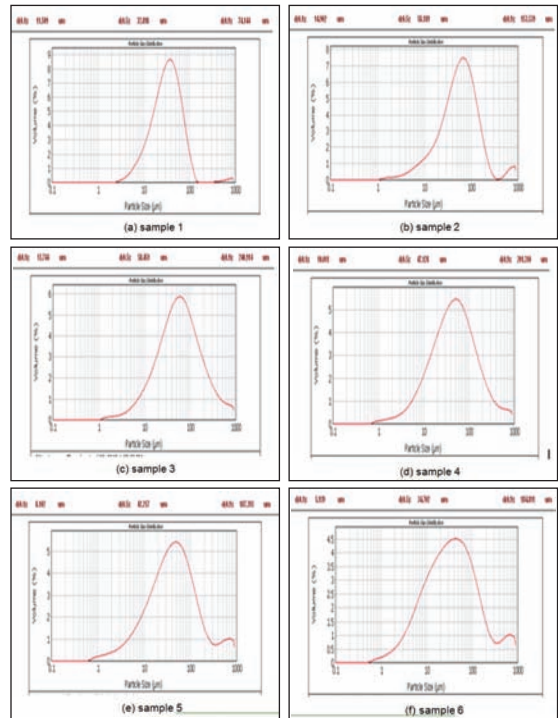


**Fig 2 (a-f) :** Particle size distribution curve in powders samples

# SYNTHESIS AND EVALUATION OF MECHANICAL BEHAVIOR OF MA 6061Al-Al<sub>2</sub>O<sub>3</sub> NANOCOMPOSITE

XRD patterns of all the powder samples are shown in Fig 3.

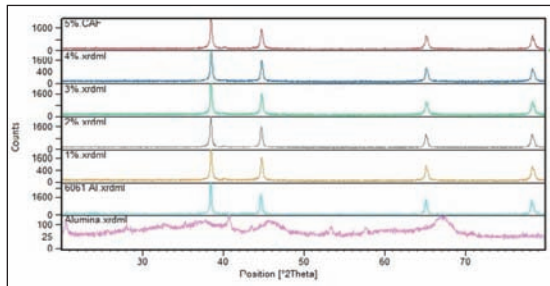


Fig 3: XRD pattern of powder samples.

XRD patterns show slight peak narrowing indicating grain enlargement in MA powder samples due to optimal mechanical processing. Using Scherrer’s formula [26], the grain size in the powder samples have been found to be as listed in the Table 2. The increase in crystallite size is due to plastic deformation of the powder particles to flake-like geometry during the mechanically processing.

The absence of sharp Al<sub>2</sub>O<sub>3</sub> peaks in the XRD patterns indicates amorphous form of the Al<sub>2</sub>O<sub>3</sub> particles or non-suitability of X-rays for studies of the nanoparticles.

### 3.2 Consolidated Specimen

The details of all the composite specimen prepared, by hot pressing and tempering (T6), have been summarized in Table 3.

Specimen No.	Details of the specimen
1	As received 6061 Al
2	MA 6061Al -1wt% Al <sub>2</sub> O <sub>3</sub>
3	MA 6061Al-2wt% Al <sub>2</sub> O <sub>3</sub>
4	MA 6061Al -3wt% Al <sub>2</sub> O <sub>3</sub>
5	MA 6061Al-4wt% Al <sub>2</sub> O <sub>3</sub>
6	MA 6061Al-5wt% Al <sub>2</sub> O <sub>3</sub>

Table 3: Details of nanocomposite specimens

TEM micrographs of the composite specimen are shown in Fig 4.

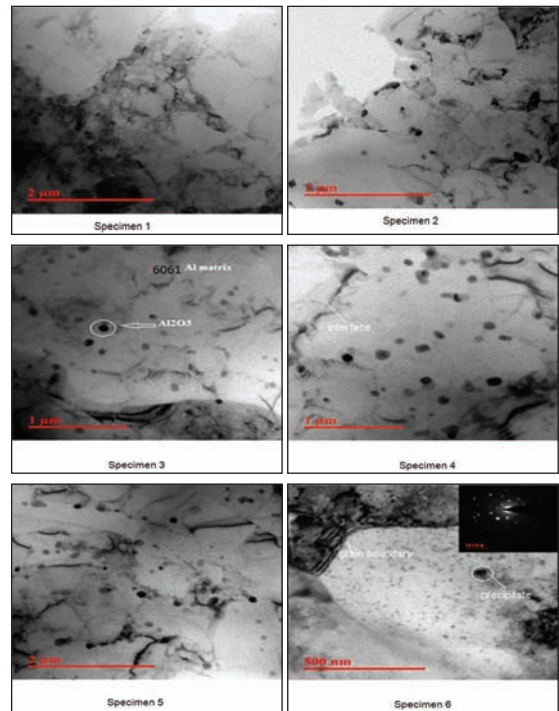


Fig 4 TEM micrographs of the nanocomposite specimen

It is clearly visible that a uniform distribution of fine precipitate and Al<sub>2</sub>O<sub>3</sub> nanoparticles has taken place. The nanoparticles are; (i) uniformly distributed in body as well as boundaries of the grains, (ii) the grains are of the submicron size, not the nano, and (iii) interface is clean devoid of much interfacial stresses. All these factors may lead to good ductility in the composite. Optimal mechanical alloying process adopted is responsible for the uniform distribution of nanoparticles. Slight grain growth has taken place during the consolidation of the composite. P/M processing is known for low processing temperature (as compared to casting), the same has provided here the clean interface. In liquid route, during solidification large residual stresses are created at the interface due to difference in

# SYNTHESIS AND EVALUATION OF MECHANICAL BEHAVIOR OF MA 6061Al-Al<sub>2</sub>O<sub>3</sub> NANOCOMPOSITE

thermal expansion coefficient of the matrix and the reinforcement. In nanocomposites, it has been established that additions of dispersed nanoparticles beyond 5 wt. % leads to large interfacial stresses due to large surface area of the nanoparticles [27].

### 3.3 Mechanical Behavior

The tensile strength and % elongation obtained for all specimens are plotted as shown in Fig 5 (a) and Fig 5(b).

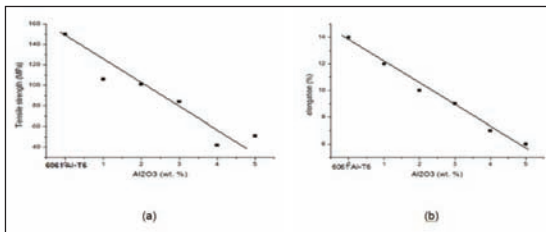


Fig 5. Tensile Strength and %elongation with varying wt. % of Al<sub>2</sub>O<sub>3</sub> in 6061 Al matrix.

It can be seen that with increasing percentage of Al<sub>2</sub>O<sub>3</sub>, tensile strength and % elongation in the nanocomposite decreases. This can probably be due to the presence of increasing amount of hard phase precipitate and nano Al<sub>2</sub>O<sub>3</sub> particles. The composite having 5 wt. % of Al<sub>2</sub>O<sub>3</sub> nanoparticles was found to have 6% elongation and gave a ductile fracture (Fig 6) establishing that the prepared nanocomposite is not brittle. The composite may exhibit dispersion strengthening effect at high temperature due to presence of Al<sub>2</sub>O<sub>3</sub> nanoparticles in the matrix.

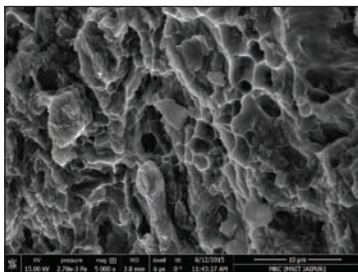


Fig 6. Fractograph of the composite having 5 wt.% Al<sub>2</sub>O<sub>3</sub> nanoparticles

Hardness obtained in all the specimens have been plotted as shown in Fig 7.

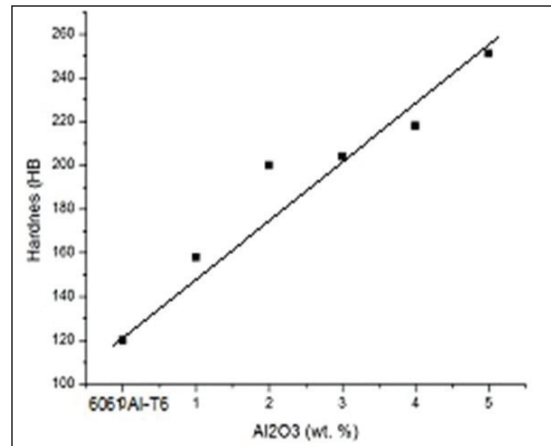


Fig 7: Hardness with varying wt% of Al<sub>2</sub>O<sub>3</sub>

The hardness obtained for 6061Al-T6 was 120 HB which is slightly higher as compared to reported value (95 HB), of its cast counterpart in literature, may be due to traces of oxides in the P/M matrix. Hardness in nanocomposite is found to increase with increasing amount of Al<sub>2</sub>O<sub>3</sub> (Fig 7). This increase in hardness can be attributed to the presence of uniformly distributed hard Al<sub>2</sub>O<sub>3</sub> nanoparticles in the composite, smaller means free path between neighboring nanoparticles and the greater constraint provided by the higher surface area of the nanoparticles. The contribution of residual stresses due to MA processing to this increased hardness may be treated as negligible. It is appreciable to note that hardness of the nanocomposite improved by over 100% to the level of 251 HB, along with preserved ductile nature of the matrix. Hardness measurement basically a resistance to shear deformation in a limited area, thus the improved hardness indicates improvement in the stiffness of 6061Al-T6. This improvement may add to the quality improvement where this alloy can be used like rail coaches, truck frames, aircraft structures etc and may find some new applications.

# SYNTHESIS AND EVALUATION OF MECHANICAL BEHAVIOR OF MA 6061Al-Al<sub>2</sub>O<sub>3</sub> NANOCOMPOSITE

## 4. Conclusions

The results obtained in this work can be summarized as follows:

Use of optimal mechanical processing of 6061Al matrix and (1-5) wt.% of nano Al<sub>2</sub>O<sub>3</sub> particles provides a uniform distribution of disperiods. Interface was found to be clean in the composite. Increasing amount of Al<sub>2</sub>O<sub>3</sub> nanoparticles (upto 5 wt. %) in the composite though resulted in decrease in tensile strength and % elongation, but improvement in hardness by over 100% lead to 251HB, with a ductile fracture.

## References

- [1] W.S Miller , L Zhuang, J Bottema, A.J Wittebrood, P De Smet, A Haszler and A Vieregge, *Recent development in aluminium alloys for the automotive industry*, Materials Science and Engineering, ,2000, 280 (1), 37–49.
- [2] Xu, C.; Xia, K.; Langdon, T.G. The role of back pressure in the processing of pure aluminum by equal-channel angular pressing. *Acta Mater.* 2007, 55, 2351–2360.
- [3] Wu, X.; Xia, K. Back pressure equal channel angular consolidation – Application in producing aluminum matrix composites with fine flyash particles. *J. Mater. Proc. Tech.* 2007, 192–193,355–359.
- [4] Goussous, S.; Xu, W.; Wu, X.; Xia, K. Al-C nanocomposites consolidated by back pressure equal channel angular pressing. *Comp. Sci. Tech.* 2009, 69, 1997–2001.
- [5] Xu, W.; Wu, X.; Honma, T.; Ringer, S.P.; Xia, K. Nanostructured Al-Al<sub>2</sub>O<sub>3</sub> composite formed *in situ* during consolidation of ultrafine Al particles by back pressure equal channel angular pressing. *Acta Mater.* 2009, 57, 4321–4330.
- [6] Li, Y.; Zhao, Y.H.; Ortalan, V.; Liu, W.; Zhang, Z.H.; Vogt, R.G.; Browning, N.D.; Lavernia, E.J.; Schoenung, J.M. Investigation of aluminum-based nanocomposites with ultra-high strength. *Mat. Sci. Eng. A* 2009, 527, 305–316.
- [7] Goussous, S.; Xu, W.; Xia, K. Developing aluminum nanocomposites via severe plastic deformation. *J. Phys. Conf. Ser.* 2010, 240, 012106.
- [8] Kubota, M.; Wu, X.; Xu, W.; Xia, K. Mechanical properties of bulk aluminium consolidated from mechanically milled particles by back pressure equal channel angular pressing. *Mat. Sci. Eng. A* 2010, 527, 6533–6536.
- [9] Tjong, S.C. Novel nanoparticle-reinforced metal matrix composites with enhanced mechanical properties. *Adv. Eng. Mat.* 2007, 9, 639–652.
- [10] Li, X.; Yang, Y.; Cheng, X. Ultrasonic-assisted fabrication of metal matrix composites. *J. Mater.*
- [11] Li, J.; Xu, W.; Wu, X.; Ding, H.; Xia, K. Effects of grain size on compressive behaviour in ultrafine grained pure Mg processed by equal-channel angular pressing at room temperature. *Mater. Sci. Eng. A* 2011, 528, 5993–5998.
- [12] Erman, A.; Groza, J.; Li, X.; Choi, H.; Cao, G. Nanoparticle effects in cast Mg-1 wt% SiC nanocomposites. *Mater. Sci. Eng. A* 2012, 558, 39–43.
- [13] Wang, Z.; Wang, X.; Zhao, Y.; Du, W. SiC nanoparticles reinforced magnesium matrix composites fabricated by ultrasonic method. *Trans. Nonferrous Met.* 2010, 20, s1029–s1032.
- [14] Eugene, W.W.L.; Gupta, M. Characteristics of aluminum and magnesium based nanocomposites processed using hybrid microwave sintering. *J. Microwave Power Electromagn. Energy* 2010, 44,14–27.
- [15] *Sci.* 2004, 39, 3211–3212.
- [16] ASM Handbook, vol. 2, *Properties and selection: Nonferrous alloys and special - purpose materials*, international handbook committee, second print 1992, PP. 17-18.
- [17] P.K. Rohatgi et al, "Scatter and Statistical Analysis of Tensile Properties of Cast SiC Reinforced A359 Alloys", Materials Science and Engineering A, vol. 398, Issues 1-2, Pages 1-14, April 2005.

## SYNTHESIS AND EVALUATION OF MECHANICAL BEHAVIOR OF MA 6061Al-Al<sub>2</sub>O<sub>3</sub> NANOCOMPOSITE

---

- [18] P. Kebabinski, S.R. Phillpot, D. Wolf, H.Gleiter. "Amorphous structure of grain boundaries and grain junctions in nanocrystalline silicon by molecular dynamics simulation", *Acta Mater* 1997; 45, PP. 87-98.
- [19] P.K. Rohatgi, B Schultz, *Material Matters*, 2.4, 16 (2007)
- [20] Benjamin, J. S., *Scientific American*, 234:48 (1976)
- [21] P.R.Soni, "Mechanical Alloying: Fundamentals and Applications", 2001, Cambridge International Science Publishing.
- [22] M. S. El-Eskandarany, K Aoki, and K.J. Suzuki. *Less-Common Met.*, 167:113 (1990).
- [23] G. B. Schaffer, and P. G. McCormick,, *Metall. Trans. A*, 21:2789 (1990)
- [24] S. Rajasekaran, N. K. Udayashankar, and Jagannath Nayak, "T4 and T6 Treatment of 6061 Al-15 Vol. % SiCP Composite", *ISRN Material Science*, 2012
- [25] Arpit Khemkha, "Synthesis and characterization of 6061Al-Al<sub>2</sub>O<sub>3</sub> P/M nanocomposite", M-tech thesis, MNIT Jaipur.
- [26] Harish Lakhotiya, Gagandeep, Chetan Saini, Ankit Goyal, K V R Rao and S L Kothari, "Structural and Optical Properties of ZnS nanoparticles doped with different concentration of Co, Springer proceedings in Physics 143, DOI:10.1007/978-3-642-34216-5\_19 (2013)
- [27] O. Kamigaito, "What can be improved by nanometer composites?", *J.Japan Society of Powder and Powder Metallurgy*, 38 (3), 315-321, 1991



# IMPROVEMENT IN TRANSPARENCY OF Nd:YAG CERAMICS THROUGH HOT PRESS SINTERING.

S P Butee, K R Kamble, Prashant Dixit, M D Joshi, S A Dhawanjewar

Department of Metallurgy and Materials Science, College of Engineering, Shivaji Nagar, Pune, India

**Abstract :** Polycrystalline Yttrium Aluminium Garnet (YAG) ceramics have been prepared by solid-state reaction and sintering route. Micro sized  $\text{Al}_2\text{O}_3$  and  $\text{Y}_2\text{O}_3$  and  $\text{Nd}_2\text{O}_3$  powders along with 0.1 wt% of  $\text{TiO}_2$  as sintering aid were mixed through ball milling, pelletized in HPS at  $900^\circ\text{C}$  and sintered at  $1600^\circ\text{C}$  for 23-27 hour to attain high sintered density and coarse grain microstructure. Result of XRD revealed occurrence of single  $\text{Y}_3\text{Al}_5\text{O}_{12}$  phase for un-doped YAG samples, whereas presence of both YAG and YAP phases was noted for Nd-doped samples. VIS-NIR Spectroscopy revealed 5 to 21% transmittance for the range of samples sintered. SEM revealed fine grains ( $< 2\mu\text{m}$ ), thin grain boundaries and fine pore size ( $\sim 0.7\mu\text{m}$ ) for the 2.5 Nd:YAG samples which showed maximum transmittance.

**Keywords**— Nd:YAG, Transparent ceramics, Hot press sintering, Density.

## I. Introduction

Transparent ceramic is an important class of advanced functional materials which has a unique combination of mechanical and optical transmission properties. When electromagnetic radiation falls on a transparent sintered body it undergoes many phenomena such as reflection, refraction, absorption due to non-homogeneity and finally gets transmitted through the other side of the sintered body. Grain boundary, the second phase inclusions, rough surfaces and pores are the main sources of scattering and absorption of light in polycrystalline materials [1]. Recently, the need for materials that combine transparency, high strength, scratch resistance, and thermal stability has been driven by the need of transparent ceramics for armor, optical, and laser applications [2]. Coble et al. [3] reported "transparent" ceramics in a patent wherein MgO doped  $\text{Al}_2\text{O}_3$  was sintered to full density and had an in-line transmission of 40-50% between 400 and 600 nm.

Yttrium Aluminum Garnet ( $\text{Y}_3\text{Al}_5\text{O}_{12}$ , YAG) is a synthetic crystal of complex cubic oxide, best known as laser host material due to its excellent

mechanical, thermal, and optical stabilities, and received considerable attention because of its interesting properties when doped with lanthanides ions such as neodymium [4], erbium, ytterbium, chromium, europium and cerium [2]. Yttrium aluminum garnet (YAG) and yttrium aluminum garnet doped with neodymium (Nd:YAG) are the most famous kind of oxide crystals widely used as the active medium in solid state lasers (SSL) [5]. The dopant, triply ionized neodymium,  $\text{Nd}^{+3}$ , typically replaces a small fraction of the yttrium ions in the host crystal structure of the yttrium aluminum garnet. It is the neodymium ion which provides the lasing activity in the crystal [6].

Polycrystalline Nd:YAG has several advantages over Czochralski single crystals including increased dopant homogeneity, lower processing temperature and time, near net shape forming, increased dopant concentrations, access to more dopants, and possibilities for increased scalability [7]. In 1995, Ikesue et al. [8, 9] showed that it was possible to obtain a laser effect with a polycrystalline YAG doped with neodymium, synthesized by a solid-state reaction. In the

## IMPROVEMENT IN TRANSPARENCY OF Nd:YAG CERAMICS THROUGH HOT PRESS SINTERING.

early 2000s, Lu et al. [10] fabricated large-scale Nd:YAG ceramic rods using precipitated powders, and achieved high efficient and high power laser emission. Nd<sup>3+</sup> ions were added in small proportions to the YAG matrix to improve its luminescent properties. They enter into solid solution within the garnet crystallographic lattice where they substitute Y<sup>3+</sup> ions species owing to similar size and electric charge criteria [11]. In the polycrystalline Nd:YAG ceramics, the doping concentration can be increased to as much as 9 wt.%, and a homogeneous distribution of Nd<sup>3+</sup> can be achieved throughout the specimen [12]. Zhang et al. [13] studied the effect of MgO and SiO<sub>2</sub> on the optical properties of transparent Nd:YAG ceramics. By using 0.1 wt.% MgO and 0.145 wt.% SiO<sub>2</sub> as the sintering aids, the fully transparent Nd:YAG ceramics with a good transparency were successfully fabricated. It was generally believed that in order to obtain transparent ceramics, pure phase, larger grain size and few pores are the crucial requirements on the ceramics. Liu et al. [14] studied the effects of grain size, grain-boundary phases and pores on the transmittance obtained in YAG ceramics. Ali et al. [2] studied the various fabrication techniques for transparent YAG ceramic and grouped them into two classes: 1) traditional solid-state reaction methods which require repeated mechanical mixing and extensive heat treatment at temperatures of 1600°C to achieve the desired phase purity; and 2) methods based on wet-chemical synthesis of a precursor material that significantly lowered the crystallization temperature of YAG and improved the phase purity of the final product such as co-precipitation [15], Sol-gel [16].

The purpose of this paper is to study effect of various process parameters on fabrication of transparent polycrystalline Nd:YAG (0–5 at % Nd) ceramics prepared by hot press sintering using 0.1 wt% TiO<sub>2</sub> as the sintering aid. The general process used here is similar to that reported by

Ikesue [8, 9] with a much simpler version. Hence, spray drying was not used, and the starting powders used were commercially available Al<sub>2</sub>O<sub>3</sub>, Y<sub>2</sub>O<sub>3</sub>, and Nd<sub>2</sub>O<sub>3</sub> powders without any prior pretreatment. The structural and optical properties of the obtained polycrystalline YAG and Nd:YAG samples were characterized using XRD, SEM and UV-Vis-NIR spectroscopy [6]. The prime goal of the present study was to improve transparency of Nd:YAG ceramics using hot pressed sintering. Accordingly, the optical and mechanical properties of hot-pressed Nd:YAG ceramics for laser applications are studied.

## II. Experimental Procedure

### A. Materials

Commercial grade Alumina, Yttrium oxide and Neodymium oxide powders were used for the synthesis of Nd:YAG ceramic pellets. These powders were supplied by Indian Rare Earths Ltd. TiO<sub>2</sub> (AR grade LOBA chemie) was selected as sintering aid. The milling container was consisting of 30 alumina balls with diameter of 5 mm with ball-to-powder ratio 10:1 confined in a 200 ml polythene bottles. The wet milling was performed using ethanol as the medium in a jar mill (Make: Varaj Engineering, 150 RPM).

### B. Preparation of neodymium-doped (0, 2.5 and 5 wt %) yttrium aluminium garnet Pellets

The stoichiometric amount of starting materials (Al<sub>2</sub>O<sub>3</sub>, Y<sub>2</sub>O<sub>3</sub>, Nd<sub>2</sub>O<sub>3</sub>) was mixed. 0.1 wt. % of TiO<sub>2</sub> was used as a sintering aid in preparation of all the samples. The milled powder slurry was then dried in an oven at 130°C for 2h. The dried powder was ground in an agate mortar and pestle. Specific surface area of milled ceramic powder was measured by Surface Area Analyzer (Model: SMART SORB 93). Subsequently milled ceramic powder with different Nd concentration was then sintered in hot press sintering machine (Model: KEJETHERM, 8 Ton, 1400°C) at 900°C for

# IMPROVEMENT IN TRANSPARENCY OF Nd:YAG CERAMICS THROUGH HOT PRESS SINTERING.

10 min hold time. Pressure applied during HPS was 30, 35 and 40 kg/cm<sup>2</sup> respectively.

The pellets so formed were then further sintered in tubular MoSi<sub>2</sub> (Model: Therlek, 1600°C) sintering furnace as per the heat treatment cycle given in Fig.1 Sintering was carried out at 1600°C.

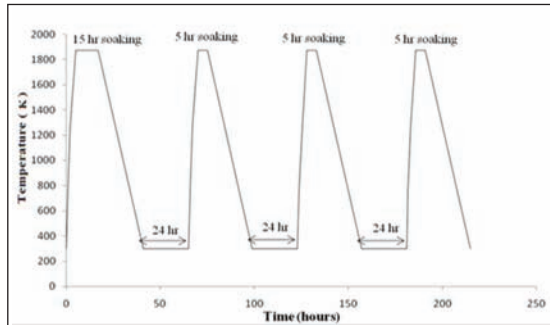


Fig. 1: Heat Treatment cycle during sintering of pellets.

All the samples were then etched by thermal etching process. Thermal etching was carried out in MoSi<sub>2</sub> sintering furnace (Model: Therlek, 1600°C) at 1490°C for 1 hour 20 minutes, Morphology of ceramics was studied by Field Emission Scanning Electron Microscope (FESEM) (Model: Zeiss- SIGMA) with accelerating voltage of 10 -15 kV. The phase transformation, which occurs at 1600°C, was observed by X-ray diffraction (Bruker AXS, D8 Advance X ray Diffractometer) in 2θ range of 20° - 80°. X - ray source was Cu - Kα with a wave length of 1.54 Å. The distribution of Al, Y, and Nd was observed by energy-dispersive spectroscopy (EDS) using Bruker detector attached to FESEM. UV-Vis-NIR spectrophotometer (Model: Beckman DU640) was used to obtain % transmission in the sintered Nd: YAG pellets.

### III. Results and Discussion

Figure 2 (a), (b) & (c) shows SEM micrographs of the un-doped and 2.5 at % and 5 at % Nd-doped milled ceramic powder respectively. It is evident

the powders are fine sized, with a wider particle size distribution and agglomerated.

BET surface area analysis is performed to obtain surface area of powders and compute its particles size. The surface area value is calculated directly from the instrument. Particle diameter is calculated by the following equation:

$$A = \frac{6}{\rho * d}$$

where A is Specific Surface Area (i.e. number of particles per gram multiplied by the surface area per particle) (m<sup>2</sup>/g), d is particle diameter and ρ is density of material. The values of the surface area (in sq.m/gm) and computed particle size (in μm) are given in Table 1. It is noted that higher Nd substitution causes an increase in the surface area of the powders, which is beneficial for sintering purpose.

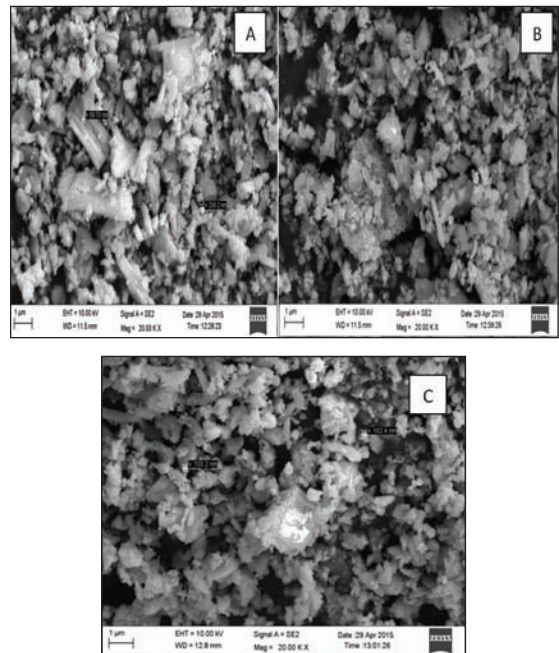


Fig. 2: SEM photo micrographs of (a) YAG, (b) 2.5% Nd:YAG, (c) 5% Nd:YAG milled ceramic powder.

# IMPROVEMENT IN TRANSPARENCY OF Nd:YAG CERAMICS THROUGH HOT PRESS SINTERING.

**Table 1: BET surface area analysis and particle size computed of 0-5 at.% Nd:YAG samples**

Composition	Surface Area (m <sup>2</sup> /gm)	Computed Particle size (μm)
0% Nd:YAG	5.92	0.225
2.5% Nd:YAG	8.37	0.159
5% Nd:YAG	9.25	0.144

Fig.3 shows XRD pattern of 0Nd:YAG-23, 2.5Nd:YAG-25 and 5Nd:YAG-27 samples where 23, 25 and 27 denote sintering time in hours. The XRD pattern shows that complete transformation to YAG phase occurs for sintering in ambient atmosphere at 1600°C for 0% Nd substitution samples. Also, with the increase in soaking time there was an increase in grain size. This is evident from the fact that as the grain size increases the crystallite size increases and the peaks became narrow and sharp. The inter-atomic length increased with the growth of crystallites, leading to the generation of strains and hence shifting of peaks was observed. The XRD pattern showed complete formation of cubic YAG phase for 23 hours of soaking time. Sintering was done for long durations to improve density of Nd:YAG samples.

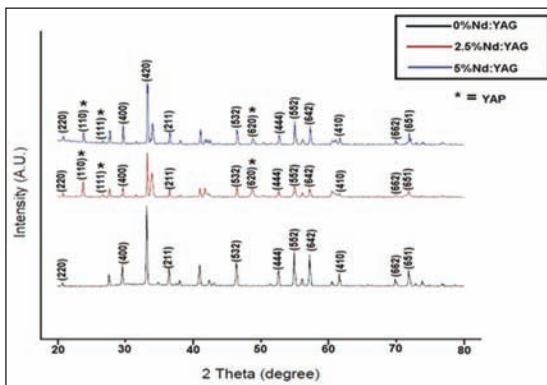


**Fig. 3: XRD pattern of YAG-23, 2.5Nd:YAG-25 and 5Nd:YAG-27 samples.**

X-ray diffraction pattern of 2.5at.% and 5wt.% Nd doped YAG pellets showed presence of YAP (perovskite phase) phase in addition to pure YAG phase. The proportion of the YAP phase has increased with increases in Nd content. In Table 2 the refined lattice parameters and % of YAG and YAP phase obtained are shown. A monotonic increase in the lattice parameters of the cubic unit cell of YAG was noted with the addition of Nd in YAG.

**Table 2: Refined lattice parameters and % YAP and YAG phase of Nd:YAG samples**

Composition	%YAP	%YAG	%TD	Unit cell Parameters (YAG)	
				a(Å)	Vol.( Å <sup>3</sup> )
YAG-23	0	100	95.60	12	1728
2.5NdYAG-25	18.28	81.72	72.42	12.002	1728.86
5NdYAG-27	28.10	71.9	72.54	12.004	1729.72

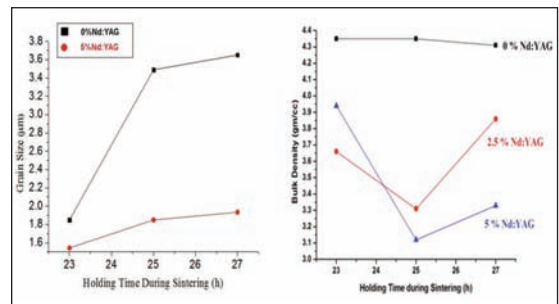


**Fig. 4: Grain growth behavior & Bulk Density of pure YAG, 2.5%Nd:YAG & 5% Nd:YAG sintered at 1600°C.**

Fig. 4 shows the grain growth behavior of pure YAG and 5%Nd:YAG samples sintered at 1600°C for 23, 25 and 27 h respectively. The average grain size increased monotonously in the range of 1.84 – 3.65 μm with increase of the sintering time. These results and close observation of table 3 indicate that the microstructure is more dense for a longer sintering time and the average grain size increases with increase of the sintering time. SEM of the sample is also conducted to measure the

## IMPROVEMENT IN TRANSPARENCY OF Nd:YAG CERAMICS THROUGH HOT PRESS SINTERING.

central grain size. Grain growth can be expressed by the following equation [17]:

$$G^a - G_0^a = K_0 t \exp(-Q/RT)$$

Where  $G$  and  $G_0$  are the average grain size after and before sintering,  $a$  is the kinetic grain growth exponent,  $T$  is the sintering temperature,  $t$  is the sintering time,  $Q$  is the apparent activation energy for grain growth,  $K_0$  and  $R$  are constants.

Fig. 4 shows measurement of bulk density of all the samples. The bulk density was measured according to ASTM C373-88 standard. Due to presence of higher amount of porosity, the obtained bulk density as noted for 2.5Nd:YAG-25 was marginally less. Also it was observed that bulk density in undoped samples was maximum.

Fig. 5 shows SEM micrographs of pure YAG samples. From Fig. 5 (a) it was observed that porosities were significantly large to cause scattering and transparency to decrease as light propagated through the sample. It was also observed that some of the grains were quite large in size while some were smaller. This also implied that uniform grain growth has not occurred in this case even though some grain growth has taken place. From figure 5(b) shows the microstructure of 2.5Nd:YAG-23 sample at 20kX. In Fig. 5, the grain size of sample (a) and sample (b) are approximately same. This shows that the Nd-doped samples shows sign of grain growth even though much densification has not taken place. From Fig. 5(c) it is observed that the porosities vary from one part of component to the other. Two types of grains appearing bright and dull can be observed in SEM of these samples. This grain contrast is only observed in 5 % Nd doped samples. The high amount of Nd doping in these samples has most likely lead to its non uniform distribution. This is quantified with the EDAX results. The weight % of the different elements present in the bright and dull grain is

given in Table 4. By comparing data of Table 4 it is evident that there exists major difference in amount of Neodymium present in bright and dark grain which is contributing to contrast otherwise all other elements are present in almost similar amount.

*Table 4: EDS showing weight % of elements present in bright (x) and dull (y) grains*

Element	Dull grains (wt.% (grain y))	Bright grains (wt.%) (grain x)
Y	34	33.8
O	28.8	26.19
Al	20.70	20.04
Nd	16.57	19.34
Total	100	100

Fig. 5(C) shows a magnified view of the two types of grains seen. It also shows that dark grains are showing a wide distribution of grain sizes while brighter grains have almost identical grain size. It appears that the phase contrast is indicative of YAG and YAP phases present in the samples. However, it could not be clearly distinguished only on the basis of EDS analysis done. Results of the SEM supported the observed density values.

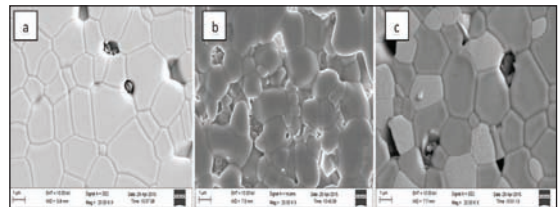


*Fig. 5: SEM photo micrographs at 20.00 kX magnification. a) YAG-23, b) 2.5NdYAG-23, c) 5NdYAG-23 showing bright (x) and dull (y) grains*

Fig.6 shows image analysis of 5Nd:YAG-23 sample using DeXel Imaging software. Image analysis was done to confirm the presence of YAG and YAP phases. The % of two different phases obtained was 65.9% and 34.1% after subtracting the porosity. These results nearly matched to the % of phases of YAG and YAP shown by XRD.

## IMPROVEMENT IN TRANSPARENCY OF Nd:YAG CERAMICS THROUGH HOT PRESS SINTERING.

Hence, the bright phase has attributed as YAG and dark phase as YAP.

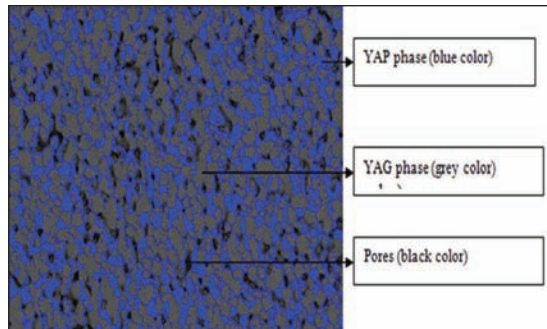


Fig.6: Image analysis of 5Nd:YAG-23 sample.

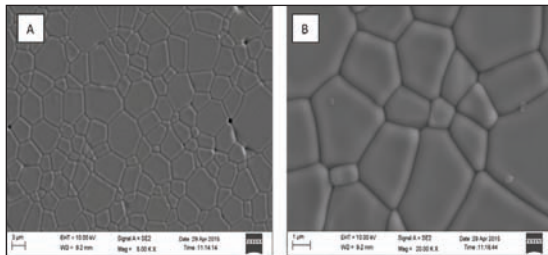


Fig. 7: SEM photo micrographs of YAG-25 sample at (a) 3.0 kX (b) 20.00 kX magnification.

Fig. 7 shows SEM photo micrographs of YAG-25. From Fig. 7(a) it is very clear by seen that the porosity is comparatively very less and the grain growth has taken place. Such densified coarse grain structure is desired for the materials to be actually used as lasers. Although this pellet showed some translucency it did not produce the same results of transparency as seen in 2.5NdYAG-23 and 2.5NdYAG-25, which can be attributed to variation of the dopant concentration [].

Fig.8 shows an interesting microstructure observed for YAG-27 samples. Two distinct regions, one with fine grains & very high densification and the other with incomplete densification with coarse grains which are separated by almost a straight line are observed.

This effect may be because of presence of density gradient introduced during hot press sintering because of skin effect of flow of electric current. This aspect is important from point of view of getting two different layers in one single sample using HPS, which can be potentially used in fabrication of functionally graded ceramics. Such variation in microstructures across a straight line can be used for dual purpose applications. For e.g in this case the region with high porosity will provide thermal insulation whereas region with negligible porosity will be providing optical transparency.

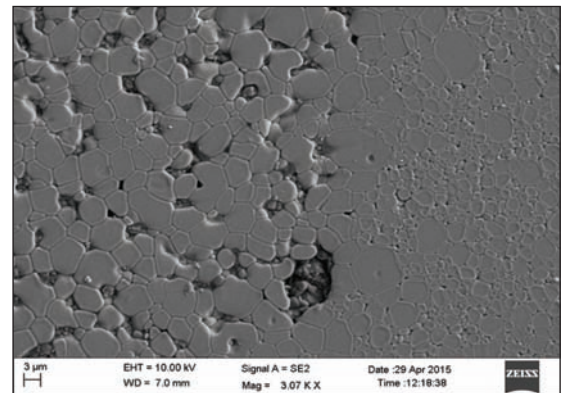


Fig. 8: SEM photo micrograph of YAG-27 at 3.0 kX magnification.

Fig. 9 shows % transmittance observed for all the sintered ceramics samples processed. The % transmittance is measured over region of 300nm-500nm wavelength. The optical transmittance of the 2.5Nd:YAG-23 at wavelength of 1064 nm was highest, i.e. 20.70% .Also, it was observed that for same amount of soaking time of 23hr.,25hr. and 27hr. the % transparency for the samples with 2.5% Nd doping showed maximum value of  $\approx 21\%$ , while samples with 5% Nd doping showed minimum of  $\approx 5.7\%$ . It was also observed that the % transparency of samples in visible region was more than that in NIR.

## IMPROVEMENT IN TRANSPARENCY OF Nd:YAG CERAMICS THROUGH HOT PRESS SINTERING.

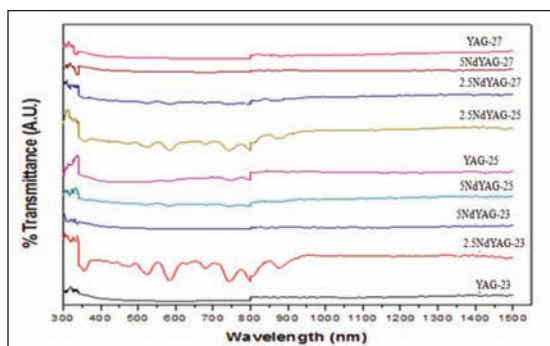


Fig. 9: VIS-NIR Transmission spectra of the different samples processed.

Table 5: % Transmission of samples at 1064 nm wavelength and near infrared (NIR) region

Sample	% Transmission at 1064nm wavelength	% Transmission in NIR (700-1500 nm)
YAG-23	7.42	8.26
<b>2.5NdYAG-23</b>	<b>20.70</b>	<b>21.03</b>
5NdYAG-23	6.18	6.7
5NdYAG-25	8.20	8.9
YAG-25	13.29	13.45
2.5NdYAG-25	15.65	16.35
2.5NdYAG-27	8.36	11.12
5NdYAG-27	5.08	5.71
YAG-27	7.10	8.17

### IV. Conclusions

Translucent Ceramics of 0, 2.5 and 5 at. % Nd:YAG were successfully fabricated from commercially available powders by the solid-state reaction and sintering method using high-purity oxide powders as the starting materials and TiO<sub>2</sub> as a sintering aid. The average particle size of milled powders decreased from 0.225 to 0.144 μm for same duration of milling with increasing Nd-doping as obtained from BET surface area analysis. XRD analysis confirmed presence of Y<sub>3</sub>Al<sub>5</sub>O<sub>12</sub> (YAG) phase in pure sintered samples. A two phase microstructure comprising of YAP

and YAG was noted for Nd doped samples. Samples with 2.5% and 5% Nd-doping showed some increased grain growth. Samples with 5% Nd-doping showed non-uniform distribution of Nd and characterized by bright and dull grains in SEM micrographs. Samples with 0% Nd-doping showed translucency with 13.45 % transmission whereas, 2.5Nd:YAG-23 sample showed maximum transmission of 21.03%.

### Acknowledgement

The authors would like to thank Prof. P. P. Deshpande at College of Engineering, Pune for valuable discussions and experimental assistance in transparency measurement of Nd:YAG ceramic. The author gratefully acknowledges the All India Council for Technical Education AICTE for their valuable support for funding the laboratory in which this work is carried out. [AICTE Ref No:8023/RID/RPS-34/(POLICY-III)(GOVT)/2011-12 & 12/AICTE/RIFD/MOD(Policy-2)-28/2012-13]

### References

- Roy Johnson, "Transparent Polycrystalline Ceramics: An Overview", *Trans. Ind. Ceram. Soc.*, **71**, 73-85, (2012).
- H. Ali, M. T. H. Abou Kana, M. A. Khedr, "Spectroscopy and Optical Properties of Sm<sup>3+</sup>:YAG Nanocrystalline Powder Prepared by Co-Precipitation Method: Effect of Sm<sup>3+</sup> Ions Concentrations", *Open J. App. Sci.*, **4**, 96-102, (2014).
- R. L. Coble, "Transparent alumina and method of preparation", US Patent 3026210, 20 March, (1962).
- A. Ikesue, K. Kamata, K. Yoshida, "Effects of Neodymium Concentration on Optical Characteristics of Polycrystalline Nd:YAG Laser Materials", *J. Amer. Ceram. Soc.*, **79**, 1921-1926, (1996).
- Y. A. Barnakov, I. Veal, Z. Kabato, G. Zhu, M. Bahoura, M. A. Noginov, "Simple route to Nd:YAG transparent ceramics". *Proc. SPIE 6216*, Laser Source and System Technology for Defense and Security II, 62160Z (May 12, 2006); doi:10.1117/12.689902

## IMPROVEMENT IN TRANSPARENCY OF Nd:YAG CERAMICS THROUGH HOT PRESS SINTERING.

---

6. S. Kostic, Z.Ž. Lazarevic, V. Radojevic, A. Milutinovic, "Study of structural and optical properties of YAG and Nd:YAG single crystals", *Mater. Res. Bull.*, **63**, 80-87, (2015).
7. S. Kochawattana, Gary L. Messing, Adam Stevenson, "Sintering and grain growth in SiO<sub>2</sub> doped Nd:YAG," *J. Euro. Ceram. Soc.*, **28**, 1527-1534, (2008).
8. A. Ikesue, A. Furusato, and K. Kamata, "Fabrication of Polycrystalline, Transparent YAG Ceramics by a Solid state Reaction Method", *J. Amer. Ceram. Soc.*, **78** [1], 225-8, (1995).
9. A. Ikesue, T. Kinoshita, K. Kamata, and K. Yoshida, "Fabrication and Optical Properties of High-Performance Polycrystalline Nd:YAG Ceramics for Solid- State Lasers," *J. Amer. Ceram. Soc.*, **78** [4], 1033-40, (1995).
10. J. Lu, M. Prabhu, K. Ueda, H. Yagi, T. Yanagitani, A. Kudryashov, Kaminskii, "Potential of Ceramic YAG Lasers", *Laser Physics*, **11** (10), 1053-1057 (2001).
11. R. Boulesteix, A. Maître, J. F. Baumard, Y. Rabinovitch, C. Sallè, S. Weber, M. Kilo, "The effect of silica doping on neodymium diffusion in yttrium aluminum garnet Ceramics: implications for sintering mechanism," *J. Eur. Ceram. Soc.*, **29**, 2517 - 2526, (2009).
12. Sang-Ho Lee, S. Kochawattana, Gary L. Messing, "Solid-State Reactive Sintering of Transparent Polycrystalline Nd:YAG Ceramics", *J. Amer. Ceram. Soc.*, **89** [6], 1945-1950, (2006).
13. H. Yang, X. Qin, J. Zhang, J. Ma, D. Tang, S. Wang, Q. Zhang, "The effect of MgO and SiO<sub>2</sub> codoping on the properties of Nd:YAG transparent ceramic", *Opt. Mater.*, **34**, 940-943, (2012).
14. M. Liu, S.W. Wang, D.Y. Tang, L.D. Chen, J. Ma, "Fabrication and Microstructures of YAG Transparent Ceramics", *Science of Sintering*, **40**, 311-317, (2008).
15. M. L. Saladino, E. Caponetti, "Co-Precipitation Synthesis of Nd:YAG Nano powders II: The Effect of Nd Dopant Addition on Luminescence Properties", *Opt. Mater.*, **32**, 89-93, (2009).
16. C.-H. Lu, H.-C. Hong, R. Jagannathan, "Sol-Gel Synthesis and Photoluminescence Properties of Cerium-Ion Doped Yttrium Aluminium Garnet Powders", *J. Mater. Chem.*, **12**, 2525-2530, (2002).
17. R. J. Brook, in "Treatise on Materials Science and Technology, Vol. 9, Ceramic fabrication processes", p. 331, edited by F. F. Y. Wang (Academic Press, New York, 1976).



# DEVELOPMENT OF LITHIUM BASED CERAMICS FOR BREEDER APPLICATION

Sathi R. Nair, Amit Sinha\* and P. K. Sinha

Powder Metallurgy Division, Materials Group, BARC, Vashi Complex, Navi Mumbai 400 703

\*Corresponding author, email: asinha@barc.gov.in

**Abstract :** In a D-T fusion reactor, the important functions of breeder blanket material include breeding of tritium, converting the kinetic energy of fusion neutrons into heat, and finally, shielding the components surrounding the blanket from energetic neutrons as well as photons. Lithium based oxide ceramics have been considered as tritium breeder material in both the Helium Cooled Pebble-Bed Blanket for DEMO and the ITER Breeding Blanket due to their good thermal properties, especially high thermal conductivity, as well as satisfactory breeding characteristics. Among these ceramics, Lithium titanate ( $\text{Li}_2\text{TiO}_3$ ) based ceramic has been proposed as breeding material for fusion reactor blankets. Using the concept of solution combustion synthesis, in the present investigation,  $\text{Li}_2\text{TiO}_3$  based ceramic powders were synthesized using  $\text{LiNO}_3$  and hydrous titania powder as starting raw materials. The process yielded phase pure  $\text{Li}_2\text{TiO}_3$  powder directly after combustion without any subsequent calcination step. The phase analysis and morphology of powders were studied using X-ray diffraction, scanning electron microscopy. The sinterability of the powder was studied by sintering at different temperature in the range of 900 - 1300°C. The process parameters were optimized to obtain the desired microstructure and density in the sintered specimens. The preliminary results suggest that the present process is one of the appropriate synthesis methods for lithium titanate based ceramics for use in test blanket module (TBM) of International Thermonuclear Experimental Reactor (ITER). Another novel breeder material based on lithium beryllium oxide has been developed in our laboratory. The preliminary details of synthesis and characterisation of lithium beryllium oxide based breeder material has also been described in the present study.

**Keywords:**  $\text{Li}_2\text{TiO}_3$ ; ITER;  $\text{Li}_2\text{Be}_2\text{O}_3$ ; XRD

## Introduction

Nuclear fusion technology has the potential to become the safe and pollution free energy source which can sustain the energy demand of India in future. A significant feature of fusion energy is that it has the potential of being an environmentally attractive energy form. In a DT fusion reactor, the important functions of breeder blanket material include breeding of tritium, converting the kinetic energy of fusion neutrons into heat, and finally shielding the components surrounding the blanket from energetic neutrons as well as photons. Lithium based oxide ceramics ( $\text{LiAlO}_2$ ,  $\text{Li}_4\text{SiO}_4$ ,  $\text{Li}_2\text{ZrO}_3$  and  $\text{Li}_2\text{TiO}_3$ ) have been considered as tritium breeder material in both the

Helium Cooled Pebble-Bed Blanket for DEMO and the ITER Breeding Blanket due to their good thermal properties, especially high thermal conductivity, as well as satisfactory breeding characteristics [1-2]. Among these ceramics,  $\text{Li}_2\text{TiO}_3$  is considered as the candidate material because of its fairly good tritium release property and low activation characteristics [3].

Conventionally,  $\text{Li}_2\text{TiO}_3$  powder is produced by solid-state reaction of a powder mixture of  $\text{Li}_2\text{CO}_3$  and  $\text{TiO}_2$  at 750 °C for 10-20 hrs [4]. Several wet chemical processes have been reported in the literature for preparation of  $\text{Li}_2\text{TiO}_3$  powder [5-7]. However, these processes are cumbersome and yields powder with poor sinterability.  $\text{Li}_2\text{TiO}_3$

powder can be prepared by solution combustion synthesis (SCS) method which is a noble process for preparation of high purity, sinter-active and nanocrystalline ceramic powders. However, this process calls for titanium ion to be in aqueous solution form. The various starting materials for titanium, which are commonly used in SCS for preparation of titanates, are  $\text{TiCl}_4$ ,  $\text{Ti}(\text{C}_6\text{H}_6\text{O}_7)_2$ ,  $\text{Ti}(\text{OC}_3\text{H}_7)_4$ ,  $\text{TiO}(\text{NO}_3)_2$  etc. These are either difficult to handle or too expensive, making the production cost of the final product higher. In the present investigation,  $\text{Li}_2\text{TiO}_3$  powder was prepared by a novel solid-liquid combustion synthesis using solid hydrous titania powder and  $\text{LiNO}_3$  as the starting materials for titanium and lithium respectively.

Among the lithium based breeder materials, lithium beryllate ( $\text{Li}_2\text{Be}_2\text{O}_3$ ) is another candidate material that exhibit fairly good tritium release property.  $\text{Li}_2\text{Be}_2\text{O}_3$  is one such solid breeder material which can be used without a multiplier in the form of beryllium or beryllium oxide. Homogeneous distribution of breeder and multiplier materials is one of the requisite parameters for better neutronics and tritium breeding performance. The problem of homogeneous distribution between the breeder and multiplier can be circumvented if one uses material like  $\text{Li}_2\text{Be}_2\text{O}_3$  because of the presence of neutron multiplier component in the host material.

In the present investigation, the synthesis and characterization of lithium titanate by solution combustion method has been described. The preliminary details of synthesis and characterisation of lithium beryllium oxide based breeder material has also been described in the present study.

## Experimental

$\text{LiNO}_3$  (AR Grade, E-Merck, India), and uncalcined hydrated titania powder ( $\text{TiO}_2 \cdot x\text{H}_2\text{O}$  where  $x = 0.97$ ; M/s Travancore Titanium Products Ltd., India) were used as starting materials for preparation of  $\text{Li}_2\text{TiO}_3$  powder. Calculated amount of aqueous solution of  $\text{LiNO}_3$  was mixed with hydrated titania powder (anatase phase, average crystallite size: 26 nm). The mixed solution was subjected to an ultrasonic treatment in order to de-agglomerate the titania powder particles. In the solution, ammonium nitrate was used in the form of an additional oxidizer. The metal ions were complexed by stoichiometric quantity of glycine (AR Grade, E-merck, India). The initial pH of mixed solution was about 6.75. A measured quantity of ammonia solution was added to the mixed solution to adjust the initial pH value to 8. During the procedure, the solution was continuously stirred using a magnetic agitator. The mixed solution was slowly dehydrated under a hot plate to form a viscous gel wherein the titania powder was uniformly dispersed.

With subsequent dehydration, the gel was slowly turned into a black mass and eventually burnt in a self propagating combustion manner to yield a white colored powdery mass.

The powders obtained after combustion reaction were characterized by X-ray diffraction (Philips Analytical, Model PW1 710) for phase analysis. The as-produced  $\text{Li}_2\text{TiO}_3$  powder after combustion synthesis was compacted in a uniaxial hydraulic press at 150 MPa and subsequently sintered at 900 – 1300 for 2 h. The microstructural analysis of the sintered samples was carried out by scanning electron microscopy (SERON AIS2100). Cylindrical sintered specimens having diameter of 12 mm were used for measurement of density using Archimedes water displacement technique.

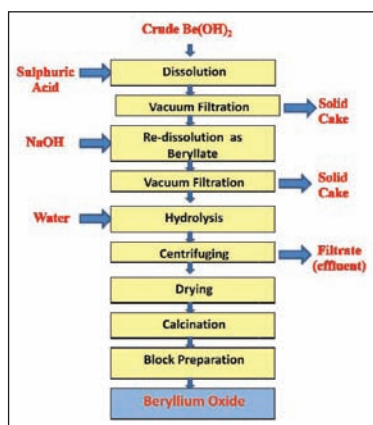


Fig. 1. Flow-sheet of production of high purity BeO powder

For the synthesis of lithium beryllate breeder material, initially, the high purity beryllium oxide was prepared from crude beryllium hydroxide. The crude hydroxide was dissolved in sulphuric acid (9N) to remove the silica. The solution was filtered. Sodium hydroxide was added to the filtrate in excess to re-dissolve the precipitate. The solution was filtered to remove the undissolved solids. The filtrate was subsequently hydrolysed to get pure beryllium hydroxide, which was washed, dried and finally calcined at 900°C that yielded high purity BeO powder. The flow sheet of production of high purity BeO is shown in Fig. 1.

Elemental impurities	Crude BeO	BeO after purification
	(ppm)	
Al	2000	17
B	<5	<1
Ca	1000	43
Cd	<5	<1
Cr	<10	6
Cu	20	6
Fe	510	78
Li	66	16
Mg	2000	60
Mn	270	42
Na	2350	150
Ni	90	30
Si	>2000	83

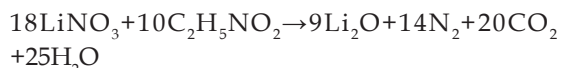
Table 1. Chemical assay of the BeO powder after purification used for synthesis of breeder material

The powder obtained after purification is of nuclear grade, the chemical assay of which is shown in Table 1. BeO and lithium carbonate powders were mixed as per the stoichiometric ratio through wet ball milling using zirconia balls in alcohol medium for 12 h. The slurry obtained after milling was dried. The powder-mixture was compacted to 10 mm diameter pellets in a hydraulic press. The phase evolution in this system was studied by reaction-sintering the green compacts at different temperatures in the range of 700 to 900°C. The phases present in the reaction-sintered compacts were analysed through XRD.

## Results and Discussions

### 3.1. Synthesis of Li<sub>2</sub>TiO<sub>3</sub> powder

The stoichiometric mixture of LiNO<sub>3</sub> and glycine resulted in flame combustion. The molar ratio of lithium nitrate to glycine was calculated according to the following formula:



When hydrous titania powder was added to the solution containing stoichiometric mixture of LiNO<sub>3</sub> and glycine, no flame combustion was observed. This indicates that titania particles act as an inhibitor for the combustion reaction. Hence, an additional oxidizer was utilized in the form of NH<sub>4</sub>NO<sub>3</sub>, which resulted in flame combustion. The Rietveld refinement of the XRD pattern of the powder produced after flame combustion using NH<sub>4</sub>NO<sub>3</sub> as extra oxidizer is shown in Fig 2. The reflections of the pattern correspond to monoclinic polymorph of Li<sub>2</sub>TiO<sub>3</sub>. The lattice parameters obtained after Rietveld refinements are in good agreement with the reported values of the monoclinic polymorph of Li<sub>2</sub>TiO<sub>3</sub>.

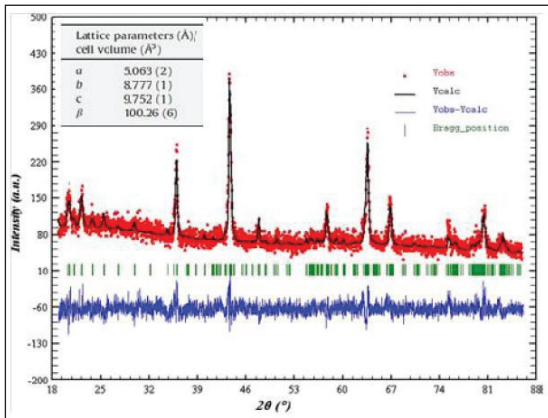


Fig. 2. Rietveld refinement pattern of lithium titanate powder

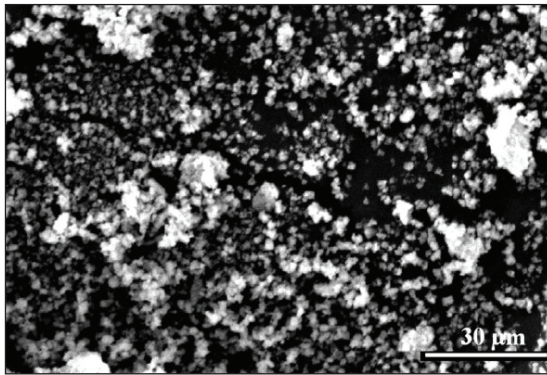


Fig. 3. SEM photomicrograph of lithium titanate powder prepared through combustion synthesis.

The above XRD result indicates that in the present investigation, the desired  $\text{Li}_2\text{TiO}_3$  phase could be produced after combustion synthesis which calls for no further calcination step for phase formation.

### 3.2 Sintering of behaviour of $\text{Li}_2\text{TiO}_3$

Fig. 3 shows the SEM photomicrograph of  $\text{Li}_2\text{TiO}_3$  powder prepared at pH 8. The powder seems to be slightly agglomerated which may be due to partial local sintering during the combustion reaction. The SEM photomicrograph of the fracture surface of  $\text{Li}_2\text{TiO}_3$  specimen sintered at  $1100^\circ\text{C}$  for 2 h which was derived from

combustion synthesized powder is shown in Fig.4. The microstructure is porous having uniform interconnected porosity.

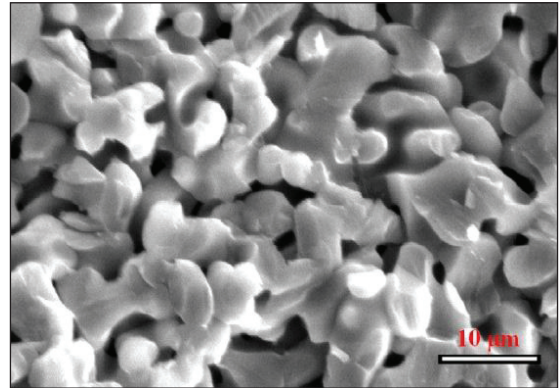


Fig. 4. Fracture surface of  $\text{Li}_2\text{TiO}_3$  ceramic specimen sintered at  $1100^\circ\text{C}$  for 2 h

In order to study the effect of sintering temperature on the densification behaviour of as synthesized  $\text{Li}_2\text{TiO}_3$  powder derived from solution of initial pH of 8.0, the green compacts were sintered at temperatures varying from  $900$  to  $1300^\circ\text{C}$  for 2 h. The relative densities of the sintered pellets are shown in Fig. 5. In general, the increase of sintering temperature increases the density of the compacts. It can be observed that  $\text{Li}_2\text{TiO}_3$  could be sintered to 90% TD at  $1300^\circ\text{C}$  which is comparable to the density obtained by rapid sintering [8]. The high density of sintered specimen of  $\text{Li}_2\text{TiO}_3$  can be attributed to small particle size of starting powder.

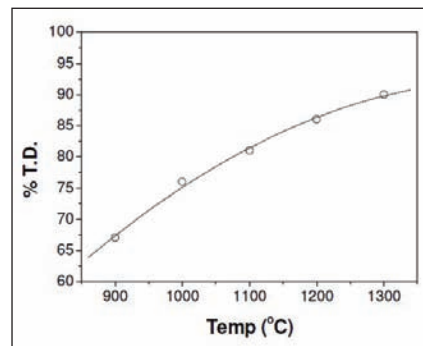


Fig. 5. Variation of sintered density of  $\text{Li}_2\text{TiO}_3$  specimens as a function of sintering temperature.

### 3.3. Synthesis of $\text{Li}_2\text{Be}_2\text{O}_3$

The high purity beryllium oxide after calcination at  $900^\circ\text{C}$  contains some soft agglomerates as shown by particle size analysis (Fig. 6) of the powder which exhibits the bimodal distribution of BeO powder particles. The soft agglomerates were broken with a ball milling operation and the particle size distribution of the billed powder is shown in Fig 7.

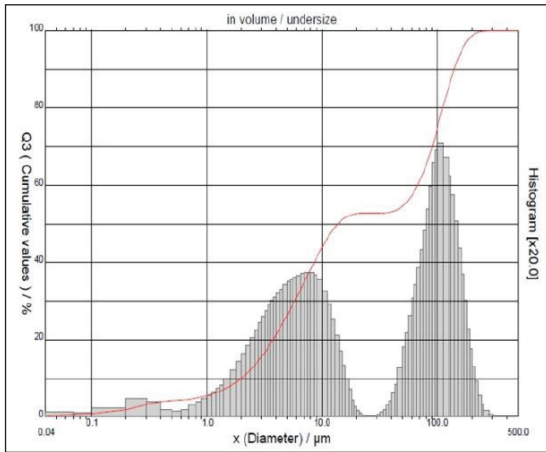


Fig. 6. Particle size distribution of calcined BeO powder

It can be observed that the powder particles of BeO after ball-milling are having a narrow size distribution with a median particle size of 1.37 μm.

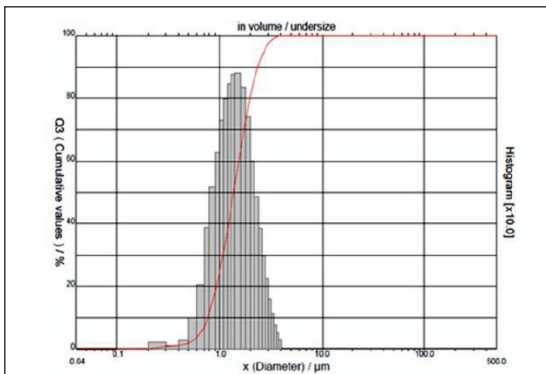


Fig. 7. Particle size distribution of ball milled BeO powder

Fig 8. shows the XRD pattern of the powder produced by grinding of the reaction-sintered compact of BeO- $\text{Li}_2\text{CO}_3$  at  $850^\circ\text{C}$  under air. The pattern exhibits all the peaks corresponding to lithium beryllate ( $\text{Li}_2\text{Be}_2\text{O}_3$ ) phase.

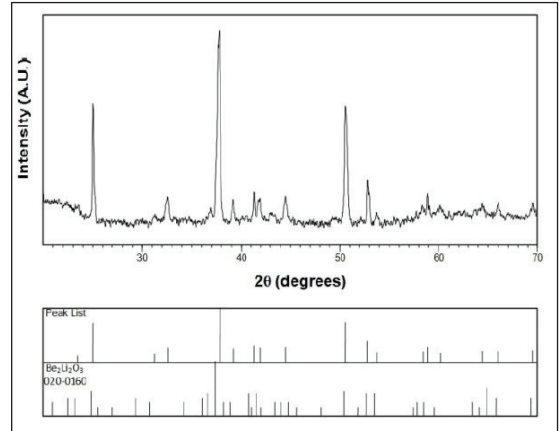


Fig. 8. XRD pattern of  $\text{Li}_2\text{Be}_2\text{O}_3$  powder produced at  $850^\circ\text{C}$

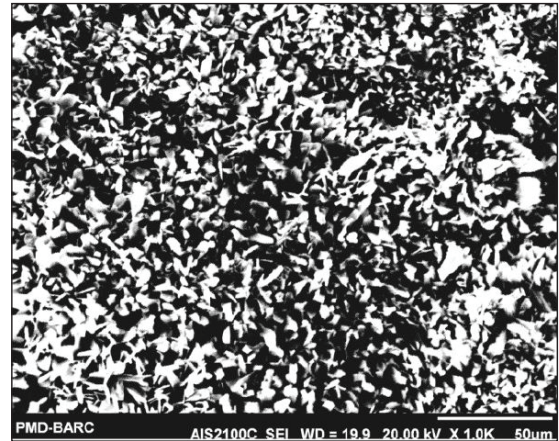


Fig. 9. SEM photomicrograph of porous lithium beryllate specimen

SEM photomicrograph of reaction-sintered lithium beryllate specimen is shown in Fig 9. The figure exhibits uniform porous microstructure of the beryllate ceramics having a sintered density of 80 % T.D.

### Conclusions

$\text{Li}_2\text{TiO}_3$  powder was prepared using a novel solid-liquid combustion synthesis that yielded directly the monoclinic phase of  $\text{Li}_2\text{TiO}_3$  after combustion. The process does not call for any additional heat treatment for phase formation. The pH of the starting solution influences the degree of agglomeration and eventual sinterability of the as-produced powder.  $\text{Li}_2\text{TiO}_3$  powder prepared using a solution pH of 8 exhibited better sinterability. Lithium beryllium oxide could be synthesized by using indigenously made high purity beryllium oxide and commercial lithium carbonate by solid state reaction and heating at 850°C

### References

- [1] N. Roux, S. Tanaka, C. Johnson, R Verrall, *Fus. Eng. Des.* **41** (1998) 31
- [2] E. Proust, L. Anzidei, M.D. Donne, U. Fischer, T. Kuroda, *Fus. Eng. Des.* **16** (1991) 73.
- [3] J.D. Lulewicz, N. Roux, G. Piazza, J. Reimann, J. van der Laan, *J. Nucl. Mater.* **283–287** (2000) 1361.
- [4] O. Renoult, J.P. Boilot, J.P. Korb, M. Boncoeur, *J. Nucl. Mater.* **223** (1995) 126.
- [5] A. Deptula, W. Lada, T. Olczak, A. G. Chmielewski, B. Sartowska, K. Goretta, C. Alvani, S. Casadio, *NUKLEONIKA* **46** (3) (2001) 95.
- [6] C. Alvani, P.L. Carconi, S. Casadio, F. Pierdominici, in: J.V. van der Laan (Ed., NRG), *Proceedings of the 7<sup>th</sup> International Workshop on Ceramic Breeder Blanket Interactions*, Petten, 1998, pp. 4-69-4-80.
- [7] C.H. Jung, J.Y. Park, S.J. Oh, H.K. Park, Y.S. Kim, D.K. Kim, J.H. Kim, *J. Nucl. Mater.* **253** (1998) 203.
- [8] Y.W. Rhee, J.H. Yang, K.S. Kim, K.W. Kang, K.W. Song, D.J. Kim, *Thermochim. Acta* **455** (2007) 86.



# FABRICATION OF (Th, Pu)O<sub>2</sub> MOX FUEL PELLETS USING POP AND CAP PROCESS FOR EXPERIMENTAL IRRADIATION IN RESEARCH REACTOR

A. K. Mishra, P. M. Khot, S. K. Shotriya, K. Subbaraya, Niraj Kumar, B. Singh, B. Surendra, P. G. Behere, Mohd. Afzal

Advanced Fuel Fabrication Facility, Bhabha Atomic Research Centre, Tarapur, India

**Abstract:** India has chalked out a nuclear power program based on its domestic resource position of uranium and thorium. Thorium utilization has been an important aspect in third stage for long term sustainability of nuclear program. As a step towards this, thorium based 300 MWe Advanced Heavy Water Reactor (AHWR) has been designed where (Th-U<sup>233</sup>)O<sub>2</sub> MOX fuel along with (Th-Pu)O<sub>2</sub> MOX will be used in equilibrium core. In order to study the behaviour of thorium based MOX fuel such as (Th-1%Pu)O<sub>2</sub> and (Th-8%Pu)O<sub>2</sub> in terms of fission gas release, fuel centreline temperature, fuel pellet swelling, and fuel grain growth experimental irradiation in research reactor is planned out which simulates actual condition of AHWR MOX fuel pin. Advanced Fuel Fabrication Facility (AFFF) has taken up the responsibility of fabrication of (Th-1%Pu)O<sub>2</sub> and (Th-8%Pu)O<sub>2</sub> MOX fuel via POP and CAP route.

(Th-1%Pu)O<sub>2</sub> and (Th-8%Pu)O<sub>2</sub> MOX was fabricated by Powder Oxide Pelletization (POP) route. Powder Oxide Pelletization route involves co-milling of milled ThO<sub>2</sub> powder with calcined PuO<sub>2</sub>, precompaction, granulation, final compaction followed by sintering in reducing atmosphere at 1650°C. Fabrication of (Th-1%Pu)O<sub>2</sub> was also carried out by Coated Agglomerate Pelletization (CAP) technique developed at AFFF. This route involves making spheroids of milled ThO<sub>2</sub> powder using extrusion and spherodization technique then coating of ThO<sub>2</sub> spheroids with desired amount of calcined PuO<sub>2</sub> powder followed by final compaction and sintering in reducing atmosphere. Necessary modifications in process parameters have been made and the tool design was so chosen to get sintered to sized pellet to avoid grinding.

(Th-1%Pu)O<sub>2</sub> and (Th-8%Pu)O<sub>2</sub> MOX pellets fabricated by POP and CAP route meets all desired specification. This paper deals with the procedure for fabrication of thorium based mixed oxide pellet by CAP as well as POP route and characterization of fuel pellets. The (Th-Pu)O<sub>2</sub> MOX pellets fabricated from POP and CAP route were characterized for density, O/M ratio, metallic impurities,  $\alpha$ -autoradiography and the results obtained were compared. The CAP route has the numerous advantages over POP route like small number of process steps and reduction of man-rem. This paper also highlights feasibility of CAP route for fabrication of (Th-Pu)O<sub>2</sub> fuel pellets.

**Keywords:** AHWR, (Th, Pu)O<sub>2</sub> MOX, POP, CAP

## 1. Introduction:

India has a three stage nuclear power program based on its domestic resource position of uranium and thorium. Thorium utilization is an important aspect in third stage of nuclear power program. Construction of thorium based 300 MWe Advanced Heavy Water Reactor (AHWR) is an important step for this purpose. (Th-Pu)O<sub>2</sub> and (Th-<sup>233</sup>U)O<sub>2</sub> is the proposed fuel for the equilibrium core of Advanced Heavy Water Reactor (AHWR) [1,2].

AFFF, BARC, Tarapur has gained considerable experience in MOX fuel fabrication. MOX has been fabricated and supplied for BWR, PHWR and FBTR. Recently AFFF has taken responsibility of (Th-Pu) MOX fuel pin fabrication for experimental irradiation in research reactor. In order to study the behavior of thorium based fuel in terms of fission gas release, fuel centerline temperature, fuel pellet swelling, and fuel grain growth experimental irradiation in research

# FABRICATION OF (Th, Pu)O<sub>2</sub> MOX FUEL PELLETS USING POP AND CAP PROCESS FOR EXPERIMENTAL IRRADIATION IN RESEARCH REACTOR

reactor is planned out which simulates actual condition of AHWR MOX fuel pin.

The mixed oxide pellets are generally prepared by the conventional powder metallurgy route. Mixed oxide (Th-1%Pu)O<sub>2</sub> fuel pellets for experimental irradiation have been fabricated successfully using ThO<sub>2</sub> and PuO<sub>2</sub> powder as a starting material through Powder oxide Pelletization (POP) as well as Coated Agglomerate Pelletization (CAP) route. Also (Th-8%Pu)O<sub>2</sub> fuel pellets has been fabricated via Powder oxide Pelletization (POP) route.

## 2. Fabrication of Mixed (Th-Pu) Oxide Fuel Pellet Via Pop Route:

The flow sheet for fabrication of (Th-1%Pu)O<sub>2</sub> and (Th-8%Pu)O<sub>2</sub> MOX fuel which is as shown in Fig.1. ThO<sub>2</sub> and PuO<sub>2</sub> powders prepared via oxalate route of specified characteristics given in Table 1 and used for fabrication of mixed (Th-Pu) fuel pellet.

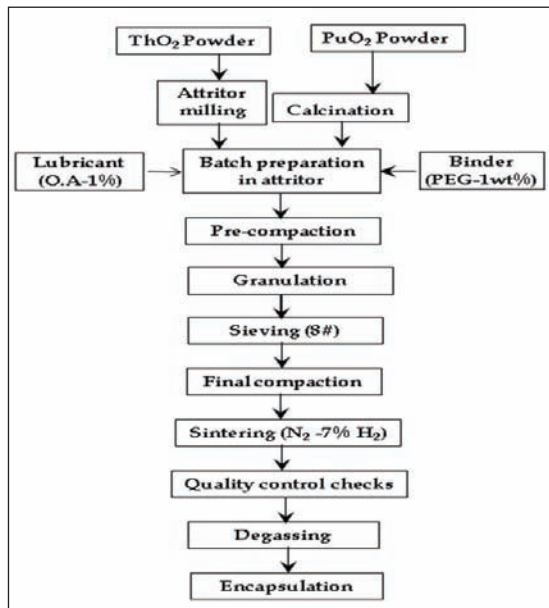


Fig. 1 Flow sheet for Powder Oxide Pelletization (POP) route for (Th-1%Pu)O<sub>2</sub> and (Th-8%Pu) O<sub>2</sub> MOX fuel fabrication

Table 1 Characteristic ThO<sub>2</sub> and PuO<sub>2</sub> powders prepared via oxalate route

Sr.No	CHARACTERISTICS	ThO <sub>2</sub> POWDER	PuO <sub>2</sub> POWDER
i)	Apparent density (gm/cm <sup>3</sup> )	0.70	1.20
ii)	Specific Surface Area	1.53	13.6
iii)	Theoretical density	10.00	11.46
iv)	Oxygen to Metal Ratio	2.00	2.00
v)	Total impurities (ppm)	<1200	< 1200

As received ThO<sub>2</sub> powder was milled in attritor at 200 rpm for 20 minutes to break its platelet morphology. Milled ThO<sub>2</sub> powder, PuO<sub>2</sub> powder with organic binder as Polyethylene Glycol and lubricant as Oleic acid were weighted in specified proportion and milled in attritor at 200 rpm for 30 minutes. Proper choice of binder and lubricant has a considerable significance in achieving desired specification of pellets [3] Mixed powder was precompacted at 6-8 TSI and pre-compacts were granulated in oscillatory granulator and sieved through # 10 mesh. Eventually, final compaction of granulated powder was done at 18-20 TSI in double acting hydraulic press and density of the compacts was kept in the range of 6.00 to 6.20 gm/cm<sup>3</sup>. Green compacts were sintered in batch type resistance furnace at 1650°C ± 25°C for 4 Hr in reducing atmosphere.

## 3. Fabrication of Mixed (Th-Pu) Oxide Fuel Pellet Via Cap Route:

### 3.1 Equipments:

**3.1.1 Extruder:** The extruder used consists of two rollers rotating in opposite direction. The first roller has holes of different sizes of 1 mm, 2 mm and 3 mm throughout. The second roller is plane and was used for forcing feed through the first roller to get extrudes. The unextruded material falling down was recycled back.

**3.1.2. Spherodiser:** The extrudes obtained from the extruder were used as a feed material to the spherodiser. It has a checker plate with 45 deg angle. It made a variable circular motion normally

# FABRICATION OF (Th, Pu)<sub>2</sub> MOX FUEL PELLETS USING POP AND CAP PROCESS FOR EXPERIMENTAL IRRADIATION IN RESEARCH REACTOR

50 - 200 rpm. If the revolution was further increased, the extrudes started to be converted into fines. The extrudes loaded in spherodiser were broken and rounded by chequered plate rotating at an optimum speed.

**3.1.2 Tablet coating pan:** The coating pan was SS 304 semi ellipsoidal size pan with a circular mouth of 250 mm dimension for charging and discharging of spheroids. Pan was mounted at an inclination of 45° to the horizontal. The tablet coating pan was provided with spiral ribbon (baffle), which was attached to the shell. The coating pan makes rotating motions both clockwise and anticlockwise at 50 rpm. The spray nozzle and hot air dryer are attachments to the coating pan for coating and drying, respectively. Spray guns are stationary which were mounted on a SS stand. The direction and angle of the spray guns can be adjusted.

### 3.2 Process:

The flow sheet for fabrication of (Th-Pu) MOX fuel which is divided in shielded and unshielded facility is as shown in Fig.2.

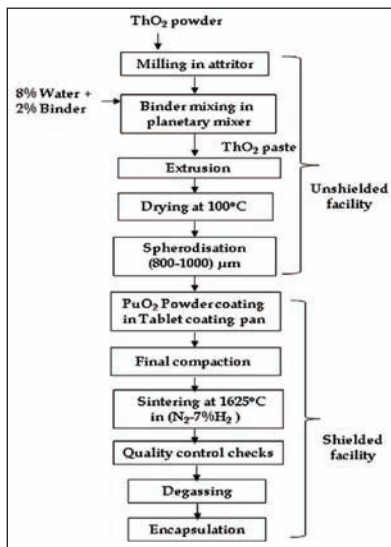


Fig. 2 Flow sheet for Coated Agglomerate Pelletization (CAP) route for (Th-1%Pu) MOX fuel fabrication

### 3.2.1 Extrusion and Spherodisation:

As received ThO<sub>2</sub> powder was milled in attritor at 200 rpm for 40 min using high chromium steel ball so as to break its platelet morphology. The milled ThO<sub>2</sub> powder was converted into free flowing agglomerate by extrusion spherodization route. The extrusion route involves mixing of milled ThO<sub>2</sub> powder with 1.2 % organic binder (polyethylene glycol), 0.8 % lubricant (oleic acid) and 8 % water in desired proportion with the help of planetary mixer. The ThO<sub>2</sub> paste obtained was extruded through the perforated rollers. ThO<sub>2</sub> extrudes so obtained were dried in an oven at 100°C for 2 h to achieve sufficient handling strength for spherodization. The dried extrudes were converted into the agglomerate with the help of spherodiser. Optimum organic emulsion addition eliminates the external lubrication requirement during compaction and helps in attaining good strength of pellet [4].

From Table 2 it was observed that agglomerate obtained through extrusion Spherodisation route shows higher tap density and narrower particle size distribution.

Table 2 Physical characteristic of Agglomerate

Agglomerate	Binder %	Apparent density (g/cc)	Tap density (g/cc)	Size (µm)
Precompacts granules	2	2.54	3.335	<1500
Spheroids	2	2.702	3.442	< 1000

### 3.2.2 Coating:

Coating of ThO<sub>2</sub> spheroids with desired amount of calcined PuO<sub>2</sub> powder were carried out in tablet coating pan with baffle rotating at 50 rpm.

### 3.2.3 Final compaction and Sintering:

Eventually final compaction of coated spheroids were carried out using tools of proper diameter at 18-20 TSI in double acting hydraulic press. Density of the green compact was found to be in the range of 6.40 to 6.60 gm/cm<sup>3</sup>. Sintering of (Th-1%Pu) MOX fuel pellet was done in batch type

# FABRICATION OF (Th, Pu)O<sub>2</sub> MOX FUEL PELLETS USING POP AND CAP PROCESS FOR EXPERIMENTAL IRRADIATION IN RESEARCH REACTOR

molybdenum resistance heating furnace under controlled reducing atmosphere (N<sub>2</sub>+ 7 Vol % H<sub>2</sub>) at 1650°C ± 25°C for 8 hr to obtain acceptable quality pellet

Physical and Chemical specification of (Th-1% Pu) MOX fuel pellet for experimental irradiation are given Table 3 and 4 respectively.

Sr.No	CHARACTERISTICS	SPECIFICATIONS
i)	Density of the pellet	90-95 % of T.D
ii)	Diameter of the pellet	9.7± 0.10 mm
iii)	L/D Ratio	0.5 to 1.0
iv)	Grain Size	5 to 50 µ

*Table 3: Physical specifications of (Th-U)O<sub>2</sub> MOX fuel pellets.*

Sr. No	CHARACTERISTICS	SPECIFICATIONS
i)	Enrichment	1± 0.10 % PuO <sub>2</sub>
ii)	O/M ratio	1.98-2.00
iii)	Total impurities	< 2500 ppm
iv)	E.B.C	<2.5 ppm

*Table 4: Chemical specifications of (Th-U) O<sub>2</sub> MOX fuel pellets.*

### 3.3 Process parameters:

The various process parameters of the CAP process i.e. organic emulsion, spheroids size, coating technique, compaction and sintering have been optimized as it has important bearing on macroscopic and atomic homogeneities in the mixed oxide fuel

## 4. Results & Discussion:

### 4.1 Density

The green and sintered density was measured geometrically. The density and O/M ratio of the pellets sintered in reducing atmosphere (N<sub>2</sub>+7%H<sub>2</sub>) at 1650°C for 4 h of different composition was compared (Table 5).

From the above results it was clear that high density (Th,Pu)O<sub>2</sub> pellet can be fabricated using POP and CAP process. It was possible to make high density (Th,Pu)O<sub>2</sub> pellet by CAP process without addition of any conventional dopants such as Nb<sub>2</sub>O<sub>5</sub>, CaO and MgO.

From the table it has been observed that (Th,1%Pu)O<sub>2</sub> pellets fabricated via CAP route showed slightly higher green density, but similar sintered density like POP route. However, (Th,8%Pu)O<sub>2</sub> pellets fabricated via POP route showed higher green density as well as sintered density as compared to (Th,1%Pu)O<sub>2</sub> pellets fabricated via POP and CAP route.

### 4.2 O/M ratio:

O/M ratio of the sintered pellet was measured thermogravimetrically (Table 5). The O/M ratio of (Th,8%Pu)O<sub>2</sub> pellet was slightly lower than that of (Th,1%Pu)O<sub>2</sub> pellet may be due to higher PuO<sub>2</sub> content which in turn increases oxygen potential.

Composition	Fabrication Method	Green Density (g/cc)	Sintered Density (g/cc) (%TD)	O/M
(Th-1%Pu)O <sub>2</sub>	POP	6.44-6.59	9.36-9.52	2.004±0.002
(Th-1%Pu)O <sub>2</sub>	CAP	6.58-6.68	9.34-9.52	2.004±0.002
(Th-8%Pu)O <sub>2</sub>	POP	6.55-6.77	9.64-9.72	2.000±0.002

*Table 5: Density and O/M ratio of (Th,Pu)O<sub>2</sub> pellets sintered in reducing atmosphere*

### 4.3 Metallic impurities:

The metallic impurities of sintered (Th,1%Pu)O<sub>2</sub> and (Th,8%Pu)O<sub>2</sub> pellet determined by atomic emission spectroscopy (AES) using DC arc as an excitation source are shown in Table 6. All the metallic elements including critical elements B and Cd were found to be within specification limits.

# FABRICATION OF (Th, Pu)O<sub>2</sub> MOX FUEL PELLETS USING POP AND CAP PROCESS FOR EXPERIMENTAL IRRADIATION IN RESEARCH REACTOR

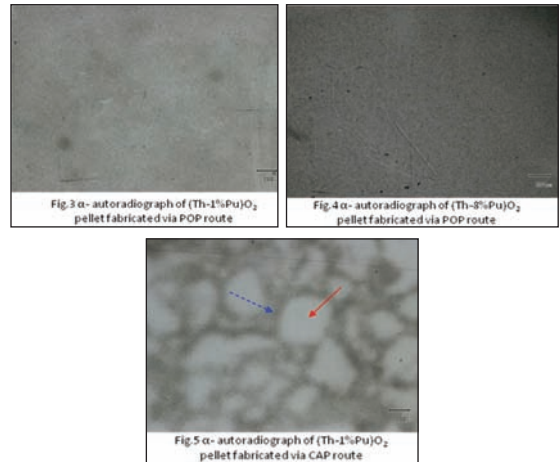
**Table 6: Metallic impurities in a typical sintered (Th,1%Pu)O<sub>2</sub> and (Th,8%Pu)O<sub>2</sub> pellet**

Sr. No	Element	Specification in ppm	(Th,1%Pu)O <sub>2</sub> sintered pellet fabricated via POP	(Th,1%Pu)O <sub>2</sub> sintered pellet fabricated via CAP	(Th,8%Pu)O <sub>2</sub> sintered pellet fabricated via POP
1	B	1	0.87	0.7	0.9
2	Cd	1	0.26	0.4	0.13
3	Cr	400	29	50	34
4	Cu	400	47	19	3.2
5	Fe	800	174	110	343
6	Mg	400	240	148	233
7	Mo	400	26	45	51
8	Na	400	< 10	20	11
9	Ni	400	< 10	41	28
10	Pb	400	< 10	20	39
11	V	400	< 10	5.4	<5
12	Zn	400	55	50	62
13	Al	25	22	18	24
14	Ca	500	56	35.7	65
15	Si	400	345.5	343.5	399

### 4.4 α-autoradiography:

The homogeneity of (Th,1%Pu)O<sub>2</sub> and (Th,8%Pu)O<sub>2</sub> fuel pellet was evaluated by α-autoradiography. The presence of fissile rich zone in mixed oxide fuel pellet leads to higher fission gas release and fuel failure due to hot spot formation [5]. So it was necessary that size of agglomerate should be as low as possible and its distribution through the matrix should be uniform.

The maximum size of Pu cluster allowed in the pellet was 400 μm. From Fig.3 and 4 it has been observed that, α-autoradiograph of (Th,1% Pu)O<sub>2</sub> and (Th,8% Pu)O<sub>2</sub> fuel pellet fabricated via POP route showed uniform distribution of plutonium in thorium matrix. It did not show any Pu agglomerate greater than 100 μm. From Fig.3 and 5 it was observed that, the homogeneity of (Th-1%Pu) MOX pellet fabricated via POP route was better than that of pellet fabricated via CAP route. The α-autoradiograph (Th-1%Pu) MOX pellet fabricated via CAP route showed non uniform distribution of plutonium in thorium matrix. The peripheral area of spheroid showing higher PuO<sub>2</sub> concentration which is indicated by dotted arrow. On the other hand, solid arrow showed in Fig. 5 indicates PuO<sub>2</sub> deficient area. The α-autoradiograph (Th-1%Pu)O<sub>2</sub> MOX pellet fabricated via CAP route didn't show any agglomerate greater than 400 μm.



In CAP route non-uniform sticking of PuO<sub>2</sub> powder to ThO<sub>2</sub> spheroids during coating leads to fissile rich and deficient area observed in α-autoradiograph. In order to achieve good homogeneity (Th-1%Pu) MOX pellet, distant diffusion (~800 μm) of plutonium atom during sintering was needed for fuel fabricated by CAP route. In POP route through mixing of particle of size 0.6 μm (ThO<sub>2</sub>) and 2-3 μm (PuO<sub>2</sub>) was carried out in attritor. The better homogeneity in (Th-1%Pu) MOX pellet fabricated via POP route is due to significant reduction in diffusion distance needed.

### 5. Conclusion:

- Significant quantity of (Th-1%Pu)O<sub>2</sub> and (Th-8%Pu)O<sub>2</sub> MOX pellets have been fabricated successfully using existing facility of AFFF, Tarapur for experimental irradiation in research reactor.
- The various process parameters of POP and CAP process for fabrication of (Th-1%Pu) O<sub>2</sub> and (Th-8%Pu)O<sub>2</sub> MOX pellet were optimized. (Th-1%Pu)O<sub>2</sub> and (Th-8%Pu)O<sub>2</sub> MOX pellets fabricated via POP and CAP route meets all desired physical and chemical specification
- (Th,1% Pu)O<sub>2</sub> and (Th,8% Pu)O<sub>2</sub> fuel pellet fabricated via POP route showed uniform distribution of plutonium in thorium matrix.

## FABRICATION OF (Th, Pu)O<sub>2</sub> MOX FUEL PELLETS USING POP AND CAP PROCESS FOR EXPERIMENTAL IRRADIATION IN RESEARCH REACTOR

---

- (Th-1%Pu)O<sub>2</sub> pellet fabricated by CAP didn't show any agglomerate greater than specified limit. However, from  $\alpha$ -autoradiograph it was observed that, the homogeneity of (Th-1%Pu) O<sub>2</sub> pellet fabricated by POP route was better to that of pellet fabricated by CAP route.
- From the above results it is possible to conclude feasibility of CAP route for fabrication of (Th-Pu)O<sub>2</sub> fuel pellets as well as it has the advantages over POP route like small number of process steps, minimization of powder handling and reduction of man-rem.

### Acknowledgement:

Authors are very thankful to all the staff members of Oxide Fuel Section (OFS) for their active support in carrying out this work.

### References:

1. A. Kakodkar, Proc. 46th General Conference of the International Atomic Energy Agency, IAEA, Vienna, 2002.
2. Design and Development of the AHWR—the Indian Thorium Fuelled Innovative Nuclear Reactor Nuclear Engineering and Design, vol. 236, pp. 683–700, (2006).
3. S.Mishra, S.N.Rahul, I.D.Godbole, A.K.Mishra, Arun Kumar and H.S.Kamath, "Use of Polyethylene Glycol and Oleic acid in Fabrication of Nuclear fuel pellets", paper presented at International Conference of PMAI, (1999).
4. P.S.Somayajulu, Y.G.Nehete, P.D.Sughathan, S.Mishra, A.K.Mishra, Arun Kumar & H.S.Kamath, "New Technique in Powder Processing and Pelletization in Nuclear Fuel Fabrication", paper presented at International Conference of PMAI, (2000).
5. B.H.Lee, Y.H.Koo, D.S.Sohn, "Nuclear Fuel Behaviour Modelling at High Burn-up and its Experimental Support", IAEA-TECHDOC-1233, IAEA, Vienna, 247, (2001).



# INFLUENCE OF HEAT TREATMENT ON CORROSION BEHAVIOR OF Co-Cr-Mo ALLOY DEPOSITED WITH LASER ENGINEERED NET SHAPING

Dr. Mantrala Kedar Mallik, Sk. Abdul Munaf

Vasireddy Venkatadri Institute of Technology, Guntur, A.P., India

**Abstract :** Electro chemical behavior of Co-Cr-Mo alloy samples deposited with Laser Engineered Net Shaping, an additive manufacturing process has been studied. The experimentation was in two stages. In first stage the samples were fabricated with three process parameters (Laser power, Powder feed rate and scan speed) at two levels. Corrosion resistance tests were conducted and the results were analyzed using grey relational analysis and ANOVA. Another set of samples with process parameters of the samples with low corrosion resistance were fabricated. Heat treatment was applied at three parameters and three levels. Again the corrosion resistance tests were conducted and analyzed. The results revealed that the corrosion resistance of Co-Cr-Mo alloy samples has been increased with LENS deposition when compared to as cast samples and further enhanced by proper heat treatment.

*Key words:* Additive manufacturing, Co-Cr-Mo, Corrosion resistance, ANOVA, Grey relational analysis.

## Introduction

Most often the characteristics of the materials vary with the composition, process of fabrication, heat treatment applied and parameters of testing etc. In such processes, properties like hardness, wear resistance, corrosion resistance etc. are studied. Microstructure and phase analysis of the material also helps in understanding the properties of the same.

Many researchers have experimented with Co-Cr-Mo alloys with different methods under different conditions. Leandre Casaban Julien et al have used electrochemical techniques to analyze the corrosion and tribological behavior of high carbon as cast Co-Cr-Mo alloy subjected to different thermal treatments in simulated body fluids. It has been observed that the increase of grain boundaries accelerate the anodic reaction. The wear particles in the protein solution tend to agglomerate and sediment near the wear tracks [1]. Roberto Alonso Gil et al have analyzed 'as cast' high carbon Co-Cr-Mo alloy immersed in Phosphate Buffered Solution (PBS) and PBS with Bovine Serum Albumin (PBS + BSA) by electro chemical technique and surface microscopy for

their corrosion and tribocorrosion behavior. It has been observed that BSA acts as lubricant and reduces the total wear. The wear rate decreases with the sliding velocity when cathodic potential was applied whereas Anodic potential does not show any affect. Both anodic and cathodic current densities increase with sliding velocity with anodic and cathodic potentials applied respectively [2]. D. Sun et al have conducted experiments on Co-Cr-Mo alloys to evaluate the abrasion - corrosion in 0.9% NaCl, phosphate buffered saline solution and bovine serum solutions and revealed that the presence of proteins increased the total specific wear rate. A severely deformed nano-crystalline layer was identified immediately below the worn surfaces [3]. M.T. Mathew et al have studied tribocorrosion behavior of Co-Cr-Mo alloy for hip prosthesis as a function of loads [4]. J. A. Ortega-Saenz et al have modified the surfaces of medical grade Co-Cr-Mo alloys samples by Plasma Nitriding, Physical Vapor Deposition (PVD) coating and the combination of the above two, to study the tribological and corrosion behavior of the samples. The results of ball-on-disc wear resistance test and potentiodynamic polarization

## INFLUENCE OF HEAT TREATMENT ON CORROSION BEHAVIOR OF Co-Cr-Mo ALLOY DEPOSITED WITH LASER ENGINEERED NET SHAPING

measurements revealed that the PVD coated surface have shown higher corrosion resistance and wear resistance and the material is good alternative in human joint application [5]. Stefano Mischler and Anna Igual Mufioz in their review mentioned that degradation of Co-Cr-Mo alloys in water lubricated contacts is critically affected by the prevailing electrochemical conditions. Wear accelerated corrosion due to de-passivation of worn areas is likely to contribute significantly in the overall contact degradation [6].

It was well established from the above and other literature survey conducted that almost all the experiments were with as-cast Co-Cr-Mo and the present investigation is an attempt to understand the corrosion behavior of Co-Cr-Mo alloy when deposited with Laser Engineered Net Shaping.

### Experimentation

Commercially available Co-Cr-Mo alloy has been selected for analysis of the effect of heat treatment on corrosion behavior the composition of which is shown in Table 1. L4 orthogonal array of Taguchi method (Three process parameters at two levels) has been applied for fabrication of samples using Laser Engineered Net Shaping (LENSTM), a rapid prototyping method for metals. The process parameters selected are, laser power (200W and 350W), Powder feed rate (5g/min and 10g/min) and Scan speed (10mm/s and 20mm/s). The powder has been deposited for five layers on a 5mm thick weld deposited plate called substrate. The surfaces of the deposits are polished with abrasive papers of grit size from 200 to 1000 followed by polishing with alumina powder for smooth surface.

*Table 1: Composition of Co-Cr-Mo alloy in weight %*

Co	Cr	Mo	Fe	C	S	B	Mn	Ni	P	Si	W
Bal	27.6	5.6	1.4	0.2	0.003	0.002	0.6	2.74	0.004	1.7	0.2

Electrochemical measurements are performed on all the samples using an SP300 BIOLOGIC™ Frequency response analyzer (Fig. 1). Open circuit potential is measured for 10 minutes. Potentiodynamic polarization tests are performed by scanning the applied potential from -0.5 to 1.5  $V_{vs}$ . SCE (Saturated Calomel Electrode) at a scanning rate of 2mVs<sup>-1</sup>. The corrosion potential ( $E_{Corr}$ ) is obtained as the potential at which the net current density is equal to zero and the corrosion current density ( $I_{Corr}$ ) is extracted from the polarization curves of the linear part of the cathodic curve (Tafel behavior). Potentiodynamic measurements are recorded for one hour and the readings are analyzed using Zview 2.70 software. By Grey relational analysis, best process parameters for high corrosion resistance is obtained.

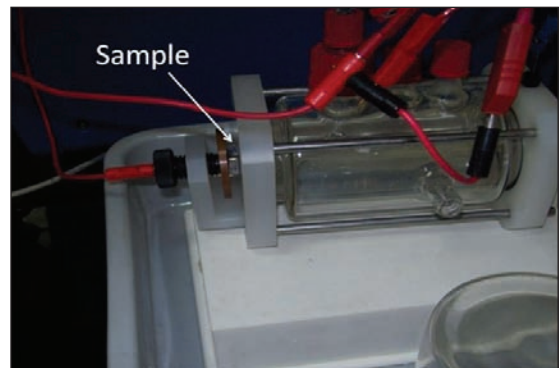


*Fig.1: Sample fixed in the apparatus for corrosion resistance test*

In the second stage, another set of nine samples are fabricated with process parameters that are found to be the least among the samples tested. Now L9 orthogonal array of Taguchi method (Three parameters at three levels) has been applied for heat treatment. The solution heat treatment has been carried out at 1200°C for 30, 45 and 60 minutes followed by water quenching. Six samples are subjected to aging at 830°C and 815°C

# INFLUENCE OF HEAT TREATMENT ON CORROSION BEHAVIOR OF Co-Cr-Mo ALLOY DEPOSITED WITH LASER ENGINEERED NET SHAPING

for 2, 4 and 6 hours and three samples are taken without aging (Table 2). All the nine samples are polished and tested for their corrosion resistance and again the Tafel plots are drawn. ANOVA (Analysis of Variance) has been applied on the corrosion resistance values to understand the effect of process parameters and heat treatment on the corrosion resistance.

*Table 2: L9 Orthogonal array of heat treatment on LENS deposited Co-Cr-Mo alloy samples*

Sl. No.	SAMPLE NO.	SOLUTION TREATMENT TIME (Min)	AGEING TEMPERATURE °C	AGEING TIME (HOURS)
1	S1	30	No Ageing	
2	S2	30	815	4
3	S3	30	830	6
4	S4	45	No Ageing	
5	S5	45	815	6
6	S6	45	830	2
7	S7	60	No Ageing	
8	S8	60	815	2
9	S9	60	830	4

## Results & Discussion

The results of the corrosion resistance tests reveal that, the corrosion resistance obtained was more than the wrought Co-Cr-Mo. ANOVA results reveal that the process parameters influence the corrosion resistance and maximum corrosion resistance can be obtained when proper process parameters are selected for deposition of samples and proper heat treatment is applied.

The Potentiodynamic curves (Tafel plots) shown in Fig. 2 reveal the corrosion behavior of the laser deposited Co-Cr-Mo samples. The two responses namely corrosion potential ( $E_{corr}$ ) and corrosion current density ( $I_{corr}$ ) are obtained from potentiodynamic tests (Table 3). Any material will have lower tendency to corrode if  $E_{corr}$  value tends to be positive and  $I_{corr}$  value to be less. To obtain the  $I_{corr}$  and  $E_{corr}$  values Tafel plots are used.

Evidently the sample P1 has shown high  $E_{corr}$  value and P2 has shown low  $I_{corr}$  value. Since there are two different responses for the output

the best samples cannot be decided directly from the values in Table 3. To convert a multivariate problem into a single response Grey relational analysis is used. The grey relational analysis is a widely accepted statistical method. To identify the best samples for high corrosion resistance, grey analysis has been applied for the values of Table 3.

The criterion for  $E_{corr}$  is higher the better and for  $I_{corr}$  is lower the better for generation of grey relation grade. The results shown in Table 4 reveal that P1 is the best sample for high corrosion resistance among the samples tested. Chromium is the material which has fewer tendencies to corrode and the sample P1 is rich in Chromium carbides [7, 8].

*Table 3: Corrosion current density and corrosion potential values of LENS deposited Co-Cr-Mo alloy samples*

Sample No.	Deposition parameters	$I_{corr}$ ( $\mu\text{A}/\text{cm}^2$ )	$E_{corr}$ (mV vs.SCE)
P1	200W, 5g/min, 10mm/s	0.103	<b>+028.85</b>
P2	200W, 10g/min, 20mm/s	<b>0.013</b>	-172.65
P3	350W, 5g/min, 20mm/s	4.628	-167.99
P4	350W, 10g/min, 10mm/s	1.258	-154.26

*Table 4: Grey relational analysis of LENS deposited Co-Cr-Mo alloy samples*

Sample No.	$E_{corr}$	$I_{corr}$	Normalized E.Max	Normalized I.Min	Delta	Grey coefficient	Grade	Order		
P1	+028.85	0.103	1.000	0.980	0.000	0.019	1.000	0.981	<b>1</b>	
P2	-172.65	0.013	0.000	1.000	1.000	0.000	0.333	1.000	0.667	<b>2</b>
P3	-167.99	4.628	0.023	0.000	0.977	1.000	0.338	0.333	0.336	<b>4</b>
P4	-154.26	1.258	0.091	0.730	0.909	0.270	0.354	0.649	0.502	<b>3</b>

The main effect plot for corrosion rate (Fig. 3) is in agreement with the results obtained that the sample P1 (200W laser power, 5g/min feed rate and 100m/s scan speed) has high corrosion resistance. The plot reveals that the process parameters have considerable influence on corrosion resistance of the material.

## INFLUENCE OF HEAT TREATMENT ON CORROSION BEHAVIOR OF Co-Cr-Mo ALLOY DEPOSITED WITH LASER ENGINEERED NET SHAPING

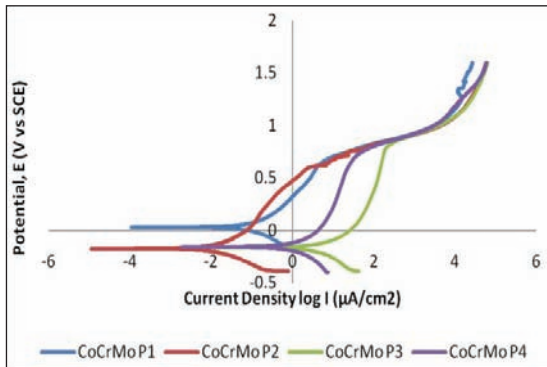


Fig. 2: Tafel plots for corrosion resistance of LENS deposited Co-Cr-Mo alloy samples

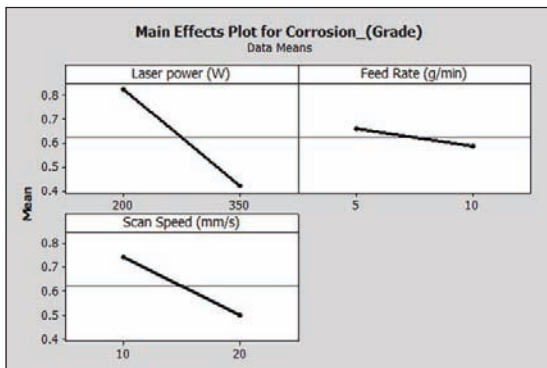


Fig. 3: Main effects plot for the corrosion grade of LENS deposited Co-Cr-Mo alloy samples

Corrosion resistance tests are conducted on the heat treated samples (S1 – S9) using the procedure mentioned earlier. Potentiodynamic curves (Tafel plots) drawn (Fig. 4) with Potential  $E$  (V vs. SCE) to Current density  $\log I$  ( $\mu\text{A}/\text{cm}^2$ ) have revealed the corrosion behavior of the heat treated samples. The  $I_{\text{corr}}$  values are decreased from  $4.628\mu\text{A}/\text{cm}^2$  (un-heat treated samples) to the range of  $0.046\mu\text{A}/\text{cm}^2$  to  $0.607\mu\text{A}/\text{cm}^2$  whereas the  $E_{\text{corr}}$  values showed mixed trend (Table 5) on applying heat treatment. The  $I_{\text{corr}}$  and  $E_{\text{corr}}$  values of as-cast Co-Cr-Mo alloy are in the range of  $0.8$  to  $5.4\mu\text{A}/\text{cm}^2$  and  $-762$  to  $-805\text{mV}$  respectively [1]. Obviously, the corrosion rate has decreased with respect to both  $I_{\text{corr}}$  and  $E_{\text{corr}}$  on

the LENS deposited samples. Further decrease in corrosion rate is evident after applying heat treatment in all the samples. This is primarily due to reduction in Cr in the matrix as a result of carbide precipitation. The chromium carbides act as temporary insulators between adjacent grains when they are precipitated along the grain boundaries. The insulation causes higher potential difference between the grains which in turn results in higher corrosion resistance [7, 8].

Table 5: Corrosion current density and corrosion potential values of heat treated LENS deposited Co-Cr-Mo alloy samples

Sample No.	$I_{\text{corr}}$ ( $\mu\text{A}/\text{cm}^2$ )	$E_{\text{corr}}$ (mV vs. SCE)
S1	0.108	-368.481
S2	0.203	-300.159
S3	0.217	-060.944
S4	0.420	<b>+064.389</b>
S5	0.438	<b>+085.128</b>
S6	0.276	-115.909
S7	<b>0.046</b>	-177.632
S8	0.607	-085.890
S9	0.390	-022.015
Un heat treated	4.628	-167.99

To study the combined effect of  $I_{\text{corr}}$  and  $E_{\text{corr}}$ , Grey Relational Analysis has been carried out (Table 6) and the results revealed that the sample S7 (samples solutionized at  $1200^\circ\text{C}$  for 45min without ageing) has highest corrosion resistance among the samples tested. The main effects plot is also in agreement with the results obtained (Fig. 5).

Table 6: Grey relational analysis of heat treated LENS deposited Co-Cr-Mo alloy samples

Sample No.	E <sub>corr</sub>	I <sub>corr</sub>	Normalized E <sub>Max</sub>	Normalized I <sub>Min</sub>	Delta	Grey coefficient	Grade	Order	
S1	-368	0.108	0.000	0.889	1.000	0.110	0.333	0.818	5
S2	-300	0.203	0.150	0.720	0.849	0.279	0.370	0.641	8
S3	-60	0.217	0.677	0.695	0.322	0.304	0.608	0.621	4
S4	64	0.420	0.954	0.333	0.045	0.867	0.916	0.428	3
S5	85	0.438	1.000	0.301	0.000	0.898	1.000	0.417	2
S6	-115	0.276	0.556	0.590	0.443	0.409	0.530	0.549	7
S7	-177	0.046	0.420	1.000	0.579	0.000	0.463	1.000	1
S8	-85	0.607	0.622	0.000	0.377	1.000	0.570	0.333	9
S9	-22	0.39	0.783	0.386	0.236	0.613	0.679	0.449	6

# INFLUENCE OF HEAT TREATMENT ON CORROSION BEHAVIOR OF Co-Cr-Mo ALLOY DEPOSITED WITH LASER ENGINEERED NET SHAPING

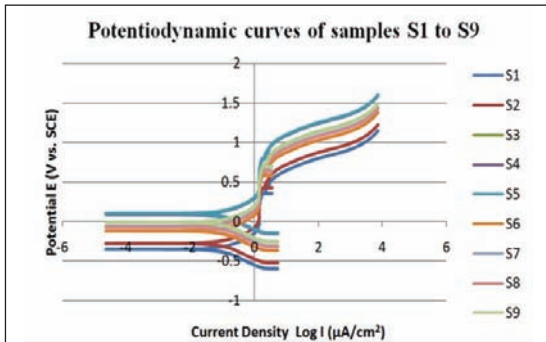


Fig. 4: Tafel plots for the heat treated LENS deposited Co-Cr-Mo alloy samples

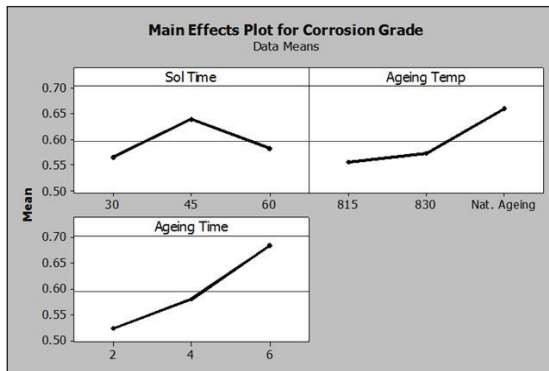


Fig. 5: Main Effects plot for corrosion grade of heat treated LENS deposited Co-Cr-Mo alloy samples

## Conclusions

The conclusions drawn from the experimentations are as follows.

The Co-Cr-Mo alloy samples have exhibited high corrosion resistance ( $0.103\mu\text{A}/\text{cm}^2$  and  $+28.85\text{ mV}$ ) than the as-cast samples ( $I_{\text{corr}}$  and  $E_{\text{corr}}$  values  $0.8\mu\text{A}/\text{cm}^2$  and  $-805\text{mV}$  respectively) with proper selection of process parameters

The corrosion resistance of LENS deposited Co-Cr-Mo alloy samples has been further increased by applying heat treatment

## References:

1. Leandre Casaban Julian, AnnaIguar Munoz, "Influence of microstructure of HC Co-Cr-Mo biomedical alloys on the corrosion and wear behavior in simulated body fluids", *Trib. Int.*, **44**, 318-329, (2011).
2. Roberto Alonso Gil, Anna Iguar Muñoz "Influence of the sliding velocity and the applied potential on the corrosion and wear behavior of HC Co-Cr-Mo biomedical alloy in simulated body fluids", *J. Mech. Behav. Biomed. Mater.*, **4**, 2090 - 2102, (2011).
3. D. Sun, J.A. Wharton, R.J.K. Wood, L. Ma, W.M. Rainforth, "Microabrasion-corrosion of cast Co-Cr-Mo alloy in simulated body fluids", *Trib. Int.*, **42**, 99-110, (2009).
4. M.T. Mathew, M.J. Runa, M. Laurent, J.J. Jacobs, L.A. Rocha, and M.A. Wimmer, "Tribocorrosion behavior of Co-Cr-Mo alloy for hip prosthesis as a function of loads: a comparison between two testing systems", *Wear*, **271**(9-10), 1210-1219, (2011).
5. J.A. Ortega-Saenz, M.A.L. Hernandez-Rodriguez, V. Ventura-Sobrevilla, R. Michalczewski, J. Smolik, M. Szczerek "Tribological and corrosion testing of surface engineered surgical grade Co-Cr-Mo alloy", *Wear*, **271**, 2125- 2131, (2011).
6. Stefano Mischler, Anna Iguar Munoz, "Wear of Co-Cr-Mo alloys used in metal-on-metal hip joints: A tribocorrosion appraisal", *Wear*, **297**, 1081-1094, (2013).
7. Kedar M Mantrala, Mitun Das, Vamsi K. Balla, Ch. Srinivasa Rao and V.V.S. Kesava Rao "Laser-deposited CoCrMo alloy: Microstructure, wear, and electrochemical properties", *J. Mater. Res.*, **29** (17), 2021-2027, (2014).
8. K. M. Mantrala, M. Das, V. K. Balla, C. S. Rao, V.V.S. Kesava Rao, "Additive manufacturing of Co-Cr-Mo alloy: influence of heat treatment on microstructure, tribological, and electrochemical properties", *Front. Mech. Engg.*, **1** (2), (2015).

